PTT-05

# Mathematical Modelling of Microstructural Development in Continuously Annealed High-Strength Steels

By
Naomi Chester
St. Catharine's College, Cambridge

Department of Materials Science and Metallurgy
Pembroke Street
Cambridge
CB2 3QZ

*A dissertation submitted for the degree of Doctor of Philosophy at the University of Cambridge*

September 1997

*"Our values are less wrong*
*than might be expected!"*

Student at the end of a first year practical class
1997

# Acknowledgements

I wish to thank Professor Alan Windle for the provision of laboratory facilities at the University of Cambridge. I am very grateful to Harry Bhadeshia for his time, enthusiasm and encouragement for this work. Many thanks are due to the technical staff in the Department of Materials Science and Metallurgy. I am also very grateful to the members of my research group, past and present, for their friendship and help, especially Catherine, John and Nick for their help in proof reading this thesis and John, Mike and Sally for help with the experimental and computing aspects of my work.

The financial support for this research was provided by British Steel Wales plc. and the European Coal and Steel Community. Thanks are due to Peter Evans of British Steel for his provision of samples and data. I am also grateful to Etienne Girault of the Department of Metallurgy and Materials Engineering, K.U. Leven, Belgium for the provision of experimental data.

The Worshipful Company of Ironmongers financed my visit and work at CEIT in San Sebastian, Spain and I am also very grateful to Isabel Gutierrez and Amai Iza Mendia of CEIT for their help in the work there.

I would like to thank all my friends in Cambridge, especially those in Methsoc who have helped keep me [in]sane during my 6 years in Cambridge. I am especially grateful to Michael and Chris for their help in the proof reading of this thesis. I am also indebted to David for his support and provision of cuddly toys over the years, as well as the use of his mathematical knowledge.

Finally I would like to thank my family, for their support and encouragement, especially to Dad for letting me become Dr Chester first!

# Abstract

The addition of an appropriate concentration of silicon to a low-alloy steel enables it to be transformed into a carbide-free microstructure which is a mixture of bainitic ferrite and carbon enriched austenite. Such steels can have outstanding mechanical properties, particularly formability and strength. The work presented in this thesis deals with alloys destined for the automobile industry where attempts are being made to reduce the weight of vehicles, while at the same time improve safety during crashes.

To do this requires a low-strength variant of a silicon-rich steel, typically of composition Fe-1.5Mn-2Si-0.15C wt.%, with a microstructure of allotriomorphic ferrite, bainitic ferrite, austenite and martensite. The purpose of the work was to better understand such steels with the particular aim of creating models for the further development of microstructure and mechanical properties.

The thesis begins with an introduction and literature survey dealing with the aim and industrial requirements, together with a discussion of relevant physical metallurgy and mechanical properties. It is demonstrated that whereas there is a great deal known about these steels there has been, with one exception, no attempt at quantitative alloy design.

Following a description of the experimental methods used throughout the work, Chapter 4 describes a new model for the kinetics of the bainite transformation. The model is based strictly on the mechanism of the bainite transformation and is compared against published and newly generated experimental data.

The model allows for the presence of prior allotriomorphic ferrite and produces excellent isothermal predictions and reasonable continuous cooling results, depending on the value of stored energy in bainite used. This stored energy is investigated in Chapter 5 where the surface relief caused by the bainite transformation is described. The relation between surface relief and the strain energy of the bainitic ferrite is discussed and justified using experimental measurements.

The transformations during intercritical annealing are investigated in Chapter 6. Firstly a model for the formation of austenite on heating is proposed. This is then coupled with existing theory for the formation of allotriomorphic ferrite during cooling, adapted for complicated cooling cycles. Two theories for the transformation of austenite to martensite are discussed and tested.

The transformation-induced plasticity phenomenon is reviewed in Chapter 8 and the microstructural changes on deformation of some intercritically annealed samples are characterised using transmission electron microscopy. Mechanical property data are then used to train neural network models for the prediction of yield strength, ultimate tensile strength, uniform elongation and the fraction of retained austenite.

Suggestions for future work are presented in Chapter 10. Details of the computer programs produced in this work and the data on which the neural network models were trained are provided in the Appendices 1-4.

# Nomenclature

| | |
|---|---|
| $\alpha$ | ferrite. |
| $\alpha'$ | martensite. |
| $\alpha_b$ | bainitic ferrite. |
| $\alpha_w$ | Widmanstätten ferrite. |
| $\alpha_1$ | one-dimensional parabolic thickening rate constant for allotriomorphic ferrite growth. |
| $a$ | width of bainite platelet in apparent shear measurement (μm). |
| $a'$ | function in equation 6.1. |
| $a_\alpha$ | lattice parameter of bainitic ferrite (Å). |
| $a_{e\gamma}$ | austenite lattice parameter after transformation (Å). |
| $a_\gamma$ | carbon enriched room temperature austenite lattice parameter (Å). |
| $a_{0\alpha}$ | room temperature ferrite lattice parameter (Å). |
| $a_{0\gamma}$ | room temperature austenite lattice parameter (Å). |
| $Ac_1$ | practical temperature at which austenite formation begins during continuous heating (°C or K). |
| $Ac_3$ | practical temperature at which austenite formation finishes during continuous heating (°C or K). |
| $Ae_1$ | equilibrium temperature at which austenite formation begins during continuous heating (°C or K). |
| $Ae_3$ | equilibrium temperature at which austenite formation finishes during continuous heating (°C or K). |
| $Ae_3'$ | paraequilibrium temperature at which austenite formation finishes during continuous heating (°C or K). |
| AFM | atomic force microscope. |
| $\beta$ | autocatalysis factor $\beta = \lambda_1\left(1-\lambda_2\bar{x}\right)$. |
| $\beta_v$ | function in equation 4.41. |
| $b$ | height in apparent shear measurement (μm). |
| b.c.c. | body-centred cubic. |
| $B_s$ | bainite-start temperature (°C or K). |
| $c$ | constant in equation 2.15. |
| $C_1$ - $C_7$ | constants. |
| $c_\alpha$ | carbon content of ferrite in wt.%. |
| $C_c$ | expansion in austenite lattice parameter caused by a unit concentration of carbon. |
| $c_\gamma$ | carbon content of austenite in wt.%. |
| $CCT$ | continuous cooling transformation. |
| $\delta$ | dilatational component of strain. |

| | |
|---|---|
| $d$ | d-spacing of lattice plane (Å). |
| $dv_e$ | change in extended volume fraction of bainitic ferrite. |
| $\varepsilon$ | ratio between the distance to an arbitrary plane and the half thickness of the allotriomorph at time $t$ for calculating allotriomorphic ferrite growth. |
| $e$ | engineering strain. |
| $e_\alpha$ | ferrite thermal expansion coefficient ($°C^{-1}$). |
| $e_\gamma$ | austenite thermal expansion coefficient ($°C^{-1}$). |
| $\phi$ | equilibrium volume fraction of allotriomorphic ferrite. |
| f.c.c. | face-centred cubic. |
| $f(x)$ | function $= \frac{x}{1\times 1!}+\frac{x^2}{2\times 2!}+\frac{x^3}{3\times 3!}+\ldots$ |
| $f_n$ | integration term in the calculation of allotriomorphic ferrite growth. |
| $\Gamma_2$ | function in equation 4.19. |
| $\gamma$ | austenite. |
| $\gamma_r$ | retained austenite. |
| $\Delta G_m$ | maximum free energy change possible during nucleation ($J\ mol^{-1}$). |
| $\Delta G_m^0$ | initial value of maximum possible free energy change on nucleation ($J\ mol^{-1}$). |
| $\Delta G^{\gamma\rightarrow\alpha}$ | free energy for growth of bainitic ferrite ($J\ mol^{-1}$). |
| $\Delta G^{\gamma\rightarrow\alpha'}$ | free energy for growth of martensite ($J\ mol^{-1}$). |
| $\Delta G_{M_s}^{\gamma\rightarrow\alpha'}$ | driving force needed to stimulate martensite transformation ($J\ mol^{-1}$). |
| $\Delta G^{\gamma\rightarrow\alpha_s}$ | free energy for austenite to supersaturated ferrite transformation ($J\ mol^{-1}$). |
| $\Delta G^{\gamma\rightarrow\gamma'+\alpha}$ | free energy for growth of Widmanstätten ferrite ($J\ mol^{-1}$). |
| $G_N$ | free energy necessary to obtain detectable degree of transformation (universal nucleation function) ($J\ mol^{-1}$). |
| $G_{SB}$ | stored energy of bainitic ferrite ($J\ mol^{-1}$). |
| $G_{SW}$ | stored energy of Widmanstätten ferrite ($J\ mol^{-1}$). |
| $h,\ k,\ l$ | indices of lattice plane. |
| $h_i$ | hyperbolic tangent transfer function. |
| $I$ | bainitic ferrite nucleation rate per unit volume. |
| $I_0$ | initial bainitic ferrite nucleation rate per unit volume. |
| $I_B$ | grain boundary steady state nucleation rate of allotriomorphic ferrite per unit area of boundary. |
| IPS | invariant-plane strain. |
| $I_{Ws}$ | bainitic ferrite nucleation rate per unit volume at $W_s$. |
| $k$ | Boltzmann constant ($1.381 \times 10^{-23}\ J\ K^{-1}$). |
| $k_0$ | constant in equation 6.1. |
| $K_1$ | function of austenite grain size $K_1 = \left(\bar{L}K_1'\right)^{-1}$. |
| $K'_1,\ K_2$ | empirical constants in equation 2.18. |

| | |
|---|---|
| $\lambda$ | wavelength of X-ray radiation (Å). |
| $\lambda_1$, $\lambda_2$ | empirical constants in equation 2.28. |
| $\bar{L}$ | mean linear intercept of random lines with austenite grain boundaries (μm). |
| $L_{initial}$ | initial length of sample in dilatation (mm). |
| $L_{final}$ | final length of sample in dilatation (mm). |
| $\Delta L$ | length change in dilatation (mm). |
| $LPE$ | log predictive error for neural network modelling. |
| $M_s$ | Martensite-start temperature (°C). |
| $M_d$ | Temperature below which austenite can transform to martensite on deformation (°C). |
| MAP | Materials Algorithms Project (see references). |
| $\eta$ | aspect ratio of allotriomorphic ferrite discs. |
| $n$ | constant in equation 6.1. |
| N-R | Nelson Riley function. |
| $O_\alpha$ | actual area of intersection of allotriomorphic ferrite discs with a plane ($m^2$). |
| $O_\alpha^{ex}$ | the sum of the extended areas of intersection of allotriomorphic ferrite discs with a plane ($m^2$). |
| $O_b$ | surface area of a plane parallel to an austenite grain boundary ($m^2$). |
| $O_B$ | total grain boundary area for allotriomorphic ferrite growth ($m^2$). |
| $p$ | constant in equation A1.1. |
| $P_\alpha$ | number of points in ferrite phase (point counting). |
| $q$ | half-thickness of allotriomorphic ferrite discs (m). |
| $Q$ | activation energy for nucleation (J $mol^{-1}$). |
| $Q'$ | constant in equation A1.1. |
| $Q_d$ | self diffusion activation energy for iron (260 kJ $mol^{-1}$). |
| $Q_0$ | activation energy for bainite nucleation (J $mol^{-1}$). |
| $Q_1$ | constant in equation 6.1. |
| $r$ | constant in equation 2.18. |
| $R$ | gas constant (8.314 J $K^{-1}$ $mol^{-1}$). |
| $\sigma$ | true stress (MPa). |
| $\sigma_\upsilon$ | estimate of the noise level of the data in neural networks "regularisation constant". |
| $\sigma_{vf}$ | standard deviation in ferrite volume fraction. |
| $\sigma_w$ | significance of inputs in neural networks. |
| $\sigma_y$ | variance in neural network prediction y. |
| $s$ | shear component of strain. |
| $s_A$ | apparent shear. |
| $SSE$ | sum of squared errors. |
| SPM | scanning probe microscope. |

| | |
|---|---|
| STEM | scanning transmission electron microscope. |
| STM | scanning tunnelling microscope. |
| $S_V$ | austenite grain surface area per unit volume ($m^{-1}$). |
| $\theta$ | maximum volume fraction of bainite (at the $T_0'$ line). |
| $\theta_b$ | Bragg angle (°). |
| $\theta_i$ | bias in neural networks. |
| $\tau$ | incubation time for the nucleation of one allotriomorphic ferrite particle (s). |
| $\tau_b$ | incubation time for the nucleation of bainite (s). |
| $\tau_f\{T\}$ | incubation time at temperature $T$ for fraction $f$ of reaction (s). |
| $t$ | time (s). |
| $\Delta t$ | time step in continuous cooling (s). |
| $t_c$ | time period long enough for bainite reaction to go to completion (s). |
| $t_m$ | measured time (s). |
| $t_n$ | test value for neural network. |
| $t_p$ | predicted time (s). |
| $t_{tot}$ | sum of times at top temperatures in neural network inputs (s). |
| $\Delta T$ | $T$-$W_s$ (K). |
| $T$ | temperature (°C or K). |
| $T_{av}$ | average top temperature in neural network inputs (°C). |
| $T_c$ | function of temperature in equation 4.47. |
| $T_S$ | cooling start temperature (°C). |
| $T_F$ | cooling finish temperature (°C). |
| *T-El* | total elongation (%). |
| TEM | transmission electron microscope. |
| $T_{en}$ | neural network model test error. |
| $T_h$ | transformation start temperature (°C). |
| $T_H$ | bainite isothermal hold temperature (°C). |
| $T_q$ | quench temperature (°C). |
| $T_0$ | line representing carbon concentrations above which the austenite to ferrite reaction can not take place without diffusion. |
| $T_0'$ | line as $T_0$ but also accounting for 400 J $mol^{-1}$ stored energy of bainite. |
| *TRIP* | transformation induced plasticity. |
| *TS* | tensile strength (MPa). |
| *TTT* | time-temperature-transformation. |
| T1 - T5 | temperatures for neural network inputs (°C). |
| $u$ | volume of bainite platelet ($m^3$). |
| $u_l$ | length of bainite platelet (set to 10 μm). |
| $u_w$ | width of bainite platelet (μm). |
| *U-El* | uniform elongation (%). |

| | |
|---|---|
| $UTS$ | ultimate tensile strength (MPa). |
| $v$ | actual volume fraction of bainite. |
| $V$ | total volume ($m^3$). |
| $\Delta V$ | volume change in dilatation ($m^3$). |
| $V_\alpha$ | actual volume fraction of allotriomorphic ferrite. |
| $V_\alpha^{ex}$ | total extended volume fraction of allotriomorphic ferrite. |
| $V_{\alpha b}$ | volume fraction of bainite. |
| $V_{\alpha'}$ | volume fraction of martensite. |
| $V_b$ | total volume fraction of allotriomorphic ferrite. |
| $V_\gamma$ | volume fraction of austenite. |
| $V_f$ | volume fraction prior ferrite. |
| $V_{final}$ | final volume in dilatation ($m^3$). |
| $V_1$, $V_2$ | volume fractions of transformation achieved during continuous cooling. |
| $w_{ij}$ | weight in neural networks. |
| $W_s$ | Widmanstätten ferrite-start temperature (°C). |
| $\xi$ | normalised volume fraction of bainite $\xi = \frac{v}{\theta}$. |
| $x$ | input to neural network. |
| $\bar{x}$ | mean carbon concentration of the alloy (mole fractions). |
| $x^{\alpha\gamma}$ | paraequilibrium mole fraction of carbon in ferrite. |
| $x^{\gamma\alpha}$ | paraequilibrium mole fraction of carbon in austenite. |
| $x_\alpha$ | equilibrium mole fraction of carbon in ferrite. |
| $x_\gamma$ | enriched austenite carbon content (mole fractions). |
| $x_{T0}$ | carbon concentration at the $T_0$ line (mole fractions). |
| $x_{T0'}$ | carbon concentration at the $T_0'$ line (mole fractions). |
| $x^{\alpha\gamma}$ | paraequilibrium carbon concentration of bainitic ferrite (mole fractions). |
| $x_m$ | carbon composition of bainite nucleus (mole fractions). |
| $x_{min}$ | minimum value of $x$. |
| $x_{max}$ | maximum value of $x$. |
| $x_N$ | normalised value of input to neural network. |
| $y$ | output from neural network. |
| $\bar{y}$ | neural network committee prediction. |
| $YS$ | yield strength (MPa). |
| $\zeta$ | extent of the allotriomorphic ferrite reaction. |
| $z$ | constant in equation A1.1. |

# Contents

# 1. Introduction

## 1.1 High Strength Steel in Cars

The energy consumption of a car during its lifetime can be split into three categories: raw materials, manufacture and fuel. As can be seen from fig. 1.1 the major part of this is the fuel consumption [Kruska and Freier, 1994] which is determined primarily by the weight of the vehicle.

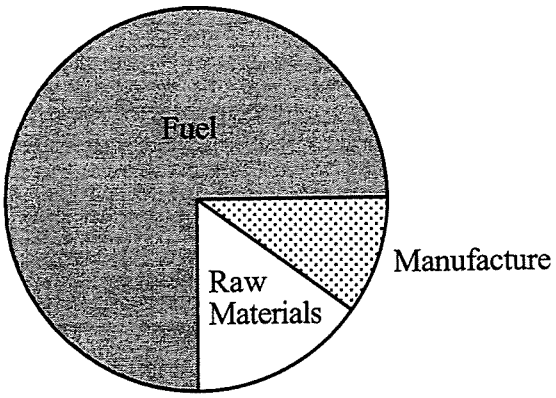


Fig. 1.1: Energy consumption of a car [Kruska and Freier, 1994].

Ever since the oil shortages of the 1970's, and subsequent tougher environmental regulations, automobile engineers have been reducing the weight of vehicles in order to boost fuel economy and reduce exhaust emissions.

At first the vehicles were reduced in size and rear-drive designs were replaced by lower-mass front-drive designs. When these weight saving strategies started to reach their limits attention turned to using more low-density materials such as plastics and aluminium in the construction of cars. As a result, today's average car contains double the amount of non-ferrous materials than a car of 1975.

The decrease in the use of iron and steel in vehicles can also be attributed to the wider application of higher-strength steels which can often perform the same structural function as mild steel but with less material. High-strength steel grades - iron alloys with yield strengths above 280 MPa - now comprise about one-fifth of the total ferrous content of new cars, and their use is growing steadily.

However, the overall weight of modern cars is increasing again [Automotive Engineer, 1994]. This is due to a greater demand for luxury items and safety features in vehicles. Manufacturers

are thus concentrating on reducing the weight of the body in white† as an important part of the reduction in the overall weight [Lowe, 1997].

Although vehicles have been manufactured with both aluminium and composite bodies, these are much more expensive to produce and the material costs are high (mild steel is about \$0.73 per kg compared to \$3.30 per kg for aluminium [Ashley, 1997]). Manufacturers also have a great deal of experience with, and equipment for using, steel and thus are reluctant to change.

A development engineer for General Motors stated "If you want to reduce mass when designing with steel there is only one thing to do - use less" [Ashley, 1997]. This is being achieved in a variety of ways. One is the design of the shape of car body parts to increase strength or stiffness whilst reducing weight. Joints may be redesigned and alternative joining methods used. For example, laser welding which can be used from just one side of the join [Ashley, 1995].

Another is the use of a variety of steels. As mentioned above, stronger steels can be used in smaller quantities for the same application. High strength low alloy and medium strength low alloy steels comprise up to 60% of the total steel content of some new cars [Ashley, 1997]. Further alloys, such as dual phase steels (520 to 1,030 MPa) containing ferrite and martensite, have so far only found limited commercial application due to their relative expense and difficulty in welding and zinc coating (for corrosion protection). Fully martensitic steels of even greater strengths are used even less due to their brittleness and limited formability.

Intercritically annealed steels, of the types investigated in this work, contain bainitic ferrite ($\alpha_b$) and retained austenite ($\gamma_r$) as well as allotriomorphic ferrite ($\alpha$) and martensite ($\alpha'$). It is possible then to obtain strengths of up to 2000 MPa and have a relatively high formability due to transformation-induced plasticity (TRIP). This is the transformation of retained austenite to martensite under the influence of an applied stress, increasing the work hardening and hence the ductility and strength of the steel.

The TRIP alloys tend to contain relatively high silicon concentrations which retard the precipitation of cementite from austenite [Owen, 1954]. Consequently, the growth of upper bainite is not accompanied by the precipitation of cementite from the carbon-enriched residual austenite. Instead, the carbon partially stabilises the austenite against martensitic transformation as the alloy cools towards ambient temperature. There are, therefore, no carbides in the microstructure and the austenite is believed to contribute greatly to formability via the TRIP effect.

† car body without trimmings.

The high silicon content of these steels leads to a deterioration in the surface finish so that they cannot be used for exterior vehicle body parts. They may nevertheless be ideal for internal, high strength uses such as side impact bars (fig. 1.2).

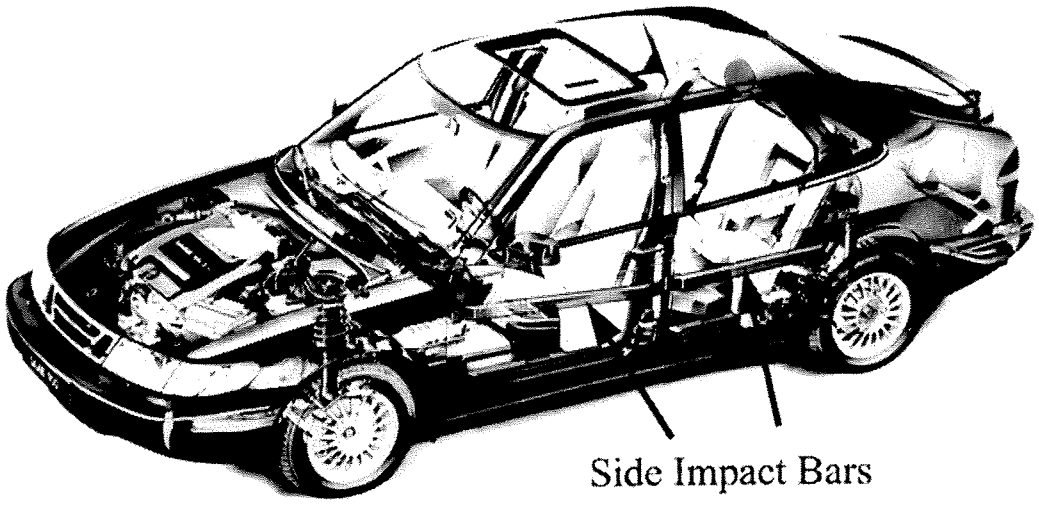


Fig. 1.2: Diagram of a SAAB 900 including side impact bars.

Rolls-Royce first fitted side impact bars to the Silver Shadow range in 1978. These were made of steel and riveted to the aluminium doors. The cars were for the USA and 1978 was the year that a lot of Federal Motor Vehicle Standards came into force.

Rolls-Royce cars now either contain pressed aluminium beams (weight 2.8 kg/car) welded to the doors of aluminium cars or pressed steel beams (weight 9 kg/car) welded to steel doors. Future Rolls-Royce models will also have steel side impact beams welded into the cars. These will be in the form of tubes, produced from high strength steel at a weight of 6.1 kg/car [Oldaker, 1997].

## 1.2 Continuous Annealing

Steels with a mixed microstructure of allotriomorphic ferrite, bainitic ferrite, retained austenite and martensite can be formed by continuous annealing through a temperature cycle as shown in fig. 1.3. Austenite forms during intercritical annealing (A - C) whilst retaining some of the original ferrite. During continuous cooling transformation (C - E) further allotriomorphic ferrite forms, whereas the growth of bainite occurs at a considerably lower temperature (F - G). The

martensite forms from remaining unstabilised austenite on quenching to room temperature, whilst austenite stabilised by a high carbon content is retained.

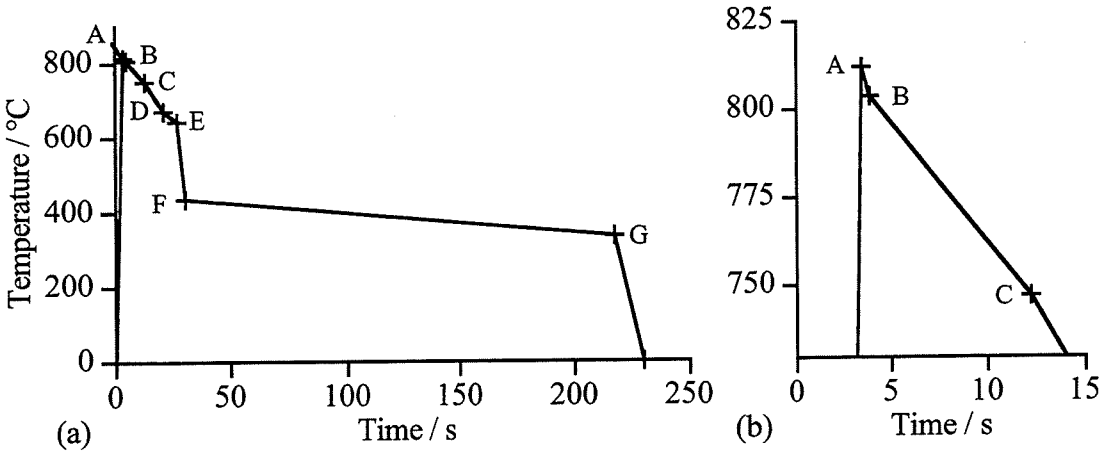


Fig. 1.3: (a) Simplified example of a continuous annealing heat treatment carried out in the British Steel pilot plant as part of this work and (b) detail of high temperature section.

Such a complex heat treatment has been selected to allow control of the various stages of the transformation and thus the final microstructure. This is achieved using a simulator consisting of a moving carriage on which 1 mm thick sheet steel samples are mounted in tension. The carriage then travels along the length of the apparatus through the heating and cooling stages. Transverse flux induction heating at high heating rates (in the order of 200 °C $s^{-1}$) is used for the initial heating followed by a series of electrically heated "hot boxes" and air/water mist cooling. This pilot plant has been constructed by British Steel to enable simulation of possible production continuous annealing cycles.

## 1.3 The Aim

The aim of this work is to mathematically model the formation of austenite, allotriomorphic ferrite, bainite and martensite during continuous annealing heat treatments and to use neural network methods to model the effects of alloy chemistry and heat treatment on the mechanical properties of these steels.

As described in fig. 1.4 the work is divided into different models, each concentrating on a different phase or property. Combined together these models should provide a useful tool for the design of new high strength steels.

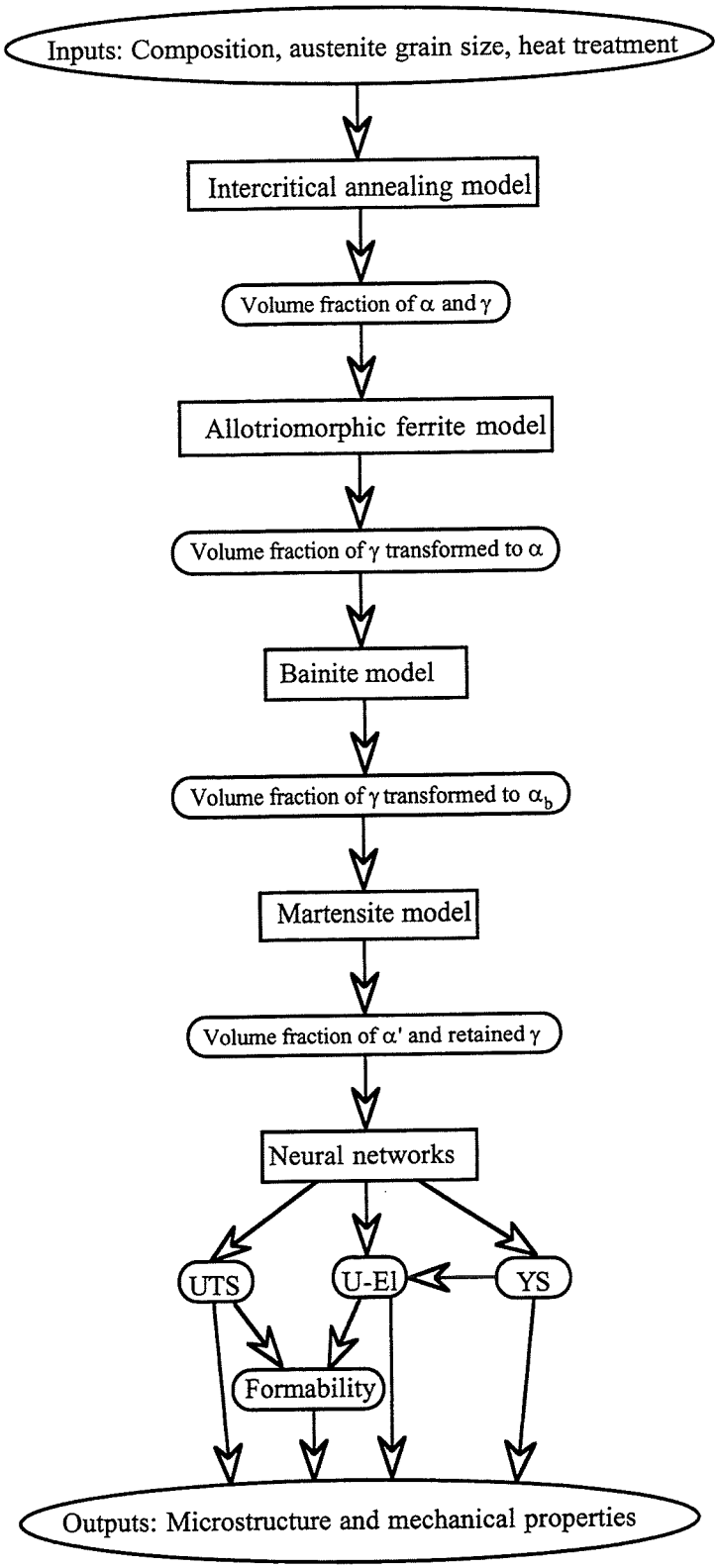


Fig. 1.4: Flow chart for the estimation of the microstructure and mechanical behaviour of continuously annealed high strength steels.

# 2. Literature Survey

## 2.1 High-Strength Steels With Mixed Microstructures

High strength steels can be produced which have a microstructure containing retained austenite, allotriomorphic ferrite, martensite and bainitic ferrite. Their hardenability is controlled by the addition of elements such as manganese, chromium and nickel. This helps to avoid any uncontrolled transformations at higher temperatures. The alloys usually contain a relatively large silicon concentration (2 wt.%) to prevent the formation of cementite (silicon has a very low solubility in cementite). Any carbon therefore partitions into the austenite, stabilising some of it to ambient temperature even though the overall carbon concentration in the alloy might be quite small.

These steels are often used in the automotive industries to reduce vehicle weight whilst maintaining strength [Tsukatani *et al.*, 1991]. The reason this mixture of phases is so useful is that the strength is not achieved at the expense of toughness.

## 2.2 Allotriomorphic Ferrite

In steel the face-centred cubic phase, austenite, is stable at high temperatures (fig. 2.1). On cooling it transforms to ferrite (body-centred cubic).

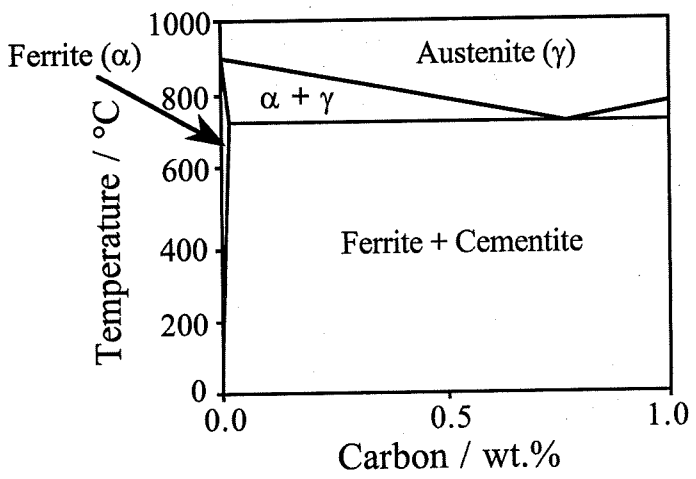


Fig. 2.1: Schematic Fe-C phase diagram.

Depending on the heat treatment and alloy chemistry there are many morphologies of ferrite that can form from austenite on cooling. The ferrite formed at the highest temperatures is in the form of allotriomorphs which nucleate at the austenite grain boundaries and have a shape which is

governed by growth predominantly along those boundaries.

Allotriomorphic ferrite is critical in determining the properties of many steels, including the TRIP steels of interest in the present work. In TRIP steels the initial formation of allotriomorphic ferrite enriches the residual austenite with carbon. When the fraction of allotriomorphic ferrite is small, the carbon content of the residual austenite is low and so most of the austenite is transformed into bainite. But excess allotriomorphic ferrite reduces the strength of the steel and can prevent enough bainite forming. There is therefore, a need to estimate the allotriomorphic ferrite content in order to design steels with good mechanical properties.

Bhadeshia *et al.* [1987] compared previous theoretical work (fig. 2.2a), where the ferrite was assumed to form a uniform thin layer over the austenite grain boundary and then to thicken, with a more realistic approach (fig. 2.2b) in which the allotriomorphs nucleate as isolated particles and then impinge to form the layers.

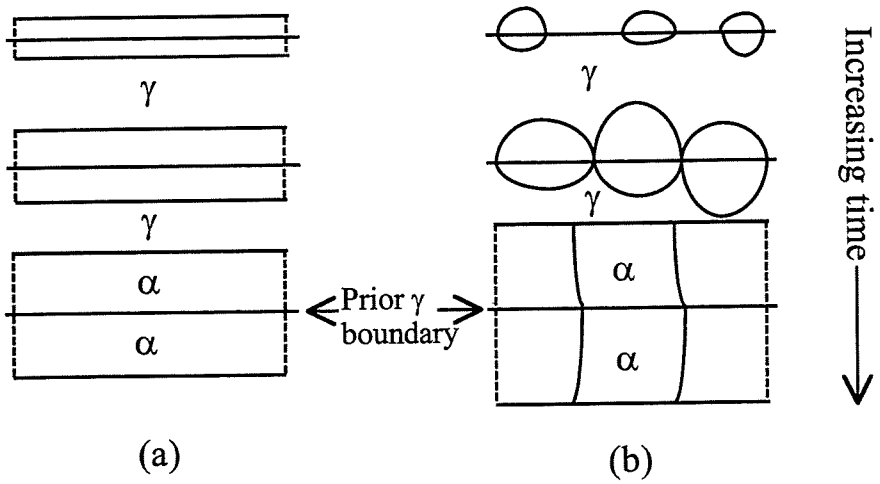


Fig. 2.2: Diagram illustrating allotriomorphic ferrite (a) as previously theoretically modelled considering growth only and (b) as modelled by Bhadeshia *et al.* [1987] considering growth and nucleation.

They assumed that the allotriomorphs before impingement are discs having their faces parallel to the austenite grain boundary plane. The discs are assumed to grow radially with the half-thickness $q$ and radius $\eta q$ varying parabolically with time according to the equation $q = \alpha_1 t^{1/2}$, where $\alpha_1$ is the one-dimensional parabolic thickening rate constant. The aspect ratio $\eta$ of the allotriomorphs is considered to be constant, because the lengthening and thickening processes are actually coupled. Consistent with the experimental evidence $\eta = 3$ [Bradley *et al.*, 1977].

The overall transformation kinetics can be modelled using Cahn's [1956] analysis of grain boundary nucleation and growth kinetics. Consider a plane surface of total area $O_b$ parallel to a particular boundary, at a distance $y$; the extended area $O_\alpha^{ex}$ is defined as the sum of the areas of

intersection of the discs with this plane. It follows that the small change $\delta O_\alpha^{ex}$ in $O_\alpha^{ex}$ due to discs nucleated between $t=\tau$ and $t=\tau+\delta\tau$ is:

$$\delta O_\alpha^{ex} = \pi O_b I_B\left[(\eta\alpha_1)^2(t-\tau)\right]\delta\tau \qquad \text{if } \alpha_1(t-\tau)^{1/2} > y \tag{2.1}$$

and

$$\delta O_\alpha^{ex} = 0 \qquad \text{if } \alpha_1(t-\tau)^{1/2} < y \tag{2.2}$$

where $I_B$ is the grain boundary steady-state nucleation rate per unit area of boundary. Only allotriomorphs nucleated for $\tau > (y/\alpha_1)^2$ can contribute to the extended area intersected by the plane at $y$; if $\tau$ takes a value less than $(y/\alpha_1)^2$, then the allotriomorph has not had sufficient time to grow the distance $y$ to the arbitrary plane. It follows that the entire extended area is given by:

$$O_\alpha^{ex} = \int_0^{t-(y/\alpha_1)^2} (\eta\alpha_1)^2 \pi O_b I_B (t-\tau)\,\mathrm{d}\tau \qquad = \frac{1}{2}\pi O_b I_B (\eta\alpha_1)^2 t^2\left(1-\varepsilon^4\right) \tag{2.3}$$

where $\varepsilon = y/(\alpha_1 t^{1/2})$, corresponding to the ratio between the distance to the arbitrary plane and the half-thickness of the allotriomorph at time $t$.

The actual area $O_\alpha$ which intersects the plane $O_b$ will be somewhat smaller than the extended area because the extended area at random includes a fraction $[1-(O_\alpha/O_b)]$ of 'phantom' area which has already transformed to ferrite. The relationship between $\delta O_\alpha^{ex}$ and a small change, $\delta O_\alpha$, in the actual area is given by:

$$\delta O_\alpha = \delta O_\alpha^{ex}\left(1-\frac{O_\alpha}{O_b}\right) \tag{2.4}$$

thus

$$O_\alpha^{ex}/O_b = \ln\{1-(O_\alpha/O_b)\} \tag{2.5}$$

Assuming that there is no interference with allotriomorphs from other boundaries, the total volume $V_b$ of material originating from this grain boundary is given by integrating $y$ between negative and positive infinity; in terms of $\varepsilon$ this gives:

$$V_b = 2\int_0^1 O_b\alpha_1 t^{1/2}\left(1-\exp\left\{-O_\alpha^{ex}/O_b\right\}\right)\mathrm{d}\varepsilon \qquad = 2O_b\alpha_1 t^{1/2} f_n\{\eta\alpha_1, I_B, t\} \tag{2.6}$$

where the factor of 2 assumes equal volume fractions for positive and negative values of $y$ and:

$$f_n\{\eta\alpha_1, I_B, t\} = \int_0^1 1-\exp\left\{-0.5\pi I_B(\eta\alpha_1)^2 t^2\left(1-\varepsilon^4\right)\right\}\mathrm{d}\varepsilon$$

If the total grain boundary area is $O_B = \sum O_b$, then, by substituting $O_B$ for $O_b$ in the above equation, the total extended volume $V_\alpha^{ex}$ of material is found. This is an extended volume, because allowance was not made for impingement of discs originating from different boundaries. Thus:

$$V_\alpha^{ex} = 2O_B\alpha_1 t^{1/2} f_n\{\eta\alpha_1, I_B, t\} \tag{2.7}$$

and if $V$ is the total volume, and $S_V$ the austenite grain surface area per unit volume, then:

$$V_\alpha^{ex}/V = 2S_V\alpha_1 t^{1/2} f_n\{\eta\alpha_1, I_B, t\} \tag{2.8}$$

This can be converted into the actual volume $V_\alpha$ using the following equation:

$$V_\alpha/(V\phi) = 1 - \exp\left\{-V_\alpha^{ex}/(V\phi)\right\} \tag{2.9}$$

where $\phi$ is the equilibrium volume fraction of ferrite, so that $V\phi$ is the equilibrium volume of ferrite in the austenite matrix. The term $\phi$ can be estimated from the phase diagram, by calculation of the tie line passing through the mean alloy composition:

$$\phi = \frac{\bar{x} - x^{\gamma\alpha}}{x^{\alpha\gamma} - x^{\gamma\alpha}} \tag{2.10}$$

where $\bar{x}$ is the average carbon content of the alloy, and $x^{\alpha\gamma}$ and $x^{\gamma\alpha}$ are the paraequilibrium carbon contents of austenite and ferrite respectively (in mole fractions). It follows that:

$$-\ln(1-\zeta) = 2(S_V/\phi)\alpha_1 t^{1/2} f_n\{\eta\alpha_1, I_B, t\} \tag{2.11}$$

where $\zeta = V_\alpha/(V\phi)$ and is often referred to as the extent of reaction. It corresponds to the volume of ferrite divided by its equilibrium volume.

The value of the integral $f_n$ tends to unity as $I_B$ increases or time increases, since site saturation occurs. In this limit, as the integral tends to unity, the above equation simplifies to one-dimensional thickening governed by the equation:

$$-\ln\{1-\zeta\} = 2(S_V/\phi)\alpha_1 t^{1/2} \tag{2.12}$$

This theory takes into account hard impingement between allotriomorphs growing from the

same, or adjacent, austenite grain boundaries. It does not take into account soft impingement (the overlap of diffusion fields) between neighbouring allotriomorphs except by uniformly increasing the austenite carbon content with transformation.

## 2.3 Bainitic Microstructures

Bainite is a non-lamellar aggregate of ferrite and carbides. The ferrite is in the form of clusters, each cluster consisting of identically orientated parallel platelets, often referred to as "sheaves" of bainite. Each platelet grows to a limiting size which is frequently less than that of the parent austenite grain. Bainitic ferrite tends to contain a high density of dislocations when compared with allotriomorphic ferrite or pearlite.

Any residual austenite which is associated with the bainitic ferrite can be in two forms. Thin films of retained austenite are trapped between the parallel platelets within any given sheaf, whilst blocky volumes of austenite are bounded by bainite sheaves growing in different orientations (fig. 2.3).

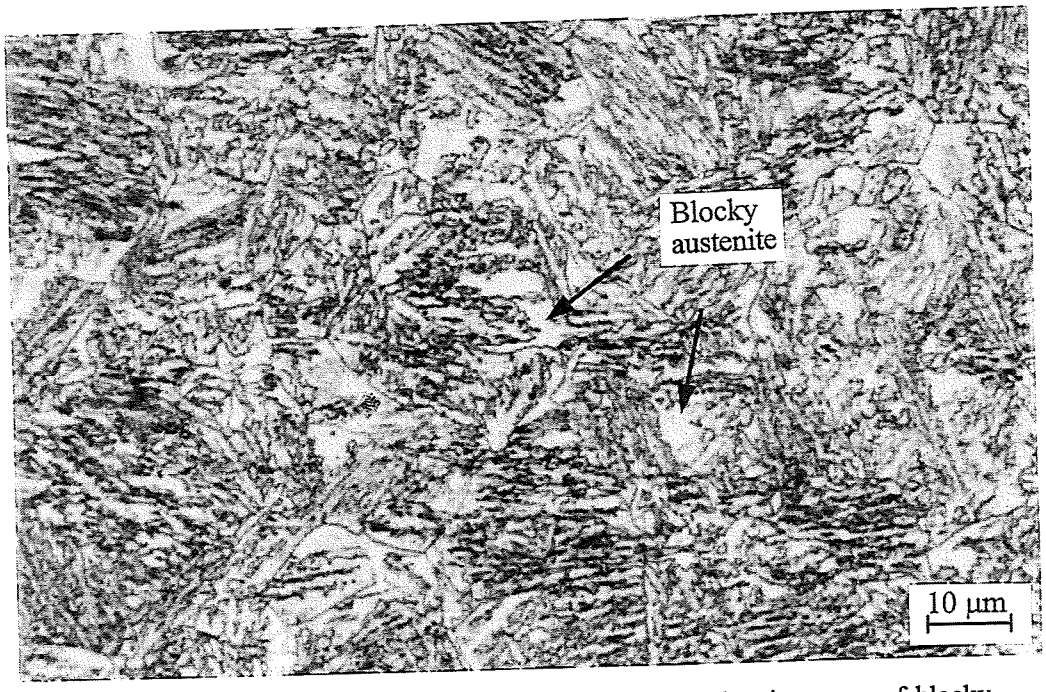


Fig. 2.3: Optical micrograph of bainitic microstructure showing areas of blocky retained austenite. Sample (Fe-0.38C-1.29Si-1.73Mn wt.%) austenitised at 1000 °C for 300 s, quenched to 450 °C and then cooled to 250 °C at a rate of 0.1 °C $s^{-1}$.

The residual austenite becomes enriched in carbon as the bainite forms because ferrite has a low solubility for carbon. The films of austenite which are surrounded by bainite plates become especially enriched and in upper bainite, which is formed at relatively high temperatures, cementite often precipitates from these films. In lower bainite, formed at lower temperatures,

cementite also precipitates within the platelets exhibiting a "tempering" orientation[†1] relationship with the parent ferrite. This precipitation within the ferrite is partly due to the slower diffusion of carbon at lower temperatures. Also there is a higher driving force for nucleation of platelets adjacent to others at these temperatures. This can hinder the partitioning of carbon into the austenite, thus giving an increased opportunity for precipitation to occur within the platelets [Bhadeshia, 1981a].

The growth of cementite is retarded in steels containing large amounts of silicon, and thus a microstructure of bainitic ferrite and carbon-enriched austenite can be obtained. This is more desirable as cementite can reduce toughness. Lower bainite on the other hand can still contain cementite precipitates within the ferrite platelets, despite a high silicon content [Bhadeshia and Edmonds, 1979].

On cooling from the bainite formation temperature range the blocky areas of austenite are often susceptible to transformation into martensite. This reaction is not affected much by the presence of the bainite [Khan and Bhadeshia, 1990a], though the bainite does stabilise the austenite in the film form.

[†1 tempering orientation relationship is found when carbides precipitate during the heat treatment of martensite. In contrast to tempered martensite, the cementite particles in lower bainite frequently precipitate in just one of the orientations forming parallel arrays at about 60° to the ferrite plate axis.]

### 2.3.1 Mechanism

*2.3.1.1 Shear transformation*

There have been many discussions about whether the bainite transformation is diffusional (like pearlite which transforms at a higher temperature) or displacive (like martensite which transforms at a lower temperature).

It has been shown, using an atom-probe technique [Bhadeshia and Waugh, 1982], that iron and substitutional atoms do not partition between the parent austenite and the bainitic ferrite. This is consistent with the existence of an atomic correspondence between the phases during transformation, as might be expected from a displacive transformation mechanism. The invariant-plane strain[†2] (IPS) surface relief caused by the growth of bainitic ferrite has been observed with a large shear strain component of 0.24 and a volume strain of 0.03 [Ko and Cottrell, 1952; Srinivasan and Wayman, 1968b; Swallow and Bhadeshia, 1996]. The final microstructure contains a high dislocation density including slip steps and sometimes

[†2 An invariant-plane strain is a deformation which allows the interface (the invariant plane) to remain undistorted and unrotated during deformation, see Chapter 5.]

mechanical twinning [Bhadeshia and Edmonds, 1979; Miihkinen and Edmonds, 1987a], which help accommodate the shape change. These observations all indicate that the iron and substitutional atoms are displaced into position during transformation.

*2.3.1.2 Carbon Partitioning*

It is known that carbon does partition between austenite and bainitic ferrite, but whether this takes place *during* or *after* the transformation is difficult to deduce [Bhadeshia and Waugh, 1981, 1982]. It has been impossible to measure the carbon content of bainitic ferrite platelets as they form to determine when carbon partitioning takes place. This is because carbon diffuses very rapidly at the high temperatures at which bainite forms. The decarburisation of the platelets was thought to take milliseconds [Kinsman and Aaronson, 1967] but this estimate was revised by Bhadeshia [1988], and then further refined using a finite difference model [Mujahid and Bhadeshia, 1992] which took into account the coupling of the diffusional fluxes in both the austenite and ferrite. Even with these calculations the decarburisation is thought to take less than a second. Thus, measuring the carbon concentration in the ferrite after formation is unlikely to reveal the actual composition that exists during growth.

Two situations are to be considered, the first being that decarburisation takes place during platelet growth, and the second that it takes place afterwards.

In the first situation the rate of formation of the platelet would be controlled by the diffusion of the carbon [Kinsman and Aaronson, 1967] and the overall reaction would halt when the carbon content of the enriched austenite reached the $Ae_3'$ $\gamma/\gamma+\alpha$ paraequilibrium phase boundary. A paraequilibrium transformation is one in which the substitutional alloying elements are unable to partition during the time scale of the experiment, although carbon, which is a fast diffusing interstitial element, redistributes between the phases and reaches "equilibrium" subject to this constraint [Hultgren, 1947; Hillert, 1953].

In the second situation the rate of growth would be controlled by lattice friction and may be greater than if diffusion-controlled. The reaction would stop when the carbon concentration in the austenite reached the $T_0$ line. This line (fig. 2.4) is lower in carbon concentration than the $Ae_3'$ and represents the concentration above which the austenite to ferrite reaction could not take place without diffusion (the $T_0'$ line takes into account 400 J $mol^{-1}$ of stored energy [Bhadeshia and Edmonds, 1980]).

The rate of growth of the platelets has been measured to be much quicker than if controlled by the diffusion of carbon during transition [Ali and Bhadeshia, 1989]. The lengthening rate of sheaves is slower than that of platelets as each platelet requires time to nucleate, but is nevertheless faster than if controlled by carbon diffusion.

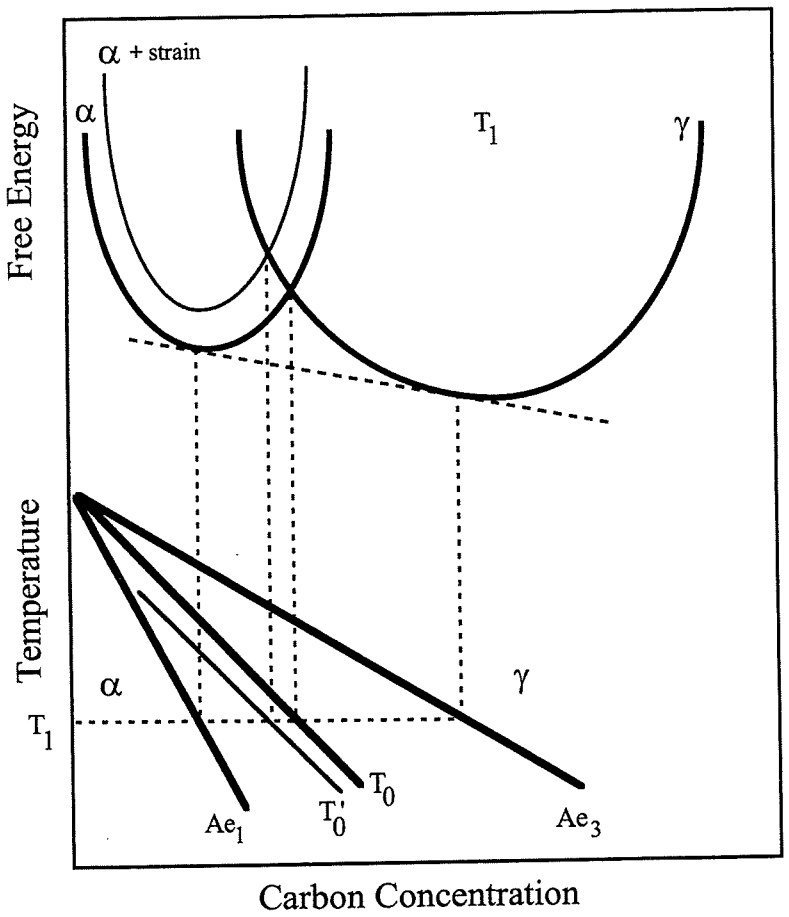


Fig. 2.4: Schematic illustration of the origin of the $T_0$ construction on the Fe-C phase diagram. Austenite (γ) with a carbon concentration to the left of the $T_0$ boundary can in principle transform to ferrite (α) without any diffusion. Diffusionless transformation is thermodynamically impossible if the carbon concentration of the austenite exceeds the $T_0$ curve. $Ae_1$ and $Ae_3$ are the equilibrium $\gamma \rightarrow \alpha$ start and finish phase boundaries respectively [Bhadeshia, 1992].

The carbon concentration in retained austenite after the reaction ceases has been measured using a variety of techniques [Bhadeshia and Waugh, 1981; Ali *et al.*, 1993; Chang and Bhadeshia, 1994; Hanzaki *et al.*, 1995]. They all show that the reaction stops well before the $Ae_3'$ line, giving rise to the term "incomplete reaction phenomenon". In some of the measurements the values were above the $T_0$ line. This may be explained by taking into account the inhomogeneous distribution of carbon within the retained austenite [Self *et al.*, 1981; Rees and Bhadeshia, 1992b]. The films of austenite trapped within the ferrite platelets can often be higher in carbon than expected from the $T_0$ line as they are unable to redistribute the carbon to the rest of the austenite. The blocky austenite thus often contains less carbon than the $T_0$ carbon concentration $x_{T0}$, and so is able to continue to transform, even though the average carbon content of the austenite is above $x_{T0}$.

From this evidence it is concluded that bainite platelets form with a carbon supersaturation and that decarburisation takes place after ferrite formation.

### 2.3.2 Growth

Each bainite platelet grows to a given size and then stops. This is due to a build up of dislocations during plastic deformation of the parent austenite, the deformation being driven by the transformation strain. The growth rate of the platelets has been measured, by Bhadeshia [1984], to be 75 $\mu m\ s^{-1}$ (at 380 °C for a Fe-0.43C-3Mn-2.02Si wt.% steel). This rate is much faster than that of the whole bainite sheaf due to the time taken to nucleate each of the platelets, and greatly exceeds that expected from diffusion controlled growth.

Thus nucleation is taken to be the time controlling step in the kinetics of bainitic ferrite formation and the effects of the growth can be neglected.

### 2.3.3 Nucleation

The nucleation of bainite is identical to that of Widmanstätten ferrite and involves the paraequilibrium partitioning of carbon [Bhadeshia, 1981a]. Thus the composition of the nucleus is different to that of the bainite platelet during growth which is diffusionless.

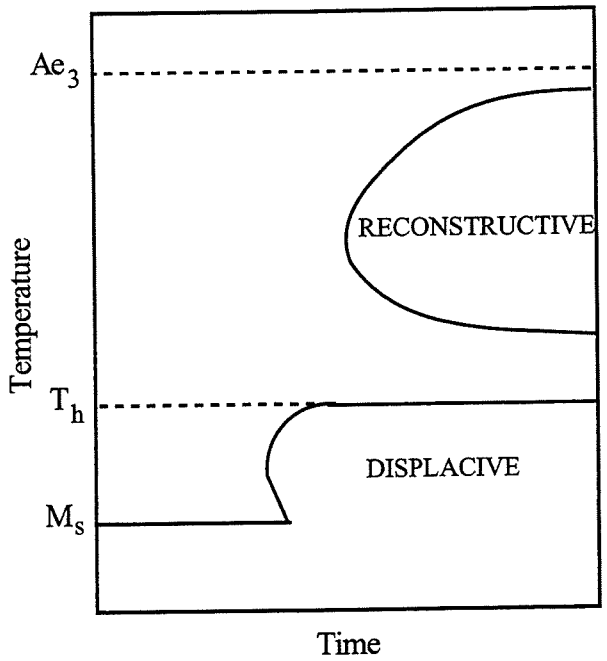


Fig. 2.5: Time temperature transformation diagram indicating the temperature $T_h$ below which displacive transformation can take place.

The transformation start temperature ($T_h$) at which either Widmanstätten or bainitic ferrite is first detectable (fig. 2.5) can be predicted for all low alloy steels with the use of the universal nucleation function [Bhadeshia, 1981a; Ali and Bhadeshia, 1990]:

$$G_N = A + B(T - 273.18) \qquad (2.13)$$

where $G_N$ is the free energy (J mol$^{-1}$) necessary to obtain a detectable degree of transformation, $T$ is the temperature in Kelvin, the constant $A$=-2540 J mol$^{-1}$ and $B$=3.637 J mol$^{-1}$ K$^{-1}$. This function was found by Bhadeshia [1981a] by fitting to data for a variety of steels (fig. 2.6).

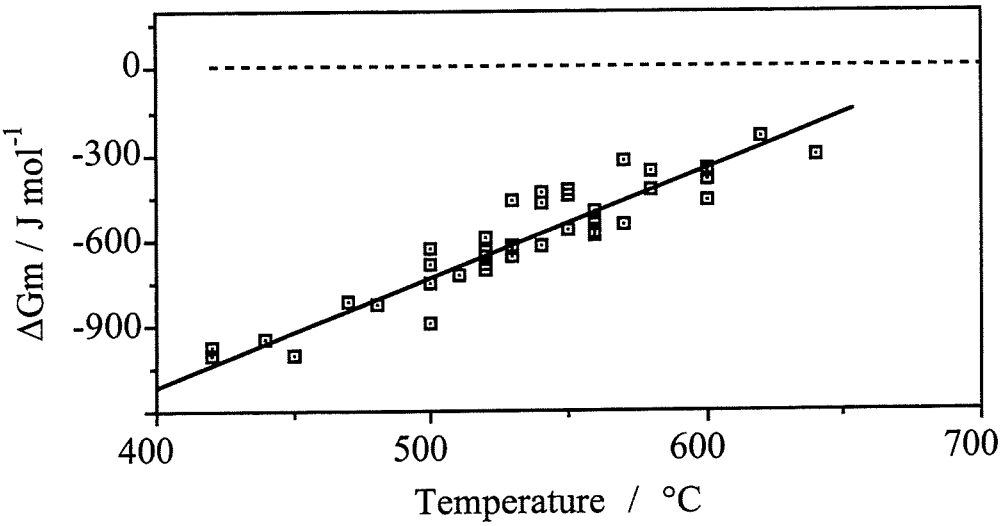


Fig. 2.6: Line representing the universal nucleation function, the free energy necessary to obtain a detectable degree of diffusionless transformation, and some experimental values for a variety of steels Bhadeshia [1981a].

Which of the two ferrite phases the nucleus grows into is dependent on the driving force available. If at $T_h$ the driving force is insufficient for the diffusionless growth of bainite, then $T_h$=$W_s$ and Widmanstätten ferrite forms. Cooling below this is necessary to reach $B_s$, the bainite-start temperature. On the other hand if sufficient driving force is available at $T_h$ for diffusionless transformation and to account for the stored energy of bainite, $T_h$=$B_s$ and only bainite forms.

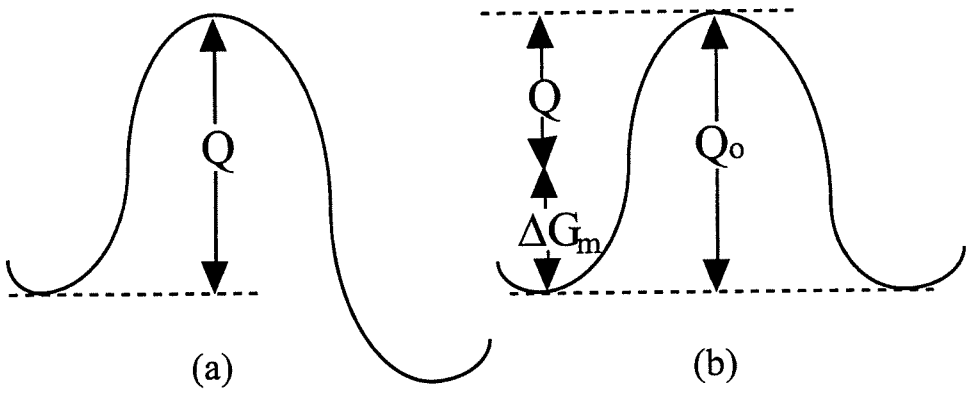


Fig. 2.7: Nucleation energy barriers for (a) classical nucleation and (b) bainitic ferrite.

In classical nucleation theory the activation energy $Q$ (fig. 2.7a) is related to the free energy change on nucleation ($\Delta G_m$) as follows:

$$Q \propto \frac{1}{(\Delta G_m)^2} \tag{2.14}$$

The nucleation of bainitic ferrite involves the motion of pre-existing embryos consisting of arrays of partial dislocations. Thus the activation energy for nucleation, $Q$, has a linear dependence on $\Delta G_m$ (fig. 2.7b) as shown (where $c$ is a constant):

$$Q = Q_0 - c|\Delta G_m| \qquad \therefore Q \propto |\Delta G_m| \tag{2.15}$$

The nucleation rate per unit volume, $I$, is given by Bhadeshia [1982c] as:

$$I = C_1 \exp\left(-\frac{Q}{RT}\right) \tag{2.16}$$

since $Q$ is linearly dependent on $\Delta G_m$, this may be written:

$$I = C_1 \exp\left[-(C_2 + C_3 \Delta G_m)/(RT)\right] \tag{2.17}$$

where $C_1$, $C_2$ and $C_3$ are constants and $R$ is the gas constant.

When deriving the universal nucleation function $G_N$, Bhadeshia [1981a, 1982a] assumed that, at the highest temperature at which ferrite can nucleate by displacive mechanism ($T_h$), all steels should have an identical nucleation rate ($I_{Th}$). Rees and Bhadeshia [1992a] showed that this would only be the case if $C_2 = C_3 r$ (where $r$ is also a constant). To take account of this equation 2.17 had to be modified to:

$$I = K_1 \exp\left[-\frac{K_2}{RT} - \frac{K_2 \Delta G_m}{rRT}\right] \tag{2.18}$$

where $K_1$ and $K_2$ are constants, denoted as such to avoid confusion with the constants of he original theory. $K_1$ represents the number density of potential sites for nucleation and at $T_h$ the equation becomes:

$$I = I_{Th} \tag{2.19}$$

regardless of alloy composition.

*2.3.3.1 Free energy change and carbon partitioning*

Carbon enrichment of untransformed austenite, due to the formation of ferrite, leads to a lowering of the free energy change as the reaction proceeds. Thus $\Delta G_m$ is a function of the volume fraction of ferrite formed. This was modelled originally by Bhadeshia [1982c] as:

$$\Delta G_m = \Delta G_m^0 \left[1 - \left(C_4 \theta \xi / C_3\right)\right] \tag{2.20}$$

where $\Delta G_m^0$ is the initial value of $\Delta G_m$ , $C_4$ is an empirical constant and $\theta$ is the maximum volume fraction of bainitic ferrite, which is calculated using the lever rule applied to the $T_0'$ curve of the paraequilibrium phase diagram:

$$\theta = \frac{x_{T_0'} - \bar{x}}{x_{T_0'} - x_\alpha} \tag{2.21}$$

The mean carbon concentration of the alloy ($\bar{x}$) is expressed as a mole fraction, $x_{T0'}$ is the carbon concentration at $T_0'$ and $x_\alpha$ the estimated carbon content of the ferrite.

$\xi$ is the normalised volume fraction of bainitic ferrite given by:

$$\xi = \frac{v}{\theta} \tag{2.22}$$

where $v$ is the actual volume fraction of bainitic ferrite.

However, with the deduced value of $C_4/C_3$ equal to 2.98, this equation predicts positive $\Delta G_m$ values above 0.34 volume fraction of bainite, regardless of temperature or alloy chemistry. This clearly is wrong since many steels form more then 0.34 volume fraction of bainite. This error was subsequently corrected as follows.

There are two criteria which must be satisfied before the formation of bainite or Widmanstätten ferrite can occur. For both phases the driving force available for nucleation $|\Delta G_m|$ (see fig. 2.8) must exceed the universal nucleation function $|G_N|$, giving:

$$\Delta G_m \leq G_N \tag{2.23}$$

The second condition, which must also be satisfied, is that the free energy change for growth of the phase should exceed the stored energy of the phase formed, giving for Widmanstätten ferrite:

$$\Delta G^{\gamma \rightarrow \gamma' + \alpha} < -G_{SW} \tag{2.24}$$

and for bainitic ferrite:

$$\Delta G^{\gamma\rightarrow\alpha} < -G_{SB} \tag{2.25}$$

where $G_{SW}$ and $G_{SB}$ are the stored energies of Widmanstätten ferrite (about 50 J mol$^{-1}$) and bainitic ferrite (about 400 J mol$^{-1}$ [Bhadeshia, 1981a]) respectively. These stored energies are due to strain energy caused by volume and shape changes on transformation to the ferrite.

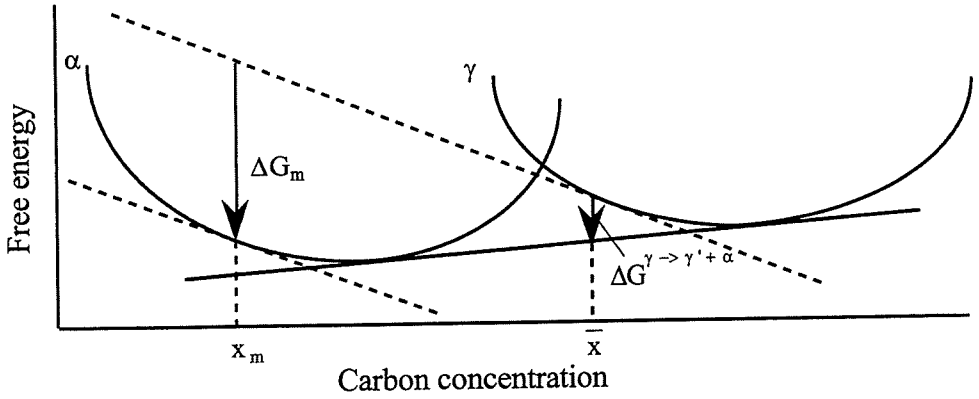


Fig. 2.8: A schematic illustration of $\Delta G^{\gamma\rightarrow\gamma'+\alpha}$, the free energy for growth of ferrite, and $\Delta G_m$, the maximum free energy change possible during nucleation, assuming that the nucleus adopts the chemical composition consistent with the maximum change in free energy.

As the austenite carbon concentration increases during transformation both $\Delta G_m$ and $\Delta G^{\gamma\rightarrow\alpha}$ will decrease. Eventually one of these criteria will not be satisfied and the reaction will cease. Rees and Bhadeshia [1992] assumed that the driving force varied linearly with the extent of reaction between its initial value $\Delta G_m^0$ and its final value producing the equation:

$$\Delta G_m = \Delta G_m^0 - \xi\left(\Delta G_m^0 - G_N\right) \tag{2.26}$$

The model also includes a growth criterion which stops the growth when the maximum fraction $\theta$ is reached.

*2.3.3.2 Autocatalysis*

The nucleation of the first platelets in bainite sheaves takes place at the austenite grain boundaries (fig. 2.9) because the imperfections within such grain boundaries lower the activation energy. As indicated above the platelets of bainite grow by a displacive mechanism and carbon partitions afterwards. The platelets grow to a certain size (about 0.3 μm wide and 10 μm long) and then stop. This is due to the build up of dislocations at the austenite/bainite interface caused by the plastic deformation which helps to accommodate the shape change associated with transformation [Bhadeshia and Edmonds, 1979].

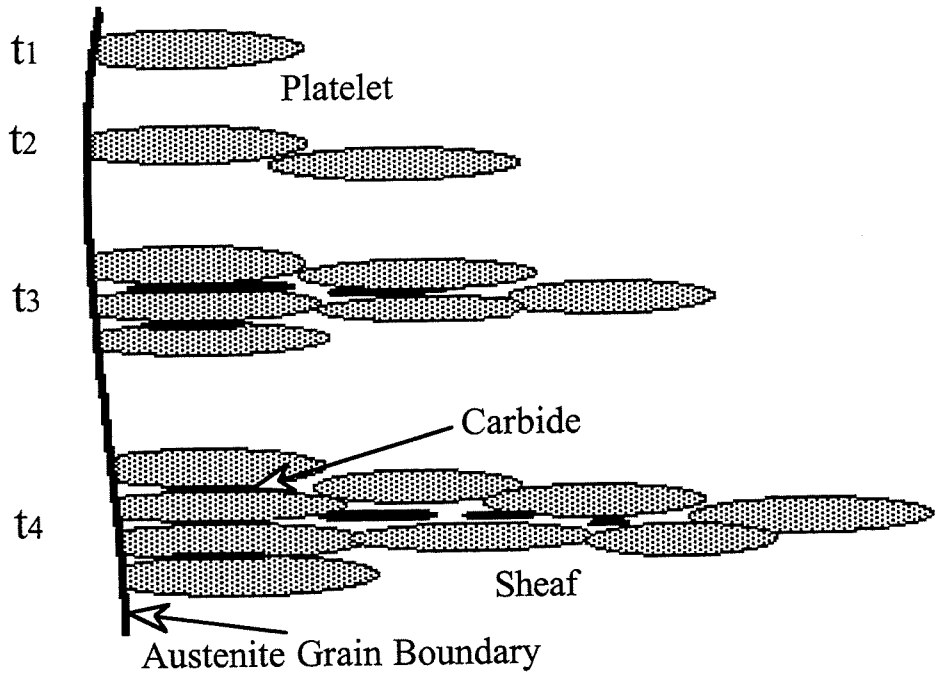


Fig. 2.9: Diagram of the growth of a sheaf of bainite, with increasing time ($t_1$ - $t_4$), from the nucleation of one platelet on the austenite grain boundary. The presence of silicon in the steel being investigated here prevents the carbide formation.

Other platelets must nucleate for the continued growth of the bainite sheaf. This is most favourable at the tip of a previous platelet as its lenticular shape leads to the carbon concentration at the tip being lower than at the sides. This preference for tip nucleation has been shown by electron microscopy and leads to the bainite sheaf being long and thin, only thickening if the less favourable adjacent nucleation takes place [Bhadeshia and Edmonds, 1980].

Autocatalysis is this further nucleation close to previously formed plates [Magee, 1969] and can be accounted for using the following equation:

$$I = I_0(1+\beta\theta\xi) \tag{2.27}$$

where $\beta$ is the autocatalysis factor [Bhadeshia, 1982c]. Steels with higher carbon concentrations eject more carbon from newly transformed ferrite. Further nucleation on the previously formed plates (autocatalysis) is inhibited by this carbon build-up. Thus it is assumed that:

$$\beta = \lambda_1(1-\lambda_2\bar{x}) \tag{2.28}$$

where $\bar{x}$ represents the mean carbon concentration of the alloy and $\lambda_1$ and $\lambda_2$ are empirical constants.

*2.3.3.3 Austenite Grain Size*

The nucleation rate for grain boundary nucleation can be taken to be proportional to the surface area of austenite grain boundaries per unit volume, $S_v$. This is related to the mean linear intercept, $\bar{L}$, of a series of random lines with austenite grain boundaries.

This effect has been incorporated into $K_1$, the number density of potential sites for nucleation, as:

$$K_1 = \left(\bar{L}K_1'\right)^{-1} \tag{2.29}$$

where $K_1'$ is an empirical constant [Rees and Bhadeshia, 1992a].

### 2.3.4 Final Equation

The volume fraction increment between times $t$ and $t + \mathrm{d}t$ is given by:

$$\mathrm{d}v = \theta\,\mathrm{d}\xi = Iu\,\mathrm{d}t \tag{2.30}$$

where $u$ is the volume of a bainite sub-unit (assumed here to be constant) and $I$ is the nucleation rate per unit volume.

As transformation proceeds, the volume of austenite available for transformation decreases, and it becomes necessary to consider the extent of 'extended volume' $\mathrm{d}v_e$. This accounts for the formation of 'phantom' nuclei within regions of ferrite already transformed and enables the use of the nucleation rate of bainite per unit volume of austenite, despite the fact that the volume of austenite is changing. For random nucleation the extended volume increment is related to the real volume increment thus:

$$\mathrm{d}v = \left(1-\xi\right)\mathrm{d}v_e \tag{2.31}$$

where

$$\mathrm{d}v_e = Iu\,\mathrm{d}t \tag{2.32}$$

which gives:

$$\theta\,\mathrm{d}\xi = \left(1-\xi\right)uI\,\mathrm{d}t \tag{2.33}$$

It follows that:

$$\frac{\mathrm{d}\xi}{\mathrm{d}t} = \frac{\left(1-\xi\right)u}{\theta}I \tag{2.34}$$

where $I$ (allowing for autocatalysis) is given by:

$$I = (1+\beta\theta\xi)K_1 \exp\left[-\frac{K_2}{RT} - \frac{K_2 \Delta G_m}{rRT}\right] \tag{2.35}$$

Substituting for $\Delta G_m$ using equation (2.25) we get:

$$I = (1+\beta\theta\xi)K_1 \exp\left[-\frac{K_2}{RT} - \frac{K_2}{rRT}\left(\Delta G_m^0 - \xi\left(\Delta G_m^0 - G_N\right)\right)\right] \tag{2.36}$$

which simplifies to:

$$I = (1+\beta\theta\xi)K_1 \exp\left[-\frac{K_2}{RT}\left(1+\frac{\Delta G_m^0}{r}\right) + \frac{K_2}{rRT}\xi\left(\Delta G_m^0 - G_N\right)\right] \tag{2.37}$$

Substituting this expression for $I$ into equation (2.34) we get:

$$\frac{d\xi}{dt} = \frac{uK_1}{\theta}(1-\xi)(1+\beta\theta\xi)\exp\left[-\frac{K_2}{RT}\left(1+\frac{\Delta G_m^0}{r}\right) + \Gamma_2\xi\right] \tag{2.38}$$

$$\text{where } \Gamma_2 = \frac{K_2\left(\Delta G_m^0 - G_N\right)}{rRT}$$

Equation (2.38) was integrated incorrectly by Rees and Bhadeshia [1992a] and has subsequently only been used numerically. In Chapter 4 this error will be corrected with a new analytical integration.

## 2.4 Martensite

The cooling of austenite to a sufficiently low temperature often results in the formation of martensite by diffusionless transformation. Any carbon in the austenite remains in solution in the new phase. Unlike allotriomorphic ferrite or pearlite, martensite forms by a deformation of the austenite lattice. Ideally, the martensite reaction is a diffusionless shear transformation, highly crystallographic in character, which leads to a characteristic lath or lenticular microstructure.

The reaction begins at the martensite-start temperature, $M_s$, which varies widely depending on alloy chemistry. The transformation progresses on cooling below $M_s$, the fraction depending on the undercooling below $M_s$. Frequently a small portion of austenite does not transform. This is called retained austenite and can be found in high alloy steels where $M_s$ is relatively low.

Martensite can also form from metastable austenite during low temperature plastic deformation. Steels which exploit this effect are called transformation induced plasticity (TRIP) steels and shall be discussed later.

### 2.4.1 Martensite reaction kinetics

*2.4.1.1 Koistinen and Marburger*

Koistinen and Marburger [1959] successfully fitted a straight line to the plot of $M_s$-$T_q$ (quench temperature) versus the logarithm of volume fraction of austenite $V_\gamma$. This gave the equation:

$$V_\gamma = \exp\left[-C_5\left(M_s - T_q\right)\right] \tag{2.39}$$

where $M_s > T_q >$ -80 °C, with $C_5 = 1.1 \times 10^{-2}$

This fitted well the available experimental data for plain carbon steels. Alloying elements were thought to affect the amount of retained austenite only by their effect on $M_s$. The amount of martensite was then calculated using the obtained value of $V_\gamma$.

The form of the Koistinen and Marburger equation has been justified theoretically by Magee [1969]. However Magee pointed out that different values of constants were required for different steels, contrary to Koistinen and Marburger's conclusions. Khan and Bhadeshia [1990a] also showed with their results that the equation fitted well but required different values of $C_5$.

*2.4.1.2 Khan and Bhadeshia*

In 1990 Khan and Bhadeshia modified the Koistinen and Marburger method of calculating the amount of martensite obtained from austenite when quenched below $M_s$. Their experimental results were obtained using dilatometry to measure the volume fraction of martensite and bainite (if formed), the austenite being the remainder. The results were obtained using a Fe-0.44C-1.74Si-0.67Mn-1.85Ni-0.83Cr-0.39Mo-0.09V wt.% steel, some samples of which had been homogenised and some in the as received condition. The heat treatments included holding samples at various isothermal bainite forming temperatures before quenching to a known temperature whilst others were quenched directly from the austenite phase.

The new theory included the autocatalysis effect, in which plates of martensite induce new embryos which are then available for further transformation. Using the assumption that each nucleus leads to the formation of a plate of constant volume and taking into account autocatalysis, the following equation was derived:

$$-\frac{\ln\left(1-V_{\alpha'}\right)}{V_{\alpha'}} = 1 + C_6\left(M_s - T_q\right) \qquad (2.40)$$

where $V_{\alpha'}$ is the volume fraction of martensite and $C_6 = 0.0029$ which was found using linear regression. This gave good agreement with all the experimental data. Some discrepancy was found for the lower volume fractions of martensite; this might be because the analysis still does not take into account the change in plate volume with degree of transformation and the variation in activation energy of nucleation sites.

## 2.5 Mechanical Properties

### 2.5.1 TRIP steels

Multiphase microstructures, which contain retained austenite, can have high strength and high levels of formability. The retained austenite is capable of transforming to martensite during straining to give an increase in work hardening rates and hence higher ductility [Nishiyama, 1978]. Such steels are known as TRIP (transformation-induced plasticity) steels.

The original TRIP steels [Zackay *et al.*, 1967] contained a lot of expensive alloying elements to retain the austenite but relatively inexpensive Si-Mn steels have been found to have the ability to retain large amounts of austenite after bainite formation.

An advantage of the bainitic microstructure is that carbon, which is used as an austenite stabiliser, is cheap, and is being used without the usual problems of brittle carbide formation. Another is that the heat treatments required to produce such steels are much simpler than the rolling and tempering processes needed when producing high strength martensitic steels. As can be seen in fig. 2.10, equivalent, if not better toughness and strength combinations than some martensitic steels can be achieved, sometimes matching those of the expensive maraging steels [Takahashi and Bhadeshia, 1991].

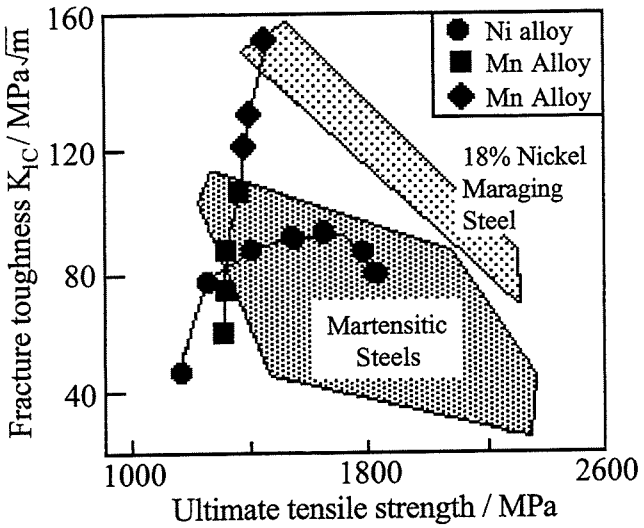


Fig. 2.10: Comparison of the mechanical properties of mixed microstructures of bainitic ferrite, martensite and austenite, versus those of quenched and tempered martensitic alloys [Miihkinen and Edmonds, 1987b].

Not only is the amount of austenite important, its stability is too. As shown later, if the manganese content of the steel is too high then martensite may be present in the steel which reduces the stability of the austenite and allows it all to transform easily, rather than gradually over a range of strains, thus reducing the TRIP effect. Additionally, a reduction in the carbon content of the remaining austenite reduces its stability.

The morphology of the austenite also affects its stability. Areas of blocky austenite between bainite sheaves are less stable than thin films between bainite platelets. This is due to constraint by the bainitic ferrite and higher carbon concentrations in the thin films. The blocky austenite areas can transform to brittle martensite too easily and reduce the ductility and toughness of the material.

### 2.5.2 Strength

*2.5.2.1 Definition of UTS and YS*

During tensile testing of a ductile metal a stress strain curve like that shown in fig. 2.11 may be obtained. The initial linear portion OA is the elastic region within which Hooke's Law is obeyed. Point A is the elastic limit defined as the greatest stress that the metal can withstand without experiencing a permanent strain when the load is removed.

For engineering purposes the limit of usable elastic behaviour is described by the yield strength (YS), point B. This is defined as the stress which will produce a small amount of permanent deformation, generally equal to a strain of 0.002 (OC in fig. 2.11).

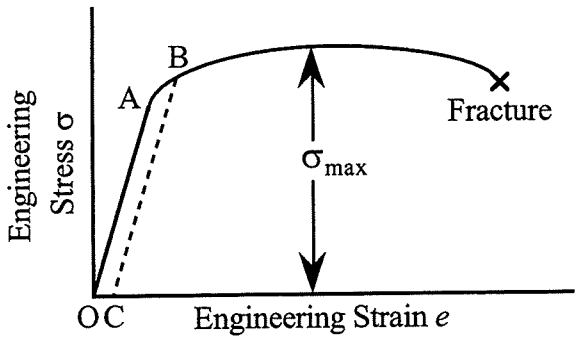


Fig. 2.11: Typical stress strain curve for a ductile metal.

As the plastic deformation of the specimen increases the metal becomes stronger (strain hardening) so that the load required to extend the specimen increases with further straining. Eventually the load reaches a maximum value. The ultimate tensile strength (UTS) is defined as this maximum load divided by the original area of the specimen.

*2.5.2.2 Factors Affecting Strength*

Edmonds and Cochrane [1990] made a study of the structure-property relationships in bainitic steels. For non-Si rich bainitic steels they proposed four factors contributing to the strength of bainitic steels:

a) the slip-band length, related to the sheaf and platelet size.
b) the dislocation structure within the platelets.
c) solid solution hardening from substitutional elements and interstitial hardening from carbon and nitrogen.
d) the dispersion hardening effect of the carbide particles.

a) and b) depend on the prior austenite grain size and dislocation content as well as the annealing heat treatment (which affects the platelet width and sheaf size). c) is dependent on the steel chemistry and, in Si-rich steels as studied here, d) is not a factor as carbide particles are avoided.

In Si-rich bainitic steels the strength seems to depend more on the morphology of the microstructure than the above factors.

The strength of a mixture of bainite and martensite is not simply a "rule of mixtures" of the strengths of the individual phases. One investigation found a peak in strength at about 0.3 volume fraction of bainite [Young and Bhadeshia, 1994]. This was thought to be due to two factors:

1) The strength of the martensite phase increases with increasing carbon content, and as bainite is formed, the austenite from which the martensite grows becomes enriched in carbon.

2) Plastic constraint effects in which the bainite strength in enhanced (especially at low volume fractions of bainite) by the surrounding relatively rigid martensite.

Fine grain size is another way of increasing the strength of a material. Bainitic microstructures have one of the smallest grain sizes obtainable in bulk materials, without resorting to powder processing, due to the sheaves of fine platelets dividing the larger austenite grains.

### 2.5.3 Uniform Elongation

The conventional measures of ductility that are obtained from the tension test are the engineering strain at fracture (usually called total elongation, T-El) and the reduction of area at fracture. Because an appreciable fraction of the plastic deformation will be concentrated in the necked region of the specimen the value of elongation will depend on the gauge length over which the measurement is taken. A way to avoid the complications from necking is to base the percentage elongation on the uniform strain out to the point at which necking begins. This is referred to as the uniform elongation (U-El).

Research has shown that the ductility of these steels is closely related to the volume fraction of retained austenite present. Also allotriomorphic ferrite, as a softer phase, can lead to a higher ductility.

### 2.5.4 Formability

Some investigations [Sakuma *et al.*, 1991; Hanzaki *et al.*, 1995; Tsukatani *et al.*, 1991] use the parameter:

$$UTS \times U\text{-}El \qquad (2.41)$$

as a formability index, where UTS is the ultimate tensile strength and U-El is the uniform elongation. This is a very rough guide to the formability of a material as the same value could be obtained for a quite strong, yet plastic sample, and a very strong but only slightly plastic material. The use of T-El instead of U-El in some papers is less useful as total elongation measurements may include necking, giving a high rating for a material which necks easily, which is an undesirable feature for formability.

### 2.5.5 Toughness

The toughness of a material can be enhanced if a crack has to traverse finely spaced interphase interfaces and also varying crystal structures. Any crack motion may also be damped by the deformation of softer phases. The bainitic microstructure contains such crack obstacles and deformation takes place within the austenite phase, the presence of which is beneficial if it is in the form of thin films between the bainite platelets and not in blocky regions between the bainite

sheaves. The films are stabilised by the relatively high carbon concentrations, but the blocky austenite can transform into brittle (high carbon) untempered martensite, which may be detrimental to toughness.

For a good combination of toughness and strength, it has been estimated that the ratio of volume fractions of film/blocky austenite must exceed about 0.9 [Bhadeshia and Edmonds, 1983a]. This ratio depends on the total volume fraction of bainite formed. For steels where carbide precipitation does not accompany the formation of bainite, the fraction of bainite that can form may be calculated, so the microstructure can be designed for toughness.

There are three ways to control this ratio and minimise the volume fraction of blocky austenite. Each involves an increase in the volume fraction of bainite [Bhadeshia and Christian, 1990]:

1) Lowering the transformation temperature allows more bainite to form as the $T_0$ carbon concentration ($x_{T0}$) is greater at lower temperatures. Lowering the temperature can however lead to the formation of lower bainite or martensite which may not be desired.
2) A reduction in the overall carbon concentration of the steel increases the extent of reaction as more bainite can form before the austenite carbon content reaches $x_{T0}$.
3) Shifting the $T_0$ curve to higher carbon concentrations with changes in substitutional alloying also allows the reaction to proceed further.

There should also be a lower limit to the carbon content of the steel, otherwise no film austenite would remain and the bainite platelets would be in contact with low angle boundaries, across which cracks easily propagate.

## 2.6 Empirical Formulae for the Calculation of Transformation Temperatures

Many papers [Khan and Bhadeshia, 1990b; Sakuma *et al.*, 1991; 1993] use Andrews' [1965] formulae to calculate the equilibrium austenite formation temperature $Ae_3$ and the practical $Ac_1$ and $Ac_3$ temperatures.

The equilibrium $Ae_3$ temperature was predicted from binary diagrams, one element being iron and the other an alloying element. From these the variation of $Ae_3$ with the weight percent of each element was determined and the factors combined to produce the following two-step method for its overall prediction.

1) Formula for many elements except carbon and nickel: (2.42)

$$Ae_3 = 910\text{-}25Mn\text{-}11Cr\text{-}20Cu+60Si+60Mo+40W+100V+700P+3\text{-}(250Al+120As+400Ti)$$

where $Ae_3$ is in °C and the elements are in wt.%. (Note: the 3 refers to sulphur and is assumed to give a constant increase, and the figures in brackets are particularly doubtful).

2) Carbon and nickel are taken together to allow for the non-linearity of the phase boundary in both of these systems. The factors are calculated by using table 1 in Andrews [1965].

There were limited experimental data available to check this formula, but Andrews claimed it should have an accuracy of ±10 °C.

| Element | $Ac_1$ | $Ac_3$ | $Ae_3$ | $M_s$ |
|---|---|---|---|---|
| C (wt.%) | 0.08 - 1.43 | 0.08 - 0.59 | 0.30 - 0.63 | 0.11 - 0.60 |
| Mn (wt.%) | 0.04 - 1.98 | 0.04 - 1.98 | 0.37 - 1.85 | 0.04 - 4.87 |
| Ni (wt.%) | 0.00 - 5.00 | 0.00 - 5.00 | 0.00 - 3.41 | 0.00 - 5.04 |
| Si (wt.%) | 0.06 - 1.78 | 0.09 - 1.78 | 0.16 - 0.30 | 0.11 - 1.89 |
| Cr (wt.%) | 0.00 - 4.48 | 0.00 - 4.48 | 0.00 - 0.98 | 0.00 - 4.61 |
| V (wt.%) | 0.00 - 2.51 | 0.00 - 0.70 | ... | ... |
| Mo (wt.%) | 0.00 - 2.61 | 0.00 - 1.05 | 0.00 - 0.33 | 0.00 - 5.40 |
| W (wt.%) | 0.00 - 4.10 | 0.00 - 4.10 | ... | ... |
| As (wt.%) | 0.00 - 0.072 | 0.00 - 0.072 | ... | ... |
| S (wt.%) | ... | ... | ... | 0.00 - 0.046 |
| P (wt.%) | ... | ... | ... | 0.00 - 0.048 |

Table 2.1: Range of compositions within which Andrews' formulae are valid.

The $Ac_1$ and $Ac_3$ temperatures were determined statistically from reported data, with compositions ranges as shown in table 2.1, and the following formulae derived:

$$Ac_1 = 723\text{-}10.7Mn\text{-}16.9Ni\text{+}29.1Si\text{+}16.9Cr\text{+}290As\text{+}6.38W \quad (2.43)$$

$$Ac_3 = 910\text{-}203\sqrt{C}\text{-}15.2Ni\text{+}44.7Si\text{+}104V\text{+}31.5Mo\text{+}13.1W\text{-}(30Mn\text{+}11Cr\text{+}20Cu\text{-}700P\text{-}400Al\text{-}120As\text{-}400Ti) \quad (2.44)$$

where $Ac_1$ and $Ac_3$ are in °C and the elements are in wt.%. The $\sqrt{C}$ in the $Ac_3$ formula was a consequence of the curvature of the phase boundary in Fe-C, but no heating-rate or starting microstructure factors were included, which are now known to be important [Yang and Bhadeshia, 1989; Gavard *et al.*, 1996].

Andrews also derived new formulae for the martensite-start temperature $M_s$. His linear formula was:

$$M_s = 539\text{-}423C\text{-}30.4Mn\text{-}17.7Ni\text{-}12.1Cr\text{-}7.5Mo \qquad (2.45)$$

in which $M_s$ is in °C and the element concentrations are in wt.%.

He also derived a 'product' formula for $M_s$ (equation. 6 in Andrews [1965]) taking into account interactions between alloy elements. This gave slightly more accurate results and 95% of the experimental results were within ± 25 °C of the prediction.

## 2.7 Heterogeneous steels

Most commercial steels are not homogeneous and this affects the microstructural changes which occur during heat treatment. The elements Ni, Mn, Mo, V and Cr all retard the bainite reaction so it is expected that solute depleted regions will transform to bainite first. It has also been shown [Khan and Bhadeshia, 1990b] that heterogeneous samples form less overall bainite because most of the nucleation occurs in the depleted areas and the enriched regions of austenite fail to accommodate as much carbon as usual, thus the transforming areas reach a carbon concentration of $x_{T0}$ quicker.

A computer model [Khan and Bhadeshia, 1990b] has been designed to model bainite transformations in banded steels by representing the sample as a series of slices, each with a uniform composition assigned from experimental measurements, and then allowing transformation to take place in each slice separately, if thermodynamically permissible. This model shows reasonable agreement with experimental data.

The martensite reaction has been shown [Khan and Bhadeshia, 1990a] to have an extended temperature range over which the reaction occurs when using segregated rather than homogenised samples. Any other differences are within experimental errors.

The effect of heterogeneous distribution of carbon during and after bainite transformation can increase the amount of bainite formed as has already been mentioned.

# 3. Experimental Techniques

## 3.1 Thermomechanical Simulator

A thermomechanical simulator is a programmable piece of equipment with the ability to simulate a specified thermal cycle on a metal specimen and monitor temperature, stress and dilatation of the specimen with time. The Thermecmastor Z simulator (manufactured by Fuji Electronic Industrial Co. Ltd.) was used to study phase transformations during accurately controlled thermal cycles by measuring the diametrical dilatation. This was measured, without contact with the specimen, by using a He-Ne laser beam with an accuracy of ±1μm. The laser beam scans and moves with the ram to ensure that the same location is monitored irrespective of perpendicular expansion or deformation. The scanning frequency of the laser is approximately 1000 Hz.

The control of the machine and the data collection are both via a computer enabling the heat treatment cycle to be programmed and monitored with ease.

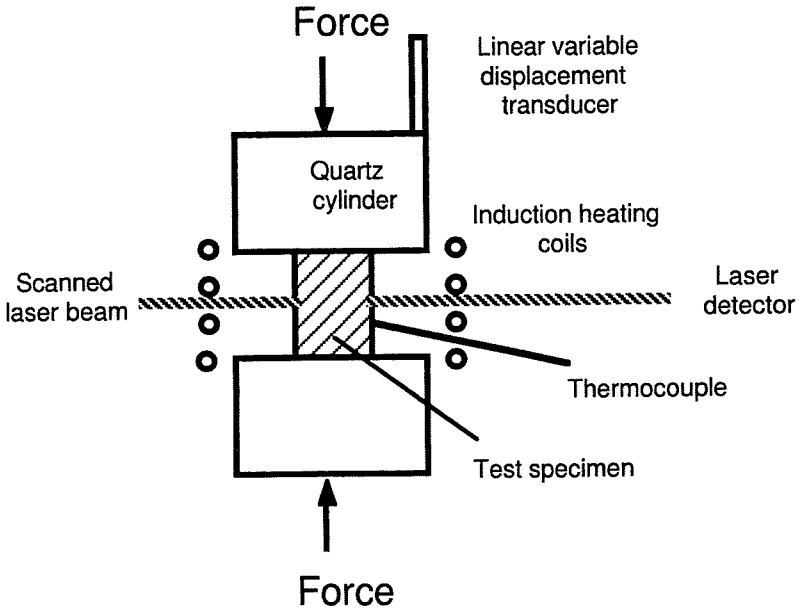


Fig. 3.1: Schematic of the thermomechanical simulator.

Heating of the specimen is achieved via a high frequency induction heating system and monitored using a platinum/platinum-rhodium thermocouple, which is spot welded to the specimen. The accuracy of the temperature measurements is ±3 °C. Heating can be done in a vacuum or an inert atmosphere of nitrogen or argon. Helium or nitrogen gases are used for rapid quenching and cooling, water is also available for rapid quenching. In this work heating was done under a vacuum and He was used during quenching. The specimens were machined

into cylinders of 8 mm diameter by 12 mm long and positioned in the simulator as illustrated in fig. 3.1.

## 3.2 Optical Microscopy

Cylindrical thermomechanical samples were cut in half (to reveal a circular cross section) for microstructural characterisation and hot-mounted in Bakelite, followed by grinding on SiC paper to 1200 grit and polishing with 6 and then 1 μm cloth coated with diamond paste. They were washed thoroughly between each stage in the preparation process, before finally etching in 2% Nital (nitric acid in methanol). Optical micrographs were taken with an Olympus microscope with a camera attached using Ilford Pan F film.

## 3.3 Thermal Etching

To measure the austenite grain size obtained after 3 minutes at 1000 °C a sample in the as-received state was mounted lengthways in Bakelite and a rectangular section ground and polished as in optical microscopy. It was then removed from the Bakelite mount and placed in the thermomechanical simulator for a heat treatment of 1000 °C for 3 minutes (see fig. 3.2 for heating cycle). This produced surface relief at the austenite grain boundaries and optical micrographs were taken.

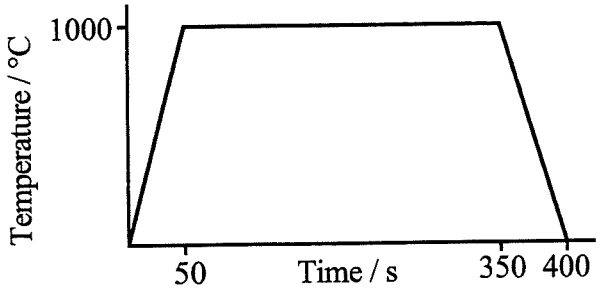


Fig. 3.2: Heat treatment in thermomechanical simulator for thermal etch.

## 3.4 Image Analysis

Optical micrographs of the thermal etched sample contained surface relief details from the formation of martensite on rapid quenching as well as the thermal groves at austenite grain boundaries. To allow measurements of the grain size, without these details contributing, the grain boundaries were traced onto acetate using an ultra fine permanent pen. This image was then analysed using a Seescan image analyser and computer to calculate the average feret diameter† and the standard deviation.

[† Feret diameter is the largest diameter, measured between parallel lines on either side of the object.]

## 3.5 Point Counting

Manual point counting was used to measure the volume fraction of prior ferrite†, from photographs in published literature, and the grain size of some experimental steels. This involved the random positioning of a square grid of points with a spacing approximately equal to the grain size (usually 1 cm), and counting the fraction of points which fell within prior ferrite grains. An average of at least 5 readings per microstructure was taken and the standard deviation calculated using equation 3.1.

$$\sigma_{vf} = V_f \sqrt{\frac{1}{P_\alpha}\left(1 - V_f\right)} \qquad (3.1)$$

where $V_f$ is the volume fraction of prior ferrite in the sample, $P_\alpha$ is the number of points falling in the α-phase and $\sigma_{vf}$ is the standard deviation of the measured $V_f$ (65% confidence).

[† Prior ferrite is allotriomorphic ferrite formed during intercritical annealing at a temperature within the ferrite and austenite phase field.]

## 3.6 X-ray Diffraction

To measure the lattice parameters of austenite and bainitic ferrite samples were heat treated in a thermomechanical simulator to produce the desired microstructures. These were machined in half (lengthways) and mounted in Bakelite for mechanical grinding and polishing of the flat surface (see optical microscopy). The samples were then removed from the Bakelite and chemically polished to remove the surface layer. The chemical polishing solution was a mixture of 5% HF, 50% $H_2O_2$ and 45% $H_2O$. The samples were soaked in this for 10 minutes and then washed with IMS (industrial methylated spirits) and air dried. This process leads to more accurate parameter measurements since the effects of deformation from machining are removed.

The Debye-Scherrer X-ray diffraction method with Cu-$K_\alpha$ radiation was used. The accelerating voltage was 45 kV and the tube current 25 mA. The Cu-$K_{\alpha 1}$ and Cu-$K_{\alpha 2}$ lines could only be resolved at the high Bragg angles ($\theta_b$). At lower angles an average of the two calculated d-spacings was used for the analysis and the data extrapolated to $\theta_b$=90°.

## 3.7 Homogenisation

To compare the effect of chemical segregation in the as-received samples some were homogenised by annealing in a furnace at 1200 °C for three days whilst they were protected by sealing in quartz tubes containing a partial pressure of pure argon. After annealing, the samples were quenched in room temperature water.

## 3.8 Atomic Force Microscopy

An atomic force microscope (AFM) is capable of high resolution observation and measurement of surface topography. The technique uses the atomic forces working between a fine probe, attached to a cantilever, and the sample surface. The attractive forces at close distances cause the cantilever to move with change in surface height. This deflection is then measured by an optical lever method, using the back of the cantilever as a mirror, and movement is detected by laser.

Cylindrical steel samples (8 mm in diameter and 12 mm in length) were machined with 2 mm and 1 mm deep flats on opposite sides of the cylinder, as illustrated in fig. 3.3.

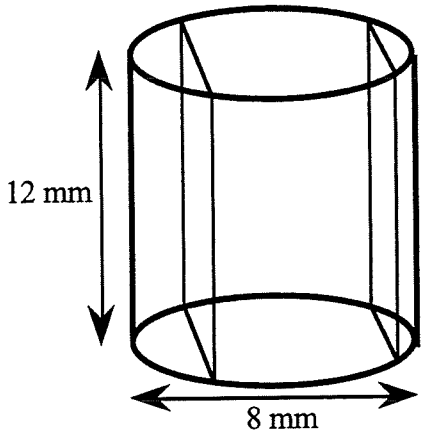


Fig. 3.3: Sample shape for heat treatment in a thermomechanical simulator followed by examination in an atomic force microscope (AFM).

The size of the samples was suitable for heat treatment in a thermomechanical simulator. One of the flats was needed to place the samples securely in an AFM and the other (2 mm deep) to make observations of surface relief. This surface was metallographically polished to a 1 μm finish and cleaned thoroughly with high purity ethanol. All subsequent handling was with gloves and any storage was in a desiccator.

All the heat treatments were carried out using a thermomechanical simulator (see section 3.1). After austenitisation at 1200 °C for 150 s the samples were cooled rapidly to the isothermal

transformation temperature using helium gas. The isothermal heat treatment used was 450 °C for either 1200 s or 400 s (the reduced time to avoid oxidation during transformation). The samples were helium quenched to ambient temperature after the 450 °C heat treatment.

The surface relief caused by the formation of bainite in the samples was then examined using a Seiko SPA300 AFM.

## 3.9 Transmission Electron Microscopy

From broken tensile testing specimens, of 1 mm thickness, 3 mm diameter discs were cut, either from near the break (deformed) or in the grip area (undeformed), fig. 3.4. These were ground to 100 μm thickness using 240 grit SiC paper and then electropolished in a 5% perchloric acid, 95% acetic acid solution at 200 mA until a small hole was detected. Once washed with absolute ethanol the samples were examined in a Philips CM 12 transmission electron microscope with STEM (scanning transmission electron microscopy) facility.

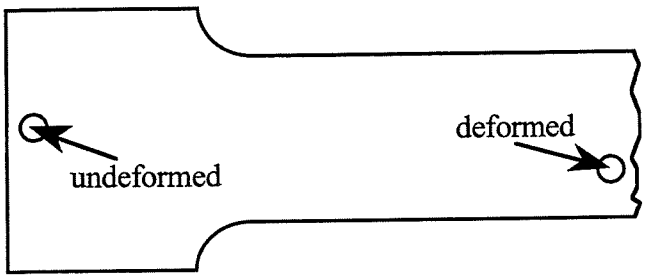


Fig. 3.4: Diagram of a broken tensile testing specimen indicating the sample positions.

# 4. Modelling The Bainite Transformation

## 4.1 Early Work

Work on the rate of bainite formation has been reviewed by Bhadeshia [1992]. All of the early work has concentrated on an empirical application of the Avrami equation [Christian, 1975] and hence cannot be applied generally in the design of steels. Even the most elementary features of the mechanism are not included, so that effects such as the incomplete reaction phenomenon cannot be predicted.

One semi-empirical model by Takahashi and Bhadeshia [1991] which includes mechanistic details has been described in Appendix 1. It builds on earlier work [Bhadeshia, 1982a] on the calculation of time-temperature-transformation diagrams. Since that work only allowed the initiation of reaction to be calculated, Takahashi and Bhadeshia adapted it for the progress of transformation beyond initiation. The 0% transformation curve was calculated for a series of increasing carbon concentrations keeping the other solutes constant. The curve for a carbon-enriched steel was assumed to correspond to that for the unenriched steel but with a fraction of bainite which would lead to the enrichment of austenite. Features such as a fundamental treatment of the $B_s$ temperature and the incomplete reaction phenomenon were incorporated. The discussion in Appendix 1 shows that although this model produces the correct trends it is not very accurate in practice.

## 4.2 Model Based on Mechanism

An empirical model, based on the bainite transformation mechanism [Bhadeshia, 1982c], was later refined by Rees and Bhadeshia [1992a]. In this model, consistent with a vast array of experimental evidence [Bhadeshia, 1982c], the growth of bainite is taken to be diffusionless, with the carbon partitioning into the residual austenite shortly after the growth of each bainite plate is stifled. This has the important consequence that transformation ceases as soon as diffusionless growth becomes thermodynamically impossible to sustain. Thus the maximum volume fraction of bainitic ferrite, $\theta$, can be calculated using the Lever Rule applied to the $T_0'$ curve of the paraequilibrium phase diagram:

$$\theta = \frac{x_{T_0'} - \bar{x}}{x_{T_0'} - x_\alpha} \tag{4.1}$$

The mean carbon concentration of the alloy ($\bar{x}$) is expressed as a mole fraction; $x_{T0'}$ is the carbon concentration at $T_0'$ and $x_\alpha$ the estimated carbon content of the ferrite.

### 4.2.1 Nucleation rate

The nucleation of bainite occurs with the paraequilibrium partitioning of carbon. The nucleation event is identified with the rapid dissociation of arrays of pre-existing dislocations; unlike classical nucleation theory this makes the activation energy for nucleation ($Q$) directly proportional to the chemical driving force ($\Delta G_m$), because the latter assists the embryo to overcome an activation barrier to dislocation motion.†

The model [Bhadeshia, 1982c; Rees and Bhadeshia, 1992a] takes into account the nucleation rate from the point where Widmanstätten ferrite ($\alpha_w$) formation becomes possible, since both $\alpha_w$ and bainite originate from the same nucleus. It is essentially only the growth mechanism which distinguishes these phases from one another.

The nucleation rate per unit volume, $I$, is given by Bhadeshia [1982c]:

$$I = C_1 \exp\left(-\frac{Q}{RT}\right) \tag{4.2}$$

Since $Q$ is linearly dependent on $\Delta G_m$, this may be written:

$$I = C_1 \exp\left[-\frac{(C_2 + C_3 \Delta G_m)}{RT}\right] \tag{4.3}$$

where $C_1$, $C_2$ and $C_3$ are constants and $R$ is the gas constant.

When deriving the universal nucleation function $G_N$, Bhadeshia [1981a, 1982a] assumed that the nucleation rate at the Widmanstätten-start temperature, $W_s$, is constant for all steels, irrespective of chemical composition. Rees and Bhadeshia [1992a] showed that this would only be the case if $C_2 = C_3 r$ (where $r$ is also a constant). To take account of this, equation 4.3 had to be modified to:

$$I = K_1 \exp\left[-\frac{K_2}{RT} - \frac{K_2 \Delta G_m}{rRT}\right] \tag{4.4}$$

where $K_1$ and $K_2$ are constants, denoted as such in order to avoid confusion with the constants of the original theory. $K_1$ represents the number density of potential sites for nucleation and at $W_s$ the equation becomes:

$$I = I_{W_s} \tag{4.5}$$

regardless of alloy composition.

[† Some of the work presented here has already been discussed in Chapter 2. It is reproduced here for clarity.]

This can be proved by going back to the original equation in Bhadeshia [1982c]:

$$I = I_{W_s} \exp\left[-\frac{C_2 \Delta T}{RTW_s} - \frac{C_3}{R}\left(\frac{\Delta G_m}{T} - \frac{G_N}{W_s}\right)\right] \tag{4.6}$$

where $\Delta T = T - W_s$, so:

$$I = I_{W_s} \exp\left[-\frac{C_2}{RW_s} + \frac{C_2}{RT} - \frac{C_3 \Delta G_m}{RT} + \frac{C_3 G_N}{RW_s}\right] \tag{4.7}$$

Also $C_2 = C_3 r$, giving:

$$I = I_{W_s} \exp\left[-\frac{C_3 r}{RW_s} + \frac{C_3 r}{RT} - \frac{C_3 \Delta G_m}{RT} + \frac{C_3 G_N}{RW_s}\right] \tag{4.8}$$

At $T = W_s$, $\Delta G_m = G_N$, so the terms in the exponential cancel and:

$$I = I_{W_s} \tag{4.9}$$

### 4.2.2 Free energy change

The enrichment of untransformed austenite with carbon partitioned due to transformation leads to a reduction in the free energy change as austenite is stabilised. Thus $\Delta G_m$ is a function of the volume fraction of ferrite formed [Bhadeshia, 1982c]. Rees and Bhadeshia [1992a] assumed that the driving force varies linearly with the extent of reaction between its initial value $\Delta G_m^0$ and its final value, producing the equation:

$$\Delta G_m = \Delta G_m^0 - \xi\left(\Delta G_m^0 - G_N\right) \tag{4.10}$$

where $G_N$ is the universal nucleation function (section 2.3.3) and $\xi$ is the normalised volume fraction of bainitic ferrite given by:

$$\xi = \frac{v}{\theta} \tag{4.11}$$

where $v$ is the actual volume fraction of bainitic ferrite and $\theta$ is the maximum volume fraction of bainitic ferrite when the austenite has a carbon content given by the $T_0'$ line.

### 4.2.3 Autocatalysis

The autocatalysis factor $\beta$, familiar in martensitic theory [Magee, 1969], describes the extent to which the formation of one plate stimulates others. For bainite autocatalysis is incorporated as follows [Bhadeshia, 1982c]:

$$I = I_0(1+\beta\theta\xi) \tag{4.12}$$

Autocatalysis must diminish as the driving force for transformation decreases due to carbon enrichment. The factor $\beta$ is therefore expressed as a function of the mean carbon concentration of the alloy, $\bar{x}$, because carbon build up in the austenite causes a decrease in the driving force for diffusionless transformation, thus inhibiting autocatalysis [Rees and Bhadeshia, 1992a]. Consequently:

$$\beta = \lambda_1(1-\lambda_2\bar{x}) \tag{4.13}$$

where $\lambda_1$ and $\lambda_2$ are empirical constants (original values were 139 and 25.46 respectively [Rees and Bhadeshia, 1992a]). $\beta$ is set in the computer model so that it cannot be less than zero.

### 4.2.4 Austenite grain size

The nucleation rate for grain boundary nucleation can be taken to be proportional to the surface area of austenite grain boundaries per unit volume, $S_v$. Nucleation is known to occur at grain boundaries since these are likely to contain appropriate arrays of dislocations. $S_v$ is related to the mean linear intercept, $\bar{L}$, of a series of random lines with austenite grain boundaries.

This effect has been incorporated into $K_1$, the number density of potential sites for nucleation, as:

$$K_1 = \left(\bar{L}K_1'\right)^{-1} \tag{4.14}$$

where $K_1'$ is an empirical constant.

### 4.2.5 Overall kinetics

The volume fraction increment between times $t$ and $t + \mathrm{d}t$ is given by:

$$\mathrm{d}v = \theta\,\mathrm{d}\xi = Iu\,\mathrm{d}t \tag{4.15}$$

where $u$ is the volume of a bainite sub-unit (assumed here to be constant) and $I$ is the nucleation rate per unit volume.

As transformation proceeds, the volume of austenite available for transformation decreases, and it becomes necessary to consider the extent of 'extended volume' $dv_e$. This accounts for the formation of 'phantom' nuclei within regions of ferrite already transformed and enables the use of the nucleation rate of bainite per unit volume of austenite, despite the fact that the volume of austenite is changing. The extended volume increment is related to the real volume increment by the equation:

$$dv = (1-\xi)dv_e \tag{4.16}$$

where

$$dv_e = Iu\,dt \tag{4.17}$$

which gives:

$$\theta\,d\xi = (1-\xi)uI\,dt \tag{4.18}$$

Substituting equations 4.4, 4.10 and 4.12 into the above expression we get the rate at which the normalised fraction of bainite changes:

$$\frac{d\xi}{dt} = \frac{uK_1}{\theta}(1-\xi)(1+\beta\theta\xi)\exp\left[-\frac{K_2}{RT}\left(1+\frac{\Delta G_m^0}{r}\right)+\Gamma_2\xi\right] \tag{4.19}$$

$$\text{where } \Gamma_2 = \frac{K_2\left(\Delta G_m^0 - G_N\right)}{rRT} \tag{4.20}$$

### 4.2.6 The integration

The model of Rees and Bhadeshia [1992a] contained an error in the final integration, so that it has subsequently only been used numerically. Here an analytical solution is proposed.

Equation 4.19 can be simplified to:

$$\frac{d\xi}{dt} = A(1-\xi)(1+B\xi)\exp[-C+D\xi] \tag{4.21}$$

where $A = \frac{uK_1}{\theta}$, $B = \beta\theta$, $C = \frac{K_2}{RT}\left(1+\frac{\Delta G_m^0}{r}\right)$, and $D = \Gamma_2$

It follows that (with $t'$ and $\xi'$ as dummy variables):

$$\int_0^t \mathrm{d}t' = \int_0^{\xi} \frac{\exp\{-[-C+D\xi']\}}{A(1-\xi')(1+B\xi')}\mathrm{d}\xi' \tag{4.22}$$

$$t = \frac{\mathrm{e}^C}{A(B+1)}\int_0^{\xi} \mathrm{e}^{-D\xi'}\left[\frac{1}{1-\xi'}+\frac{B}{1+B\xi'}\right]\mathrm{d}\xi' \tag{4.23}$$

$$t = \frac{\mathrm{e}^C}{A(B+1)}\left[\int_0^{\xi} \mathrm{e}^{-D\xi'}\left(\frac{1}{1-\xi'}\right)\mathrm{d}\xi' + \int_0^{\xi} \mathrm{e}^{-D\xi'}\left(\frac{B}{1+B\xi'}\right)\mathrm{d}\xi'\right] \tag{4.24}$$

Solving these integrals separately by substitution:

$$\int_0^{\xi} \mathrm{e}^{-D\xi'}\left(\frac{1}{1-\xi'}\right)\mathrm{d}\xi' \xrightarrow{\phi=1-\xi'} -\int_1^{1-\xi} \frac{\mathrm{e}^{-D+D\phi}}{\phi}\mathrm{d}\phi \tag{4.25}$$

where $\mathrm{d}\phi = -\mathrm{d}\xi'$, thus:

$$= \mathrm{e}^{-D}\int_{1-\xi}^{1} \frac{\mathrm{e}^{D\phi}}{\phi}\mathrm{d}\phi \tag{4.26}$$

Using a standard integral [Rektorys, 1969] this becomes:

$$= e^{-D}\left[\ln|\phi| + \frac{D\phi}{1\times 1!} + \frac{(D\phi)^2}{2\times 2!} + \frac{(D\phi)^3}{3\times 3!} + \ldots\right]_{1-\xi}^{1} \tag{4.27}$$

Defining the function:

$$f(x) = \frac{x}{1\times 1!} + \frac{x^2}{2\times 2!} + \frac{x^3}{3\times 3!} + \ldots \tag{4.28}$$

Thus the first integral becomes:

$$\mathrm{e}^{-D}\left(f(D) - \ln(1-\xi) - f\left(D(1-\xi)\right)\right) \tag{4.29}$$

For the second integral:

$$\int_0^{\xi} \mathrm{e}^{-D\xi'}\left(\frac{B}{1+B\xi'}\right)\mathrm{d}\xi' \xrightarrow{\psi=1+B\xi'} \int_1^{1+B\xi} \frac{\mathrm{e}^{\frac{D}{B}(1-\psi)}}{\psi}\mathrm{d}\psi \tag{4.30}$$

where $d\psi = B d\xi'$, thus giving:

$$= e^{D/B} \int_{1}^{1+B\xi} \frac{e^{\frac{-D\psi}{B}}}{\psi} d\psi \tag{4.31}$$

$$= e^{D/B}\left[ \ln|\psi| - \frac{D\psi}{B} + \frac{(D\psi/B)^2}{2\times 2!} + \frac{(-D\psi/B)^3}{3\times 3!} + \ldots \right]_1^{1+B\xi} \tag{4.32}$$

Define:

$$E = \frac{D}{B} \tag{4.33}$$

Thus the second integral becomes:

$$e^{E}\left(\ln|1+BE| + f\left(-(E+D\xi)\right) - f(-E)\right) \tag{4.34}$$

Combining these 2 integrals back into equation 4.24 we get:

$$t = \frac{e^{C}}{A(B+1)} \left\{ \begin{matrix} e^{E}\left(\ln|1+B\xi| + f\left(-(E+D\xi)\right) - f(-E)\right) \\ -e^{-D}\left(\ln(1-\xi) + f\left(D(1-\xi)\right) - f(D)\right) \end{matrix} \right\} \tag{4.35}$$

where $A = \frac{uK_1}{\theta}$, $B = \beta\theta$, $C = \frac{K_2}{RT}\left(1 + \frac{\Delta G_m^0}{r}\right)$, $D = \Gamma_2$ , $E = \frac{D}{B}$

$$\text{and } f(x) = \frac{x}{1\times 1!} + \frac{x^2}{2\times 2!} + \frac{x^3}{3\times 3!} + \ldots$$

This series for $f(x)$ is convergent for all $x$. In the computer program written to implement equation 4.35 the function is calculated to 20 terms, by which point $f(x)$ has converged for all values of $x$ used.

### 4.2.7 The computer program

The theory stated above has been coded into a computer program which requires an input of chemical composition (C, Si, Mn, Ni, Mo, Cr, V in wt.%), isothermal transformation temperature (°C) and austenite grain size (μm). There are also options for calculations of continuous cooling and intercritical annealing effects which are described in sections 4.5 and 4.6. The other values required in equation 4.35 are calculated within the program (see Appendix 2 for a full description of the program and the FORTRAN code).

The $T_0$ and $T_0'$ carbon concentrations are required as a function of temperature to estimate the limiting volume fractions. This is achieved by initially guessing the carbon concentration and calculating the free energy change of composition-invariant transformation of austenite to ferrite as described by Bhadeshia and Edmonds [1980]. Newton's iteration method is then used to refine the carbon concentration until the error in the free energy is less than 10 J mol$^{-1}$ (subroutine AXTO [MAP]). To calculate the $T_0'$ curve a value of 400 J mol$^{-1}$ of stored energy is added to the free energy of ferrite and the equations solved as for $T_0$.

Equation 4.35 is of a form such that the time required to form a given volume fraction of ferrite can be calculated. To calculate the volume fraction formed during a specified time, the volume fraction is increased in steps of 0.01, from 0, until the calculated time is greater than that required (subroutine ROUGH [MAP]). This is then repeated in a smaller range to find the volume fraction for the required time to an accuracy of 0.0001 (subroutine FINE [MAP]).

The new relationship given by equation 4.35 was used to refine the fitting constants $K'_1/u$, $K_2$, $\lambda_1$ and $\lambda_2$ originally found by Rees and Bhadeshia [1992a]. This was achieved using experimental data published by Bhadeshia [1982c] for steels of compositions: Fe-0.39C-2.05Si-4.08Ni, Fe-0.22C-2.03Si-3.0Mn and Fe-0.44C-1.74Si-0.67Mn-1.85Ni-0.83Cr-0.39Mo-0.09V (all in wt.%) by minimising the sum of squared errors (*SSE*):

$$SSE = \sum[\ln(t_p) - \ln(t_m)]^2 \qquad (4.36)$$

where $t_p$ is the predicted time and $t_m$ the measured time to achieve a specified fraction of transformation. The results are illustrated in figs. 4.1a and b.

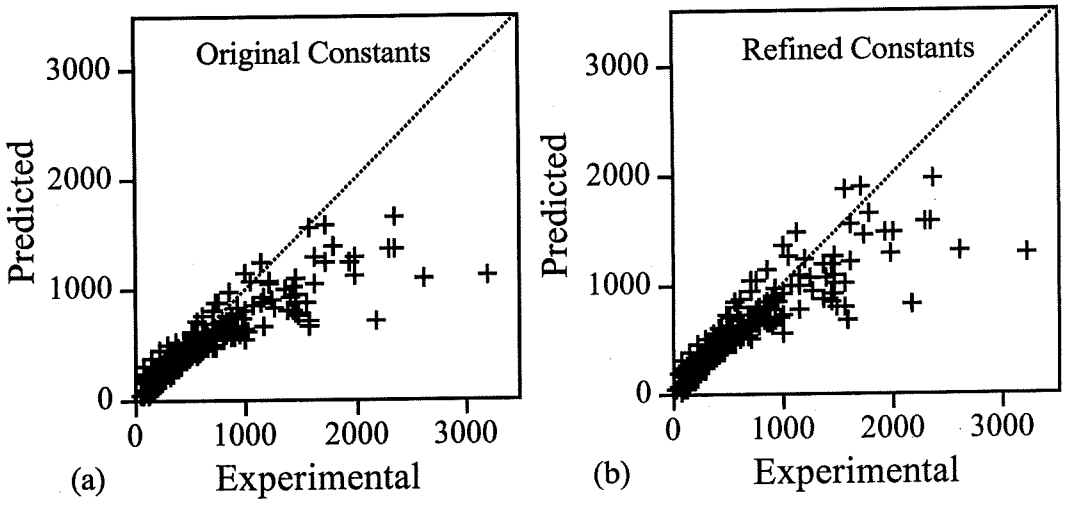


Fig. 4.1: Comparison of predicted and measured times (s) using equation 4.35 and (a) the original and (b) the refined constants.

The original and refined constants are as shown in table 4.1 along with the corresponding values of *SSE*. These refined constants were used for all the predictions shown in this work.

| Constant | $K'_1/u$ / mm$^{-1}$ s | $K_2$ / J mol$^{-1}$ | $\lambda_1$ | $\lambda_2$ | *SSE* / s$^2$ |
|---|---|---|---|---|---|
| Original | 33.900 | 2.065x10$^4$ | 139.00 | 25.460 | 30.8 |
| Refined | 34.456 | 2.098x10$^4$ | 147.50 | 30.327 | 27.4 |

Table 4.1: Original and refined constants for equation 4.35.

## 4.3 Experimental

To further test the model, dilatation measurements taken during the transformation of a steel of composition Fe-0.38C-1.29Si-1.73Mn (wt.%) were analysed. The heat-treatments (fig. 4.2) were carried out on cylindrical steel samples, 8 mm in diameter and 12 mm in length, in an adapted Thermecmastor Z Simulator as described in section 3.1.

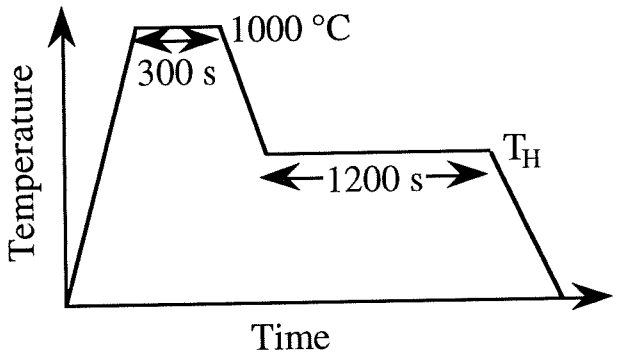


Fig. 4.2: Heat treatment used to study the kinetics of the bainite transformation.

Six different values of the holding temperature $T_H$ (330, 355, 380, 405, 430 and 455 °C) were chosen between the calculated $B_s$ and $M_s$ temperatures (478 and 323 °C respectively) to characterise the formation of bainite.

### 4.3.1 Thermal expansion coefficients of austenite and ferrite

The thermal expansion coefficients of austenite and ferrite are required in order to convert dilatation measurements into fraction of bainitic ferrite. Measurements for the steel of composition Fe-0.38C-1.73Mn-1.29Si wt.% were carried out on a thermomechanical simulator.

For ferrite the sample was heated to 600 °C and held for 30 minutes to ensure that all the retained austenite transformed to a mixture of ferrite and carbides, and that any martensite was

tempered. The effect of the very small fraction of carbides was neglected in the analysis. The sample was then cooled at a rate of 1 °C $s^{-1}$ and the change in dilatation measured. The mean expansion coefficient in the range 300 to 500 °C was found to be 1.57 x $10^{-5}$ $°C^{-1}$ to an accuracy of ± 0.25 x $10^{-5}$ $°C^{-1}$.

The austenite expansion coefficient was measured by heating the steel sample to 1000 °C and holding it at that temperature for 5 minutes to obtain a fully austenitic microstructure, followed by cooling at a rate of 1 °C $s^{-1}$ to 500 °C and quenching to room temperature. Fig. 4.3b shows the dilatation measurements made during this heating cycle. The austenite expansion coefficient ($e_\gamma$) was found to be 2.41 x $10^{-5}$ $°C^{-1}$ (± 0.25 x $10^{-5}$ $°C^{-1}$).

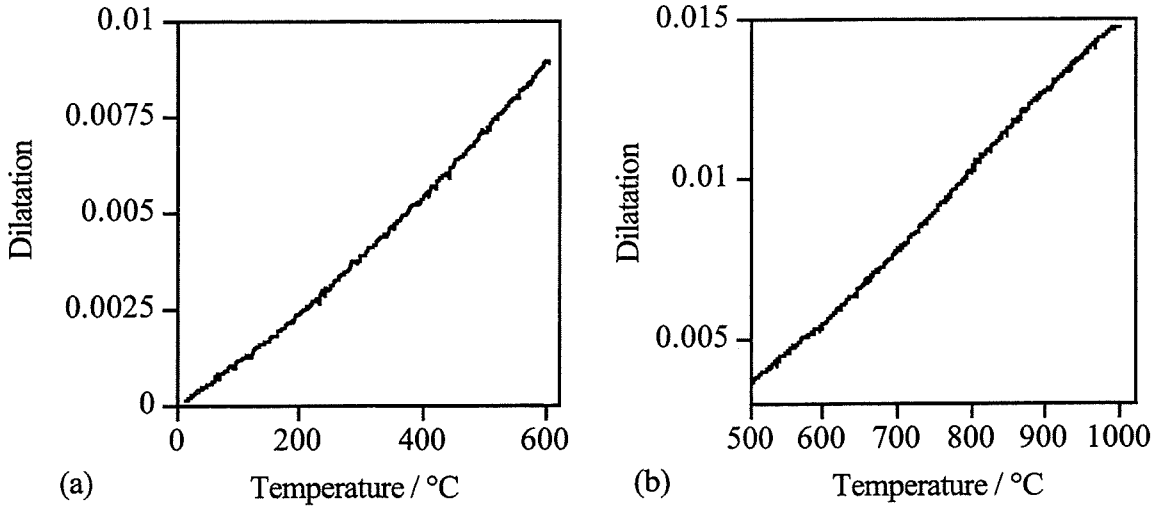


Figs. 4.3(a) and (b): Dilatation measurements during cooling at 1 °C $s^{-1}$ of a Fe-0.38C-1.29Si-1.73Mn wt.% steel sample for ferrite and austenite respectively. The expansion coefficients are clearly not constant but are here assumed to be so.

### 4.3.2 Lattice Parameters

The lattice parameters of austenite and ferrite were required for converting dilatations into volume fraction of bainite formed (see section 4.3.4).

The ferritic sample given the heat treatment to measure the expansion coefficient (section 4.3.1) was also used to measure the lattice parameter. The austenite measurements were made on a bainitic sample prepared by holding a homogenised Fe-0.38C-1.29Si-1.73Mn wt.% steel sample at 1000 °C for 3 minutes, cooling to 330 °C and holding for half an hour, and then cooling rapidly to room temperature. Thus the parameter measured was that of retained austenite with an enriched carbon content.

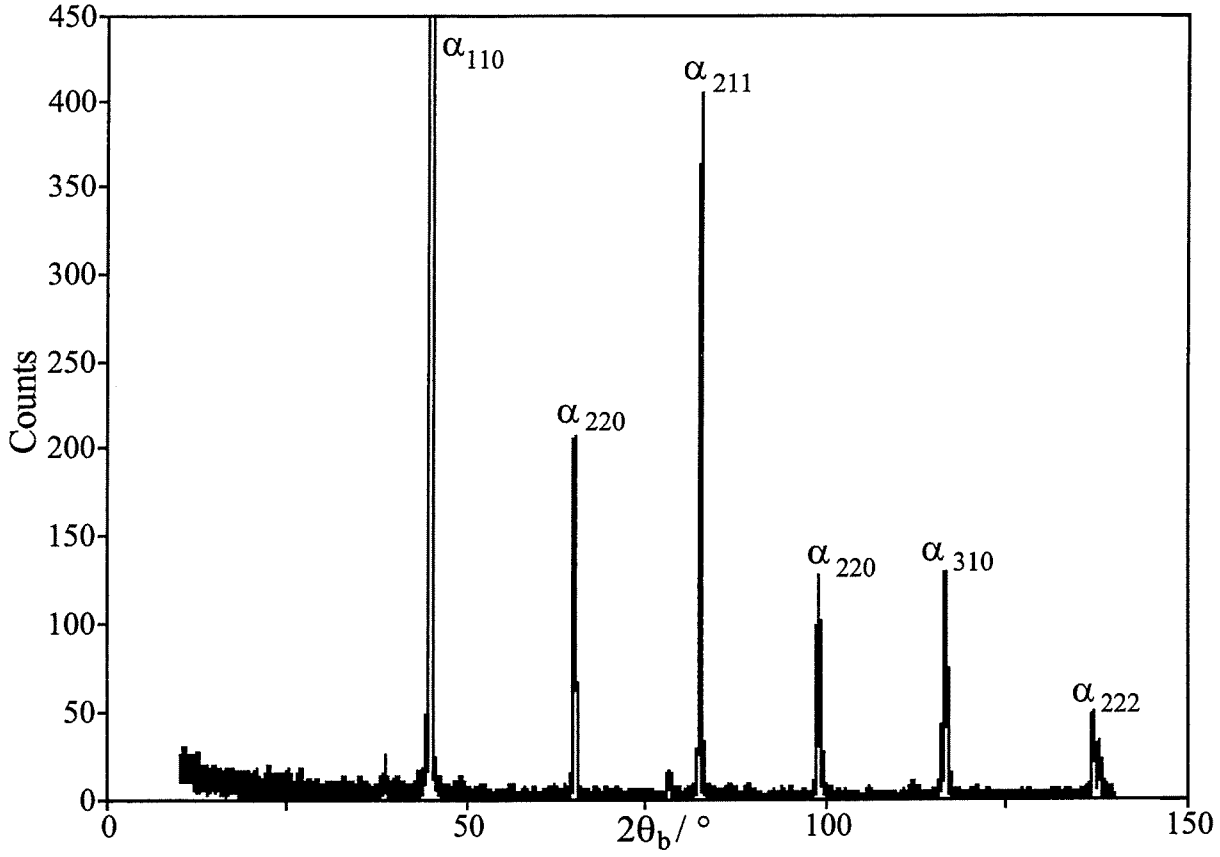


Fig. 4.4: X-ray diffraction trace for a ferritic sample of Fe-0.38C-1.29Si-1.73Mn wt.% steel.

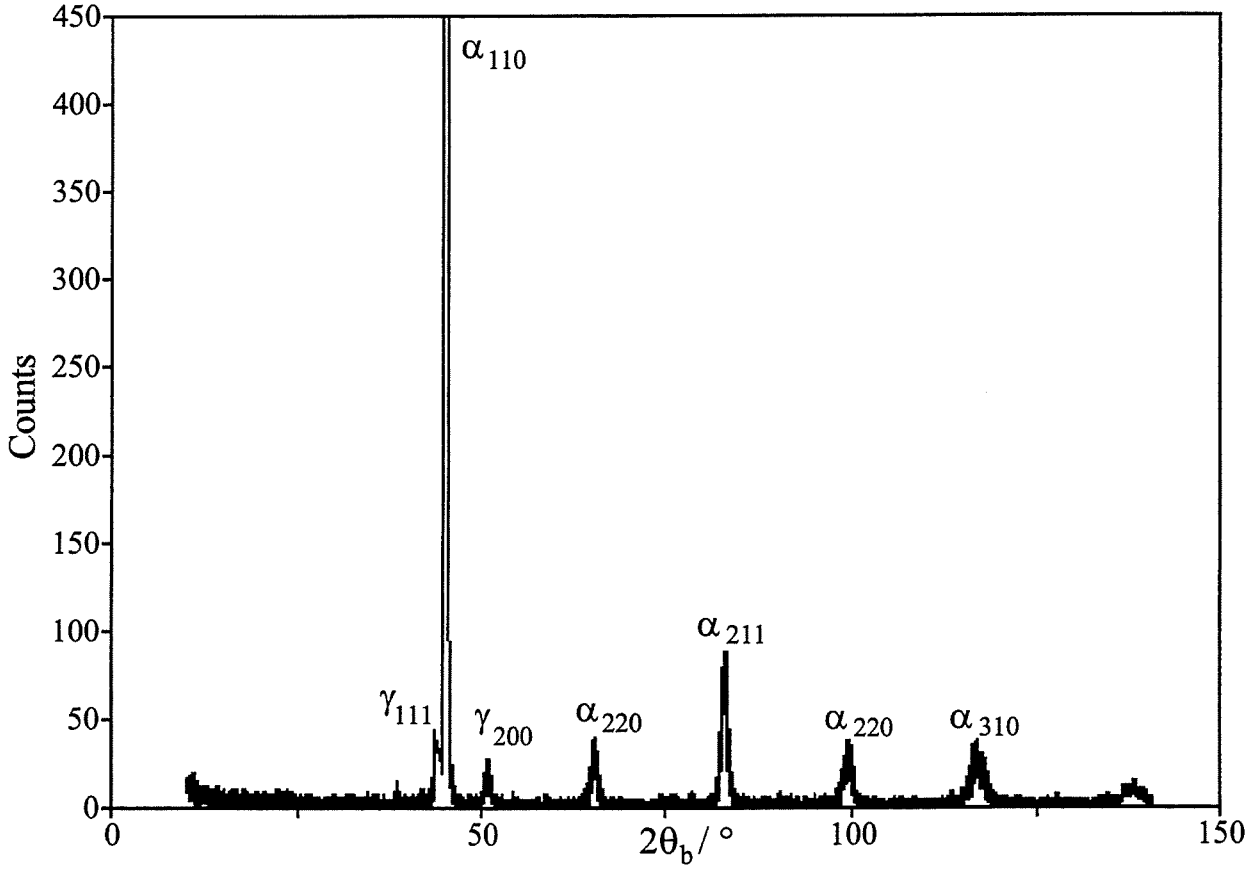


Fig. 4.5: X-ray diffraction trace for a bainitic sample of Fe-0.38C-1.29Si-1.73Mn wt.% steel.

The samples were chemically polished in a solution of 5% HF, 50% $H_2O_2$ and 45% $H_2O$. Measurements were then made using X-ray diffraction with Cu-$K_\alpha$ radiation as described in experimental techniques section 3.6. Figs. 4.4 and 4.5 show the diffraction intensity graphs for the ferrite and bainitic samples respectively as a function of Bragg angle $\theta_b$.

$$a_0 = d\sqrt{h^2 + k^2 + l^2} \tag{4.37}$$

Equation 4.37 (where $a_0$ is the lattice parameter, $d$ is the d-spacing for the reflecting plane of atoms and $h$, $k$, and $l$ are the indices of the plane) was used along with the values of $d$ calculated by an X-ray diffraction analysis program ($\lambda=2d\sin\theta_b$) to calculate the lattice parameters for each peak. Errors in measurements are minimised at $2\theta_b = 180°$ (due to the sine function) [Cullity (1978)], so by plotting calculated lattice parameters as a function of $\theta_b$, and extrapolating to $\theta_b = 90°$, an accurate estimate of the lattice parameters may be obtained.

Fig. 4.6 shows this plot for the ferrite lattice parameter using the Nelson-Riley (N-R) function for extrapolation [Nelson and Riley, 1945]:

$$\frac{\cos^2\theta_b}{\sin\theta_b} + \frac{\cos^2\theta_b}{\theta_b} \tag{4.38}$$

This function was chosen for its good accuracy at high angles. The ferrite lattice parameter was extrapolated to N-R = 0 (equivalent of $\theta_b$ =90°) and found to be 2.8655 ± 0.0005 Å. This value was used in the dilatation analysis program (section 4.3.4) as the room temperature ferrite lattice parameter $a_{0\alpha}$.

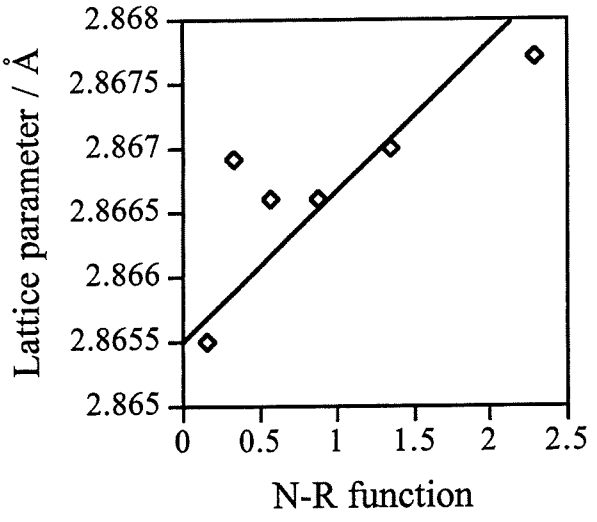


Fig. 4.6: Lattice parameter measurements versus N-R function of $\theta_b$.

The same procedure could not be used for the retained austenite because only two diffraction peaks were available, so the value corresponding to the higher $\theta_b$ was used. This value was $a_\gamma$ =3.592 Å for the carbon enriched austenite, which is related to the un-enriched value ($a_{0\gamma}$) by:

$$a_\gamma = a_{0\gamma} + C_c\left(\bar{x} - x_\gamma\right) \qquad (4.39)$$

with $C_c$ being the expansion caused by a unit concentration of carbon, and $\bar{x}$ and $x_\gamma$ being the carbon content of the alloy and of the enriched austenite respectively. As $x_\gamma$ was unknown, the value of $a_{0\gamma}$ was taken as that which gave the measured $a_\gamma$ when analysing measurements made during the isothermal hold at 330 °C. This gave the value $a_{0\gamma}$ = 3.56525 ± 0.0005 Å.

### 4.3.3 Austenite grain size

The austenite grain size of Fe-0.38C-1.73Mn-1.29Si wt.% steel, after austenitisation at 1000 °C for 3 minutes, was measured using thermal etching (section 3.3) to reveal the grain boundaries. The boundaries were then traced from optical micrographs (fig. 4.7) for image processing, from which a mean feret diameter of 16 ± 11 μm was measured, the large deviation being due to a bimodal distribution of sizes.

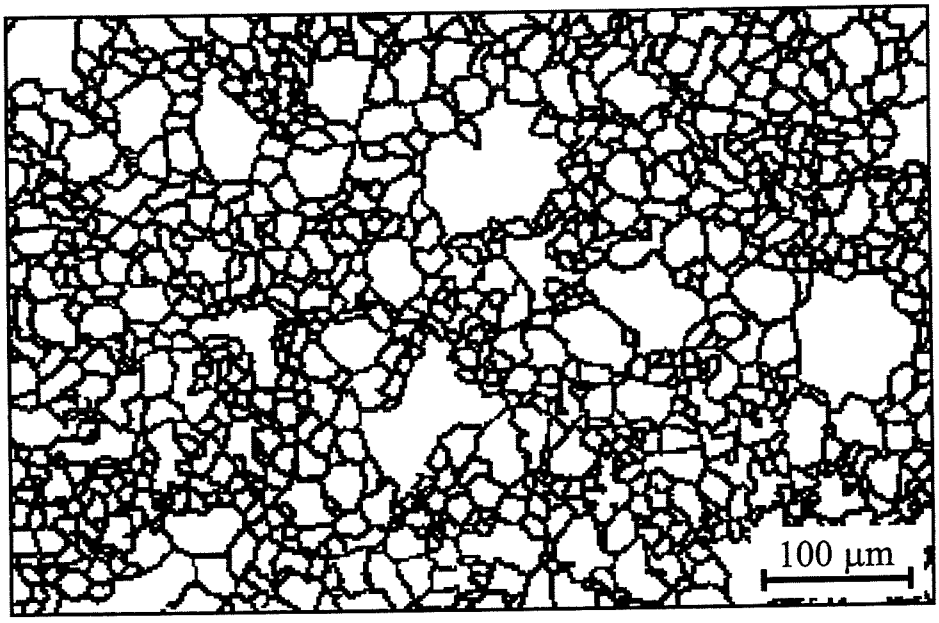


Fig. 4.7: Austenite grain boundary traces from optical micrograph.

This measured feret diameter compares well with the mean linear intercept, which, measured from fig. 4.7, is 17.5 ± 1.6 μm. This error was used in the calculations as it is a better indication of the measurement accuracy and less dependent on the bimodal size distribution.

### 4.3.4 Dilatation analysis

As austenite and bainite are the only phases present during isothermal transformation it is possible to convert dilatation measurements into volume fraction transformed [Bhadeshia *et al.*, 1991].

Firstly the dilatometry readings are converted from length change into volume change by assuming isotropic strain:

$$\frac{\Delta V}{V_{final}} \approx 3\frac{\Delta L}{L_{final}} \tag{4.40}$$

where the change in the dimension measured $\Delta L = L_{final} - L_{initial}$, and similarly for the volume $V$.

This relative volume change can be calculated by:

$$\frac{\Delta V}{V_{final}} = 1 - \frac{a_\gamma^3}{\beta_v + a_{e\gamma}^3} \quad \text{with} \quad \beta_v = \frac{2a_\alpha^3 - a_{e\gamma}^3}{1 + \left[\left(2V_\gamma a_\alpha^3\right)/\left(V_\alpha a_{e\gamma}^3\right)\right]} \tag{4.41}$$

where $V_\gamma$ and $V_\alpha$ are the volume fractions of austenite and bainite respectively. The austenite lattice parameter after transformation, $a_{e\gamma}$, is a function of the volume fraction of bainite, due to the austenite carbon concentration increasing when the carbon is partitioned from the bainitic ferrite.

The measured thermal expansion coefficients ($e_\alpha$ and $e_\gamma$) are used to calculate the lattice parameters of the untransformed austenite, $a_\gamma$, and bainite, $a_\alpha$:

$$a_\gamma = a_{0\gamma}\left[1 + e_\gamma(T - 298)\right] \tag{4.42}$$

$$a_\alpha = a_{0\alpha}\left[1 + e_\alpha(T - 298)\right] \tag{4.43}$$

where $T$ is the absolute temperature, and $a_{0\gamma}$ and $a_{0\alpha}$ are the room temperature (20 °C) lattice parameters measured and calculated as shown in section 4.3.2.

The volume fraction of bainite formed is calculated by solving equation 4.41 iteratively because of the dependence of $V_\gamma$ and $a_{e\gamma}$ on each other.

## 4.4 Isothermal Transformations

This section contains a comparison between the experimental data and calculations using equation 4.35 for steel of composition Fe-0.38C-1.73Mn-1.29Si (wt.%) (fig. 4.8).

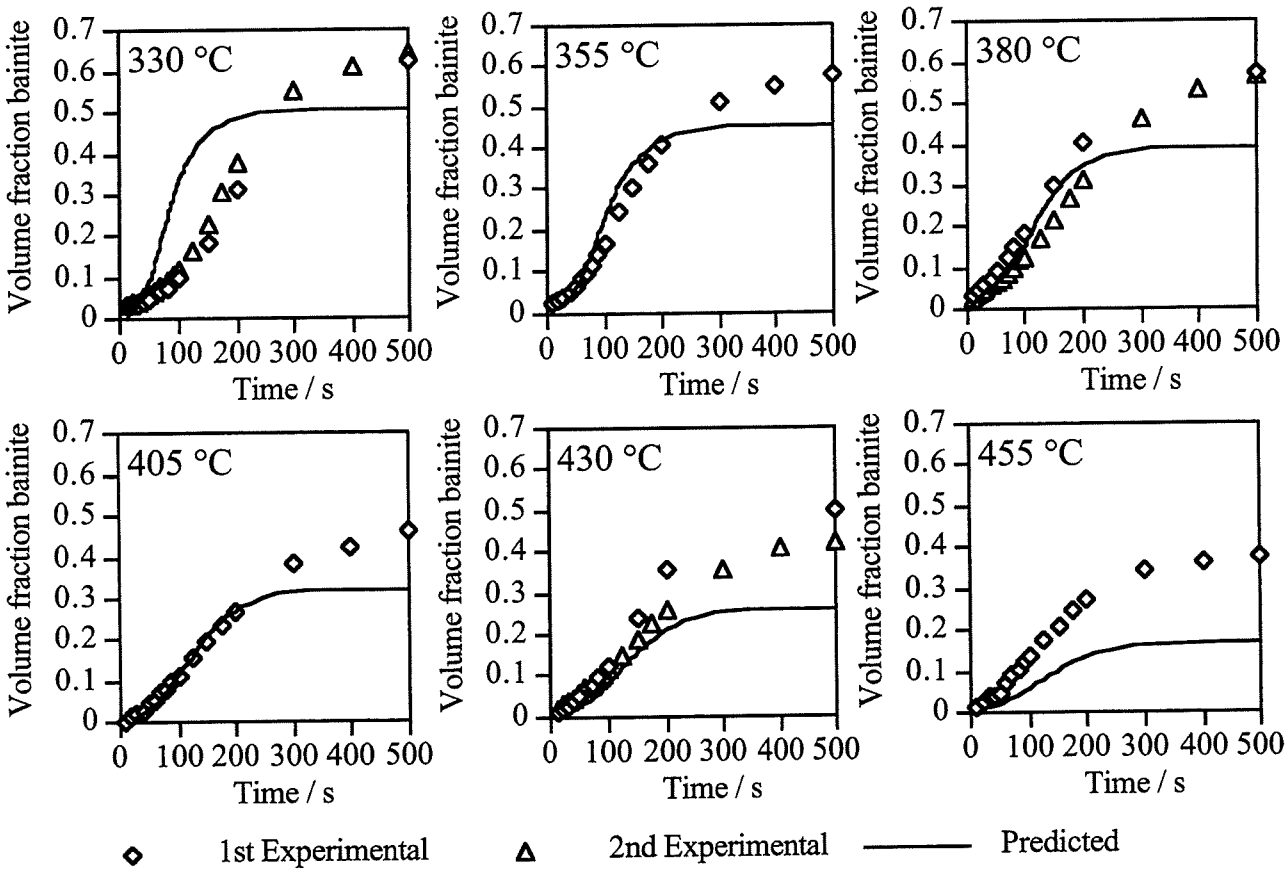


Fig. 4.8: Experimental and predicted isothermal transformation kinetics of bainite in Fe-0.38C-1.29Si-1.73Mn (wt.%) steel.

Errors in these predictions due to thermal expansivity were found to be ± 5 %, which is too small to be displayed on these plots. The errors in measured grain size and the lattice parameters were also insignificant in these plots.

The rate of reaction is predicted correctly for 405 °C, but is underestimated for higher temperatures and overestimated for lower temperatures. The sub-unit volume $u$ has been assumed to be constant in the calculations. However, it is known that the plate volume actually decreases with transformation temperature.

Recent work by Papadimitriou and Fourlaris [1997] emphasises the well known [Bhadeshia, 1992] change in sub-unit size with temperature (fig. 4.9). The microstructure shows bainite with two different platelet thicknesses. This was obtained by partially transforming the sample at 420 °C and then reducing the temperature to 290 °C for further bainite transformation.


Fig. 4.9: TEM micrograph of bainite sub-units of two different widths corresponding to transformation ($\alpha_1$) at 420°C for 30 minutes and then ($\alpha_2$) at 290 °C for 21 days for steel Fe-0.9C-3.9Si wt.% [Papadimitriou and Fourlaris, 1997].

Consistent with Chang [1995], a linear relation between the volume and temperature was chosen (fig. 4.10), with the sub-unit width ($u_w$) given by:

$$u_w = 0.001077T - 0.2681 \qquad (4.44)$$

where $T$ is temperature in °C (range 250 - 500 °C) and $u_w$ is in μm. This gives widths of between 184 and 44 nm for the heat treatments in fig. 4.9 at 420 and 290 °C respectively. These are reasonable values, but smaller than measured from the figure (490 - 730 nm at 420 °C and 50 - 170 nm at 290 °C) which may be partly because the section examined may not be normal to the habit planes.

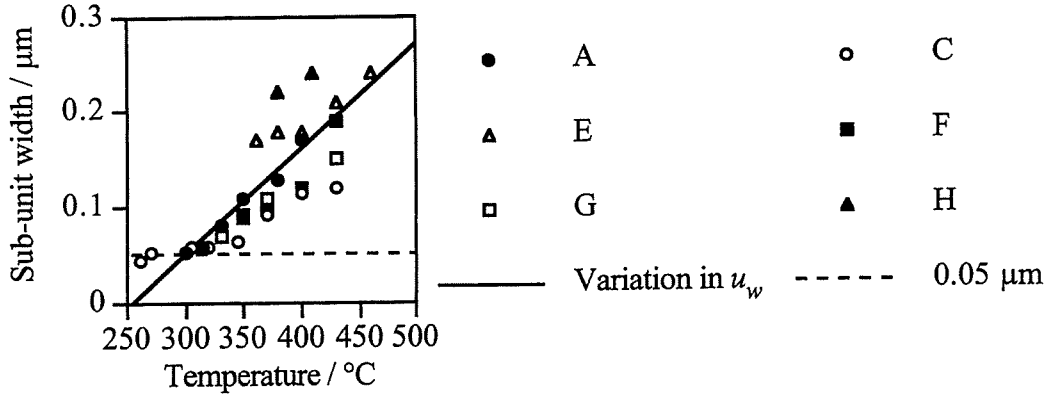


Fig. 4.10: Variation of measured bainite sub-unit width with isothermal transformation temperature. Data from Chang [1995] for 6 steels with compositions as shown in table 4.2. Solid line is best fit chosen for calculation of variation of $u$ for use in model.

| Alloy | C | Si | Mn | Ni | Cr | P | S | N |
|---|---|---|---|---|---|---|---|---|
| A | 0.27 | 1.98 | 2.18 | 0.02 | 1.9 | 0.015 | 0.012 | 0.0054 |
| C | 0.46 | 2.10 | 2.15 | 0.02 | - | 0.014 | 0.013 | 0.0062 |
| E | 0.10 | 1.77 | 2.12 | 2.0 | 0.02 | 0.013 | 0.012 | 0.0053 |
| F | 0.26 | 1.85 | 2.10 | 0.02 | - | 0.015 | 0.013 | 0.0086 |
| G | 0.26 | 1.93 | 2.04 | 0.02 | 1.02 | 0.015 | 0.010 | 0.0069 |
| H | 0.01 | 1.63 | 1.99 | 0.03 | 1.97 | 0.013 | 0.011 | 0.0080 |

Table 4.2: Chemical compositions (wt.%) of the steels studied by Chang in fig. 4.10.

A minimum of 0.05 μm was set for $u_w$ to avoid negative values. The sub-unit length $u_l$ was assumed to be 10 μm and the overall sub-unit volume given by:

$$u = (u_l)^2 \times u_w \tag{4.45}$$

and converted into $mm^3$. This calculation was incorporated into the "constant" $K'_I/u$, the initial value of which was adjusted to be unchanged at $T$=405 °C.

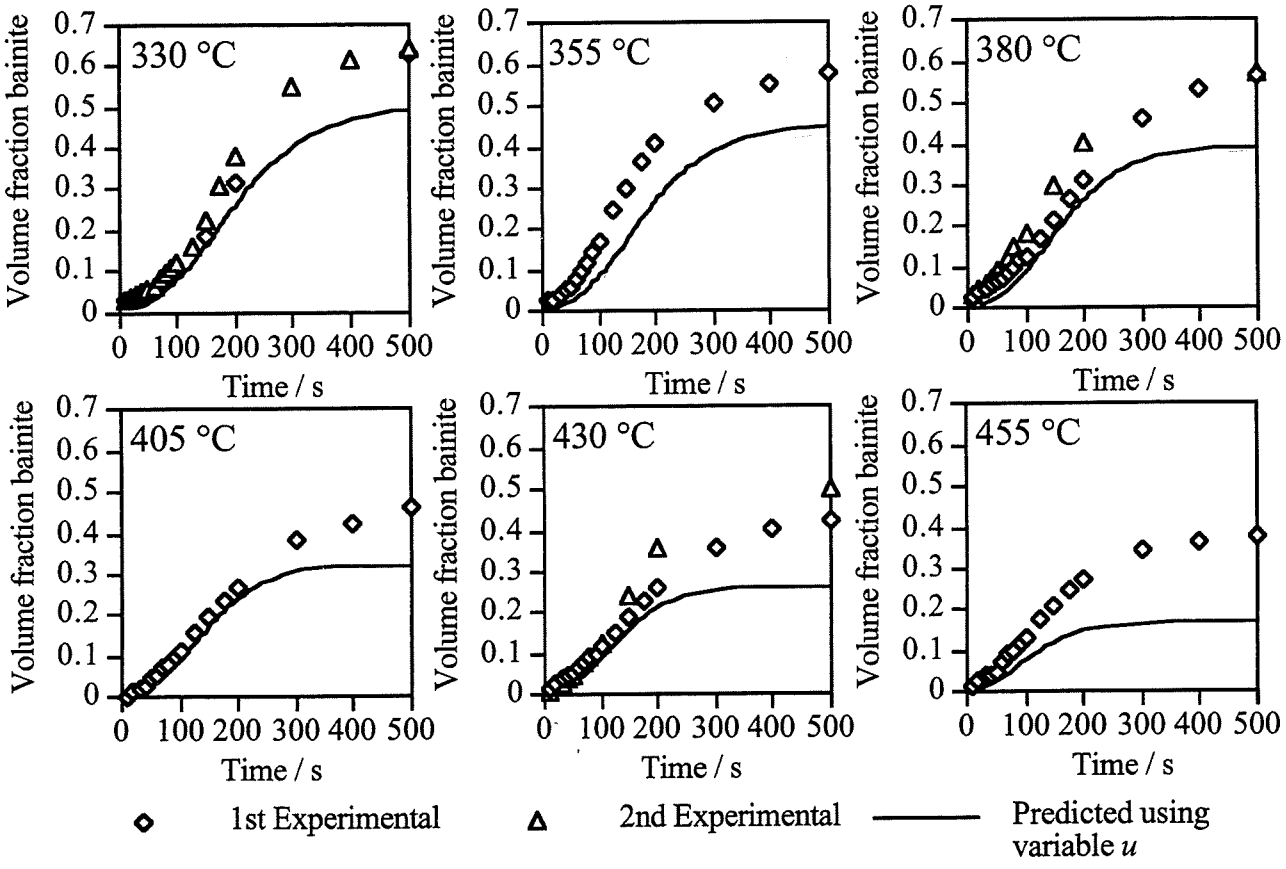


Fig. 4.11: Experimental and predicted isothermal transformation kinetics of bainite for Fe-0.38C-1.29Si-1.73Mn (wt.%) steel. Prediction including a linear variation in the bainite sub-unit size ($u$) with temperature.

Fig. 4.11 shows the model predictions where the dependence of $u$ on temperature is allowed for. The agreement is good but there is a consistent under-estimation of the limiting volume fraction. To investigate this the carbon concentration of austenite at the final measured volume fraction for each temperature was calculated from the experimental data. This was done by assuming that there was only austenite and bainitic ferrite present and that the ferrite had a carbon concentration of about 0.03 wt.%. The results are shown in fig. 4.12 along with calculated $T_0$ and $T_0'$ lines (see section 4.2.7). The reaction seems to stop somewhere between the $T_0$ and $T_0'$ lines, so it is not surprising that the limiting fraction is underestimated since the calculations rely on the $T_0'$ curve.

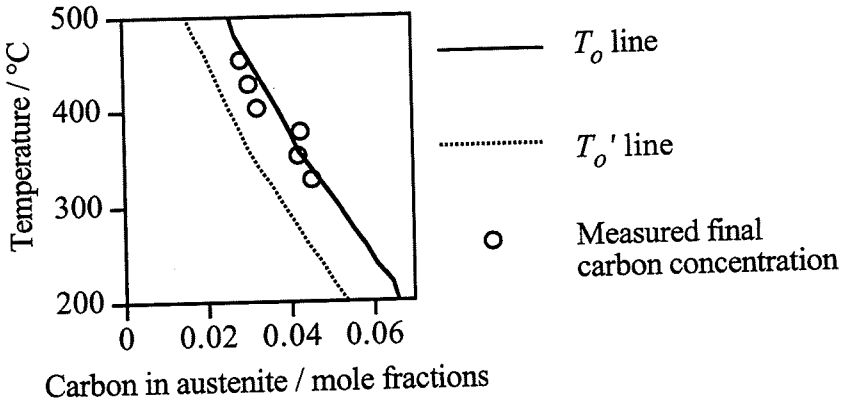


Fig. 4.12: Comparison of the carbon concentrations of austenite at the point where the bainite transformation stops (Fe-0.38C-1.29Si-1.73Mn wt.%) with calculated $T_0$ and $T_0'$ lines.

The agreement improves if the calculations allow the maximum carbon concentration in austenite to be given by the $T_0$ curve (fig. 4.13); the reason for this will be discussed in Chapter 5.

The exception for this over-prediction is for $T_H = 330$ °C where a slight under-prediction is still maintained. This may be explained by the presence of lower bainite, the carbides within which reduce the austenite carbon content, thus allowing larger volume fractions of bainite to form than predicted.

Isothermal transformation at $T_H = 480$ °C, which is close to the $B_s$ temperature, has been shown to produce pearlite in this steel (fig 4.14). This indicates that predictions close to the $B_s$ temperature cannot be tested using dilatometry due to the interference from the transformation of other phases.

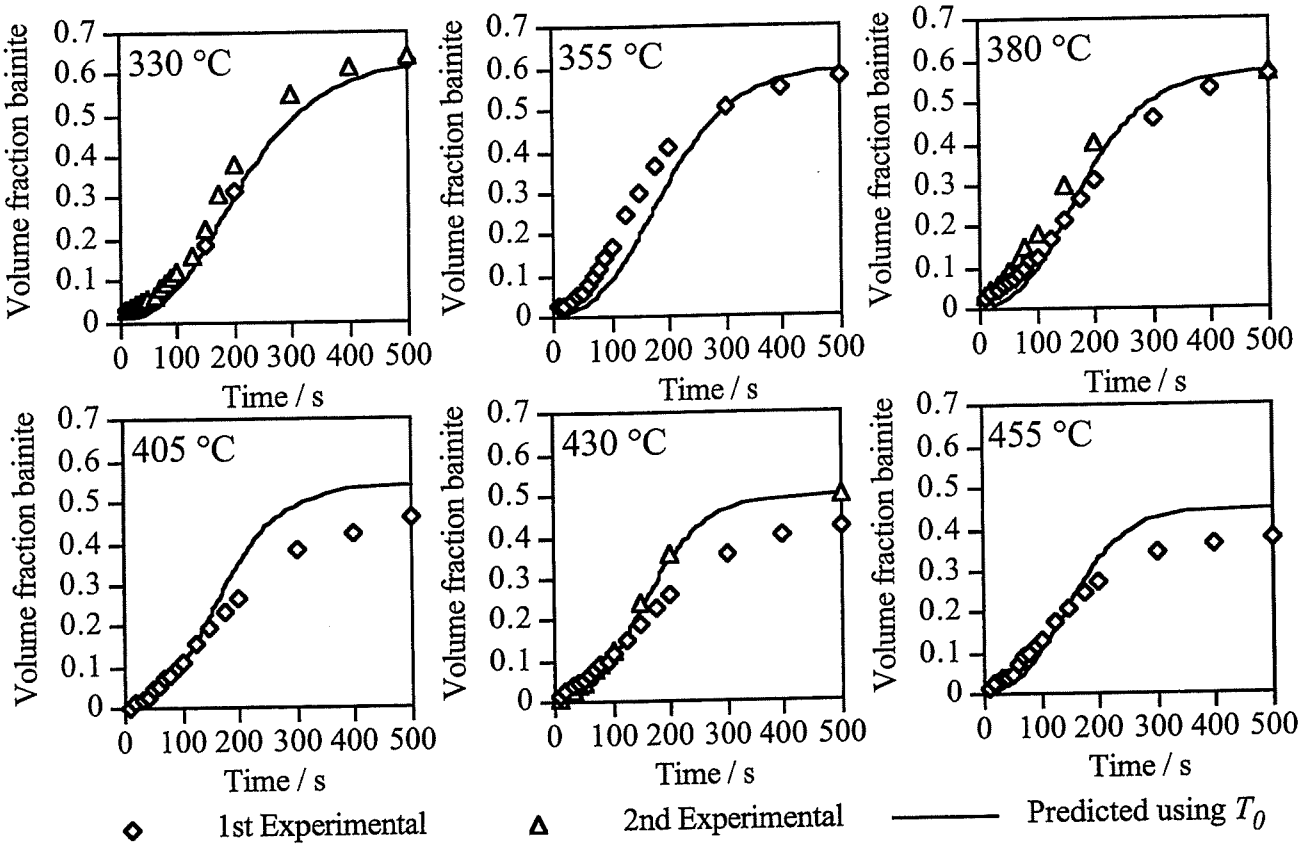


Fig. 4.13: Experimental and predicted isothermal transformation kinetics of bainite for Fe-0.38C-1.29Si-1.73Mn (wt.%) steel. Prediction including variation of bainite sub-unit size with temperature and $T_0$ line for maximum volume fraction.

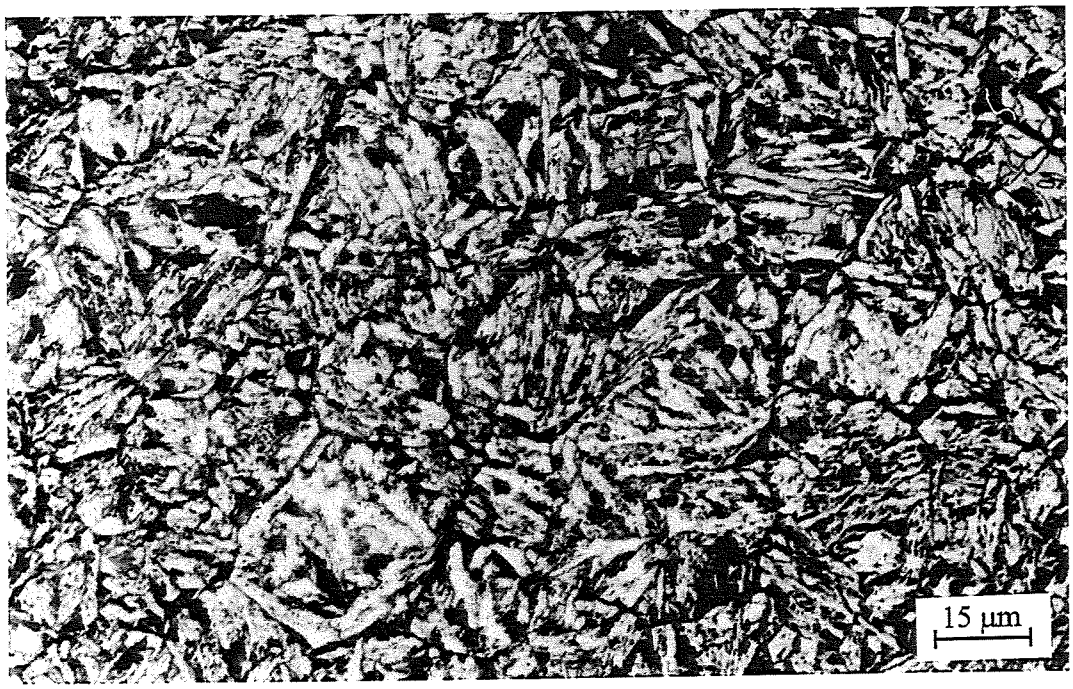


Fig. 4.14: Optical micrograph of Fe-0.38C-1.29Si-1.73Mn wt.% steel held at $T_H$ = 480 °C. Etched with 2% Nital to show dark areas of pearlite.

### 4.4.1 Testing the model with another steel

A steel of composition Fe-0.26C-1.47Si-1.50Mn wt.% was used to further validate the model. $T_H$ values of 390, 490, 450, and 480 °C were chosen between $B_S$ (530 °C) and $M_S$ (392 °C). The grain size was found, by mean linear intercept method, to be 6.6 ± 0.7 μm and the thermal expansivities were 2.65 x $10^{-5}$ and 1.69 x $10^{-5}$ °$C^{-1}$ (± 0.75 x $10^{-5}$ °$C^{-1}$) for austenite and ferrite respectively.

The results are displayed in fig. 4.15 and show good agreement between experiment and prediction.

The error bars on the experimental results are due to uncertainties in the measurement of the thermal expansivity of austenite for this steel. These errors were estimated to be ±15 % of the measured value. Prediction errors for this 0.26 wt.% carbon steel, due to the variation in grain size, were found to be insignificant.

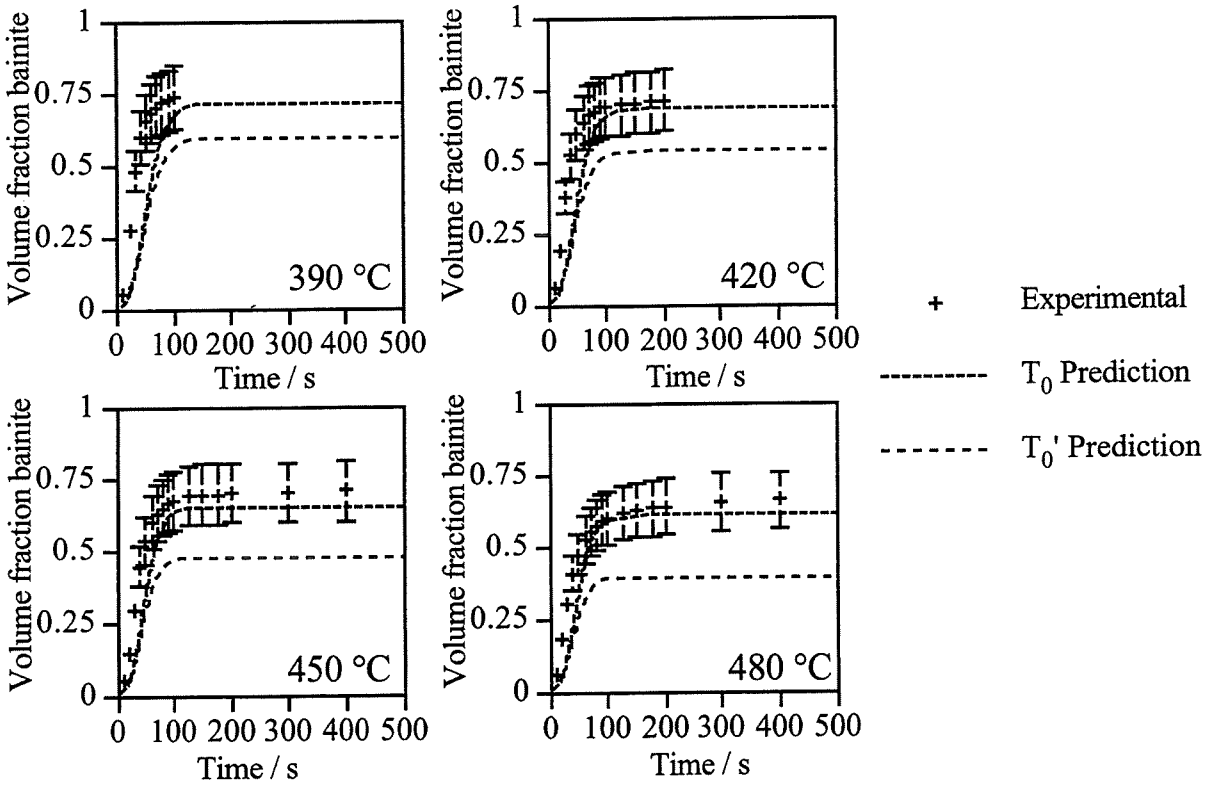


Fig. 4.15: Isothermal predictions of bainite transformation kinetics compared to experimental results for Fe-0.26C-1.47Si-1.50Mn wt.% steel.

## 4.5 Continuous Cooling Transformation

### 4.5.1 Continuous cooling and the Scheil rule

Scheil's additive reaction rule was used to calculate the kinetics of the bainite transformation during continuous cooling heat treatment [Scheil, 1935; Christian, 1975]. The Scheil rule is strictly applicable in (isokinetic) circumstances where there is only one temperature dependent function. This applies in the present case since the theory is based on nucleation. Growth rates are not included in the analysis since each nucleus is assumed to lead to a certain volume of transformation, consistent with the mechanism of transformation.

An additive reaction implies that the total time to reach a specified stage of transformation can be obtained by adding the fractions of the time to reach this stage isothermally until the sum reaches unity [Christian, 1975]. This can be generally described by:

$$\int_0^t \frac{dt}{\tau_f\{T\}} = 1 \qquad (4.46)$$

where $\tau_f\{T\}$ is the isothermal time to a certain volume transformed and $t$ is the time to the same volume for the non isothermal reaction.

This was used in this work by cutting the cooling curve into small isothermal steps (fig. 4.16) and calculating the volume fraction formed in the first isothermal step, $V_1$. The temperature was then reduced to the next step and the time, $t_1$, required to form volume fraction $V_1$ of bainite was calculated for the new temperature. The time at the temperature step, $\Delta t$, was then added to $t_1$ and the fraction of transformation, $V_2$, for this total time was then calculated and assumed to be the net transformation. This was repeated for the whole of the cooling curve.

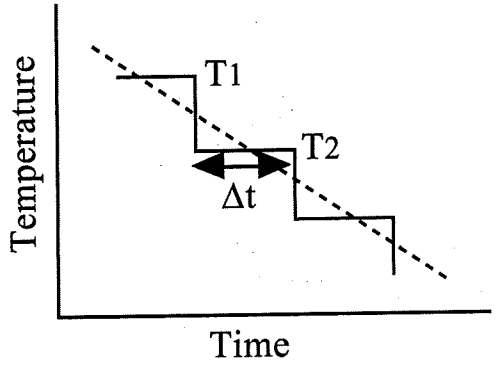


Fig. 4.16: Continuous cooling curve cut into isothermal steps for Scheil's additive reaction rule.

The computer model has been designed to deal with constant or variable cooling rates, down to a temperature of 20 °C or $M_s$, whichever is reached first.

### 4.5.2 Experimental

Samples of Fe-0.38C-1.29Si-1.73Mn wt.% steel were austenitised at 1000 °C for 300 s and then He gas quenched to a cooling start temperature, $T_S$, of 450 °C. They were then cooled at a variety of rates (0.05 - 5.0 °C $s^{-1}$) to the cooling finish temperature, $T_F$, of 200 °C and He gas quenched to room temperature (fig. 4.17).

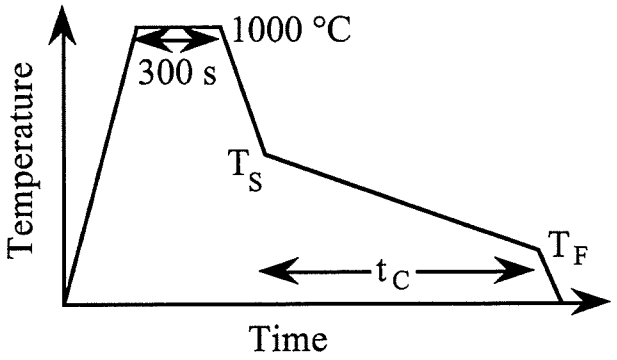


Fig. 4.17: Heat treatment used to study the kinetics of the bainite transformation during continuous cooling.

Dilatation measurements taken during these heat treatments were converted into volume fractions of bainite formed and compared against theory. This was done by first allowing for the dilatation due to the thermal expansivity of the steel (dotted line in fig. 4.18 parallel to the dilatation before transformation).

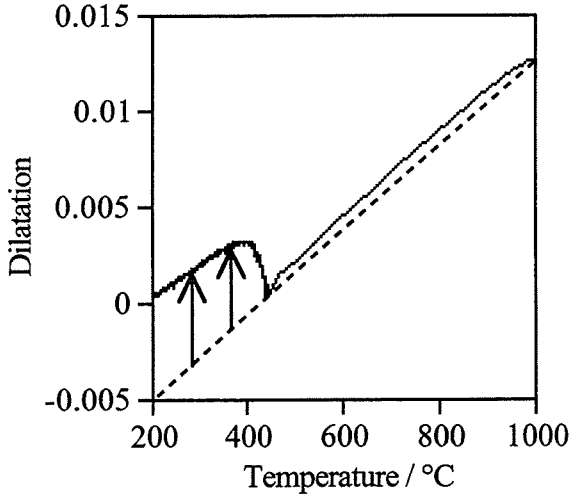


Fig. 4.18: Converting continuous cooling dilatation to allow for thermal expansivity before calculation of bainite formation. Dotted line to allow for thermal expansivity and arrowed lines indicate dilatations to be converted into bainite volume fractions.

The starting temperature of 450 °C was chosen because it is below the $B_s$ temperature. Experimental data obtained when cooling from above $B_s$ were difficult to interpret due to the formation of pearlite (figs. 4.19 and 4.20).

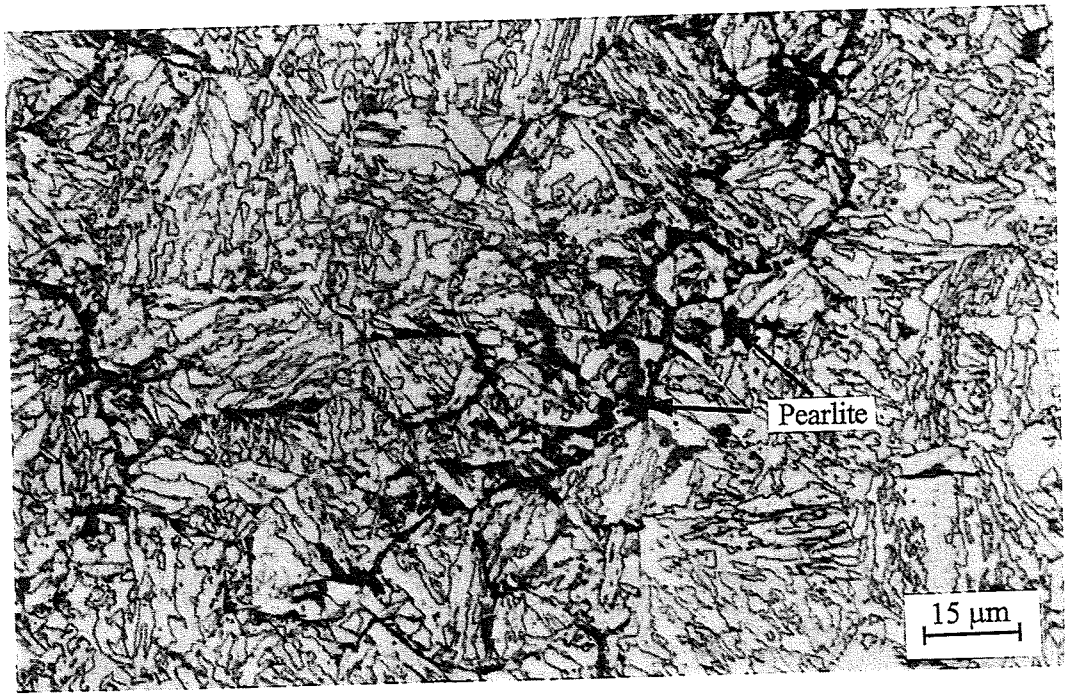


Fig. 4.19: Optical micrograph of continuous cooling sample of Fe-0.38C-1.29Si-1.73Mn wt.% steel with cooling rate 0.1 °C $s^{-1}$ from 525 °C to 300 °C. Etched with 2% Nital to show the presence of pearlite.

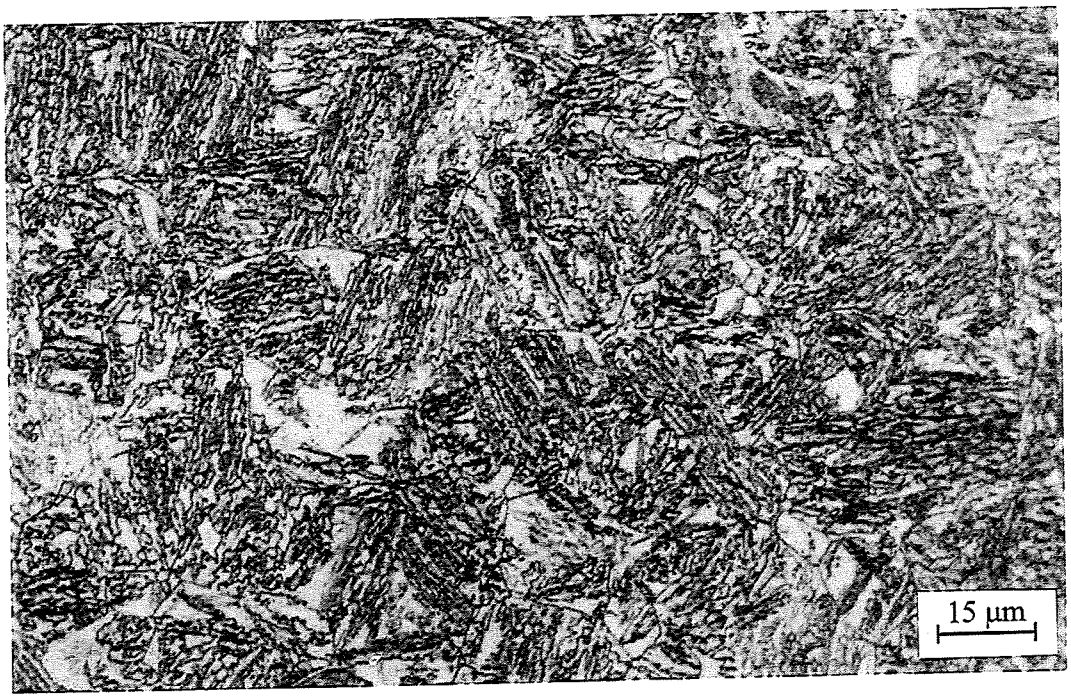


Fig. 4.20: Optical micrograph of continuous cooling sample of Fe-0.38C-1.29Si-1.73Mn wt.% steel with cooling rate 0.1 °C $s^{-1}$ from 450 °C to 250 °C. Etched with 2% Nital to show the bainitic microstructure.

### 4.5.3 Continuous cooling results

The dilatation measurements are shown in fig 4.21 and the corresponding comparisons with predictions in fig. 4.22.

At slow cooling rates (0.05 and 0.1 °C $s^{-1}$) the predicted volume fraction is limited by the maximum allowed at a given temperature by the incomplete reaction phenomenon. On the other hand, at faster cooling rates the volume fraction is limited by the kinetics of bainite formation. This explains the predicted shapes of the graphs.

The errors in experimental results, due to the inaccuracy of thermal expansivity (found to be the largest contributor to the errors), were calculated to be approximately ±5% of the values and thus too small to appear on the graphs.

For the bainite transformations (0.05, 0.1 and 0.5 °C $s^{-1}$) the initial rates were predicted well, especially using $T_0'$ as the limiting volume fraction, but the total extent of transformation was overestimated.

Only when cooling at 5.0 °C $s^{-1}$ has the model predicted the formation of martensite (thus stopping the bainite transformation at $M_s$ (315 °C) with only 0.01 volume fraction of bainite having formed). However, in the experimental results martensite alone formed for cooling rates of 1.0 and 5.0 °C $s^{-1}$. (The dilatation converted into bainite volume fraction for 1.0 and 5.0 °C $s^{-1}$ cooling rates is actually due to the formation of martensite as can be seen by the reduced starting temperature).

Fig. 4.23 shows the predicted variation in the martensite-start temperature $M_s$ of the residual austenite on cooling at various rates (using Khan and Bhadeshia's [1990a] model, Chapter 7). For cooling at 5.0 °C $s^{-1}$ the predicted $M_s$ temperature is the same as the transformation temperature at 315 °C and thus the bainite reaction ceases. Martensite was also formed during cooling experiments at 1.0 °C $s^{-1}$. Predictions for this rate in fig. 4.23 show the transformation temperature and the predicted $M_s$ temperature to be very close.

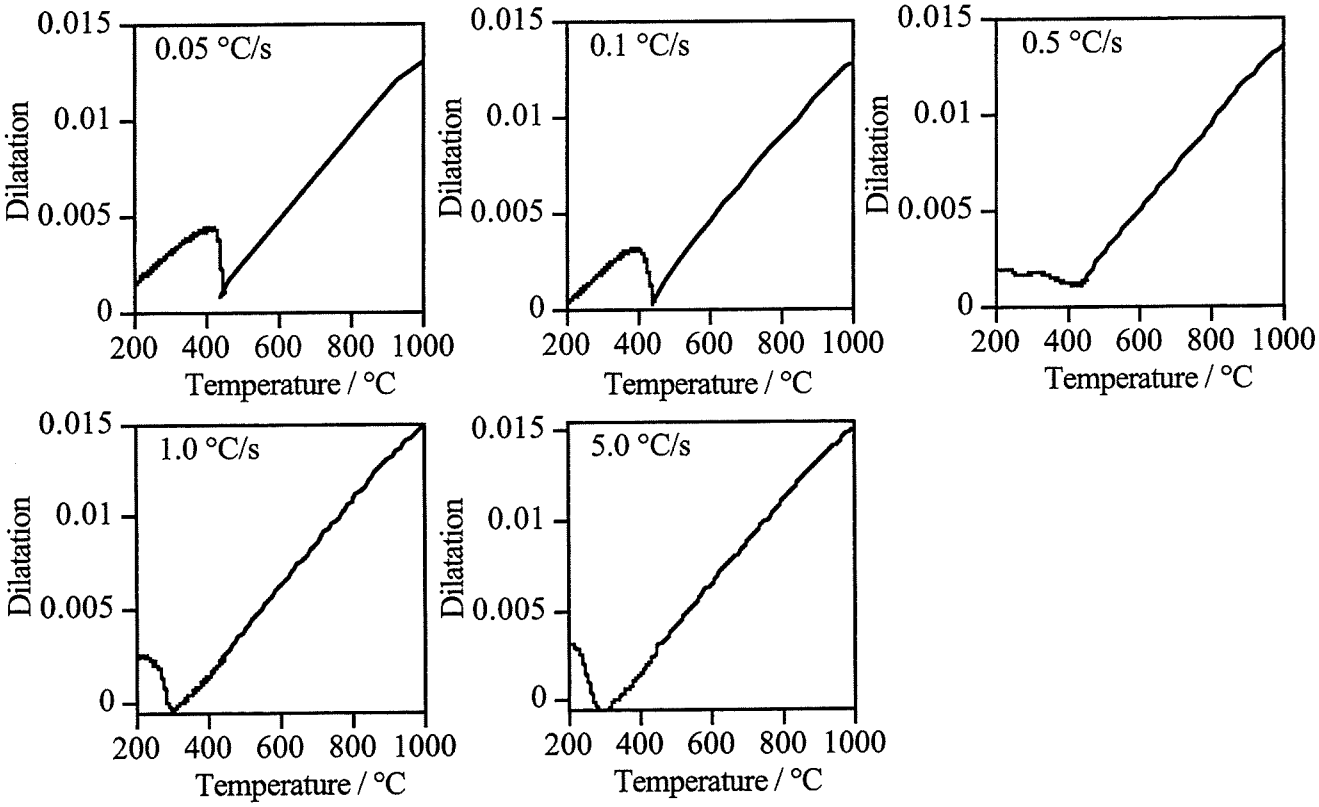


Fig. 4.21: Dilatation curves for continuous cooling 450 - 200 °C at different rates for steel Fe-0.38C-1.29Si-1.73Mn wt.% (corresponding to 2nd measured in fig. 4.22).

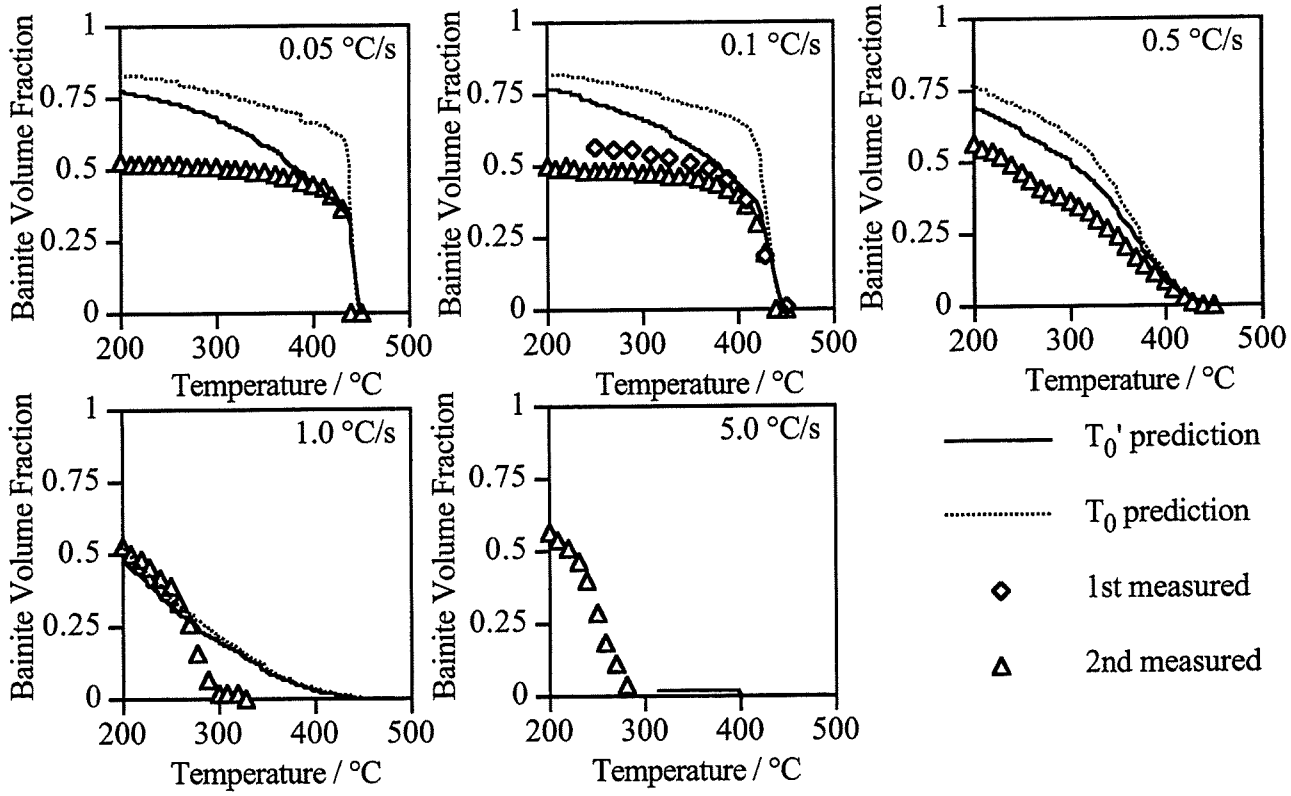


Fig. 4.22: Continuous cooling predictions and experimental results for cooling rates between 0.05 and 5.0 °C/s for Fe-0.38C-1.29Si-1.73Mn wt.% steel.

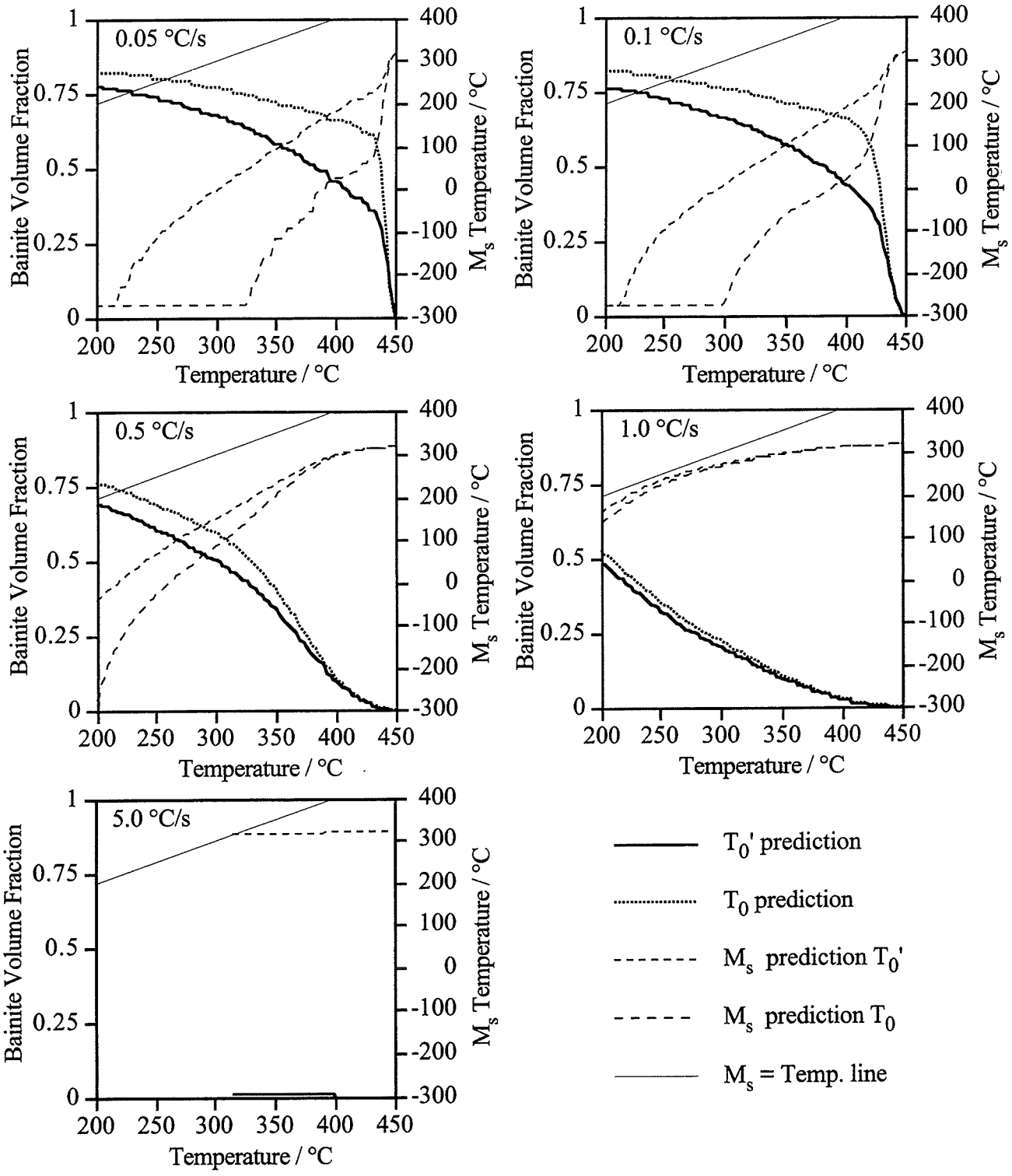


Fig. 4.23: Predicted bainite transformation curves (using $T_0$ and $T_0'$ lines) and corresponding $M_s$ temperatures of the remaining austenite for continuous cooling of Fe-0.38C-1.29Si-1.73Mn wt.% steel. $M_s$ = Temp. line indicates if the transformation temperature has reached $M_s$ and thus if martensite forms.

The experimental results are also shown in fig. 4.24 on a *CCT* (continuous cooling transformation) diagram calculated using the computer model. There is no 0% transformation

line as cooling was started below $B_s$. Fig. 4.25 is a predicted *CCT* diagram for cooling from the $Ae_3$ temperature for the same steel.

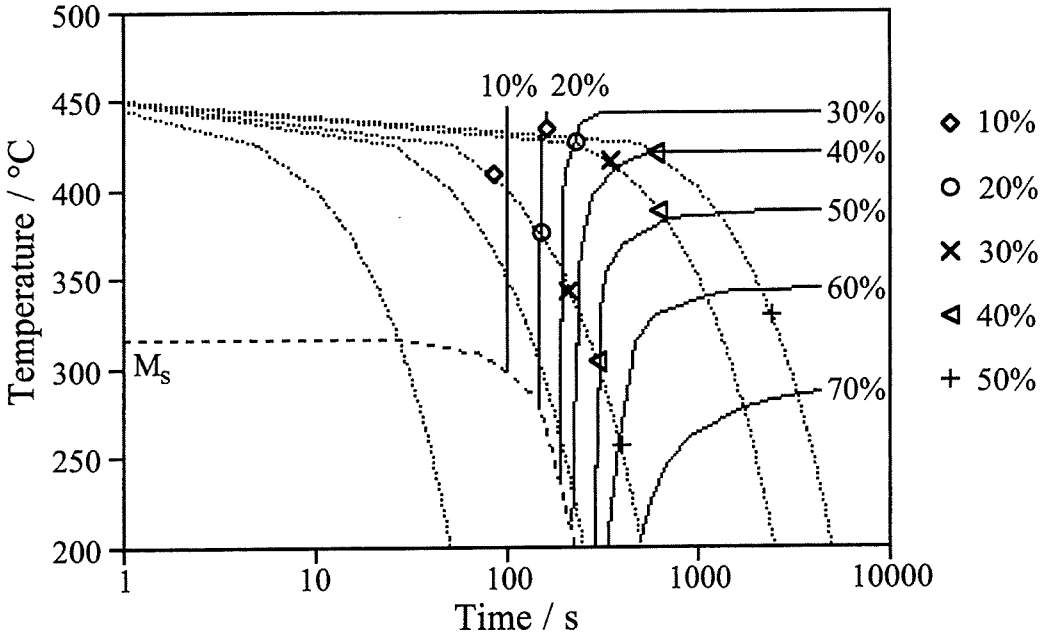


Fig. 4.24: Calculated *CCT* diagram with experimental data points for Fe-0.38C-1.29Si-1.73Mn wt.% steel. Dotted lines are cooling curves at rates of: 5, 1, 0.5, 0.1 and 0.05 °C $s^{-1}$.

These results confirm that the estimates are reasonable although there is an over-prediction of the final volume fractions.

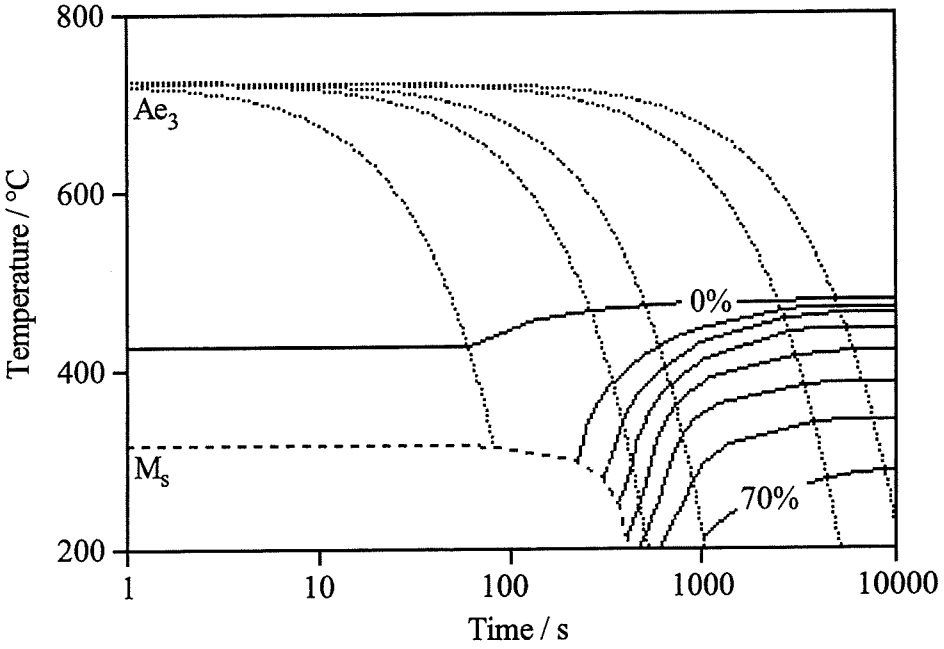


Fig 4.25: Complete calculated *CCT* diagram cooling from $Ae_3$ temperature for Fe-0.38C-1.29Si-1.73Mn wt.% steel. Dotted lines are cooling curves at rates of: 5, 1, 0.5, 0.1 and 0.05 °C $s^{-1}$.

The 0% line on fig. 4.25 does not join the $M_s$ line as expected. This is due to 0.01 volume fraction of bainite being predicted by 427 °C irrespective of cooling rate (see prediction for 5.0 °C $s^{-1}$ in fig 4.23). The maximum predicted is 0.02 volume fraction of bainite when it should be zero. This amount is undetectable experimentally and well within experimental errors.

## 4.6 Allotriomorphic Ferrite

Due to intercritical annealing and transformation on subsequent cooling, allotriomorphic ferrite is often present prior to the formation of bainite. To allow for this the ferrite is assumed to have the following effect on the bainite transformation:

1) There is an increase in the carbon concentration of the austenite from which the bainite transforms.
2) There is a reduction in the volume of austenite from which the bainite can form.

Both of these effects can easily be accounted for as follows.

The carbon content of ferrite is very small and is given approximately by [Bhadeshia, 1982b]:

$$x_\alpha = 0.001528 - 0.008816T_c + 0.0245T_c^2 - 0.04217T_c^3 + 0.006966T_c^4 \qquad (4.47)$$

where $x_\alpha$ is the mole fractions of carbon in ferrite and $T_c = \frac{T-273}{900}$ where $T$ is the absolute temperature at which the ferrite forms, in the range $T$ = 950 - 1200 K. Note that a polynomial equation like this is necessary to capture the retrograde shape of the ferrite solubility curve.

This is converted into wt.%:

$$c_\alpha = \left(\frac{1201.15}{55.84}\right) x_\alpha \qquad (4.48)$$

This equation is strictly only valid for Fe-C alloys, but is a good approximation for low-alloy steels in general. The enriched carbon content of the austenite in wt.% is then:

$$c_\gamma = \frac{\left(\bar{x} - c_\alpha V_\alpha\right)}{V_\gamma} \qquad (4.49)$$

where $\bar{x}$ is the mean carbon content of the alloy, $V_\alpha$ is the volume fraction of "prior"

allotriomorphic ferrite and $V_\gamma$ is the volume fraction of austenite given by:

$$V_\gamma = 1 - V_\alpha \tag{4.50}$$

The bainite transformation is then calculated assuming there is 100% austenite at this enriched carbon concentration and the predicted bainite, austenite and martensite volume fractions are subsequently multiplied by $V_\gamma$.

The allotriomorphic ferrite volume fractions can either be measured or calculated using theory as in Chapter 6.

### 4.6.1 Prior allotriomorphic ferrite results

Attempts to check this theory with published experimental data have been hindered due to the lack of suitable data. Two sets of data [Bandoh *et al.*, 1988; Matsumura *et al.*, 1987a] were found with only the austenite grain size measurements missing.

The Bandoh *et al.* [1988] data were found to be unreproducible as predictions showed that with 0.57 volume fraction of prior ferrite in a 0.4 wt.% carbon steel the $B_s$ temperature should be 344 °C whereas the experimental results were from isothermal transformation at 400 °C.

For the Matsumura *et al.* [1987] data the predictions stopped at 0.25 volume fraction bainite due to the carbon content of the austenite reaching the $T_0$ line. However, the experimental results achieved up to 0.56 volume fraction.

It is speculated that this might be explained partly by the chemical inhomogenities in the experimental steels with bainite forming in manganese depleted regions.

#### *4.6.1.1 Data by Jacques et al.*

Work by Jacques *et al.* [1997] on Fe-0.11C-1.50Si-1.53Mn wt.% cold-rolled sheet steel is suitable for comparison with this model. The samples were intercritically annealed in a dilatometer and then helium quenched to isothermal transformation temperatures in the bainite transformation region. The volume fraction of austenite and its carbon content were measured using X-ray diffraction.

Fig. 4.26a shows the bainite kinetics results for samples intercritically annealed at 750 °C for 4 minutes followed by isothermal holds at 375, 416 and 450 °C. The prior allotriomorphic ferrite volume fraction was 0.63.

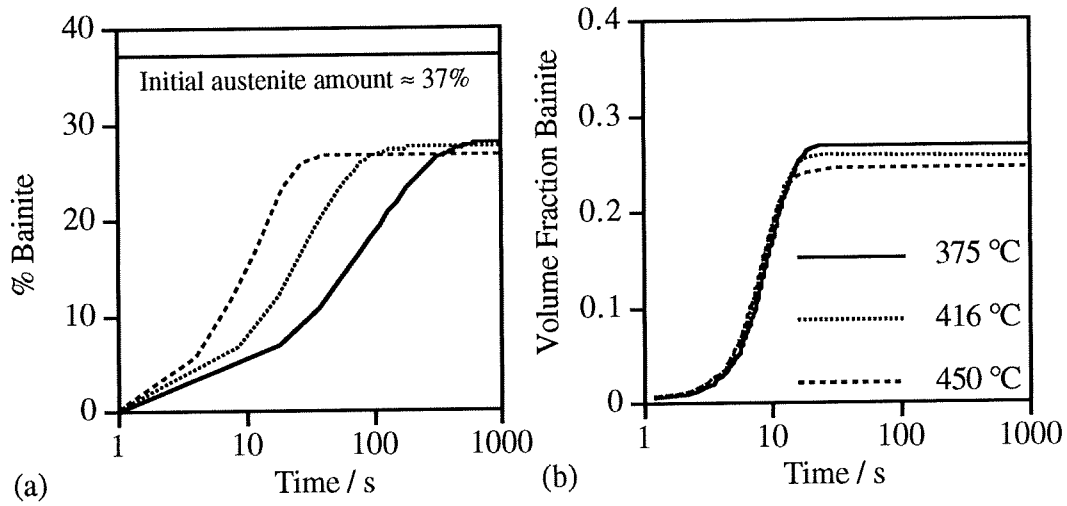


Fig. 4.26(a): Bainite transformation kinetics in the presence of 0.63 volume fraction of prior allotriomorphic ferrite for Fe-0.11C-1.50Si-1.53Mn wt.% steel [Jacques *et al.*, 1997] and (b) predictions for this data.

The calculations (fig. 4.26b) assumed an austenite grain size of 1μm based on the approximate size of the residual austenite images published by Jacques *et al.* [1997]. There is good agreement with respect to the final volume fractions using the $T_0$ line, but the calculated rates do not vary as much as those obtained experimentally.

It may be the case that the carbon is not distributed evenly within the austenite after the intercritical annealing. At higher temperatures the carbon can homogenise more readily but such considerations have not been allowed for in the model.

Another factor affecting the transformation rate will be the change in grain size of the retained austenite with the amount of allotriomorphic ferrite. This does not affect these results as the grain size used is that after intercritical annealing, but this factor must be taken into account for future comparisons.

Other work by Girault [1997] (using the same steel and methods as Jacques *et al.*, [1997]) revealed changes as a function of intercritical annealing time (fig. 4.27). The residual austenite volume fraction observed was almost constant and thus the effects cannot be attributed to transformation.

The main reason for this effect is the difference in austenite grain sizes. The austenite formed for shorter times is likely to have a finer grain size than the longer annealing times. This results in more grain boundary area from which the bainite can nucleate, increasing the growth rate.

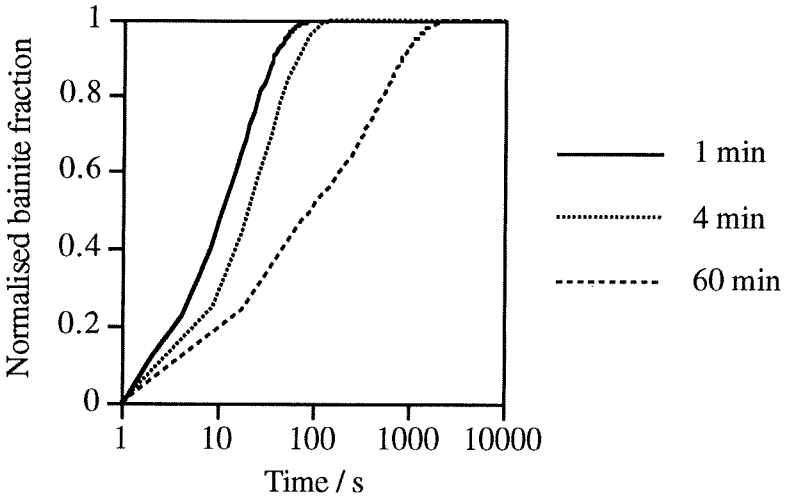


Fig 4.27: Bainite kinetics in Fe-0.11C-1.50Si-1.53Mn wt.% steel samples intercritically annealed at 760 °C for different times and then transformed at 415 °C [Girault, 1997].

This change may also be due to the partitioning of manganese into the austenite during long intercritical annealing times. This causes a build up of manganese at the austenite/ferrite grain boundary which stabilises the austenite and slows the nucleation of bainite.

This model has not taken into account the distribution of allotriomorphic ferrite formed during intercritical annealing. If a uniform layer forms on the austenite grain boundaries (fig. 4.28a) then the bainite nucleation is slowed by high carbon (and possibly manganese) concentrations at the ferrite/austenite grain boundary, thus possibly requiring nucleation on defects within the grain.

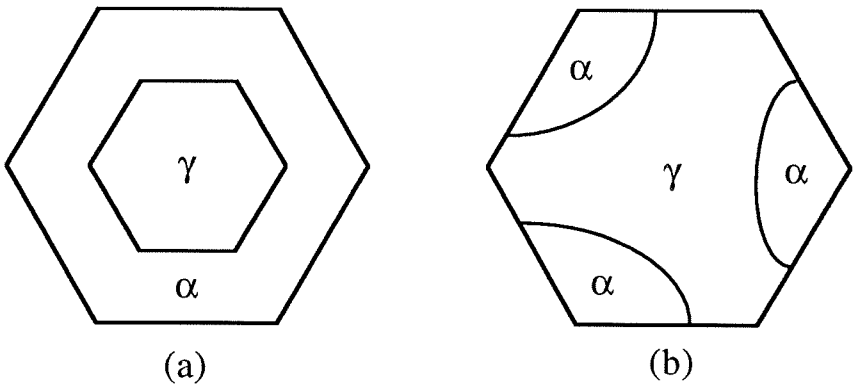


Fig. 4.28: Schematic diagrams of possible evolution of allotriomorphic ferrite within austenite grains.

If the ferrite forms as in fig. 4.28b then this effect is reduced as there is still austenite grain boundary from which bainite can form. Type (b) is the case observed by Jacques *et al.* and Girault in their work and thus this factor does not need to be taken into account here, but might be required in future work.

## 4.7 Conclusions

A model for the kinetics of the bainite transformation [Rees and Bhadeshia, 1992a] has been corrected and compared to experimental data for two steels. It is found that the inclusion of a variable bainite sub-unit width with transformation temperature improved the predicted transformation rate. The limiting bainite volume fractions have been shown to be between those predicted using the $T_0$ and $T_0'$ lines. This will be discussed further in Chapter 5.

Using Scheil's additive reaction rule this model has been adapted for continuous cooling reactions, giving reasonable rate predictions but with an underestimation of the final volume fractions for steel Fe-0.38C-1.29Si-1.73Mn wt.%.

Allowances for the presence of allotriomorphic ferrite have been incorporated into the model so that the austenite carbon content is increased and the overall volume fractions of the other phases are reduced. These predictions are in good agreement with data by Jacques *et al.* [1997] and Girault [1997] but require further work on grain size and grain boundary modification effects.

# 5 Atomic Force Microscopy and Stored Energy due to Bainite Transformation

It was emphasised in the previous chapter that the maximum volume fraction of bainitic ferrite at any temperature depends on the stored energy which has been estimated to be 400 J mol$^{-1}$ [Bhadeshia, 1981a]. A neglect of this stored energy leads to an over-estimation of the transformed fraction (fig. 5.1a). On the other hand, a stored energy of 400 J mol$^{-1}$ leads to an under prediction of the final volume fractions (fig. 5.1b).

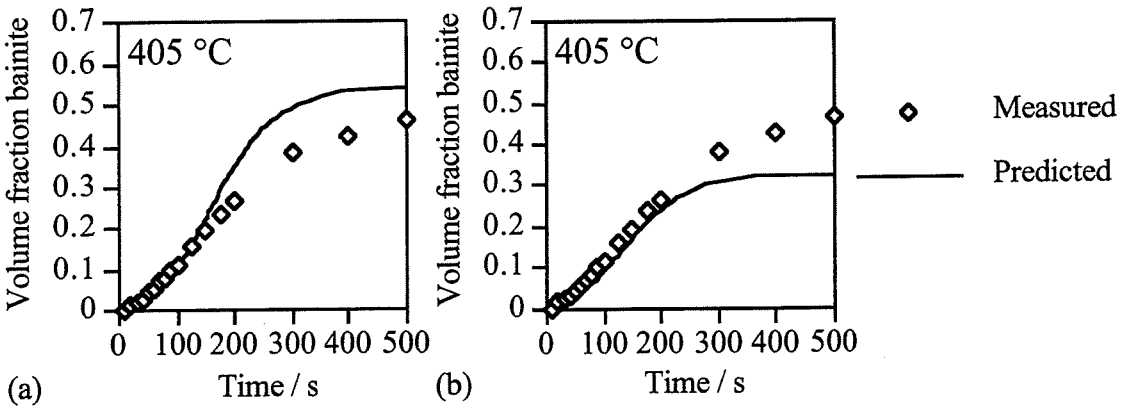


Fig. 5.1: Measured and predicted isothermal transformation kinetics of bainite for Fe-0.38C-1.29Si-1.73Mn wt.% steel (a) using $T_0$ line and (b) using the $T_0'$ line.

The value of 400 J mol$^{-1}$ of stored energy assumes that there is no plastic accommodation of the shape change within the bainitic ferrite or the surrounding austenite. The purpose of the work presented in this chapter is to investigate the surface relief due to bainite transformation to determine whether plastic deformation does occur in the steel investigated and thus whether the use of a smaller value for stored energy is physically justified.

## 5.1 Surface Relief

The Bain Strain is a homogeneous pure deformation which can change the f.c.c. crystal structure of austenite into the b.c.c. structure of ferrite (fig. 5.2). This deformation leads to a Bain orientation relationship of:

$$[001]_\gamma \parallel [001]_\alpha \text{ and } [100]_\gamma \parallel [110]_\alpha$$

which is not observed experimentally.

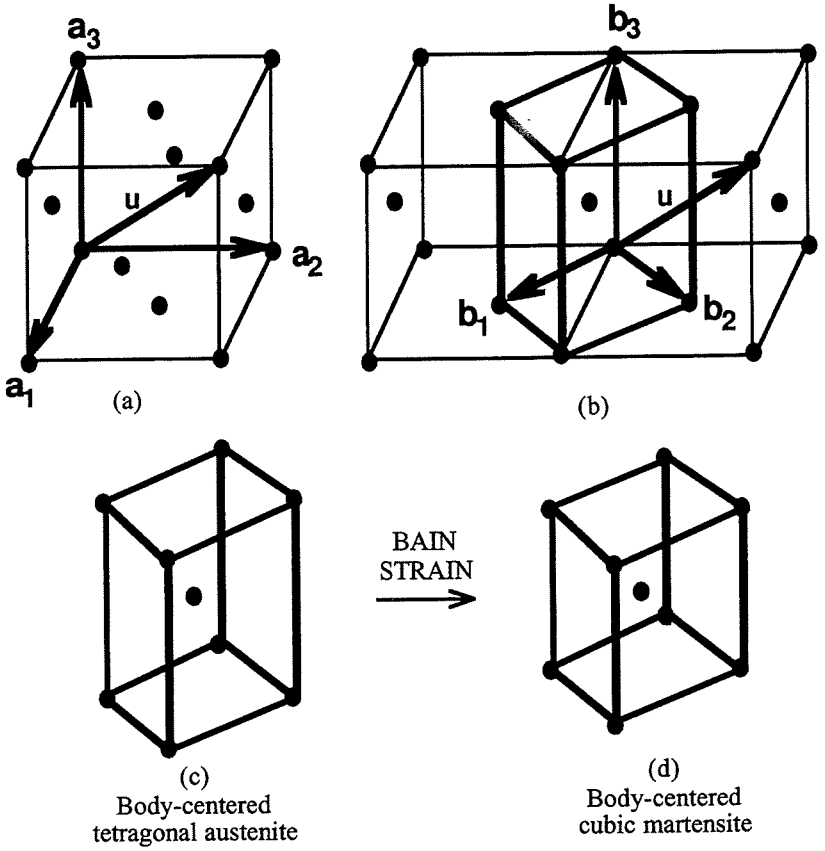


Fig. 5.2: An illustration of the Bain deformation [Bhadeshia, 1992]. (a) conventional face-centred cubic unit cell. (b) relation between the f.c.c. and body-centred tetragonal unit cell representations of austenite. (c) and (d) Bain Strain deforming the austenite lattice into a body-centred cubic lattice.

This can be corrected by combining the deformation with a rigid body rotation to give a net lattice deformation which leaves a single line unrotated and undistorted (an invariant-line strain, line z-y in fig. 5.3c).

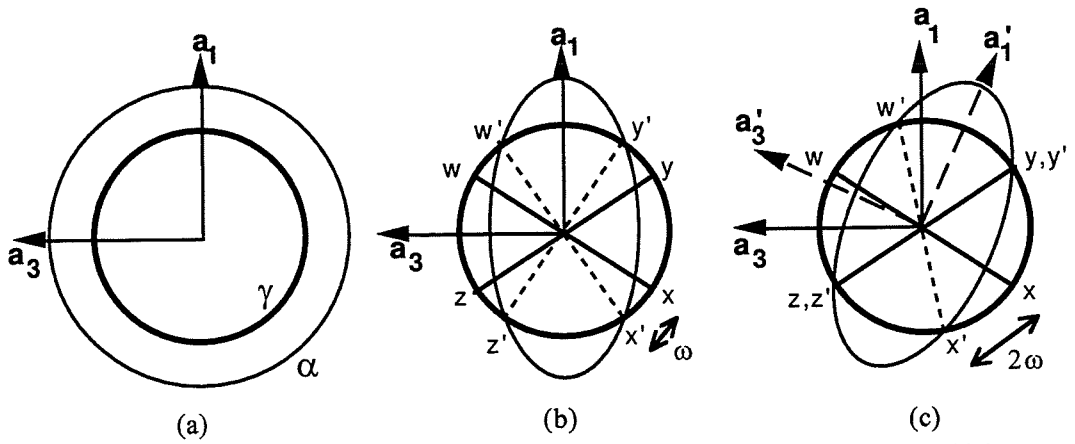


Fig 5.3: The effect of Bain Strain on the austenite represented (a) as a sphere which then deforms into (b) an ellipsoid of revolution. The invariant-line strain is obtained by combining the Bain Strain with a rigid body rotation of angle $\omega$ (c).

A transformation of this type would lead to a great deal of strain as the product grows due to the low degree of fit between the parent and product lattices. However, by adding a further inhomogeneous lattice-invariant deformation (shear or twinning, fig 5.4d and e), the combination of deformations appears macroscopically to be an invariant-plane strain (IPS) [Bowles and Mackenzie, 1954].

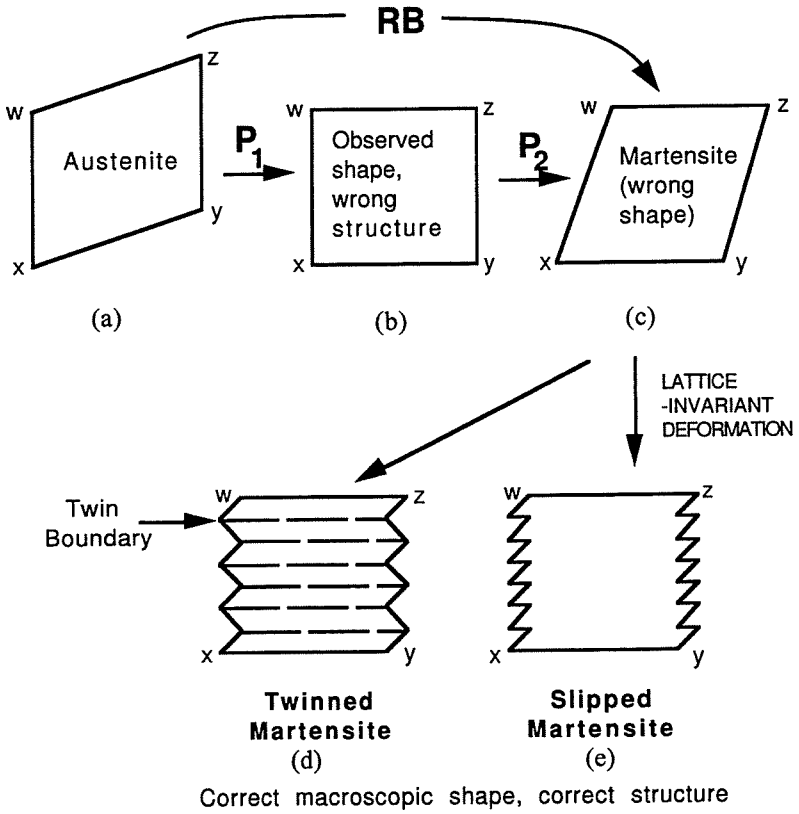


Fig 5.4: Deformation sequence to get martensitic ferrite of correct orientation and observed macroscopic shape. In bainitic ferrite only slip (e) occurs and not twinning (d) [Bhadeshia, 1992].

An invariant-plane is one which is unrotated and undistorted, so that a greater degree of fit is achieved between the austenite and ferrite. This invariant-plane is known as the habit plane and the nature of the strain is as illustrated in fig. 5.5, where $s$ and $\delta$ represent the shear and dilatational components of the strain.

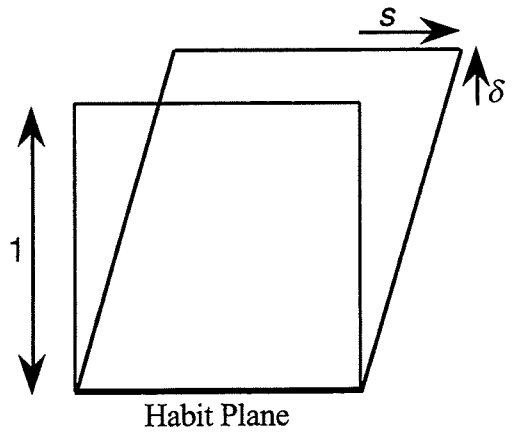


Fig 5.5: Invariant-plane strain with shear strain $s$ and dilatational strain $\delta$: dilatational strain is directed normal to the habit plane.

An implication of the IPS shape deformation is that the product phase must be in the form of a thin plate whose habit plane is the invariant-plane. This minimises the strain energy due to the IPS shape change. For both Widmanstätten ferrite and martensite it is possible to observe the plates optically, and thus establish the nature of the shape deformation by measuring the deflection of scratches on a surface which was polished flat before transformation.

However, the bainitic microstructure, consisting of sheaves of fine ferrite platelets of only about 0.3 μm in thickness, is below the limit of optical microscopy [Sandvik, 1982]. Attempts at optical measurements on bainite have led to low values of $s$ of about 0.13 [Srinivasan and Wayman, 1968b], which are inconsistent with theoretical values in the range 0.22 - 0.28 [Bhadeshia, 1980; Srinivasan and Wayman, 1968b; Ohmori, 1971]. This is because light microscopy can only reveal the average shape deformation over the whole of a bainite sheaf and not of a single sub-unit. Thus higher resolution methods are required.

Sandvik [1982] used TEM to determine, from the displacement of twin boundaries by sub-units, that the value of $s$ is close to 0.22. Swallow and Bhadeshia [1996] have successfully used an atomic force microscope to measure the deformation of single bainite sub-units in a Fe-0.24C-2.18Si-2.32Mn-1.05Ni wt.% steel. Their results indicated the maximum value of shear strain to be $0.26 \pm 0.02$ and are included in fig. 5.15.

## 5.2 Stored Energy in Bainite

Much of the stored energy of bainite comes from the strain energy due to the invariant-plane strain shape change accompanying transformation. For bainite the strain energy due to this shape change has been calculated to be about 400 J $mol^{-1}$ [Bhadeshia, 1981a]. This is smaller

than the corresponding term for martensite, which is between 900 and 1400 J mol$^{-1}$ [Bhadeshia, 1981b].

The value of 400 J mol$^{-1}$ for the stored energy in bainite was calculated from the free energy versus temperature curves for Fe-0.39C-4.08Ni-2.05Si wt.% steel as shown in fig 5.6 [Bhadeshia, 1981a].

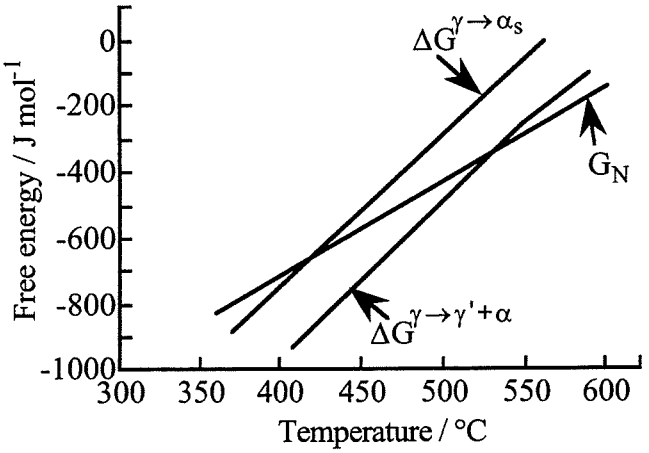


Fig. 5.6: Free energy vs. temperature curves for Fe-0.39C-4.08Ni-2.05Si wt.% steel [Bhadeshia, 1981a]. $G_N$ is the universal nucleation function, $\Delta G^{\gamma\rightarrow\alpha_s}$ is the free energy change for the austenite to super-saturated ferrite transformation and $\Delta G^{\gamma\rightarrow\gamma'+\alpha}$ is the free energy change for the transformation of austenite to enriched austenite and ferrite of equilibrium carbon content.

The $\Delta G^{\gamma\rightarrow\alpha_s}$ curve was calculated using equation 6 of [Bhadeshia, 1981b] which is an adaptation of theory originally by Lacher [1937] and Fowler and Guggenhiem [1939].

The transformation from Widmanstätten ferrite to bainite was found to occur in the region of 470 °C for the Fe-0.39C-4.08Ni-2.05Si wt.% steel. Thus the value of stored energy in bainite, $G_{SB}$, was estimated to be 400 J mol$^{-1}$ since $\Delta G^{\gamma\rightarrow\alpha_s}_{470} \approx$ -400 J mol$^{-1}$ (fig. 5.6).

There is some uncertainty about the value of stored energy of bainite. The 400 J mol$^{-1}$ is for an isolated platelet, but it may be more appropriate to consider the sheaf as a whole, in which case the stored energy would be smaller since the apparent shear component of the shape deformation reduces when averaged over the sheaf containing austenite or carbides [Srinivasan and Wayman, 1968b].

Bainite forms at relatively high temperatures where both austenite and ferrite have low yield strengths. Consequently the strain energy due to the shape change can be reduced by plastic relaxation [Christian, 1979]. The plastic deformation causes an increase in dislocation density

but also reduces the strain energy due to the elastically accommodated shape change. Thus it may be the case that the stored energy of 400 J $mol^{-1}$ should be taken as an upper limit.

## 5.3 Atomic Force Microscopy

The atomic force microscope (AFM) belongs to a family of instruments known as scanning probe microscopes (SPM). The first SPM was the scanning tunnelling microscope (STM) for which its inventors, Gerd Binnig and Heinrich Rohrer, were awarded the 1986 Nobel Prize for Physics.

All SPM instruments operate by placing a very fine probe close to the sample to 'feel' the surface as the probe is scanned across it in a raster pattern. As it moves across the surface the probe moves up or down to maintain a constant height relationship with the sample. The raster movements (in the x-y plane) and the up and down (z-axis) movements, in response to the probe/sample interactions, are stored in the system computer to generate a three-dimensional representation of the sample surface [Lin *et al.*, 1993].

The various types of SPM differ only in the method that is used to sense the sample surface and in the relationship between the probe and the sample. The AFM is the most universal of these methods since it can be used to image any type of material, whereas other methods are more restricted (for example the STM requires the sample to be an electrical conductor). It also has the advantage that it can be used to image samples in different environments such as liquid immersion, ultra-high vacuum and low temperatures.

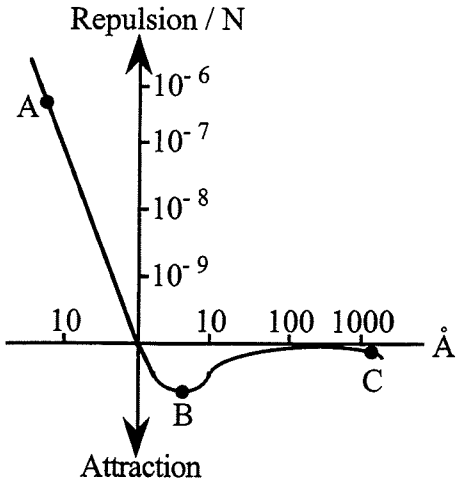


Fig. 5.7: Relationship between AFM probe-to-sample distance and forces. A-B repulsive and B-C attractive [Seiko Instruments Ltd, 1993].

In AFM operation a force relationship is established between the probe and the sample [Binnig *et al.*, 1986]. As the probe and sample are moved close together the force between them due to

van der Waals and other forces is initially attractive. As the probe gets closer repulsive interatomic forces become dominant (fig. 5.7). AFM instruments can be operated in either the attractive or repulsive regimes depending on the detection technique used [Seiko Instruments Ltd, 1993]. The SPA300 microscope used in this research works in the repulsion range $10^{-7}$ to $10^{-11}$ N.

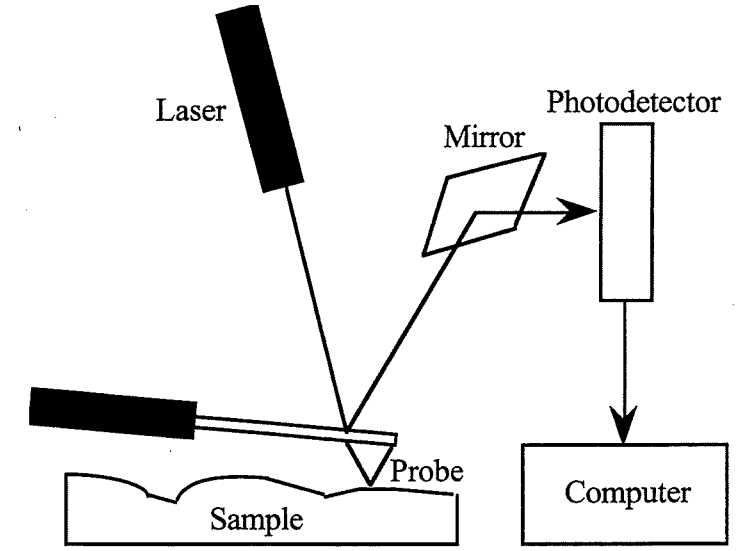

Fig. 5.8: AFM light-lever method of detecting movement of the probe.

The probe/sample forces are measured by placing the probe on a very small spring cantilever which converts the effect of these forces into displacement. A common method for measuring this movement is the optical lever method where the back surface of the cantilever is made into a mirror from which a laser beam is reflected (fig. 5.8). This is then detected by a multisection photodetector giving an accuracy in the Ångstrom range [Lin *et al.*, 1993].

## 5.4 Experimental Method

Samples of steel Fe-0.26C-1.47Si-1.50Mn wt.% were prepared as shown in the experimental chapter, section 3.8. The heat treatments were as shown in table 5.1.

| Samples | Austenite time at 1200 °C | Time at 450 °C |
|---|---|---|
| A, B, C, and D | 150 s | 1200 s |
| E and F | 150 s | 400 s |

Table 5.1: Heat treatments for AFM samples.

The shorter bainite transformation time for samples E and F was chosen to reduce surface oxidation. This was set to 400 s as dilatation results showed that the transformation was near completion by 400 s.

Complete elastic accommodation of the shear due to the bainite platelet results in surface relief approximately as shown in fig. 5.9a. Plastic deformation of the surrounding austenite leads to a relaxation of the surface as shown in fig. 5.9b.

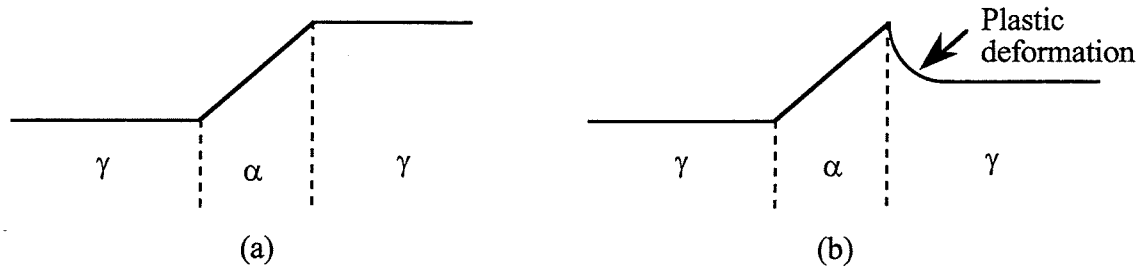


Fig. 5.9: Surface deformation if platelet of bainite is (a) elastically or (b) plastically accommodated.

The AFM computer allows two-dimensional cross sections of platelets to be drawn. These, as shown in the results section, can give an indication to the degree of plastic deformation that has occurred. A measurement of the apparent shear ($s_A$) can be made from scans taken normal to the habit plane trace using the equation:

$$s_A = \frac{b}{a}$$

where $a$ and $b$ are as shown in fig. 5.10a. This is the apparent shear because the platelet is not necessarily at 90° to the sample surface (fig. 5.10b), causing a reduction in the shear value. The affect of dilatation $\delta$ has been ignored since $s >> \delta$ ($s \approx 0.26$ [Swallow and Bhadeshia, 1996] and $\delta \approx 0.014$ [Srinivasan and Wayman, 1968]). Thus the largest measured apparent shear is taken to be the actual shear.

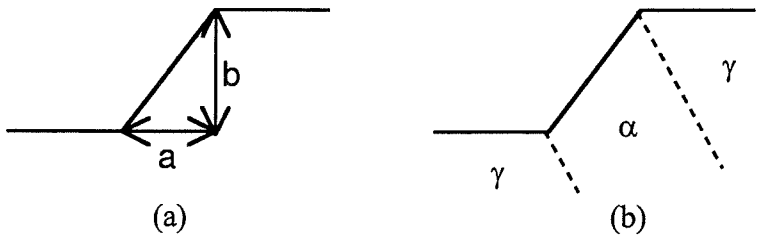


Fig. 5.10: (a) Measurement of shear and (b) possible orientation of platelet leading to an apparent shear being less than the actual value.

## 5.5 Results

The AFM computer allows various methods of displaying the obtained surface data. Fig. 5.11 is a solid model showing surface relief due to bainite platelets in sample E.

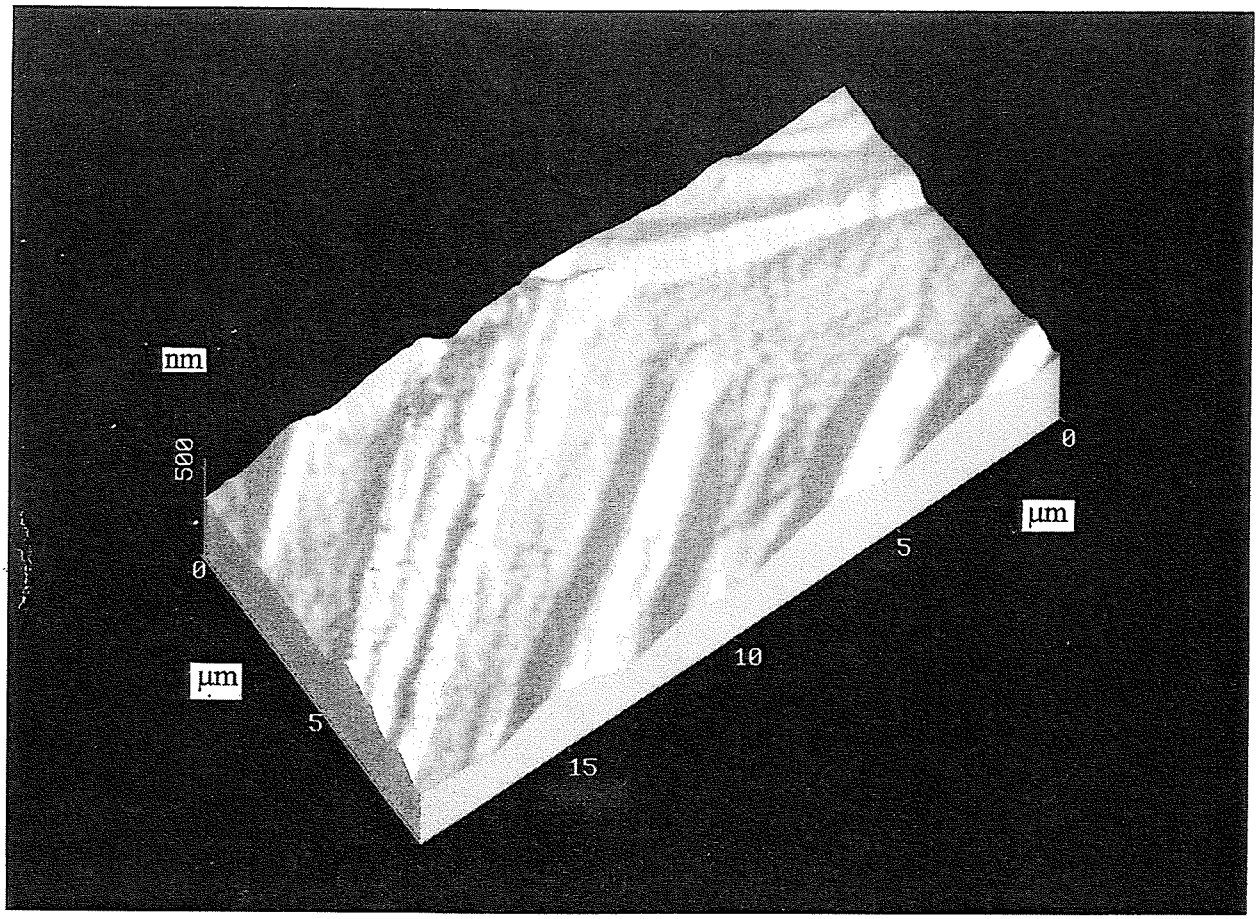


Fig. 5.11: AFM solid model image of surface relief due to bainite platelets in sample E.

The surface relief of a sample that was not heat treated after metallographic preparation is shown in fig. 5.12. This image is presented in a similar resolution to the surface relief images from transformed specimens to enable a comparison to be made. It is evident that the magnitude of the transformation relief is far greater than the polishing relief.

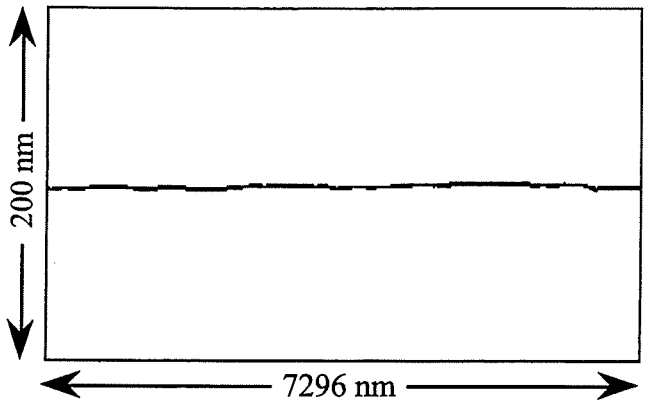


Fig. 5.12: AFM measurement of topography of untransformed metallographically polished sample [Swallow and Bhadeshia, 1996].

The cross sections of observed bainite platelets are shown in figs. 5.13 and 5.14. In fig. 5.13a the plastic deformation in the austenite ($\gamma$) is shown alongside the relatively undeformed bainite platelet ($\alpha_b$). This illustrates the relative softness of the austenite in comparison with the ferrite, as well as confirming the presence of plastic deformation which reduces stored energy.

With some cross sections it was difficult to determine which side of the surface relief was the ferrite and which the deformed austenite (fig. 5.13b). In these cases the shear measurements were taken for both sides and the average value used (and error calculations adapted accordingly).

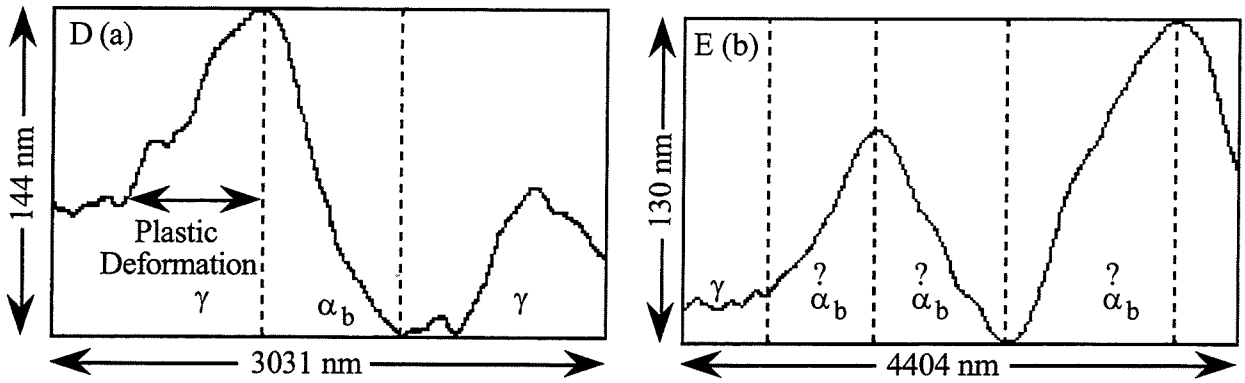


Fig. 5.13: Cross sections through bainite platelets of samples D and E.

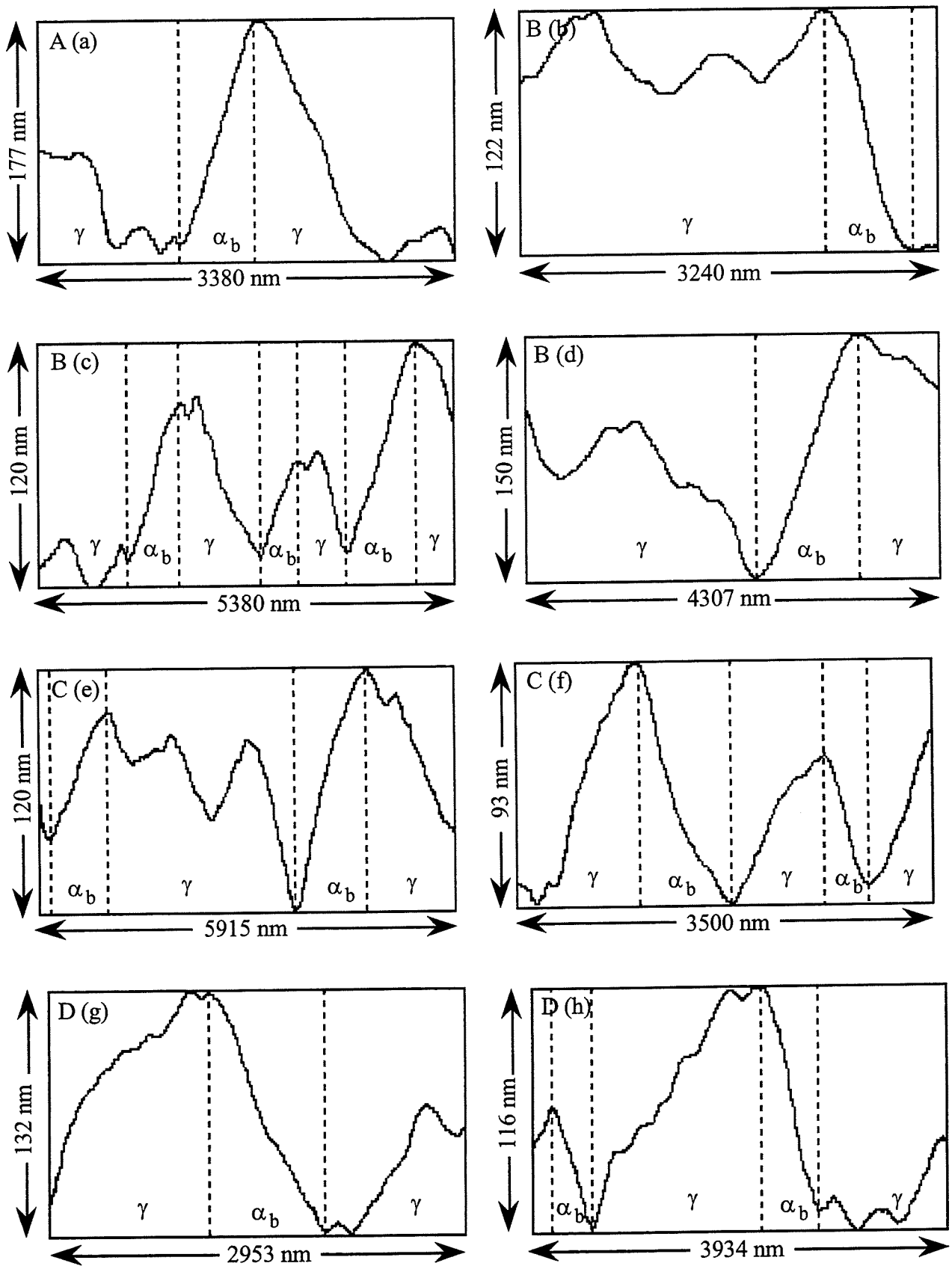


Fig. 5.14 (a - h): Cross sections through bainite platelets for samples A to D.

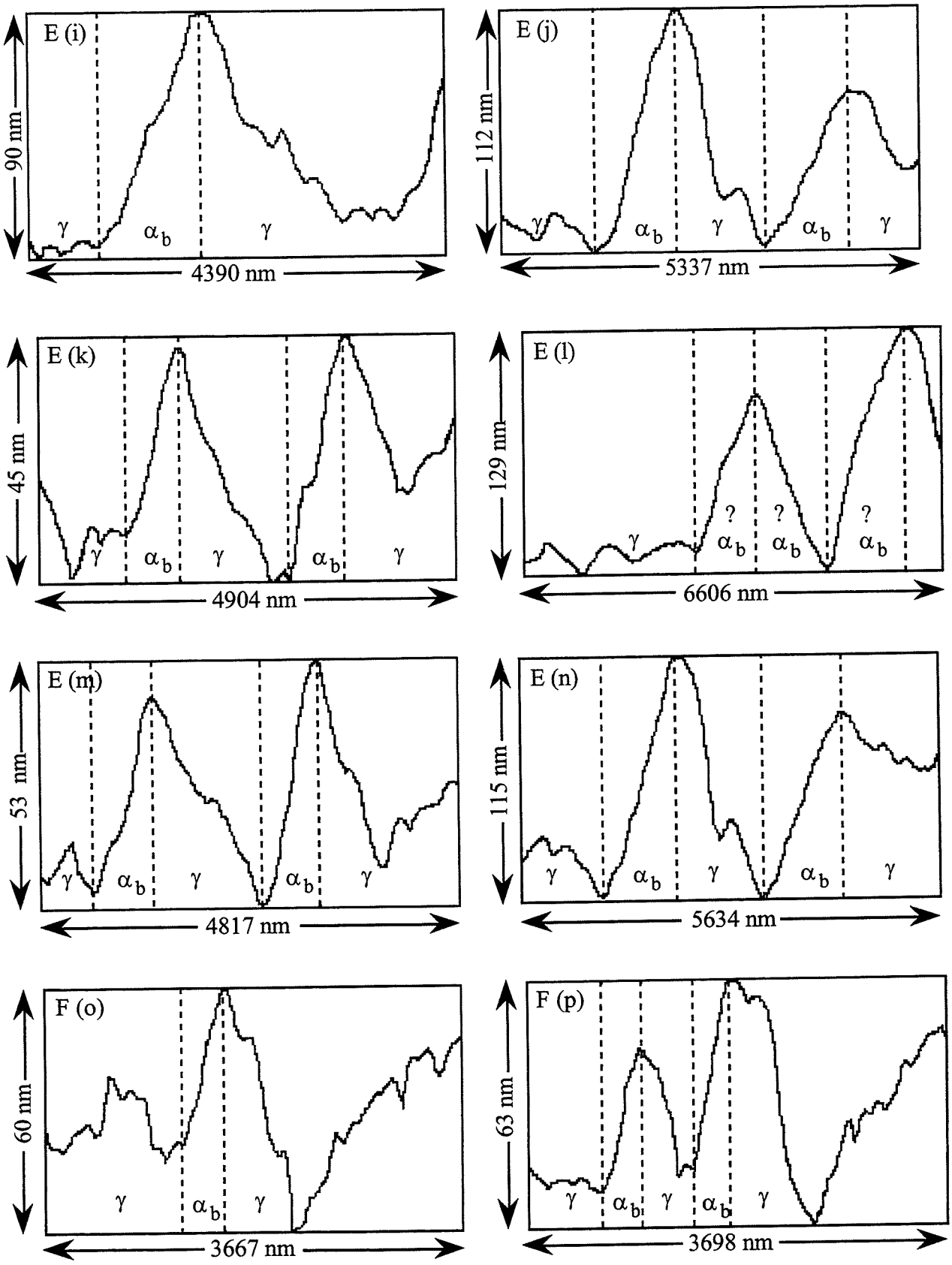


Fig. 5.14 (i - p): Cross sections through bainite platelets for samples E and F.

The measured apparent shear values are shown in table 5.2 and fig. 5.15, along with values obtained by Swallow and Bhadeshia [1996] for steel of composition Fe-0.24C-2.18Si-2.32Mn-1.05Ni wt.%. This shows that, within experimental errors, the results for both steels are in good agreement .

| Sample | $s_A$ | Error |
|---|---|---|
| Swallow and Bhadeshia | 0.21 | 0.02 |
| Swallow and Bhadeshia | 0.20 | 0.02 |
| Swallow and Bhadeshia | 0.26 | 0.02 |
| Swallow and Bhadeshia | 0.24 | 0.02 |
| Swallow and Bhadeshia | 0.23 | 0.02 |
| Swallow and Bhadeshia | 0.19 | 0.02 |
| Swallow and Bhadeshia | 0.19 | 0.02 |
| Swallow and Bhadeshia | 0.18 | 0.02 |
| A | 0.253 | 0.0253 |
| B | 0.179 | 0.0179 |
| B | 0.155 | 0.0155 |
| B | 0.093 | 0.0093 |
| B | 0.112 | 0.0112 |
| B | 0.137 | 0.0137 |
| C | 0.069 | 0.0069 |
| C | 0.118 | 0.0118 |
| C | 0.116 | 0.0116 |
| C | 0.129 | 0.0129 |
| D | 0.188 | 0.0188 |
| D | 0.154 | 0.0154 |
| D | 0.145 | 0.0145 |
| D | 0.194 | 0.0194 |
| E | 0.080 | 0.0080 |
| E | 0.102 | 0.0102 |
| E | 0.064 | 0.0064 |
| E | 0.053 | 0.0053 |
| E | 0.067 | 0.0067 |
| E | 0.102 | 0.0102 |
| E | 0.082* | 0.0109 |
| E | 0.060 | 0.0060 |
| E | 0.078 | 0.0078 |
| E | 0.114 | 0.0114 |
| E | 0.087 | 0.0087 |
| E | 0.097 | 0.0097 |
| E | 0.079* | 0.0140 |
| F | 0.181 | 0.0181 |
| F | 0.102 | 0.0102 |
| F | 0.144 | 0.0144 |

Table 5.2: Measured apparent shear values from this work and Swallow and Bhadeshia [1996]. * indicates averaged values from ambiguous platelets.

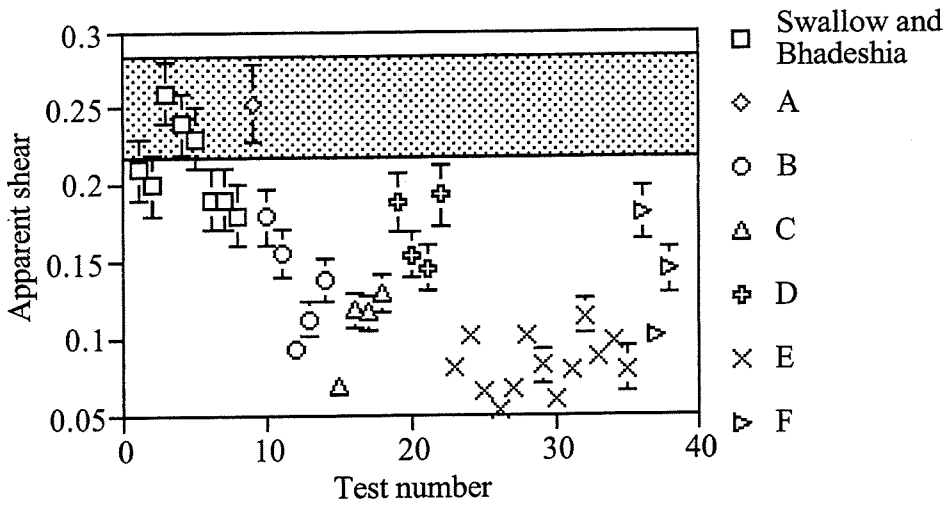


Fig. 5.15: Measured values of apparent shear against test number. Shaded region represents range of theoretically predicted values of $s$ depending on various assumptions about mode of lattice-invariant shear, etc. Tests 1-8 from Swallow and Bhadeshia [1996]. Some errors are too small to be plotted.

The experimental errors of ±10 % were calculated to take into account measurement accuracy of the distances and the accuracy of drawing the cross section at 90° to the platelet.

## 5.6 Conclusions

The presence of plastic deformation in austenite surrounding bainite platelets has been confirmed. This indicates that the amount of stored energy in bainite is lower than 400 J $mol^{-1}$, which was the value calculated [Bhadeshia, 1981a] assuming no plastic accommodation of the strains due to transformation.

The apparent shear values of bainite platelets have been measured using an AFM, and these agree with values obtained by Swallow and Bhadeshia [1996] who, consistent with theory, found the maximum apparent shear to be about 0.26 ( ± 0.02).

# 6. Intercritical Annealing Model

## 6.1 Introduction

Continuously annealed steels of typical chemical composition Fe-0.2C-2.0Si-1.5Mn wt.% have a microstructure which is a mixture of allotriomorphic ferrite and harder regions containing bainitic ferrite, martensite and carbon-enriched retained austenite. The allotriomorphic ferrite generally occupies about 60-70% of the microstructure and is retained during intercritical annealing or is produced during continuous cooling transformation. The presence of the large amount of silicon prevents the precipitation of cementite during the transformation to bainite. The carbon that is rejected from the supersaturated bainitic ferrite into the residual austenite stabilises it so that nearly 10-15% of the final microstructure might consist of retained austenite. This austenite is believed to contribute greatly to formability via transformation-induced plasticity (see Chapter 8).

These steels are heat treated in industry on continuous annealing lines which involves a complicated heating and cooling cycle. Austenite forms during intercritical annealing (between $Ac_1$ and $Ac_3$); its volume fraction depends on the kinetics of transformation. The $Ac_1$ and $Ac_3$ temperatures are the non-equilibrium counterparts of $Ae_1$ and $Ae_3$ as shown in fig. 6.1. It is necessary therefore to understand $Ac_1$ and $Ac_3$ as a function of the steel composition and heating-rate.

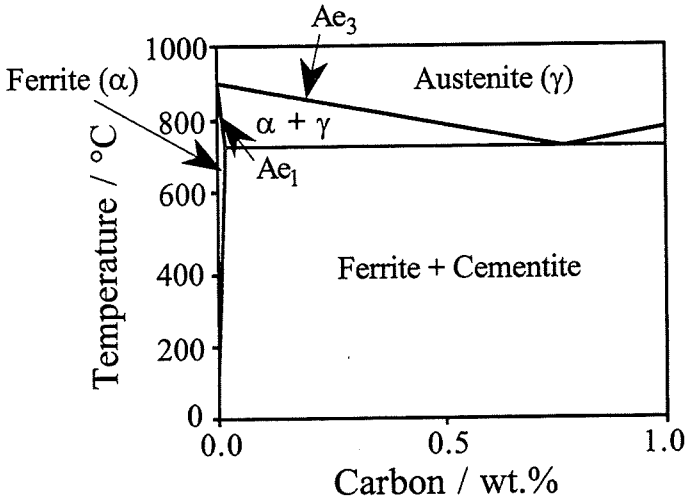


Fig. 6.1: Fe-C phase diagram with $Ae_1$ and $Ae_3$ temperature lines indicated.

To calculate the volume fraction of allotriomorphic ferrite and austenite prior to the bainite transformation requires an ability to estimate the following phenomena:

1) the formation of austenite during heating to a temperature between $Ac_1$ and $Ac_3$.

2) the transformation of austenite to allotriomorphic ferrite on cooling below $Ac_1$.

This chapter deals with a method for modelling the first of these phenomena.

## 6.2 Formation of Austenite During Heating

### 6.2.1 The problem

The formation of austenite during heating differs in many ways from those transformations that occur during the cooling of austenite. For cooling transformations, the kinetics of decomposition follow the classical C-curve behaviour, in which the rate goes through a maximum as a function of the undercooling below the equilibrium transformation temperature. This is because diffusion becomes sluggish with decreasing temperature, but the magnitude of the driving force for the $\gamma \rightarrow \alpha$ transformation increases with the undercooling. On the other hand, both the diffusion coefficient and the driving force increase with the extent of superheat above the equilibrium temperature, so that the rate of austenite transformation must increase indefinitely with temperature, fig. 6.2.

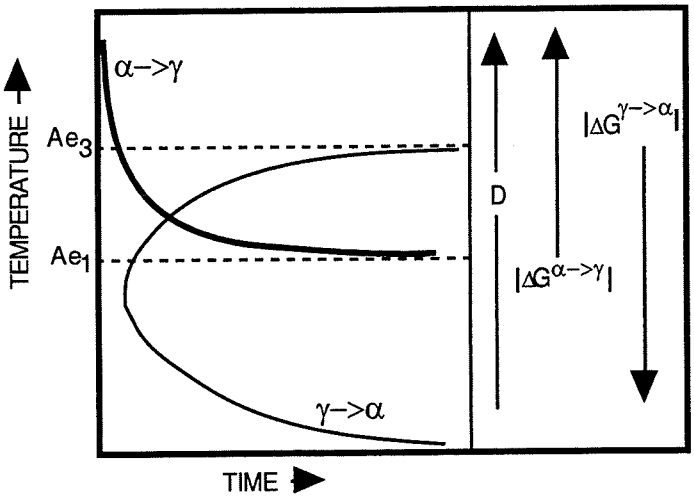


Fig. 6.2: The time-temperature-transformation curves for the $\gamma \rightarrow \alpha$ reaction, and for the reverse $\alpha \rightarrow \gamma$ transformation. $\alpha$ and $\gamma$ represent ferrite and austenite, respectively. $\Delta G$ represents the chemical driving force for transformation; D is the rate-controlling diffusion coefficient [Bhadeshia, 1992].

There is another important difference between the transformation of austenite, and the transformation to austenite. In the former case, the kinetics of transformation can be described completely in terms of the alloy composition and the austenite grain size. By contrast, the microstructure from which austenite may grow can be infinitely varied. Many more variables are therefore necessary to describe the kinetics of austenite formation. The extent to which the starting microstructure has to be specified remains to be determined, but factors such as particle size, the distribution and chemistry of individual phases, homogeneity, the presence of non-metallic inclusions, *etc.* should all be important.

This discussion highlights the complexity of the problem. A fundamental attempt at modelling the formation of austenite is therefore unlikely to be of general value, except at slow heating rates consistent with the achievement of equilibrium. Some aspects of the difficulties involved have been reviewed recently for a variety of starting microstructures [Bhadeshia, 1992]. Models of specific metallurgical approaches exist but none are of general applicability for the reasons described earlier [Hillert, *et al.*, 1971; Yang and Bhadeshia, 1989 and Atkinson *et al.*, 1995].

### 6.2.2 Prediction of $Ac_1$ and $Ac_3$

Recent work [Gavard *et al.*, 1996] has addressed the complex problem of austenite formation using an alternative approach. The formation of austenite during the continuous heating of steels was investigated using neural network analysis with a Bayesian framework [MacKay, 1992a-c; 1993]. An extensive database consisting of the detailed chemical composition, $Ac_1$ and $Ac_3$ temperatures, and the heating rate was compiled for this purpose, using data from published literature. The results from the neural network analysis are found to be consistent with what might be expected from phase transformation theory.

| | Composition / wt.% | | | | | | | | | |
|---|---|---|---|---|---|---|---|---|---|---|
| Steel | C | Mn | Si | S | P | Al | N | Cu | Ni | Cr |
| 1 | 0.38 | 1.73 | 1.29 | 0.006 | 0.013 | 0.041 | - | - | - | - |
| 2 | 0.203 | 1.42 | 1.43 | 0.004 | 0.005 | 0.013 | 0.003 | 0.031 | 0.010 | 0.008 |
| 3 | 0.26 | 2.10 | 1.85 | 0.013 | 0.015 | - | 0.009 | 0.200 | - | - |

Table 6.1: Compositions of the steels used in this chapter.

The neural network models produced by Gavard *et al.* [1996] were trained on data for heating rates in the range 0.03 - 50 °C $s^{-1}$. Predictions made with these models are shown in figs. 6.3a and b for steels 1 - 3 in table 6.1 and heating rates of 5, 10 and 20 °C. The model confidence limits are as indicated. The experimental values were obtained by dilatation as described below. The error bars for the experimental values are ±5 °C (only visible in fig. 6.3a) and a scatter of results for each heating rate can also be seen. These predictions are thought to be reasonable and will be used in this work.

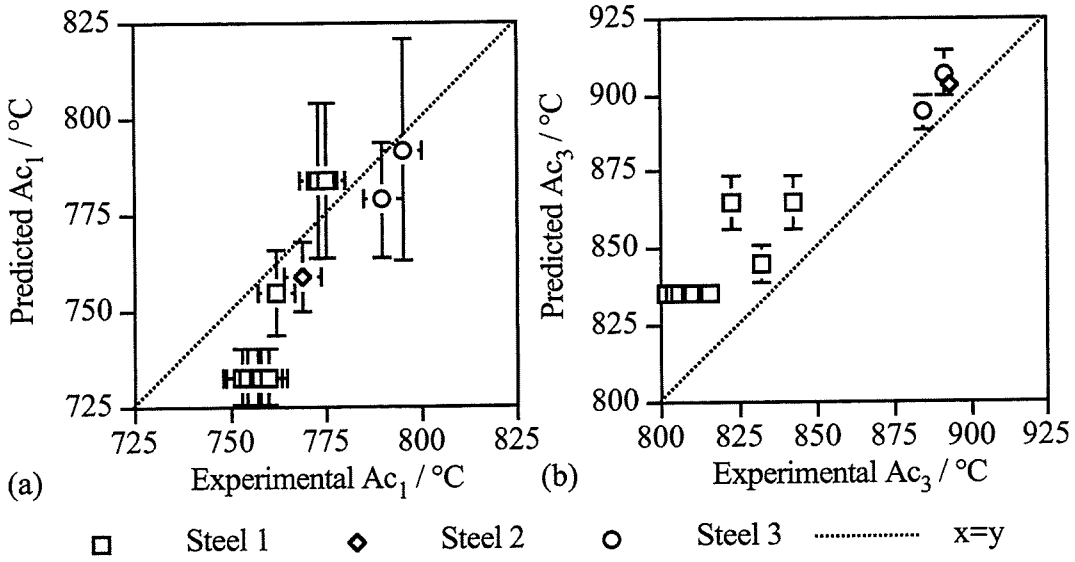


Fig. 6.3: Predicted and experimental (a) $Ac_1$ and (b) $Ac_3$ temperatures for steels 1-3 in table 6.1 at heating rates of 5, 10 and 20 °C $s^{-1}$. The predictions were made using the neural network models by Gavard *et al.* [1996] and the model confidence limits are shown (where large enough to be plotted).

### 6.2.3 Austenite volume fraction predictions

To make further use of the above neural network models of $Ac_1$ and $Ac_3$ there needs to be a method of predicting the volume fraction of austenite as a function of these temperatures, which implicitly include heating rate effects. This has been achieved by considering the distinctive contraction during heating through the $Ac_1$ and $Ac_3$ temperature range (fig. 6.4).

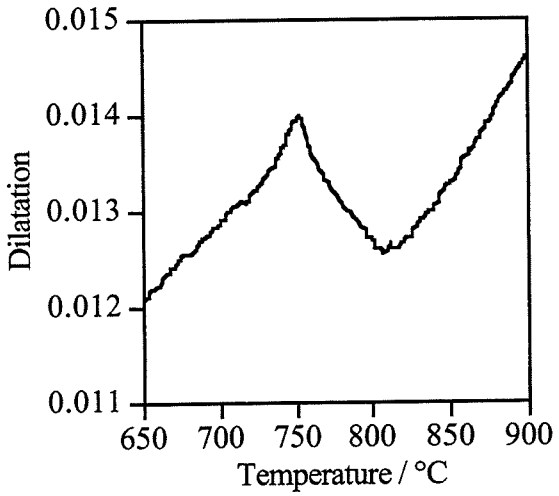


Fig. 6.4: Dilatation measurements for steel 1 heating at 5 °C $s^{-1}$ through the austenite formation temperature range.

This contraction is due to the relative volumes of the austenite and ferrite phases and can be approximately converted into the volume fraction of austenite as shown in fig. 6.5.

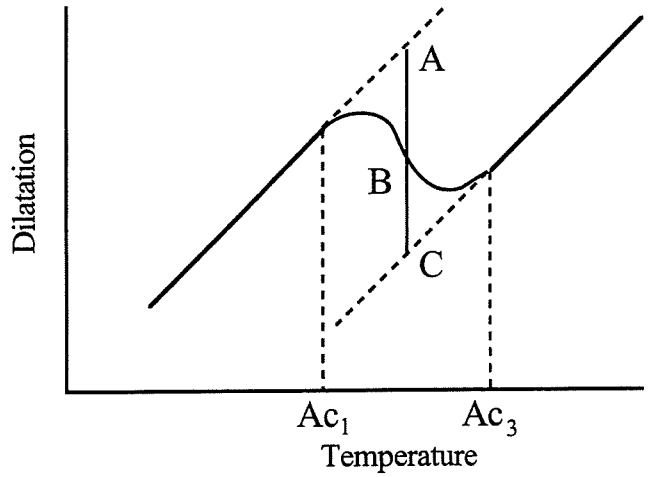


$$\text{Volume fraction of austenite} = \frac{AB}{AC}$$

Fig. 6.5: Method used to calculate volume fraction of austenite during heating from dilatation data.

*6.2.3.1 Experimental*

Cylindrical steel samples, of the compositions shown in table 6.1, were heated in a thermomechanical simulator (section 3.1), from room temperature to 1000 °C at rates of 5, 10 and 20 °C $s^{-1}$. The starting microstructures were either bainite, retained austenite and martensite or allotriomorphic ferrite and pearlite. Dilatation measurements taken during heating were analysed as shown in fig. 6.5 and 186 data sets were obtained.

To model the austenite formation an equation was required so that when $T = Ac_1$ the volume fraction of austenite ($V_\gamma$) is zero and when $T = Ac_3$ the transformation to austenite is complete. Equation 6.1 was chosen:

$$V\gamma = \frac{1 - \exp\left\{-k_0 \exp\left(\frac{-Q_1}{kT}\right)\left[\frac{T - Ac_1}{Ac_3 - Ac_1}\right]^n\right\}}{a'} \qquad (6.1)$$

which has the form of an Avrami equation, where $T$ is the absolute temperature, $k$ is the Boltzmann constant and $a'$ is a function so that at $T = Ac_3$ :

$$1 = \frac{1 - \exp\left\{-k_0 \exp\left(\frac{-Q_1}{kAc_3}\right)\left[\frac{Ac_3 - Ac_1}{Ac_3 - Ac_1}\right]^n\right\}}{a'} \qquad (6.2)$$

and hence:

$$a' = 1 - \exp\left\{-k_0 \exp\left(-Q_1/kAc_3\right)\right\} \qquad (6.3)$$

The optimum constants were obtained, by fitting to the experimental data, as $k_0 = 0.0206$, $n = 0.849$ and $Q_1/k = 0.12 \times 10^{-6}$ K. The optimum fit being shown in fig. 6.6. It should be noted that $\exp\left(\frac{-Q_1}{kT}\right)$ is insignificant at these values, indicating that the $Ac_1$, $Ac_3$ term is more important in this calculation.

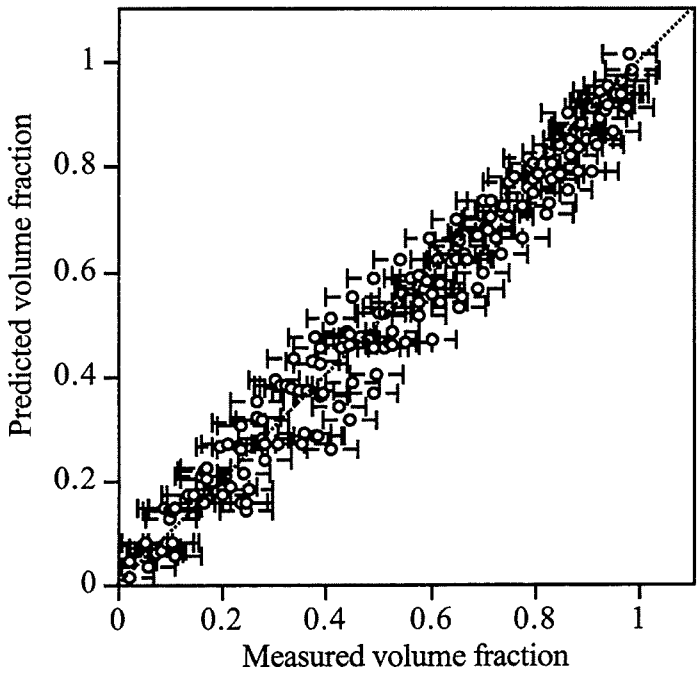


Fig. 6.6: Measured volume fractions of austenite and values predicted with equation 6.1 using the optimised constants.

A prediction of the volume fraction of austenite between $Ac_1$ and $Ac_3$ for steel 1, heated at a rate of 5 °C $s^{-1}$, was calculated using equation 6.1. This is shown in fig. 6.7 and correlates to the experimental dilatation curve in fig. 6.4.

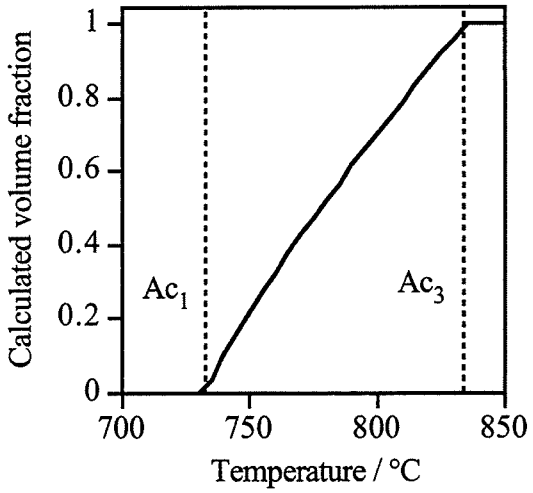


Fig. 6.7: Predicted volume fraction of austenite formed during heating through $Ac_1$ and $Ac_3$ at 5 °C $s^{-1}$ for steel 1.

Samples of sheet steel of composition Fe-0.19C-1.45Mn-1.61Si wt.% were heated at a rate of 200 °C $s^{-1}$ to various temperatures between $Ac_1$ and $Ac_3$ and then quenched. These experiments were carried out at British Steel Wales and point counting of the martensite phase after quenching provided a measurement of austenite volume fractions of the samples at the intercritical annealing temperatures. These austenite volume fractions are shown in fig. 6.8 in comparison with calculations.

The Gavard *et al.* neural network models were only trained for heating rates up to 50 °C $s^{-1}$ and thus predictions at 200 C $s^{-1}$ are unlikely to be accurate. A variety of heating rates were tried and, as can be seen in fig. 6.8, a rate of 20 °C $s^{-1}$ gave the best agreement with the experimental results.

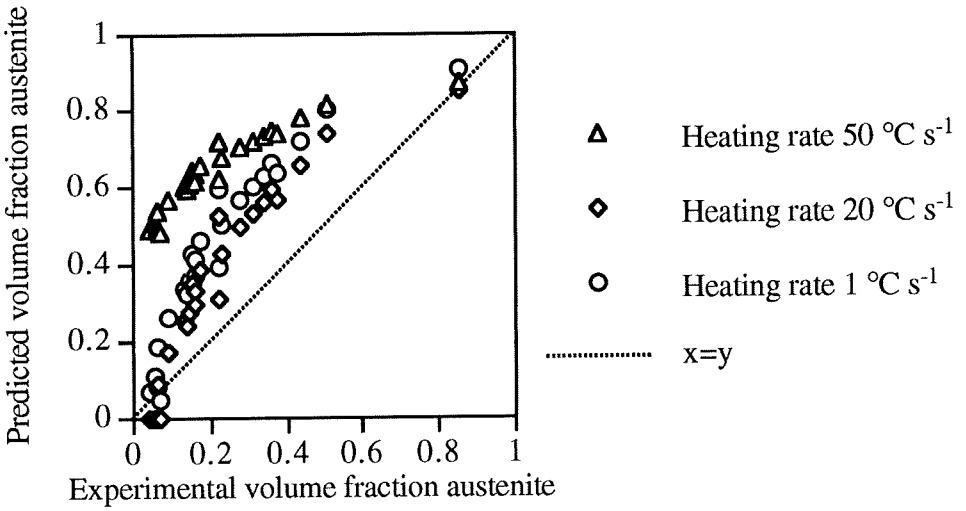


Fig. 6.8: Experimental and predicted volume fractions of austenite as a function of the intercritical annealing temperature (732-893 °C) for Fe-0.19C-1.45Mn-1.61Si wt.% sheet steel. Experimental heating rate 200 °C $s^{-1}$, prediction heating rates 1, 20 and 50 °C $s^{-1}$. Experimental errors could not be calculated as the number of points used was not supplied.

The results in fig. 6.8 indicate an over-prediction of the retained austenite values. Some of this might be accounted for by the presence of retained austenite as well as martensite in the quenched samples. This retained austenite would be fairly indistinguishable optically from the ferrite and thus not counted during point counting.

## 6.3 Ferrite Formation from Austenite on Cooling

On cooling from the intercritical annealing temperature, allotriomorphic ferrite may grow from the austenite, depending on the alloy and the cooling rate. A published model for ferrite formation, as described in section 2.2, can be used to estimate this transformation [Bhadeshia *et al.*, 1987].

This model may be combined with the above one for austenite formation to predict the total allotriomorphic ferrite content of the steel prior to bainite transformation.

## 6.4 Conclusions

A model of austenite formation on heating into the intercritical annealing temperature range has been produced and optimised with experimental data. This has been combined with neural network models [Gavard *et al.*, 1996] of $Ac_1$ and $Ac_3$ to allow the austenite volume fraction to be predicted with only knowledge of the chemical composition of the steel, the heating rate and the intercritical annealing temperature. This assumes that, after transformation to austenite, the remaining phase is allotriomorphic ferrite and not the bainite, pearlite or martensite of the initial microstructure.

# 7. Martensite Formation and Retained Austenite

## 7.1 Introduction

When austenite is supercooled to a sufficiently low temperature it transforms into martensite which can be very hard when the alloy contains carbon. This can occur in the final stage of a continuous cooling heat treatment with the martensitic decomposition of any residual austenite. The transformation rarely consumes all of the austenite, some of which is consequently retained.

The extent of martensitic transformation depends on the stability of the austenite and the temperature to which the sample is cooled. The reaction begins at the martensite-start temperature, $M_S$, which is mainly a function of the alloy chemistry. Further transformation takes place only on cooling beyond $M_S$, the fraction depending on the undercooling below $M_S$ [Christian, 1975].

Unlike allotriomorphic ferrite or pearlite, martensite forms by a deformation of the austenite lattice as explained in Chapter 5 (fig. 5.4). The reaction is a diffusionless shear transformation, highly crystallographic in character, with a characteristic lath or lenticular microstructure [Bilby and Christian, 1956].

An ability to estimate the volume fraction of martensite formed on cooling is important for designing the microstructure and mechanical properties of a steel. The strength and toughness are dependent on the martensite phase and the ductility can be sensitive to the retained austenite content [Sakuma *et al.*, 1992].

## 7.2 Calculation of $M_S$

To model martensite transformation in a mixed microstructure requires a knowledge of the carbon concentration within the residual austenite. This is achieved by assuming that any ferrite has a very low carbon content, here taken to be 0.03 wt.% [Bhadeshia and Edmonds, 1983a] and that the remainder is partitioned into the austenite. The $M_S$ temperature of the austenite can then be calculated for the carbon enriched austenite.

The $M_S$ temperature of any steel can in principle be estimated by balancing the driving force needed to stimulate transformation, $\Delta G_{M_S}^{\gamma\rightarrow\alpha'}$, against that available as a function of temperature, $\Delta G^{\gamma\rightarrow\alpha'}$.

The free energy change $\Delta G^{\gamma\rightarrow\alpha'}$ differs from the corresponding term $\Delta G^{\gamma\rightarrow\alpha}$ for the transformation of austenite to ferrite of the same composition because the latter does not allow for Zener ordering of the carbon atoms [Zener, 1946; Fisher, 1949].

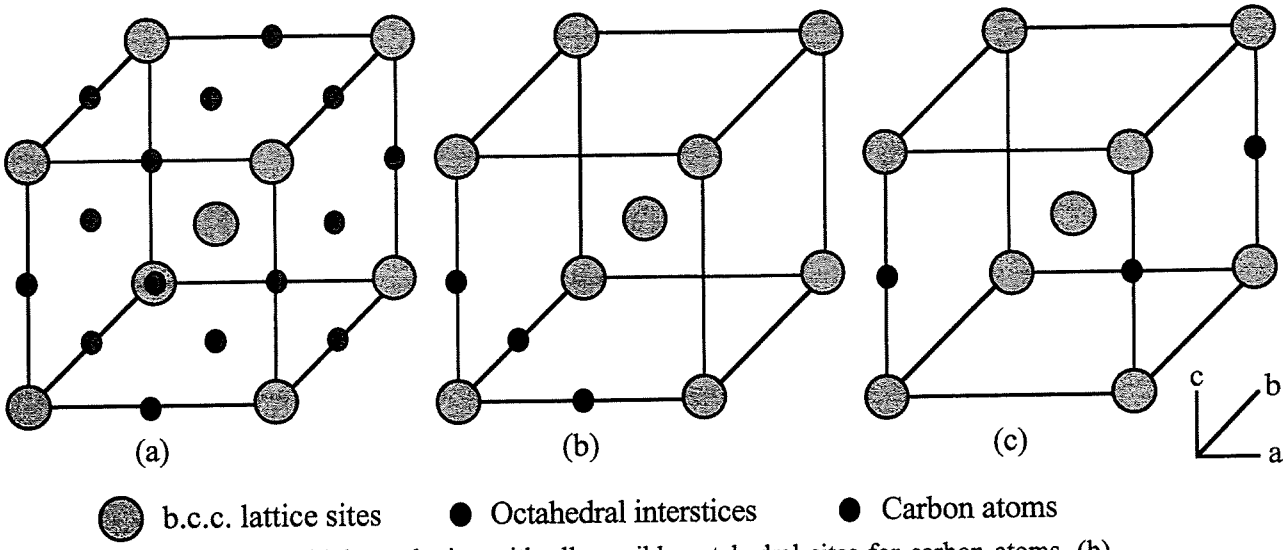


Fig. 7.1: (a) b.c.c. lattice with all possible octahedral sites for carbon atoms, (b) carbon atoms randomly orientated and (c) Zener ordering of carbon atoms.

Zener ordering (fig. 7.1c) is the ordering of carbon atoms within the b.c.c. lattice to one group of octahedral interstices along the c-axis. This causes an expansion along the c-axis and a smaller contraction along the other two orthogonal axis resulting in a tetrahedral unit cell.

Equation 1 in [Bhadeshia and Edmonds, 1980] was used to calculate the free energy change for the transformation of austenite to martensite, $\Delta G^{\gamma\rightarrow\alpha'}$ (function FTO1, [MAP]). This method is based on the Lacher [1937] and Fowler and Guggenheim [1939] formulae and includes Zener ordering [Fisher, 1949]. Substitutional alloying elements are allowed for by their effects on the magnetic and non-magnetic components of the free energy change accompanying the $\gamma\rightarrow\alpha$ transformation in pure iron [Bhadeshia, 1981b and c]. This free energy was calculated for a range of temperatures and linear regression used to fit a straight line to the data.

The driving force for nucleation at the $M_s$ temperature, $\Delta G_{M_s}^{\gamma\rightarrow\alpha'}$ was then calculated using equation 7.1:

$$\Delta G_{M_s}^{\gamma\rightarrow\alpha'} = -1.086.9 + 2941.8x_\gamma - 9.6016\times10^5 x_\gamma^2 + 2.5382\times10^7 x_\gamma^3 - 1.8488\times10^8 x_\gamma^4 \quad (7.1)$$

where $\Delta G_{M_s}^{\gamma\rightarrow\alpha'}$ is taken to be a function of the austenite carbon content, $x_\gamma$, in mole fraction and is valid for a range 0.01 - 0.06 mole fraction of carbon. Bhadeshia [1981b] obtained this equation by curve fitting to line B in fig. 7.2 which is based on theory by Lacher [1937] and Fowler and Guggenheim [1939] [Bhadeshia, 1981b and c] (subroutine MSTART, [MAP]). It

can be noted from fig. 7.2 that equation 7.1 is only valid for this theory and other thermodynamic models can produce quite different results. The details and merits of the different models are discussed in [Bhadeshia, 1981b] but the main point is that equation 7.1 must only be used with the thermodynamic model which generated curve B.

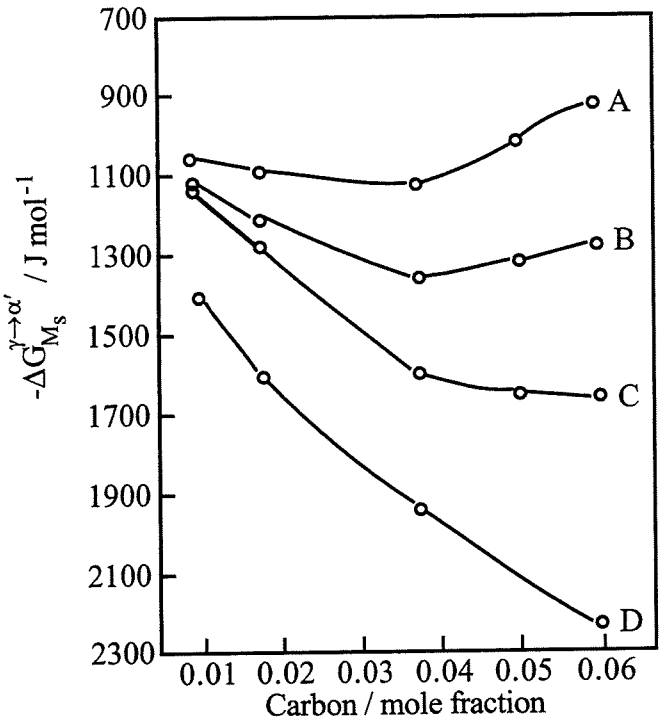


Fig. 7.2: Variation of free energy change accompanying martensitic transformation at $M_s$ as a function of carbon content. Curve A [Fisher, 1949], B [Lacher, 1937; Fowler and Guggenhiem, 1939], C [Bell and Owen, 1967] and D [Imai *et al.*, 1965], figure from [Bhadeshia, 1981b].

The $M_s$ temperature was then calculated as the temperature on the free energy line which corresponds to where the free energy and the driving force are equal (fig. 7.3).

This approach assumes that the carbon distribution in the austenite is homogeneous, which we know is not the case as the thin films around the bainite platelets are higher in carbon concentration than the larger blocky areas. It also assumes that the other alloying elements have not partitioned, which is dependent on the original steel and on the intercritical annealing process.

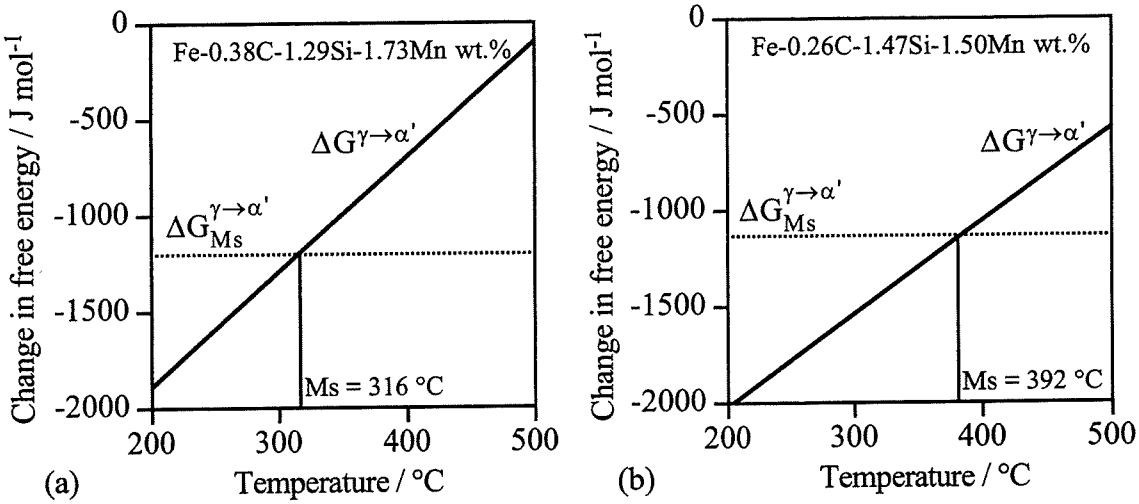


Fig. 7.3: Illustration of the calculations used to calculate the $M_s$ temperatures of steels with compositions (a) Fe-0.38C-1.29Si-1.73Mn wt.% and (b) Fe-0.26C-1.47Si-1.50Mn wt.%.

## 7.3 Calculation of Martensite Volume Fraction†

### 7.3.1 Koistinen and Marburger

Koistinen and Marburger [1959] successfully fitted a straight line to the plot of $M_S$-$T_q$ (quench temperature) versus the logarithm of volume fraction of austenite $V_\gamma$. This gave the equation:

$$V_\gamma = \exp\left[-C_5\left(M_s - T_q\right)\right] \qquad (7.2)$$

where $M_s > T_q > -80$ °C, with $C_5 = 1.1 \times 10^{-2}$

The relationship fitted the available experimental data well for plain carbon steels. Alloying elements were thought to affect the amount of retained austenite only by their effect on $M_s$, the amount of martensite was then calculated using the obtained value of $V_\gamma$.

The form of the Koistinen and Marburger equation has been justified theoretically by Magee [1969]. But Magee pointed out that different values of constants were required for different steels, contrary to Koistinen and Marburger's conclusions. Khan and Bhadeshia [1990a] also showed with their results that the equation fitted well but required different values of $C_5$.

### 7.3.2 Khan and Bhadeshia

In 1990 Khan and Bhadeshia [1990a] modified the Koistinen and Marburger method of calculating the amount of martensite obtained from austenite when quenched below $M_s$. Their

[† Some of the work presented here has already been discussed in Chapter 2. It is reproduced here for clarity.]

experimental results were obtained using dilatometry to measure the volume fraction of martensite and bainite (if formed), the austenite being the remainder. The results were obtained using a Fe-0.44C-1.74Si-0.67Mn-1.85Ni-0.83Cr-0.39Mo-0.09V wt.% steel, some samples of which had been homogenised and some in the as received condition. The heat treatments included holding some samples at various isothermal bainite-forming temperatures before quenching to a known temperature, whereas others were quenched directly from the austenite phase.

The new theory included the autocatalysis effect, in which plates of martensite induce new embryos which are then available for further transformation. Using the assumption that each nucleus leads to the formation of a plate of constant volume and taking into account autocatalysis, the following equation was derived:

$$-\frac{\ln\left(1-V_{\alpha'}\right)}{V_{\alpha'}} = 1 + C_6\left(M_s - T_q\right) \qquad (7.3)$$

where $V_{\alpha'}$ is the martensite volume fraction and $C_6 = 0.0029$, found by using linear regression. This gave good agreement with all the experimental data. Some discrepancy was found for the lower volume fractions of martensite, perhaps because the analysis still does not take into account the change in plate volume with degree of transformation and the variation in activation energy of nucleation sites.

## 7.4 Comparison with experimental data

Independent microstructural data for steel of composition Fe-0.43C-3.0Mn-2.02Si-0.01Cr-0.01Ni wt.% were obtained by Bhadeshia and Edmonds [1983a]. The homogenised samples were austenitised in a dynamic argon atmosphere and then isothermally transformed in a molten tin bath covered with a layer of active charcoal. The isothermal bainite transformation temperatures were 270 and 363 °C (as indicated in table 7.1) and a variety of microstructures were obtained by varying the isothermal transformation times between 5 and 2015 minutes.

The quantitative metallography was carried out using a Quantimet image analysing computer and X-ray analysis [Bhadeshia and Edmonds, 1983a].

The theory above was used to calculate the carbon concentrations of the remaining austenite following the bainite transformation, and to predict the volume fractions of martensite using both the Koistinen and Marburger and the Khan and Bhadeshia models.

| Temperature | Measured volume fractions | | | Predicted martensite volume fraction | |
|---|---|---|---|---|---|
| (°C) | Bainite | Austenite | Martensite | K + M | K + B |
| 363 | 0.39 | 0.27 | 0.34 | 0.20 | 0.33 |
| 270 | 0.22 | 0.10 | 0.68 | 0.42 | 0.63 |
| 363 | 0.02 | 0.11 | 0.87 | 0.62 | 0.87 |
| 270 | 0.045 | 0.08 | 0.875 | 0.60 | 0.85 |
| 363 | 0.005 | 0.10 | 0.895 | 0.64 | 0.89 |
| 363 | 0.005 | 0.085 | 0.91 | 0.64 | 0.89 |

Table 7.1: Experimental microstructure data from [Bhadeshia and Edmonds, 1983a] and predicted martensite volume fractions for steel Fe-0.43C-3.0Mn-2.02Si-0.01Cr-0.01Ni wt.%. K+M = Koistinen and Marburger [1959], K+B = Khan and Bhadeshia [1990a].

As can be seen in table 7.1 and fig. 7.4 the Khan and Bhadeshia model (K + B) is in good agreement with the experimental data. This is not the case for the Koistinen and Marburger model (K + M) which consistently under-predicts the martensite volume fraction.

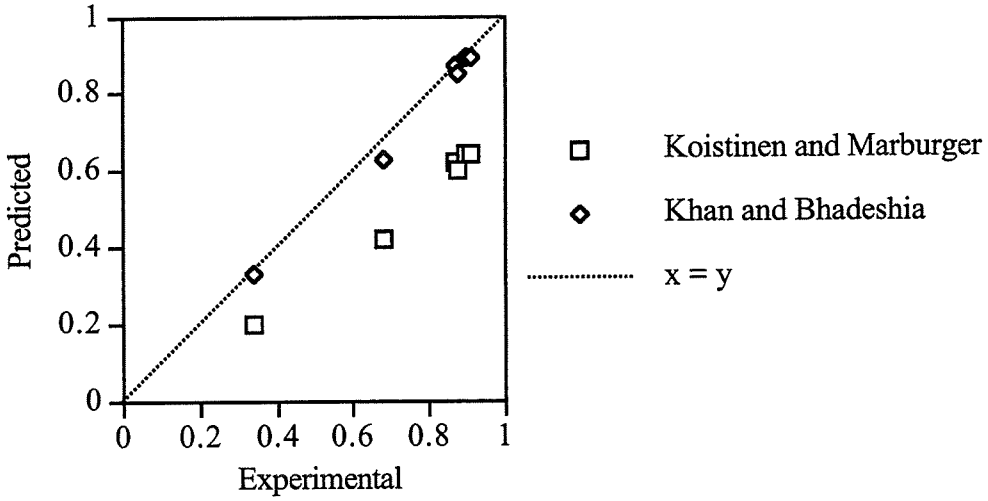


Fig. 7.4: Comparison between experimental and predicted martensite volume fractions for steel Fe-0.43C-3.0Mn-2.02Si0.01Cr-0.01Ni wt.%, using both models.

This theory has been combined with the bainite kinetics model of Chapter 4 so that, during continuous cooling, if the $M_s$ temperature of the austenite becomes greater then the actual temperature then the bainite reaction stops and the martensite fraction is calculated assuming the final temperature to be 20 °C. The martensite which would form on subsequent cooling to 20 °C is also estimated.

## 7.5 Conclusions

A theory for the calculation of $M_s$ temperature of remaining austenite, after the formation of bainite, has been presented. This was then used, with data from Bhadeshia and Edmonds [1983a], to compare the Koistinen and Marburger [1959] and Khan and Bhadeshia [1990a] models for the prediction of volume fraction of bainite formation.

The Khan and Bhadeshia model was chosen for the present work as it gave the best agreement with the experimental data.

# 8. Microstructural Characterisation of Continuously Annealed High-Strength Steels

## 8.1 Introduction

Continuously annealed steels, of the type being investigated in this work, contain a mixed microstructure of allotriomorphic ferrite, bainitic ferrite, martensite and retained austenite. The mechanical properties of such steels are believed to be influenced strongly by the distribution of the retained austenite and its behaviour during deformation.

This chapter contains the results of an investigation of the microstructure of such continuously annealed steels, using transmission electron microscopy to characterise the heat-treated state and the microstructure after cold-deformation.

## 8.2 The Effects of Microstructure on TRIP

TRIP (transformation-induced plasticity) is the enhancement of work hardening due to transformation of retained austenite to martensite during deformation (fig. 8.1) leading to an increase in uniform elongation and hence ductility [Nishiyama, 1978]. This effect was originally discovered by Zackay *et al.* [1967] in steels containing large quantities of expensive alloying elements including Cr and Ni but has since been observed in relatively inexpensive Si-Mn alloys [Takahashi and Bhadeshia, 1991].

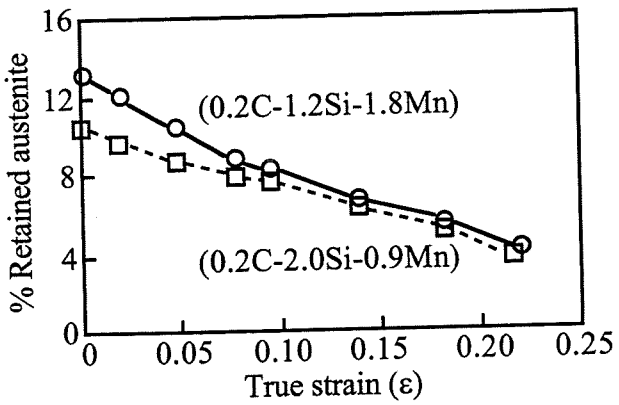


Fig. 8.1: Change in retained austenite content of two steels with progress of deformation as martensite forms [Sakuma *et al.*, 1991]. The units of concentration are wt.%.

Note that in fig. 8.1 the 1.2 wt.% Si steel contains more austenite prior to deformation than the 2.0 wt.% Si steel. However on deformation these become equal as the higher austenite contents are less stable and thus transform more easily. This will be discussed in more detail later.

Wakasa and Nakamura [1977] have shown that an effect of TRIP is to delay the onset of necking in tensile specimens. This is illustrated in fig. 8.2 where the peak in each elongation-to-necking curve is due to the TRIP effect delaying necking between $M_s$ and $M_d$†. The peak is at higher temperatures for greater austenite fractions, and consequently lower carbon concentrations, because $M_s$ and $M_d$ increase with reduction in austenite carbon content.

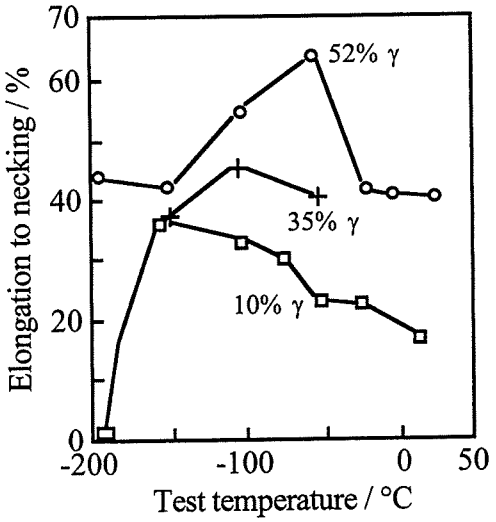


Fig. 8.2: Variation of elongation to necking with test temperature in deformed tensile specimens of a Fe-Cr-Ni alloy containing 10%, 35% and 52% retained austenite [Wakasa and Nakamura, 1977].

If micro-necking takes place during deformation the necked region is hardened more by strain-induced martensite than the rest of the specimen, so the neck no longer grows and deformation occurs in an adjacent region [Bressanelli and Moskowitz, 1966; Tamura *et al.*, 1970], causing the delay in necking described above.

[† $M_d$ is the temperature below which austenite can transform to martensite on deformation.]

### 8.2.1 Austenite

The effect of microstructure on the TRIP phenomenon is, as expected, dominated by the austenite phase, the other phases influencing the properties of the austenite [Imai *et al.*, 1992]. The austenite contribution can be split into two factors: (a) its amount and (b) its stability.

As shown by Hanzaki *et al.* [1995] an increase in the volume fraction of austenite increases the ductility of the steel (fig. 8.3). However large volume fractions of austenite do not necessarily give the optimum microstructure as the austenite stability is also a factor.

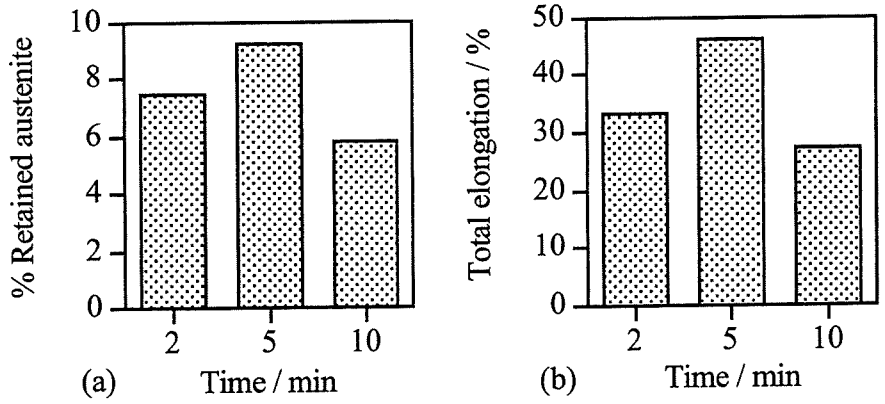


Fig. 8.3: Change in (a) % retained austenite and (b) total elongation (T-El) with time at 400 °C where bainite transformation occurs, for Fe-0.22C-1.55Si-1.55Mn-0.035Nb-0.028Al wt.% steel [Hanzaki *et al.*, 1995].

TRIP is dependent on the gradual transformation of austenite to martensite during straining. If all the austenite transforms easily then none remains to provide work hardening at higher strains. Also, very stable austenite, which does not transform on straining, obviously cannot contribute to the TRIP effect. The optimum microstructure therefore contains austenite with a range of stabilities to allow a gradual transformation to martensite.

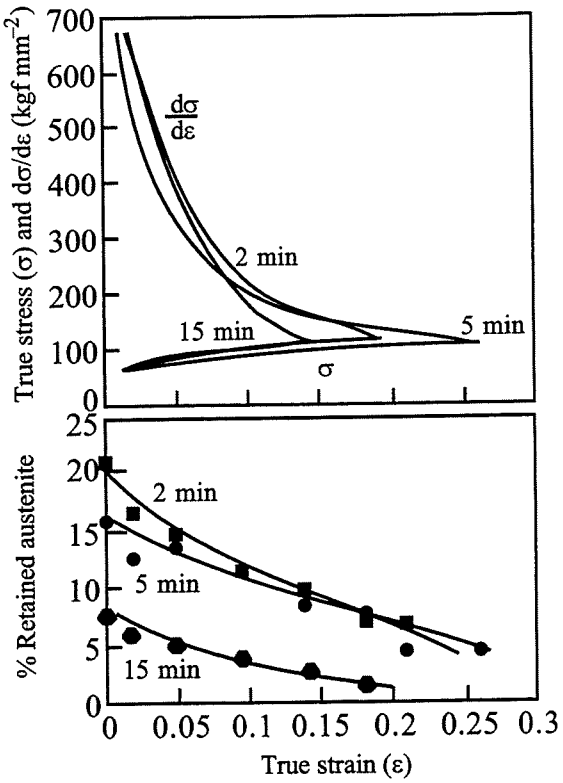


Fig. 8.4: Changes in retained austenite content and work-hardening rate with tensile strain for Fe-0.395C-1.493Si-0.835Mn wt.% steel [Matsumura *et al.*, 1987].

This is illustrated in fig 8.4 where the sample transformed to bainite for two minutes has a larger initial retained austenite content than the other samples, but this transforms to martensite much faster than the one which was allowed to transform for five minutes giving a lower fraction of more stable austenite. The austenite in the sample held for 15 minutes was as stable as that in the five minute sample (retained austenite reduction rate similar), but, as there was much less austenite to start with, the work hardening and maximum strain were lower than in the other samples.

One method for stabilising austenite is to increase its carbon content. As Tomita and Okawa [1993] have shown, if the carbon content of the austenite is reduced then the austenite is less stable (fig. 8.5). This mechanical stability was measured using X-ray diffraction to measure the volume fraction of austenite in tensile specimens. The carbon content of the austenite varied with transformation temperature because, at the lower temperatures, more bainite formed and thus higher austenite carbon contents were obtained.

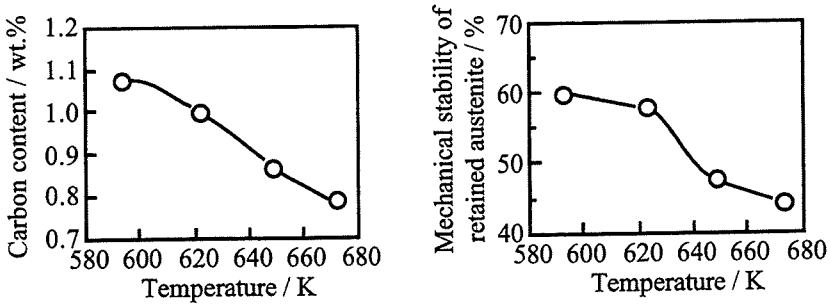


Fig. 8.5: Effect of isothermal bainite transformation temperature on carbon content and mechanical stability of retained austenite in a Fe-0.41C-1.7Si-0.8Mn-0.8Cr-0.41Mn-1.76Ni wt.% steel [Tomita and Okawa, 1993].

Another dominant effect is the size and morphology of the retained austenite. Large, blocky areas of austenite between bainite sheaves are lower in carbon content and also less constrained than smaller areas, thus they transform easily to martensite [Bhadeshia and Edmonds, 1983a; 1983b; Tomita and Okawa, 1993]. This can often occur on cooling to room temperature (before deformation) resulting in brittle untempered martensite which is detrimental to mechanical properties.

Brandt and Olson [1992] showed that, during isothermal bainite transformation, the mechanical stability of retained austenite continues to increase after the carbon content had reached a maximum. This was shown to be due to the smaller size of retained austenite pools for longer bainite transformation times. After a while a maximum is reached beyond which the further transformation to bainite reduces the TRIP effect as the reduction in the volume fraction of

austenite has more of an effect than the increase in stability (Steel A in fig. 8.6) [Sakuma *et al.*, 1991].

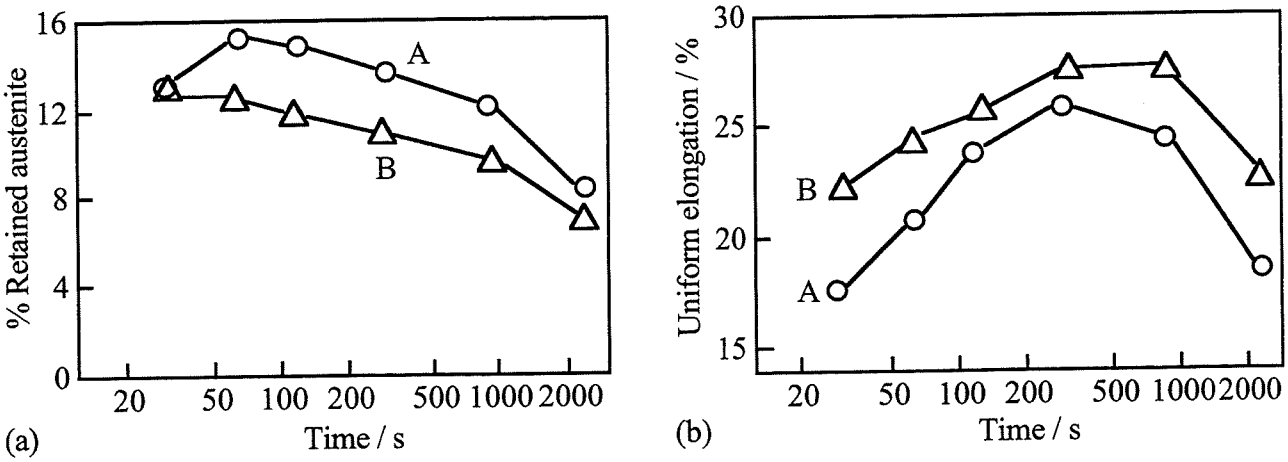


Fig. 8.6: Variation of (a) austenite and (b) uniform elongation with time at 400 °C. Steel compositions: A 0.2C-1.2Si-1.8Mn and B 0.2C-2.0Si-0.9Mn wt.% [Sakuma *et al.*, 1991].

### 8.2.2 Allotriomorphic ferrite

The presence of allotriomorphic ferrite in TRIP steels prior to the formation of bainite aids the stabilisation of the retained austenite by increasing the carbon content of the austenite and also by reducing the effective austenite grain size.

Intercritical annealing, within the austenite and ferrite two-phase field of the phase diagram, of a ferrite (and pearlite) sample, can lead to very fine austenite particles nucleating on the ferrite grain boundaries. These are beneficial as they are more stable than larger volumes of austenite [Sakuma *et al.*, 1991; 1992].

Intercritical annealing for long times can also lead to the segregation of silicon to the ferrite and manganese to the austenite [Sakuma *et al.*, 1992]. This manganese enrichment can increase the austenite stability, and its hardenability by retarding the ferrite transformation.

### 8.2.3 Bainite

The thin films of retained austenite within bainite sheaves are a good source of stable austenite. This fine film-like retained austenite has a higher yield strength and, hence, plastic deformation of the austenite is more difficult [Bhadeshia and Edmonds, 1983a]. Thus it has a higher resistance to the martensitic shear transformation. This is also aided by the fact that the thin films of austenite have a higher carbon concentration as carbon cannot redistribute from isolated areas of austenite.

As stated above there is an optimum amount of bainite for the TRIP effect. Too little and the areas of austenite are too large, too much and there is not enough austenite retained. This can be controlled by varying both bainite transformation temperature and time (fig. 8.7).

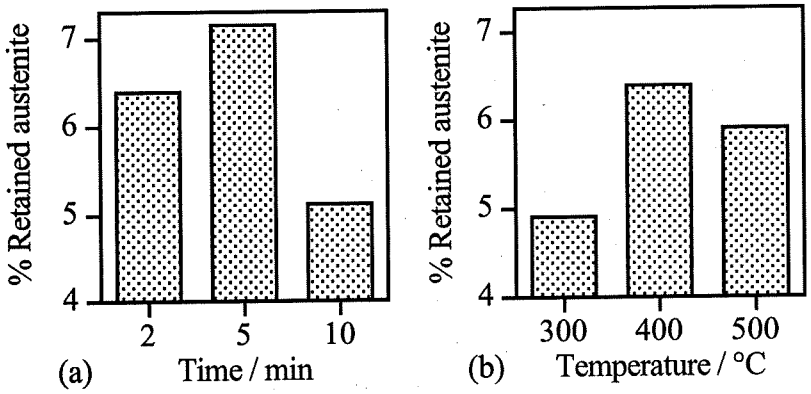


Fig. 8.7: Dependence of % retained austenite on the time and temperature of bainite transformation in a Fe-0.19C-1.5Si-1.54Mn wt.% steel [Hanzaki *et al.*, 1995]. (a) held at 400 °C and (b) held for 2 minutes.

### 8.2.4 Martensite

The presence of martensite plates formed on cooling below $M_s$ reduces the toughness and ductility of the steel whilst increasing the strength [Sakuma *et al.*, 1992].

The deformation of austenite can induce martensite to form above the $M_s$ temperature because the stress provides a mechanical driving force. There is a maximum temperature, $M_d$, below which martensite can form on deformation of a steel containing retained austenite. Above $M_d$ the energy barrier to martensite formation cannot be overcome by the strain induced mechanical driving force. The range $M_s$ to $M_d$ determines the temperatures at which the TRIP effect can be obtained and this varies with steel composition [Tamura *et al.*, 1970].

For Fe-Ni and Fe-Cr-Ni alloys Tamura *et al.* [1970] showed that the morphology of strain-induced martensite was very fine and often very different from the plate-like martensite formed during cooling below $M_s$. They also showed that this change is dependent on the alloy.

## 8.3 Experimental

1 mm thick sheet steels, of compositions as shown in table 8.1, were continuously annealed on a pilot rig at British Steel Wales. The heat treatments were typically as shown in fig. 8.8 and table 8.2. These alloys were chosen as typical carbide-free bainitic steels to allow a comparison between the compositions. Samples with an 80 mm gauge length and 20 mm width were cut from the sheets and tested in tension on a 100 kN ZWICK 1474 machine. The cross head speeds were 2.5 mm minute$^{-1}$ up to the proof stress and then 50 mm minute$^{-1}$ until fracture.

Retained austenite volume fractions obtained by X-ray diffraction measurements on one of the broken ends of each sample were supplied by British Steel Wales and compared with values for the undeformed steels.

| Steel | C wt.% | Mn wt.% | Si wt.% | S wt.% | P wt.% | N wt.% | Sol. Al wt.% |
|---|---|---|---|---|---|---|---|
| H265 | 0.171 | 1.42 | 1.73 | 0.009 | 0.012 | 0.0064 | 0.033 |
| H271 | 0.249 | 0.94 | 1.65 | 0.009 | 0.011 | 0.0064 | 0.046 |
| H273 | 0.255 | 1.94 | 1.21 | 0.009 | 0.011 | 0.0062 | 0.025 |
| H280 | 0.238 | 1.43 | 1.49 | 0.005 | 0.012 | 0.0056 | 0.022 |

Table 8.1: Steel compositions.

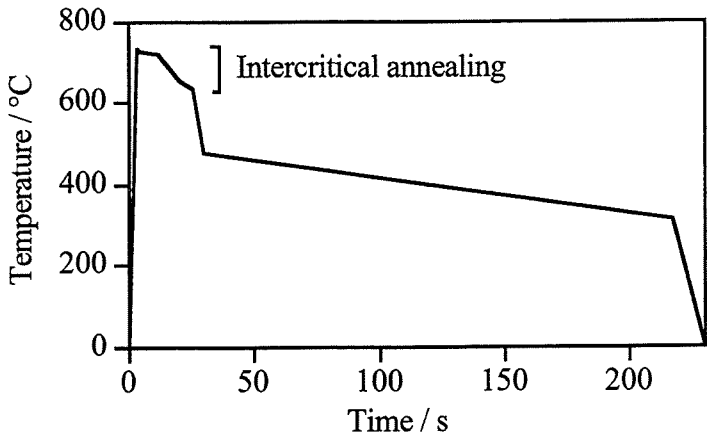


Fig. 8.8: Example of typical continuous annealing heat treatment.

| Temp. / °C | 0 | 732 | 725 | 720 | 653 | 635 | 479 | 313 |
|---|---|---|---|---|---|---|---|---|
| Time / s | 0 | 3.7 | 4.1 | 12.2 | 20.6 | 26.3 | 29.9 | 217.9 |

Table 8.2: Example of typical continuous annealing heat treatment. the time refers to the point where the temperature is reached.

Transmission electron microscopy (TEM) samples were taken from both the deformed and undeformed areas of the broken tensile testing specimens (fig. 8.9). They were prepared by electropolishing in a 5% perchloric acid, 95% acetic acid solution, as described in section 3.9, and examined in a Philips CM 12 transmission electron microscope with scanning transmission electron microscopy (STEM) facility. The STEM method was chosen to provide high resolution images of larger areas than TEM.

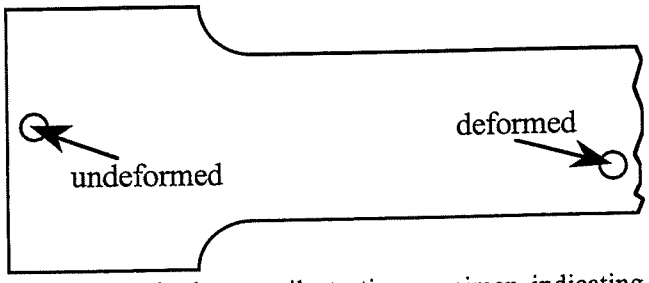


Fig. 8.9: Diagram of a broken tensile testing specimen indicating the sample positions.

## 8.4 Results and Discussion

A scanning transmission electron micrograph (fig. 8.10) of deformed steel H265 shows that during the intercritical annealing (the high temperature section of the heat treatment, see fig. 8.8) areas of austenite formed whilst other areas of allotriomorphic ferrite remained. On subsequent cooling the austenitic areas then transformed partially into a mixture of bainitic ferrite, martensite, pearlite and some of the austenite was retained.

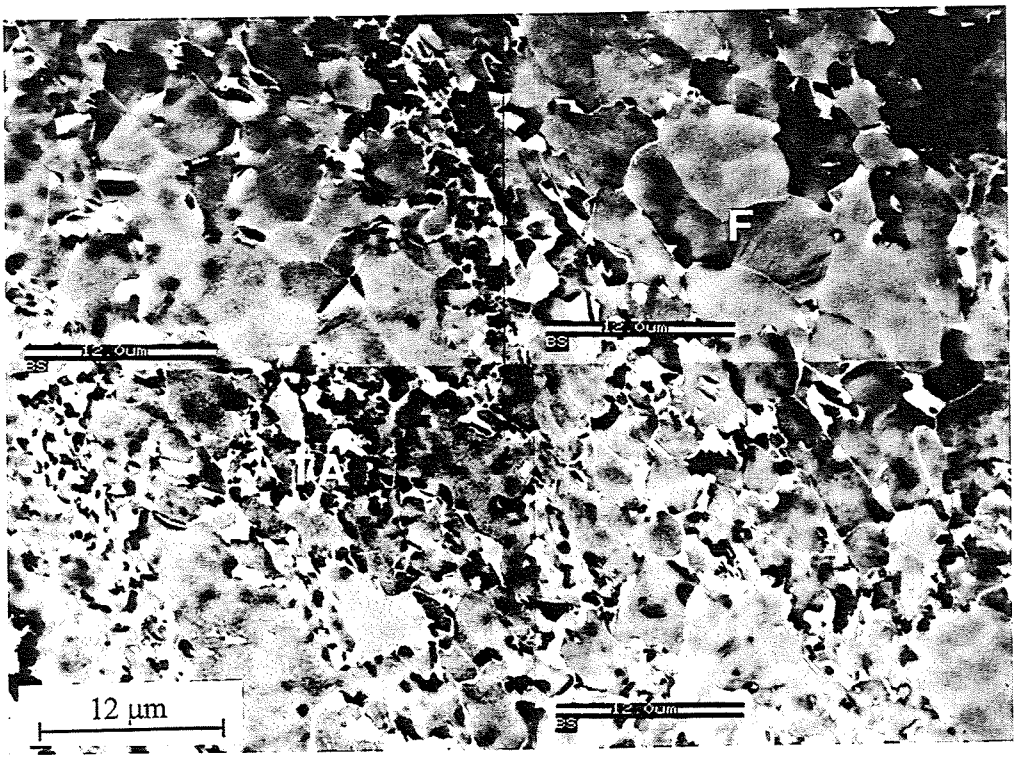


Fig. 8.10: Scanning transmission electron micrograph of deformed steel H265 (Fe-0.17C-1.4Mn-1.7Si) illustrating intercritically annealed ferrite (F) and transformation products of intercritically formed austenite (TA).

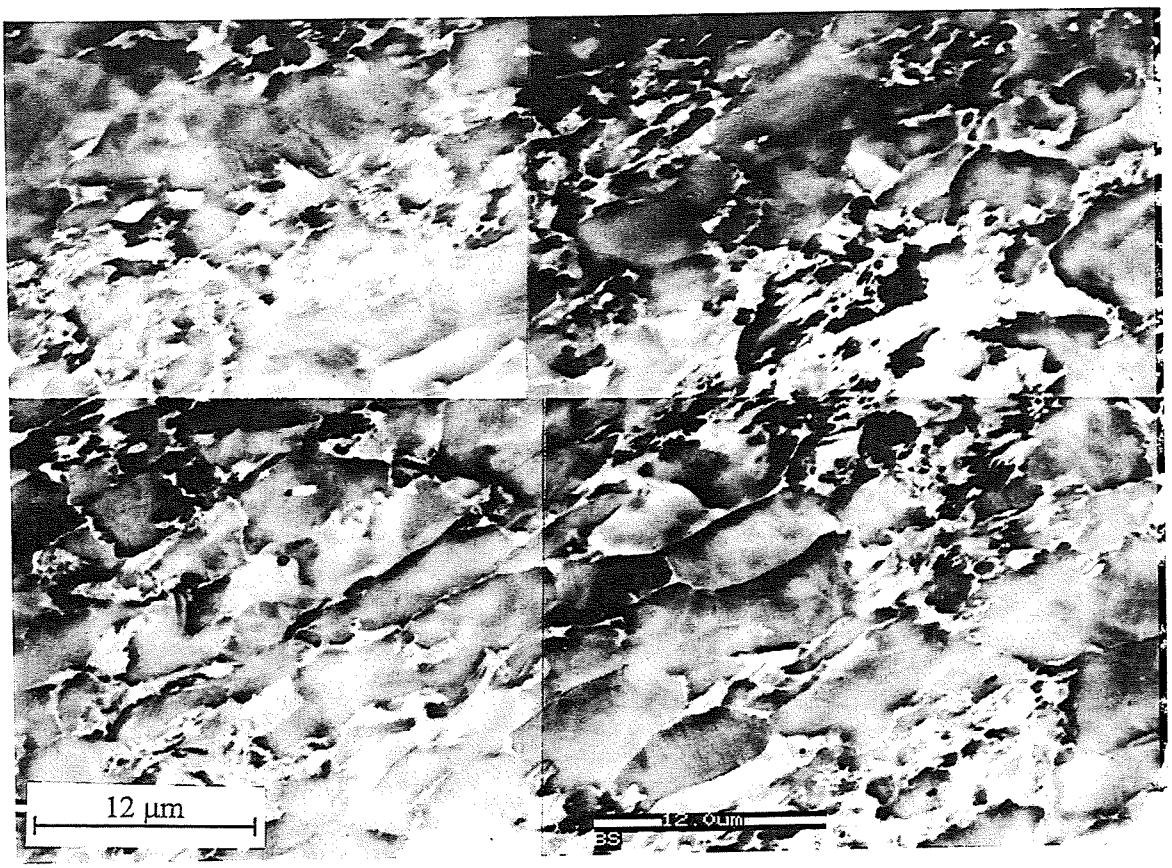


Figs. 8.11(a) (above) and 8.11(b) (below): STEM micrographs of deformed and undeformed steel H271 (Fe-0.25C-0.9Mn-1.7Si) respectively showing elongation of allotriomorphic ferrite grains in only the deformed sample.

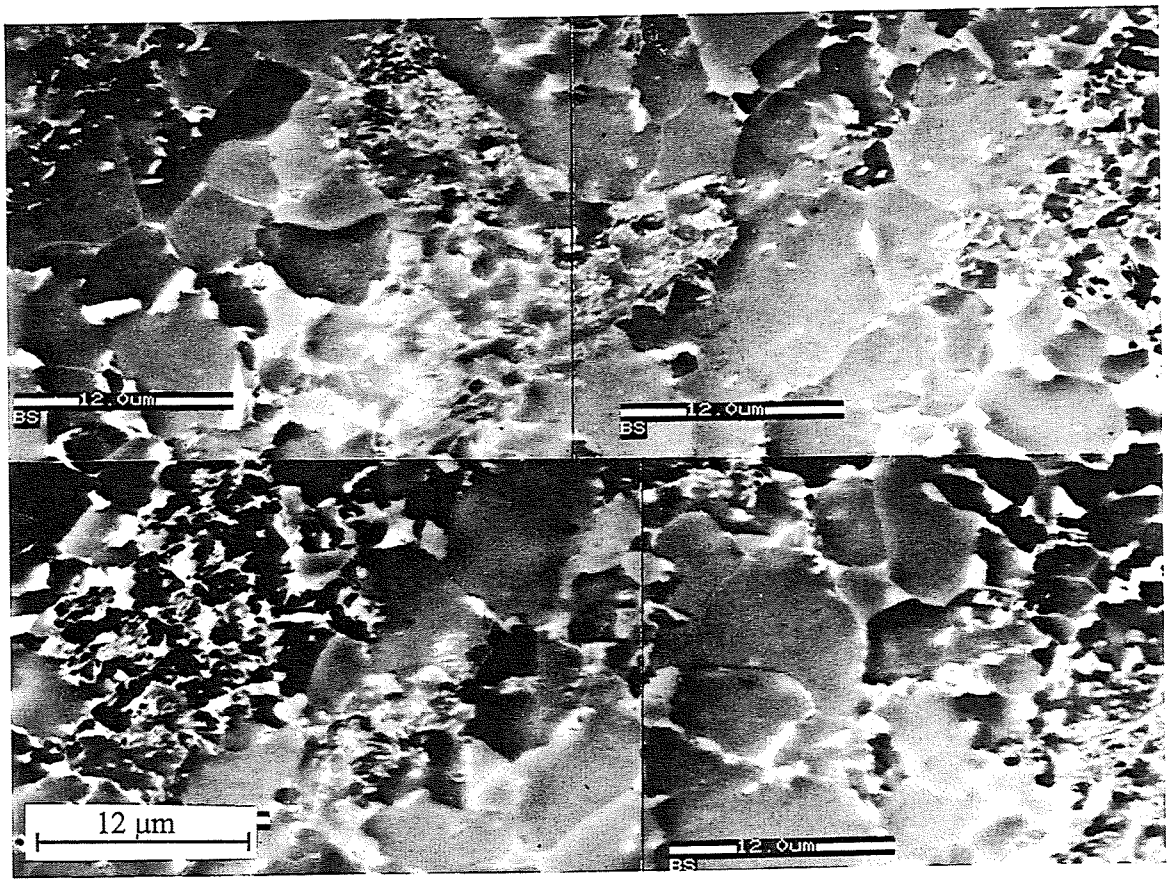

On deformation the allotriomorphic ferrite grains distorted and the direction of deformation can clearly be seen, for example in fig. 8.11a compared with fig. 8.11b. Also the dislocation density in the allotriomorphic ferrite increased with deformation (fig. 8.12).

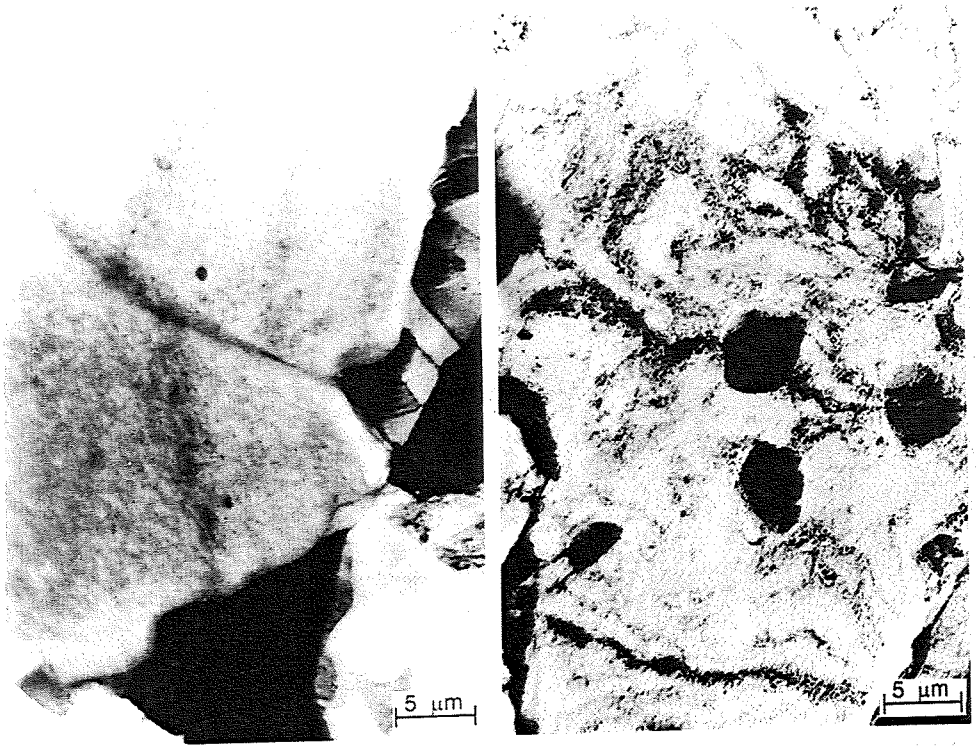


Fig. 8.12: TEM micrographs of steel H265 (Fe-0.17C-1.4Mn-1.7Si) in the undeformed (left) and deformed (right) states illustrating high dislocation density in the deformed sample.

Some areas of retained austenite were identified in undeformed samples either by diffraction pattern analysis (figs. 8.13 and 8.14) or the presence of stacking faults (fig. 8.15). Little austenite was observed in the deformed samples. This indicates that the deformation was to some extent accommodated by a TRIP effect (transformation-induced plasticity) in which energy was absorbed by the transformation of retained austenite to martensite.

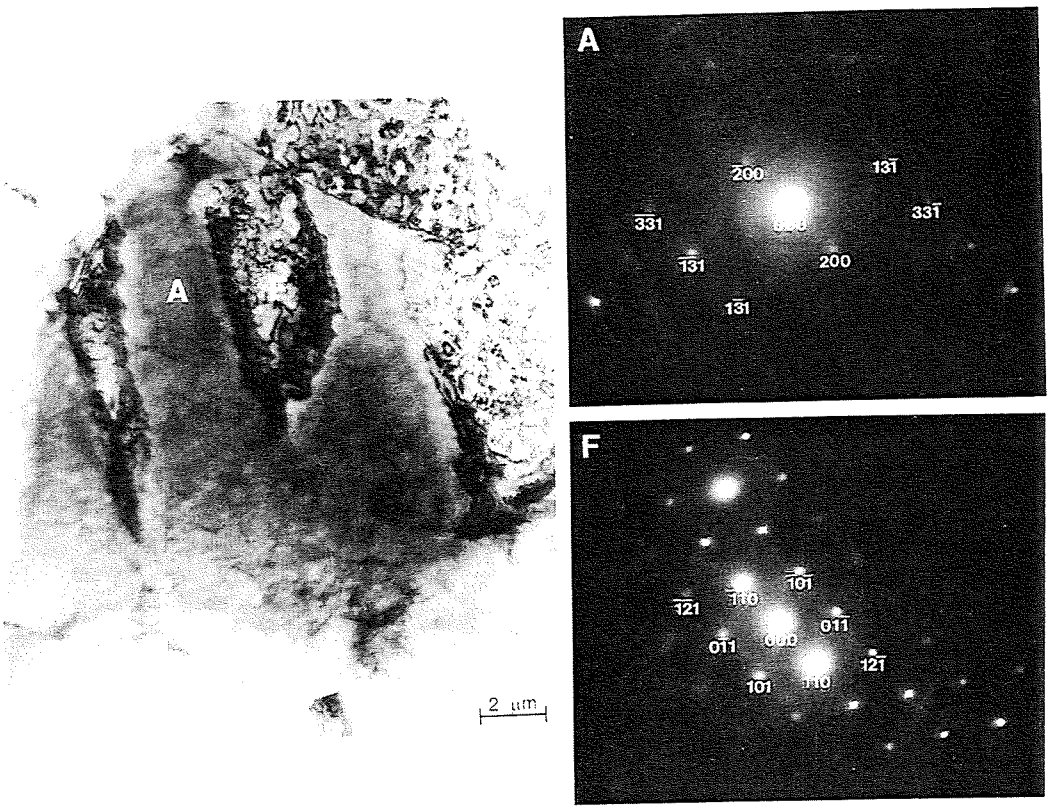


Figs. 8.13 (above) and 8.14 (below): TEM micrographs and diffraction patterns of steels H271 (Fe-0.25C-0.9Mn-1.7Si) and H265 (Fe-0.17C-1.4Mn-1.7Si) respectively showing austenite (A) and ferrite (F). Note two ferrite zones were identified in fig. 8.14 as the diffraction pattern was taken close to a ferrite/ferrite grain boundary.

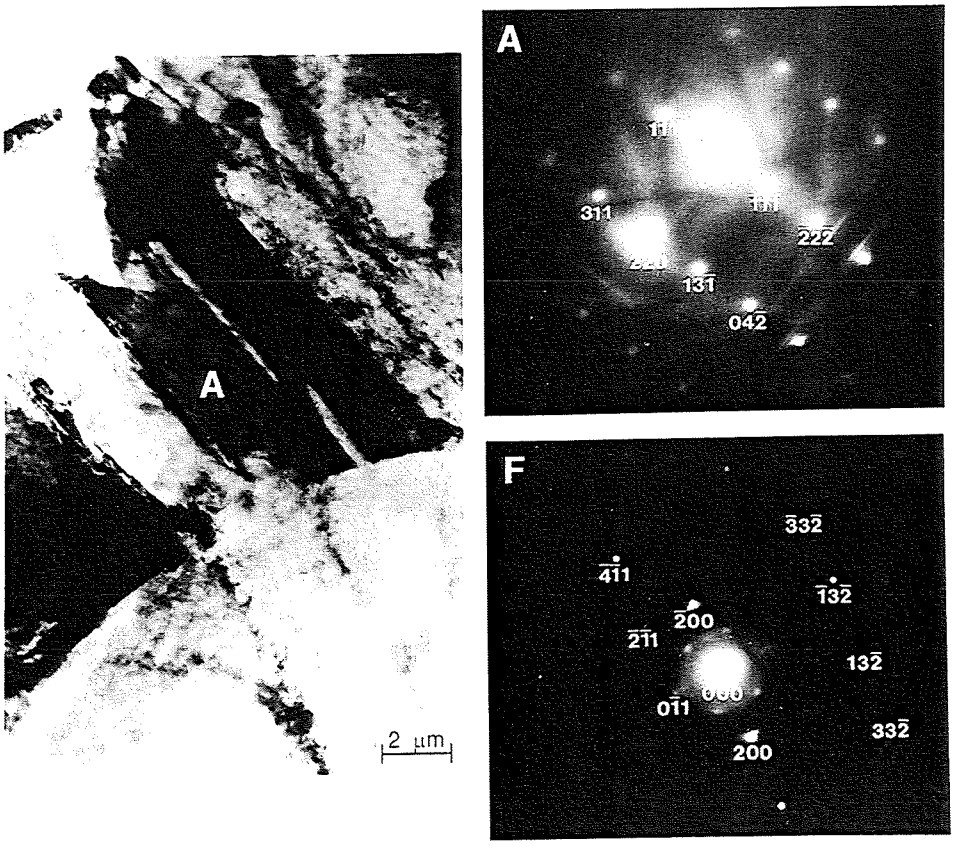

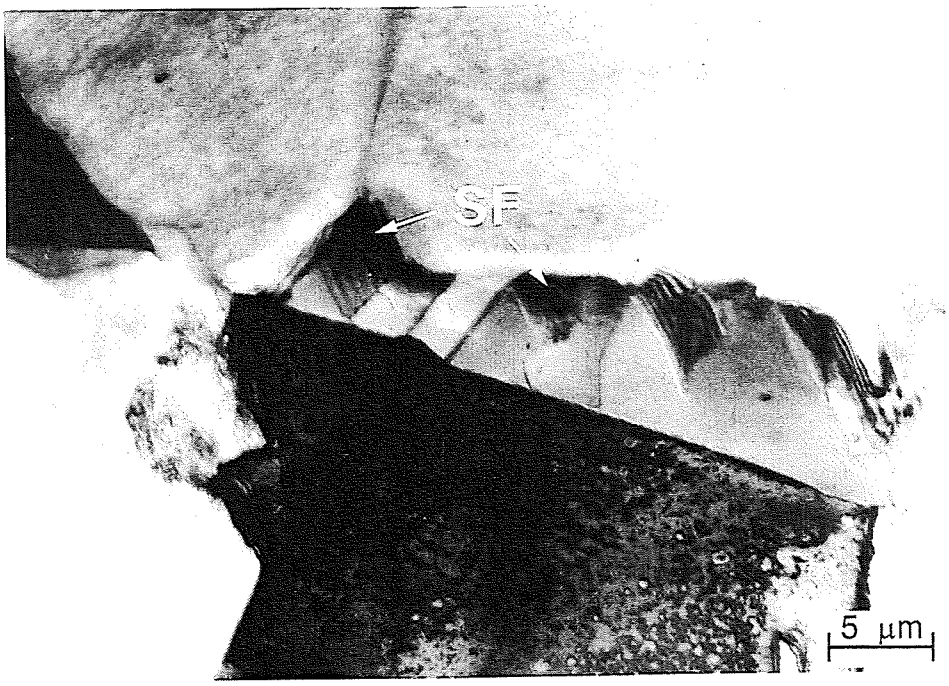


Fig. 8.15: TEM micrograph of stacking faults (SF) within austenite in undeformed steel H265 (Fe-0.17C-1.4Mn-1.7Si).

This TRIP effect is confirmed by fig. 8.16 in which the tensile strengths of these steels, obtained by British Steel Wales, are related to the change in % austenite on deformation. The tensile strength increased as the austenite transformed to martensite because the strength is related to the total martensite content [Bressanelli and Moskowitz, 1966]. No such correlation was found for elongation measurements as the elongation is related to the *rate* of the austenite to martensite transformation [Tamura *et al.*, 1969].

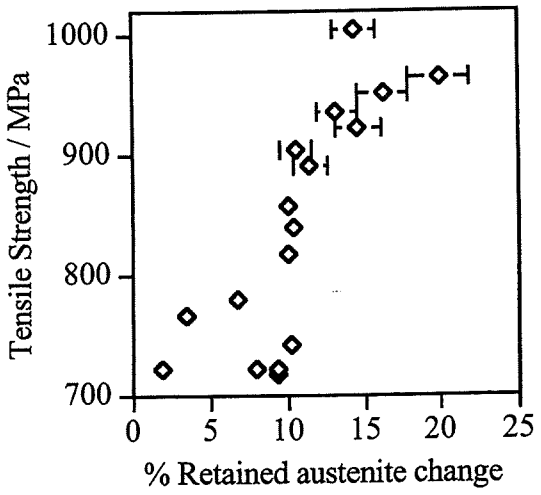


Fig. 8.16: Plot of tensile strength of continuously annealed steel samples versus % retained austenite change on deformation for all steels in table 8.1. Measurement errors were 10% of the measured austenite fractions.

As mentioned in section 8.2.1, the least stable areas of austenite are the large blocky areas, like that shown in fig. 8.13. These are more likely to transform on deformation [Bhadeshia and Edmonds, 1993a]. Films of retained austenite within bainite sheaves are more stable, due to high carbon contents and small size, and so can still be found in deformed samples (fig. 8.17).

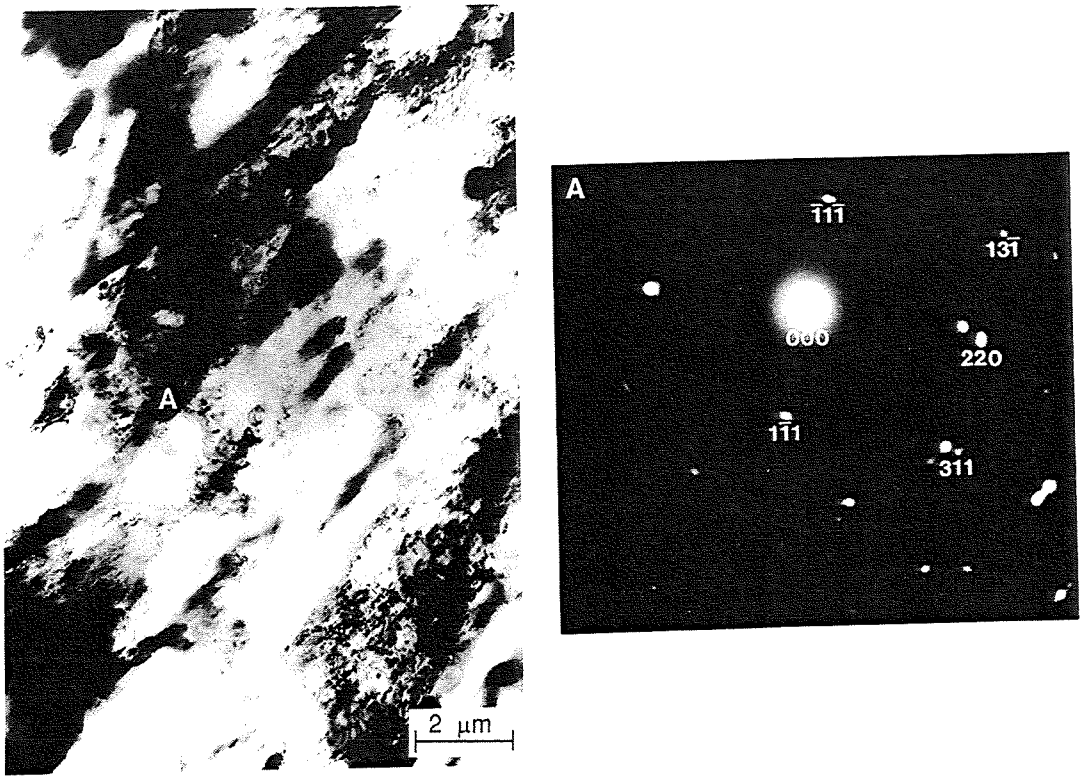


Fig. 8.17: TEM micrograph of deformed steel H271 (Fe-0.26C-1.9Mn-1.2Si) showing retained austenite films (A) within bainite and corresponding austenite diffraction pattern.

Large fractions of bainite are required to reduce the areas of blocky austenite and increase the amount of stabilised austenite. Only one area of bainite was identified in these samples (fig. 8.17). This might be statistical, due to the small number of samples observed, or because there was little bainite present. The predicted volume fractions of bainite expected, using the calculations described in Chapter 4, are shown in table 8.3 along with the predicted volume fractions of allotriomorphic ferrite formed at intercritical annealing (using calculations described in Chapter 6).

| Steel | Composition (wt.%) | Vol. fraction prior ferrite | Vol. fraction bainite |
|---|---|---|---|
| H265 | 0.17C-1.4Mn-1.7Si | 0.63 ± 0.03 | 0.09 ± 0.04 |
| H271 | 0.25C-0.9Mn-1.7Si | 0.59 ± 0.03 | 0.15 ± 0.07 |
| H273 | 0.26C-1.9Mn-1.2Si | 0.42 ± 0.03 | 0.12 ± 0.03 |
| H280 | 0.24C-1.4Mn-1.5Si | 0.55 ± 0.03 | 0.08 ± 0.04 |

Table 8.3: Predicted volume fractions of prior allotriomorphic ferrite and bainite for the steels in table 8.1 (austenite grain size assumed to be 16 μm).

It can be seen from table 8.3 that the lower carbon steels (H265 and H280) contain less than 10% bainite, hence the difficulty in observing this phase. The observed bainite in fig. 8.17 is in steel H271 which is predicted to contain the largest volume fraction of bainite.

This bainite fraction is further altered in the presence of pearlite as carbon is trapped in the cementite layers of this phase. Areas of pearlite were identified in both undeformed and deformed samples (figs. 8.18 and 8.19). These would have formed during the heat treatment before cooling to the bainite transformation temperature. The presence of pearlite is undesirable in the mixed microstructure due to the detrimental effects on mechanical properties [Burns and Pickering, 1964]. This pearlite could be avoided by cooling more rapidly to the bainite transformation temperature or by alloying (increasing silicon content can delay the austenite to pearlite transformation [Tsukatani *et al.*, 1991]).

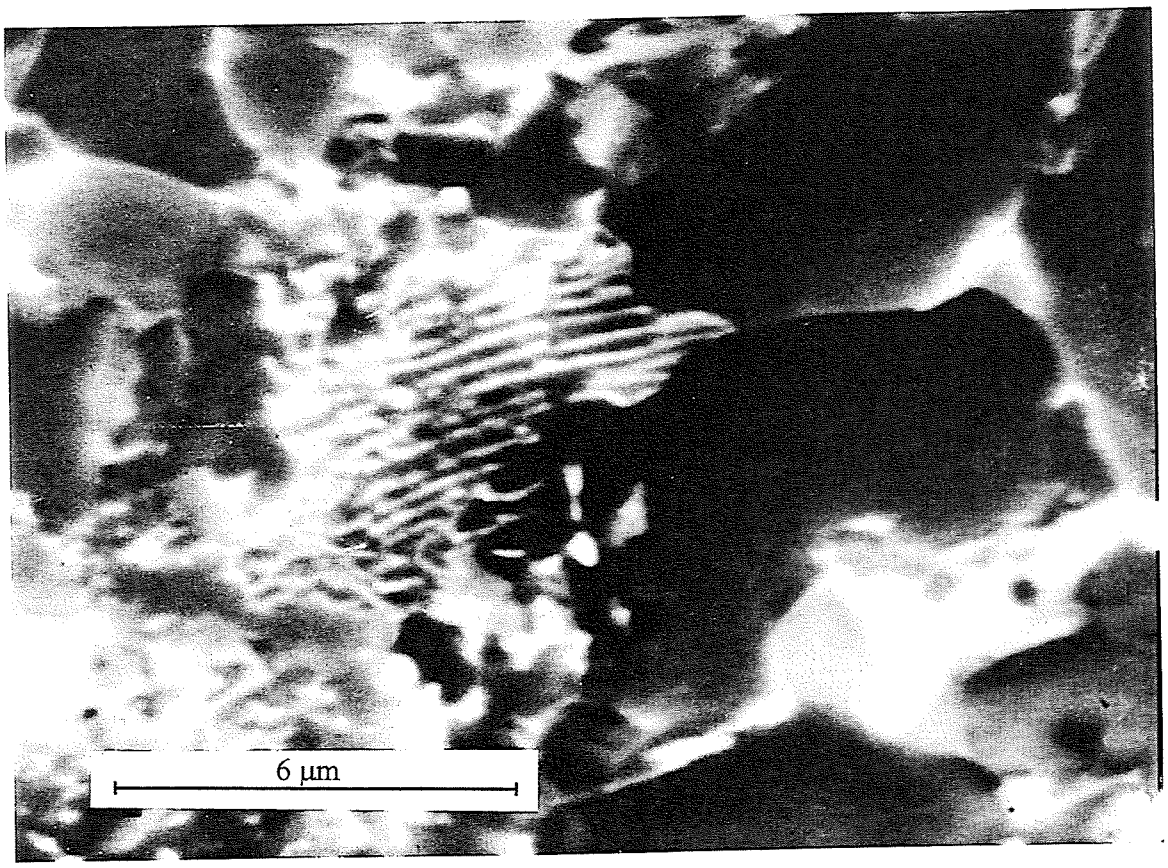


Figs. 8.18 (above) and 8.19 (below): Micrographs of pearlite in steel H271 (Fe-0.25C-0.9Mn-1.7Si). STEM of undeformed and TEM of deformed respectively, showing cementite diffraction pattern of point C and dark field image using $04\bar{2}$ spot.

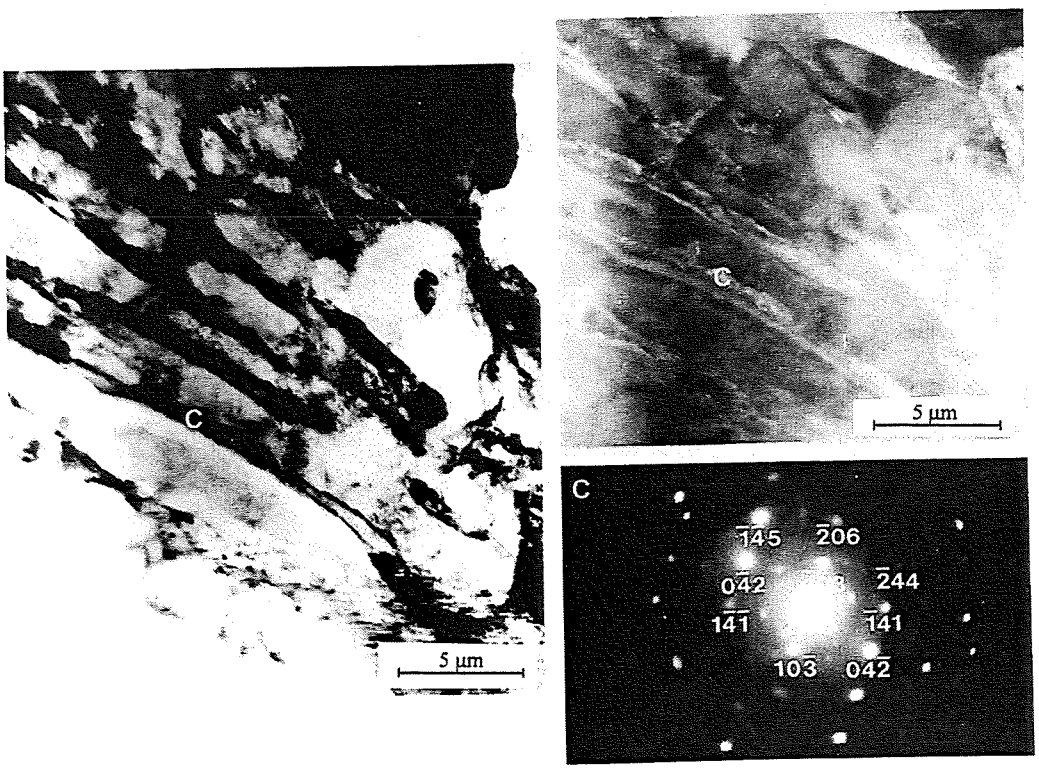


Figs. 8.20 (above) and 8.21 (below): TEM micrographs and diffraction patterns of steels H271 (Fe-0.26C-1.9Mn-1.2Si) and H280 (Fe-0.24C-1.4Mn-1.5Si) respectively showing martensite plates formed during the heat treatment including diffraction patterns of the twins (T) within plates M1 and M2.

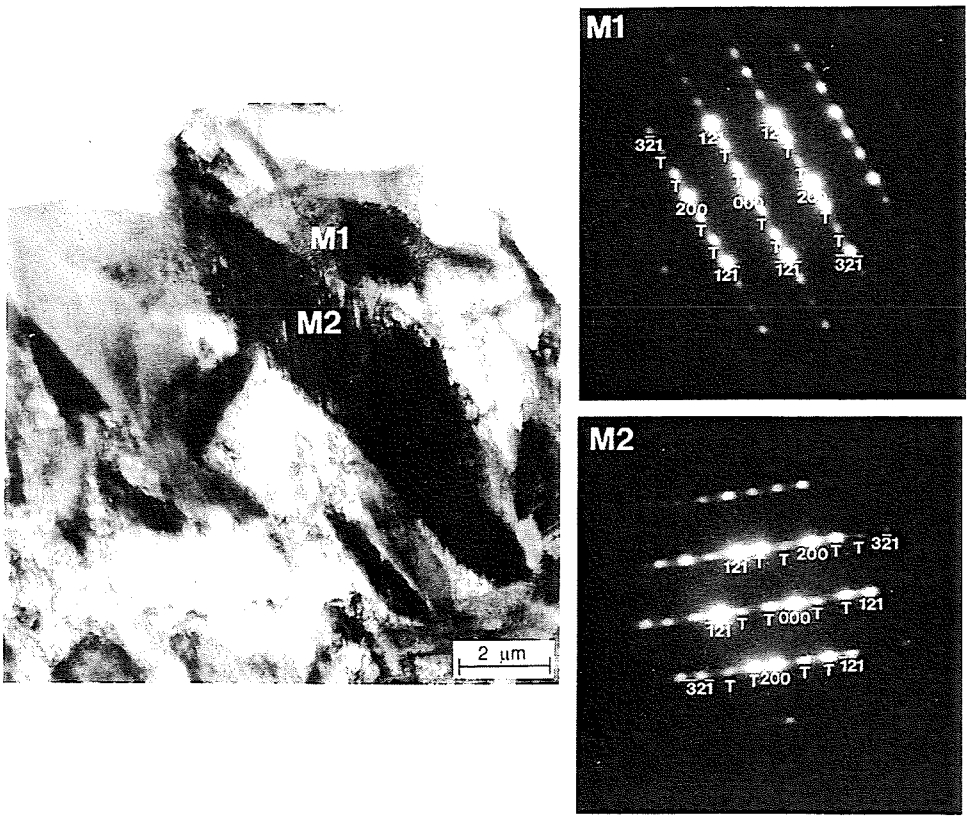

Plates of martensite which formed during the heat treatment (i.e. not due to deformation) were observed in the undeformed samples (figs. 8.20 and 8.21). Twinning in the martensite plates is observable in fig. 8.21 and the diffraction spots due to this were identified. This indicates that the austenite, from which the martensite formed, had a high carbon content as lower carbon martensite plates are not fully twinned [Porter and Easterling, 1981]. The presence of this martensite reduces the toughness and ductility of the steel whilst increasing the strength [Sakuma *et al.*, 1992].

Non-parallel variants of martensite plates can grow co-operatively with neighbouring plates. This leads to the zig-zag morphology observed in fig. 8.20 which is commonly observed to accompany burst formation in lenticular martensite [McDougall and Wayman, 1992].

There was no identification of strain-induced martensite in the deformed samples, but this might be due to the fine size and irregular shape of such a phase allowing it to be obscured by the deformed pearlite and bainite.

## 8.5 Conclusions

Characteristics of the mixed microstructure have been observed including blocky austenite in undeformed samples, the presence of plate martensite formed from high-carbon unstable austenite during the final cooling and an increase in dislocation density in allotriomorphic ferrite due to deformation.

A correlation between the amount of austenite transformed during deformation and the tensile strength was observed for these steels. These data, along with data for other steels and for other mechanical properties, have been analysed with the use of neural networks and are presented in Chapter 9.

# 9. Neural Network Analysis of Retained Austenite and Mechanical Properties

## 9.1 Introduction

The mechanical properties of bainitic TRIP steels depend on the microstructure, especially the volume fraction and distribution of high carbon retained austenite. This relationship has been investigated with a quantitative analysis of experimental data using a neural network within a Bayesian framework.

An analysis like this requires an identification of the important variables controlling the mechanical properties. These are discussed first in order to set the scene for the neural network analysis.

## 9.2 Factors Controlling Mechanical Properties

### 9.2.1 Intercritical annealing temperature

Intercritical annealing is the heat treatment of a steel between the $Ac_1$ and $Ac_3$ temperatures, thus producing a mixture of allotriomorphic ferrite and austenite. It is this process which determines which phases are present before bainite formation and thus the properties of the ultimate mixed microstructure.

Matsumura *et al.* [1987] showed that for a Fe-0.4C-1.5Si-0.8Mn wt.% steel an increase in the intercritical annealing temperature from below $Ac_1$ to above $Ac_3$ showed an increase in the both the ultimate tensile strength (UTS) and yield strength (YS). The elongation also increased as the temperature reached $Ac_1$, but then declined with further elevation of temperature. It appears that the best formability (represented by the multiplication of tensile strength and elongation) could be obtained at an intercritical annealing temperature just above $Ac_1$ (fig. 9.1).

These observations were for the microstructure obtained from a 5 min hold at the intercritical annealing temperature followed by a quench to a 5 min hold at 400 °C. Below $Ac_1$ a pearlite/ferrite mixture was obtained, thus explaining the poor strength and ductility. Just above $Ac_1$ a microstructure of ferrite, bainite and austenite was obtained. Increasing the temperature further increased the bainite content but reduced both the ferrite and austenite contents (reduction in ferrite leading to less carbon in austenite, thus more bainite forms and less austenite is retained). The strength increases with the reduction of ferrite content and the

ductility decreases with reduction of austenite content and, as the proportional change in ductility is greater the formability is also reduced.

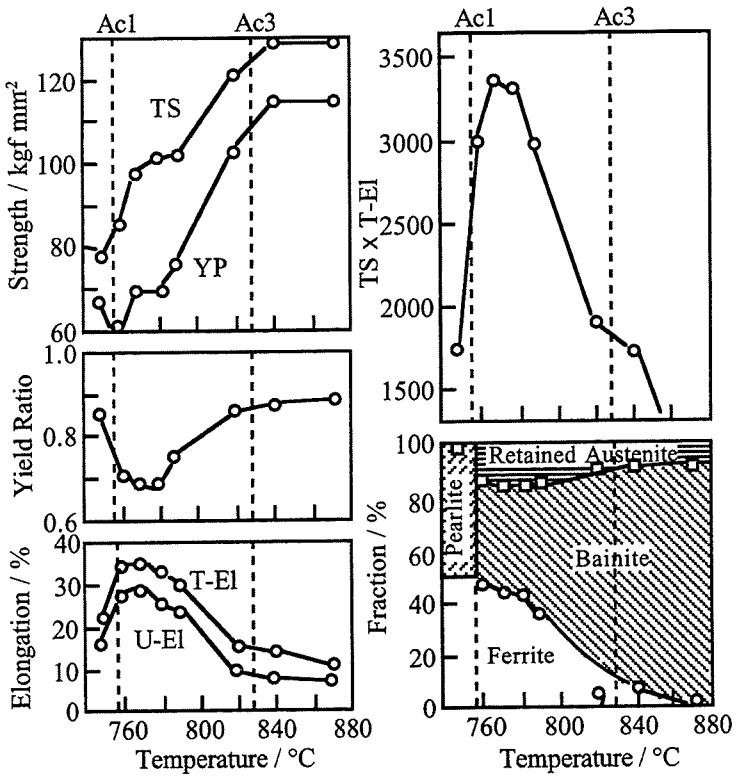


Fig. 9.1: Changes in mechanical properties, yield point (YP), tensile strength (TS), yield ratio (YP/TS), total (T-El) and uniform elongation (U-El), formability (TSxT-El), and microstructure with intercritical annealing temperature for 0.4C-1.5Si-0.8Mn wt.% steel [Matsumura *et al.*, 1987].

It should be noted that at high temperatures silicon can partition into the ferrite [Matsumura *et al.*, 1987], thus reducing its ability to stabilise the austenite and hence decreasing the ductility.

### 9.2.2 Intercritical annealing time

A short intercritical annealing leads to very little austenite and consequently a low ductility for the final microstructure. Time is also required to dissolve any carbides present in the original microstructure. However, excessive annealing at high temperatures leads to a deterioration in ductility [Matsumura *et al.*, 1987], possibly due to the long-range partitioning of manganese and silicon between the phases [Sakuma *et al.*, 1992], because manganese enriched austenite is highly stable and does not contribute to the TRIP effect. Thus an intermediate intercritical annealing time, at the temperature chosen, is required for optimum properties. For example 5 minutes at 770 °C prior to bainite transformation at 400 °C for 5 minutes [Matsumura *et al.*, 1987].

### 9.2.3 Cooling rate from intercritical annealing

The introduction of a slow cooling step from high intercritical annealing temperatures (for example from 820 °C to 700 °C at a rate of 4 °C $s^{-1}$), before quenching to bainite transformation temperatures, has been shown to lead to a marked improvement in austenite stability and to promote the TRIP effect [Matsumura *et al.*, 1987].

A slow cool, to a temperature just above that for pearlite formation allows a greater quantity of ferrite to form. This increases the austenite carbon content making it more stable and allowing more to be retained to ambient temperature. Another factor is that in a slowly cooled sample the ferrite has an opportunity to obtain equilibrium and has a low carbon concentration, which promotes its ductility. However ferrite formed during rapid cooling retains excess carbon, which may precipitate as fine carbides leading to poor formability at low temperatures.

Rapid cooling (> 50 °C $s^{-1}$) after a slow cooling period is required to avoid pearlite formation, which would reduce the quantity of austenite and its carbon content [Matsumura *et al.*, 1987].

### 9.2.4 Bainite transformation time

The variation of properties with isothermal bainite transformation time can be complicated by the composition of the steel. For example for a Fe-0.22C-1.55Si-1.55Mn-0.035Nb wt.% steel [Hanzaki *et al.*, 1995] the UTS is found to increase with transformation time but for a similar alloy without niobium (Fe-0.2C-1.2Si-1.55Mn wt.%) there was little dependence of the UTS upon time [Sakuma *et al.*, 1991]. Reduction in $M_S$ and solid solution strengthening by niobium stabilises the austenite. Thus longer transformation times are required to form bainite and hence the UTS increases with time.

For a 0.14C-1.21Si-1.57Mn wt.% steel, held at 400 °C, Sakuma *et al.* [1992] showed that in samples transformed for short periods (1 min in fig. 9.2), continuous yielding and low YS to UTS ratios were observed. This is consistent with the deformation behaviour of dual-phase steels which contain martensite and confirms that little bainite formed during the short transformation time.

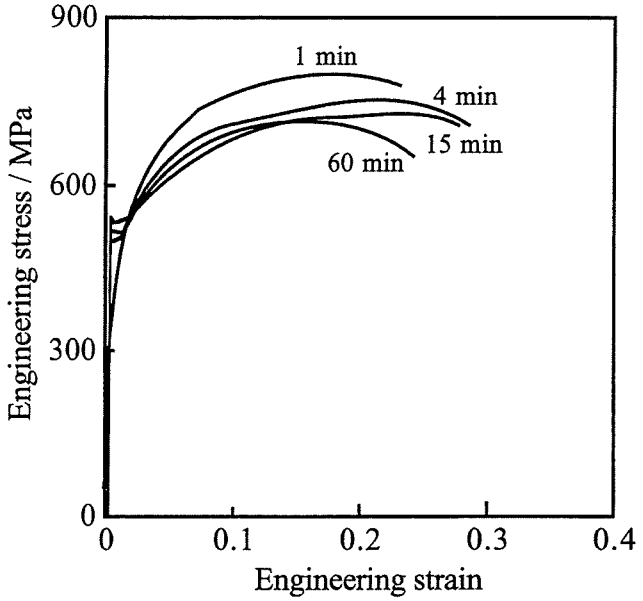


Fig. 9.2: Engineering stress-strain curves for 0.14C-1.21Si-1.57Mn wt.% steel transformed at 400 °C for the times indicated [Sakuma *et al.*, 1992a].

With increasing transformation time there was a transition to discontinuous yielding (fig. 9.2) and the yield strength increased. Also, with an increase in transformation time, the UTS initially decreased, but then remained almost constant at the onset of yield point elongation. Uniform elongation reached a maximum when the transformation time was between 4 and 15 minutes (fig. 9.3).

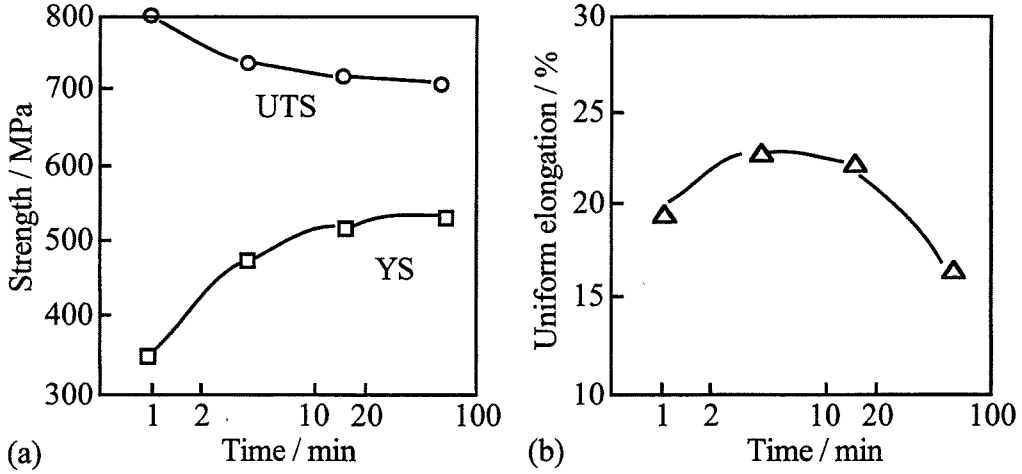


Fig. 9.3: Changes in (a) strength and (b) uniform elongation as a function of bainite transformation time at 400 °C for 0.14C-1.21Si-1.57Mn wt.% steel [Sakuma *et al.*, 1992].

These observations can be explained by the bainite transformation becoming sluggish at or below 400 °C. Thus after one minute very little bainite had formed and, during quenching, much of the austenite transformed to martensite. Longer transformation times allowed more

bainite to form and thus less martensite, reaching an optimum microstructure between 4 and 15 minutes.

### 9.2.5 Bainite transformation temperature

It is widely accepted that the strength of bainite decreases as the transformation temperature is raised and there are many results in the literature which are consistent with this general observation [Sakuma *et al.*, 1991, 1992; Hanzaki *et al.*, 1995; Miihkinen and Edmonds, 1987b and Tomita and Okawa, 1993]. But Sakuma *et al.* [1991] also observed that steels with a large manganese concentration show an increase in UTS as the temperature is raised above about 400 °C (fig. 9.4). This is due to the much increased retained austenite content. The strength increment caused by strain-induced transformation of this austenite to martensite compensates for the strength decrease when the bainite grows at the higher temperatures.

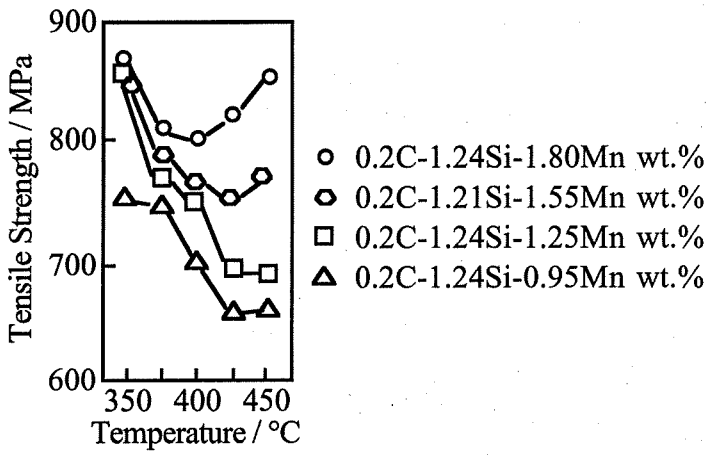


Fig. 9.4: Effect of bainite transformation temperature on tensile strength with change in manganese content [Sakuma *et al.*, 1991].

The effect of bainite transformation temperature on ductility depends on the variation in retained austenite volume fraction and stability. In the studies by Hanzaki *et al.* [1995] and Sakuma *et al.* [1992] the volume fraction of austenite goes through a maximum at 400 °C for both the Si-Mn and Si-Mn-Nb steels. The formability indices (multiplication of tensile strength and elongation) also show this maximum.

The volume fraction of retained austenite depends on two factors: isothermal transformation of austenite to bainite as a function of time at a given temperature and subsequent athermal transformation of austenite to martensite on cooling to room temperature. Transformation at higher temperatures lead to faster bainite formation and so less austenite is retained. Lower temperatures lead to sluggish bainite transformation and so a lesser stabilisation of the remaining austenite, a greater fraction of which then transforms to martensite. Thus the maximum retained austenite is obtained at an intermediate temperature when the optimum volume fraction of bainite is formed.

### 9.2.6 Silicon

Silicon is well known to inhibit cementite formation during the tempering of martensite in steels [Owen, 1954]. This is generally explained by the relative insolubility of silicon in cementite requiring it to partition at the transformation front. The resulting accumulation of silicon inhibits the further development of cementite.

An increase in the silicon concentration from 1.0 wt.% to 1.5 wt.% results in a change of microstructure from bainite and pearlite to bainitic ferrite and retained austenite [Tsukatani *et al.*, 1991] as the inhibition of cementite formation delays the austenite to pearlite transformation, as illustrated on the *CCT* (continuous cooling transformation) diagrams shown in fig. 9.5.

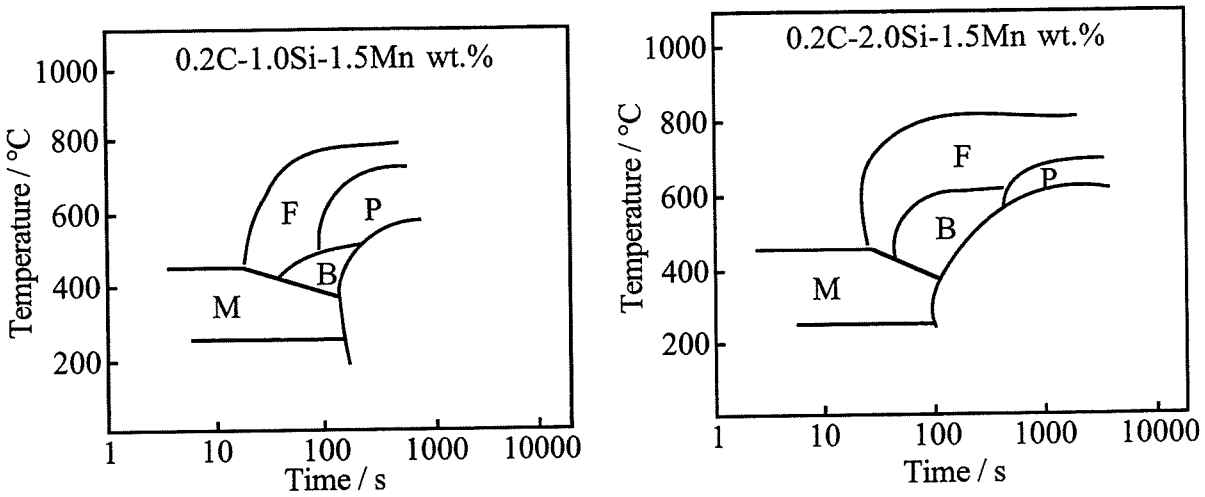


Fig. 9.5: Change in *CCT* diagram as a function of silicon content [Tsukatani *et al.*, 1991]. F = allotriomorphic ferrite, P = pearlite, B = bainite and M = martensite.

A larger silicon concentration of 2.0 wt.% results in greater volume fractions of austenite being retained, giving an increase in ductility [Sakuma *et al.*, 1991; Tsukatani *et al.*, 1991]. The ultimate tensile strength also increases with increasing silicon content, possibly due to solid-solution strengthening [Edmonds and Cochrane, 1990]. Thus an increase in silicon from 1.0 to 2.0 wt.% leads to an improvement in the formability index (tensile strength multiplied by elongation) [Sakuma *et al.*, 1991; Tsukatani *et al.*, 1991].

The yield strength, on the other hand, decreases with increasing silicon concentration [Tsukatani *et al.*, 1991]. This may arise from the presence of mobile dislocations and residual stress introduced during the austenite to martensite transformation.

### 9.2.7 Manganese

Manganese improves the hardenability of steel by increasing the stability of the austenite relative to ferrite. This leads to a shifting the austenite to ferrite reaction on the *CCT* curve to longer times (fig. 9.6). Thus an increase in manganese content makes it possible to avoid high temperature transformations and hence to obtain martensite at low cooling rates. An optimum concentration of 1.5 wt.% Mn is often chosen for 2 wt.% Si steels as experience shows that the bainite transformation range can be reached without transformation at higher temperatures at practical cooling rates.

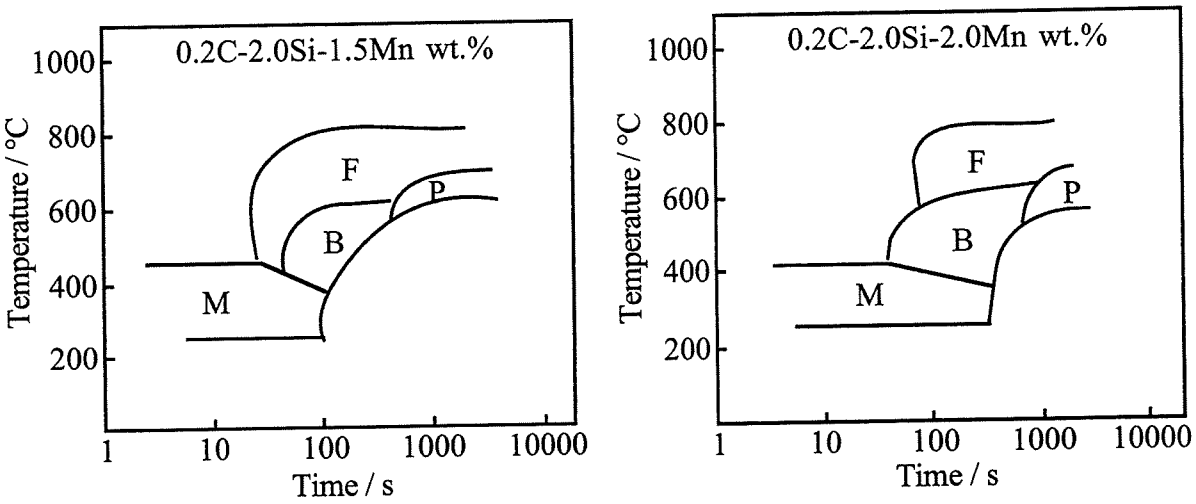


Fig. 9.6: Change in *CCT* diagram as a function of manganese content [Tsukatani *et al.*, 1991]. F = allotriomorphic ferrite, P = pearlite, B = bainite and M = martensite.

As with silicon, the ultimate tensile strength increases with manganese due to solid-solution strengthening [Edmonds and Cochrane, 1990] and the yield strength decreases with additions of manganese (fig. 9.7) [Tsukatani *et al.*, 1991].

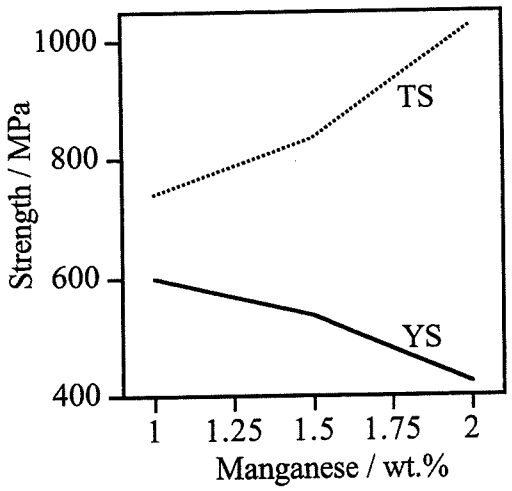


Fig. 9.7: Changes in tensile strength (TS) and yield strength (YS) as a function of manganese content in a 0.2 wt.% carbon, 2.0 wt.% silicon steel held at 400 °C for 30 minutes and then furnace cooled [Tsukatani *et al.*, 1991].

In a steel of 0.2 wt.% C and 2.0 wt.% Si concentration the volume fraction of retained austenite increases significantly as the manganese content increases from 1 wt.% to 1.5 wt.%, but decreases, or stays constant, with further additions to 2.0 wt.% Mn (fig. 9.8) [Sakuma *et al.*, 1991; Tsukatani *et al.*, 1991].

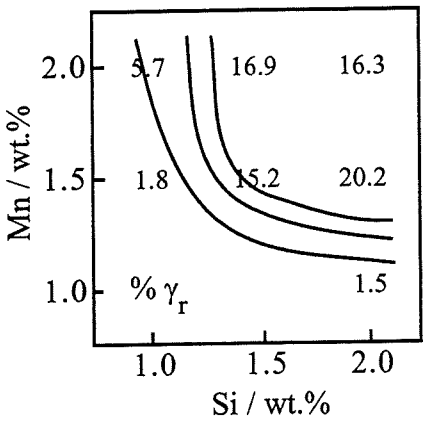


Fig. 9.8: Change in % retained austenite as a function of Si and Mn content in 0.2 wt.% C steels held at 400 °C for 30 minutes and furnace cooled [Tsukatani *et al.*, 1991]. Solid lines correspond to equal retained austenite contents of 5, 10 and 15 %.

The microstructural changes due to increasing manganese content above 1.5 wt.% are expected to result in differences in strain-induced transformation behaviour and work-hardening rate. The martensite fractions increase with manganese content, due to increased hardenability as mentioned above. The presence of this martensite is thought to diminish the TRIP effect so that most of the retained austenite can easily transform to martensite at an early stage of straining because the external stress directly propagates to the austenite through the hard martensite phase. A lower manganese steel also contains more ferrite, which has a superior ductility to martensite.

## 9.3 The Data

The data were compiled from experiments done at British Steel Wales using a laboratory continuous-annealing simulator with four hot boxes, using transverse-flux induction heating, to give a typical heat treatment as shown in fig. 9.9.

Thermocouples were placed along the 1 mm thick sheet steel specimens (compositions within the range shown in table 9.1) and the temperature continuously measured throughout the heat treatment. This thermal cycle was simplified to seven temperature regimes (A - G as shown in fig. 9.9) and six time intervals.

A significant number of the data sets were collected with only 6 temperature regimes as one less heating box was used in the earlier experiments. To be able to use this data the temperature E was set to the same as D and the time between steps D and E was set to zero.

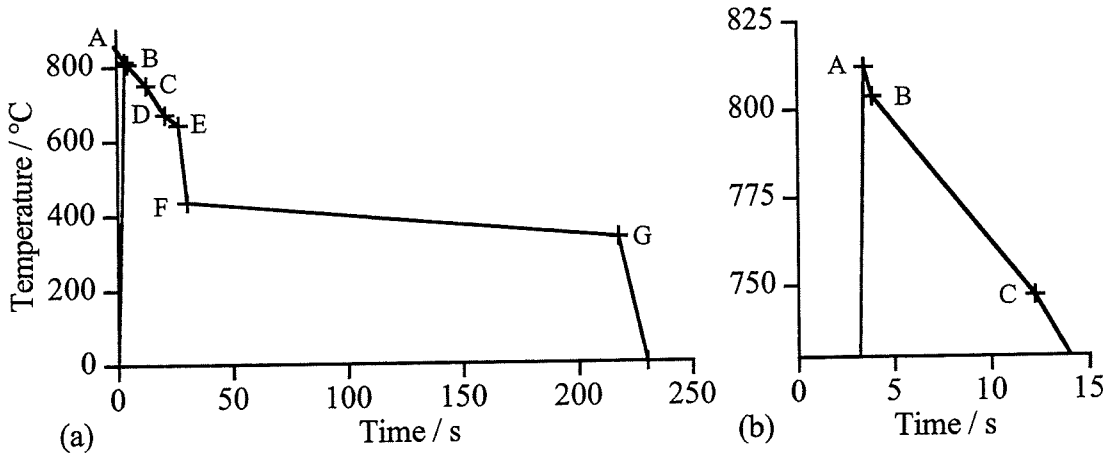


Fig. 9.9(a): Annealing thermal cycle and (b) enlargement of top section.

These data were further simplified by taking the weighted average of the top three temperatures and assuming this temperature was held for the total time, $t_{tot}$, between A and C. The average top temperature ($T_{av}$) was calculated using equation 9.1:

$$\frac{1}{T_{av}} = -\frac{R}{Q_d}\ln\left\{\frac{\sum_i t_i \exp(Q_d/RT_i)}{t_{tot}}\right\} \qquad (9.1)$$

where $Q_d$ is the self diffusion activation energy of iron (260 kJ mol$^{-1}$ [Samsonov, 1968]), $R$ is the gas constant (8.314 J K$^{-1}$ mol$^{-1}$), $T_i$ is the average of the temperatures $A$ and $B$ or $B$ and $C$ (for the 2 values of $i$) and $t_i$ is the time between these temperatures.

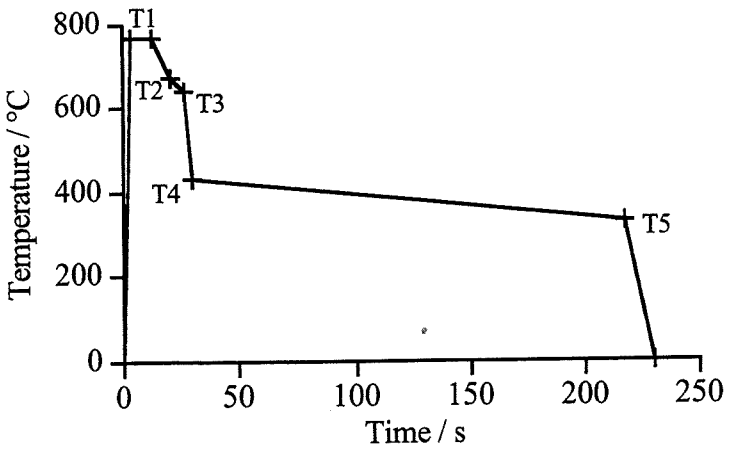


Fig. 9.10: Simplified annealing cycle.

This gave a simplified annealing heat profile as shown in fig. 9.10.

Samples were taken adjacent to the thermocouples for mechanical testing. The volume fraction of retained austenite was measured at British Steel using X-ray diffraction to an accuracy of ±10% of the value obtained.

Ninety-six sets of data (see Appendix 3) were used in the analysis. The dataset was randomly separated into two parts, one of which was used for training the model and the other half for testing. This procedure is needed because a model that fits the training data very well might be over-complicated and specific to those data. Thus testing the model using previously unseen data indicates whether it generalises well. The range of variables used is shown in table 9.1. Predictions outside this range can be attempted, but are likely to have large calculated error bars.

| Variable | Range | Mean | Standard deviation | Test set 1 | Test set 2 |
|---|---|---|---|---|---|
| T1 / °C | 695-815 | 761 | 32.0 | 766.4 | 764.6 |
| T2 / °C | 593-710 | 672 | 22.4 | 676.0 | 670.0 |
| T3 / °C | 434-678 | 580 | 48.2 | 676.0 | 640.0 |
| T4 / °C | 205-535 | 455 | 52.7 | 424.0 | 430.0 |
| T5 / °C | 135-363 | 237 | 67.8 | 355.0 | 330.0 |
| Time T1 / s | 8.0-9.8 | 9.15 | 0.36 | 9.3 | 8.7 |
| Time T1/2 / s | 2.1-8.4 | 5.26 | 1.78 | 2.8 | 8.4 |
| Time T2/3 / s | 0.9-5.9 | 2.51 | 1.57 | 0.0 | 5.6 |
| Time T3/4 /s | 0.9-4.6 | 2.14 | 0.88 | 2.8 | 3.5 |
| Time T4/5 /s | 51.9-192.2 | 175.6 | 37.1 | 105.9 | 188 |
| Carbon / wt.% | 0.171-0.255 | 0.183 | 0.026 | 0.171 | 0.238 |
| Manganese / wt.% | 0.94-1.94 | 1.447 | 0.154 | 1.440 | 1.430 |
| Silicon / wt.% | 1.21-1.73 | 1.44 | 0.103 | 1.410 | 1.490 |
| % Retained austenite | 2.8-20.7 | 11.2 | 3.38 | 13.7 | 15.1 |
| Yield strength / N $mm^{-2}$ | 316-616 | 410 | 70.3 | 368.2 | 447 |
| UTS / N $mm^{-2}$ | 577-1003 | 779 | 91.6 | - | - |
| Uniform elongation / % | 7.4-23.0 | 17.5 | 2.9 | - | - |

Table 9.1: Input and output variables used for training and testing models. Test sets 1 and 2 are individual sets from the training data.

The spread of data within the ranges shown in table 9.1 is also important for confidence in the model. Fig. 9.11 shows the distribution of each input, ordered by size. It can be seen that

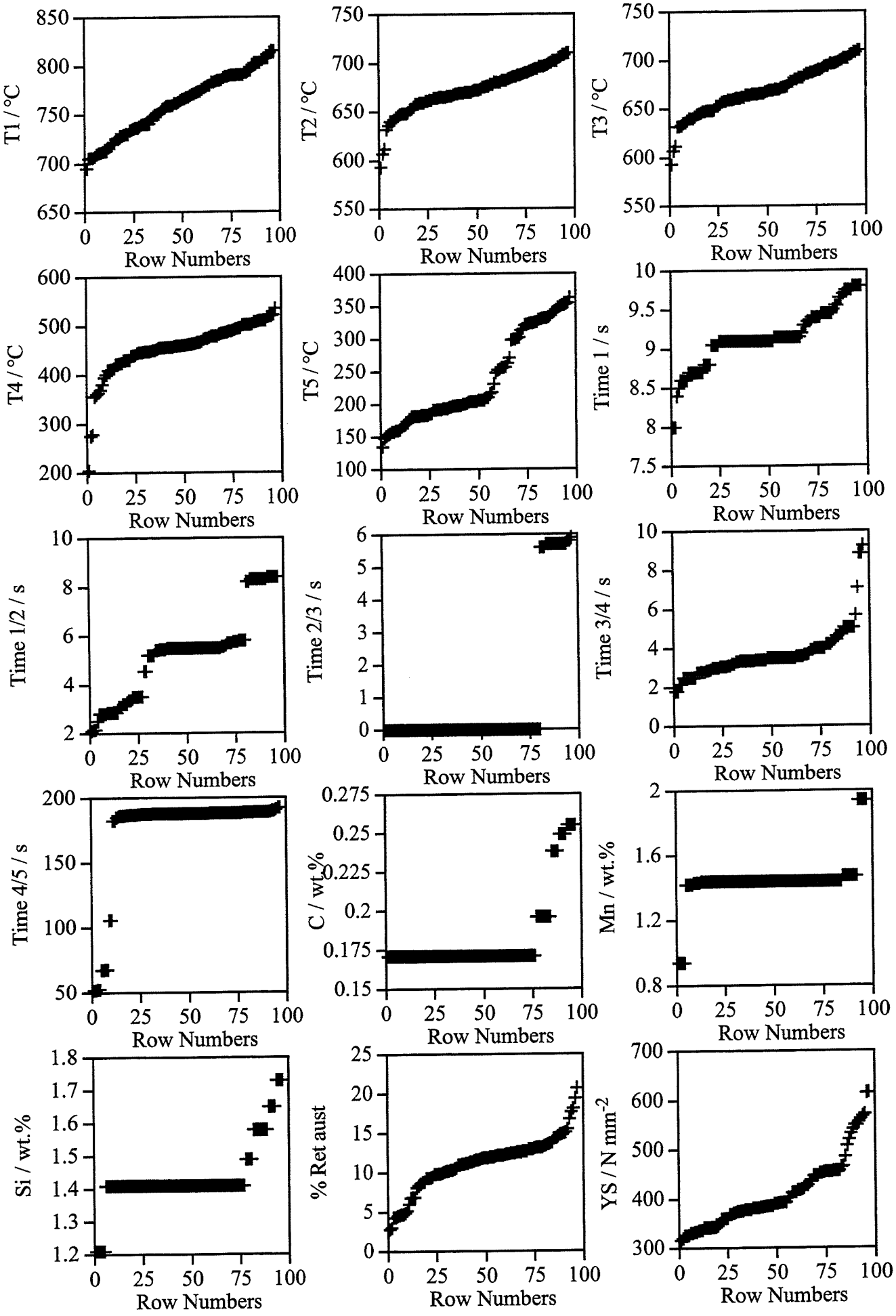


Fig. 9.11: The range and spread of each input, ordered by size.

some of the inputs only have a few values, thus making predictions between those values less reliable (e.g. manganese contents at 1.25 or 1.75 wt.%). This too is reflected in the error bars estimated by the model.

## 9.4 A Description of the Neural Network

In normal regression methods the analysis begins with the prior choice of a relationship (usually linear) between the output and input variables. A major advantage of the neural network is that it can in principle find the best fit relationship automatically, irrespective of the complexity with which the variables might be associated. Only the input and output data have to be presented to the computer, which in effect tries out all kinds of relationships in its search for an optimum fit.

Both the input and output variables were first normalised within the range ±0.5 as follows:

$$x_N = \frac{x - x_{min}}{x_{max} - x_{min}} - 0.5 \qquad (9.2)$$

where $x_N$ is the normalised value of $x$ which has maximum and minimum values given by $x_{max}$ and $x_{min}$ respectively. This normalisation was necessary to enable subsequent comparison of the significance of each variable.

Several neural network models were created using the data from table 9.1. These varied in terms of their complexity and of the random seeds used to start the training process. The networks consisted of 13 - 15 inputs (one for each variable $x$), a number of hidden units (controlling the complexity of the model) and an output representing the property to be predicted (fig. 9.12).

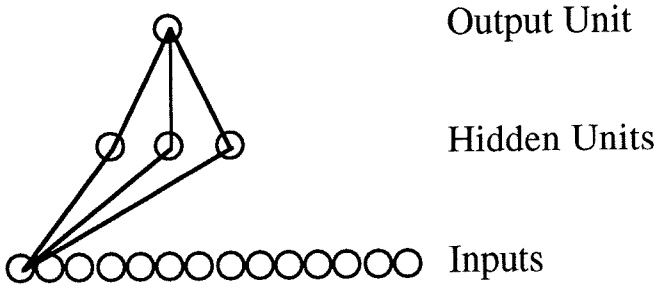


Fig. 9.12: A typical network used in the analysis. Only the connections originating from one input unit are illustrated.

Linear functions of the inputs $x_j$ are operated on by a hyperbolic tangent transfer function:

$$h_i = \tanh\left(\sum_j w_{ij}^{(1)} x_j + \theta_i^{(1)}\right) \tag{9.3}$$

so that each input contributes to every hidden unit. The bias is designated $\theta_i$ and is analogous to the constant that appears in linear regression. The strength of the transfer function is in each case determined by the weight $w_{ij}$. The transfer to the output $y$ is linear:

$$y = \sum_i w_i^{(2)} h_i + \theta^{(2)} \tag{9.4}$$

The specification of the network structure, together with the set of weights is a complete description of the formula relating the inputs to the output. The weights are determined by training the network; the details of which are described elsewhere [MacKay 1992a-c, 1993; Bhadeshia *et al.* 1995]. The training involves a minimisation of the regularised sum of squared errors. The term $\sigma_\nu$ used below is the framework estimate of the noise level of the training data.

The complexity of the model is controlled by the number of hidden units (figs. 9.12 and 9.14), and the values of the regularisation constants ($\sigma_w$), one associated with each of the inputs, one for the biases and one for all weights connected to the output. The regularisation constants represent the significance of input variables. Consequently, the model-perceived significance of each input variable can be compared against metallurgical theory.

The inferred noise level ($\sigma_\nu$) decreases as the number of hidden units increases. However, the complexity of the model also increases with the number of hidden units. A high degree of complexity may not be justified, and in an extreme case, the model may in a meaningless way attempt to fit the noise in the experimental data. MacKay has made a detailed study of this problem and has defined a quantity (the *evidence*) which comments on the probability of a model. The evidence framework was used to control the regularisation constants and $\sigma_\nu$.

Since the experimental data were randomly partitioned into test and training datasets the ability of a model to generalise could be examined by checking its performance on the unseen test data. The test error ($T_{en}$) is a reflection of the ability of the model to predict the values in the test data ($t_n$):

$$T_{en} = 0.5\sum_n (y_n - t_n)^2 \tag{9.5}$$

It is popular to use the test error as the default performance measure whereby the model with the lowest test error is reckoned to be best. But in many applications predictions can be made with error bars. It is then reasonable to compare models in terms of their predictive performance as measured by the log predictive probability of the test data. Under the log predictive error, as contrasted with the test error, the penalty for making a wild prediction is much less if the wild prediction is accompanied by appropriately large error bars [MacKay, 1997]. The log predictive error (*LPE*), assuming that for each example $m$ the model gives a prediction $\left(y^{(m)}, \sigma_y^{(m)^2}\right)$ is:

$$LPE = \sum_m \left[ \frac{1}{2} \left( t^{(m)} - y^{(m)} \right)^2 \Big/ \sigma_y^{(m)^2} + \log\left( \sqrt{2\pi} \sigma_y^{(m)} \right) \right] \qquad (9.6)$$

The best models, once chosen, can be combined into a committee in the hope of attaining more reliable results. The models were ranked in order of highest *LPE* first and committees of increasing size were formed. A single prediction can then be made by a committee by averaging the predictions of each of the models within it:

$$\bar{y} = \frac{1}{L} \sum_l y^{(l)} \qquad (9.7)$$

where $L$ is the number of models in the committee and $y^{(l)} \pm \sigma_y^{(l)}$ is the estimate of a particular model $l$. The variance of the committee's predictive distribution is given by:

$$\sigma^2 = \frac{1}{L} \sum_l \sigma_y^{(l)^2} + \frac{1}{L} \sum_l \left( y^{(l)} - \bar{y} \right)^2 \qquad (9.8)$$

which is the variance of the mean plus the mean of the variances. The test error of the predictions made by a committee of $L$ models each with $n$ lines of test data, is calculated in a similar manner to the test error of a single model:

$$T_{en} = 0.5 \sum_n \left( \bar{y}_n - t_n \right)^2 \qquad (9.9)$$

The predictions from such committees will be discussed and tested in the results section.

### 9.4.1 Testing the sensitivity

The validation of these neural network models is often done by keeping all the inputs constant and varying one at a time. This can be useful but also misleading. The inputs are often dependent on one another (especially when retained austenite is an input, as can be seen by

the strong dependence of retained austenite on the top temperature (T1, fig. 9.17)) and thus changing one and keeping the others constant is not entirely valid. Also the trends observed, due to the complexity of the model, can depend on all the other inputs chosen. For example in figs 9.13a and b the opposite trends are observed for the variation of ultimate tensile strength with time 1 due to the use of testing set 1 or set 2 as the constant input values (table 9.1).

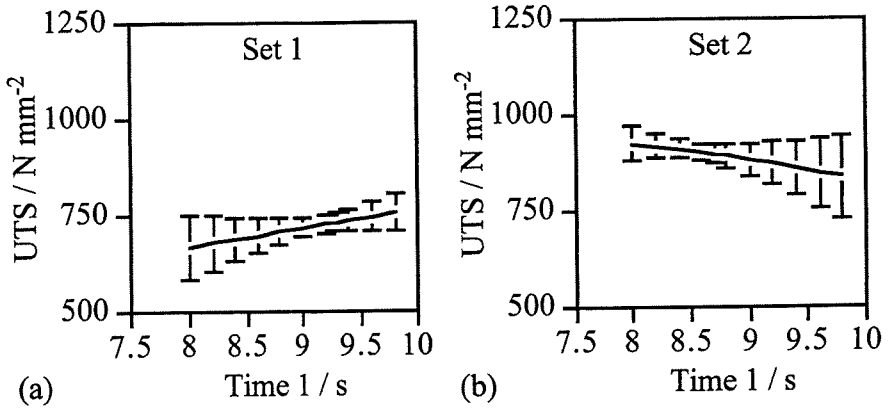


Fig. 9.13: Variation in committee model predictions of ultimate tensile strength with change in time 1. The other inputs were kept constant at values in (a) set 1 and (b) set 2 of table 9.1.

The values in set 2 (table 9.1) were chosen to be the constant inputs for testing these models. This was because set 1 contained data from an early experiment with only 6 temperature steps. Thus T2 was set to equal T3 and the time 2/3 is zero which makes testing T2, T3 and time 2/3 difficult. Also the composition of set 1 data is different from that of many of the other steels (fig. 9.11) so that variations may lead to large error bars. It should be noted however that 79 of the 96 data sets used to train these models were of set 1 type and hence confidence limits in T2, T3 and time 2/3 predictions may be large.

## 9.5 Results and Discussion

### 9.5.1 Retained austenite model

*9.5.1.1 Results*

Various complexities of model were obtained using between 1 and 8 hidden units with inputs of the temperatures, times and composition. The noise level, $\sigma_\nu$, was set to 0.14 (value found to give best log predictive error values) to allow for noise in the experimental data. This noise was due to the % retained austenite values being measured by X-ray diffraction to an accuracy of 10 %. The test errors and log predictive errors for each model are shown in fig. 9.14.

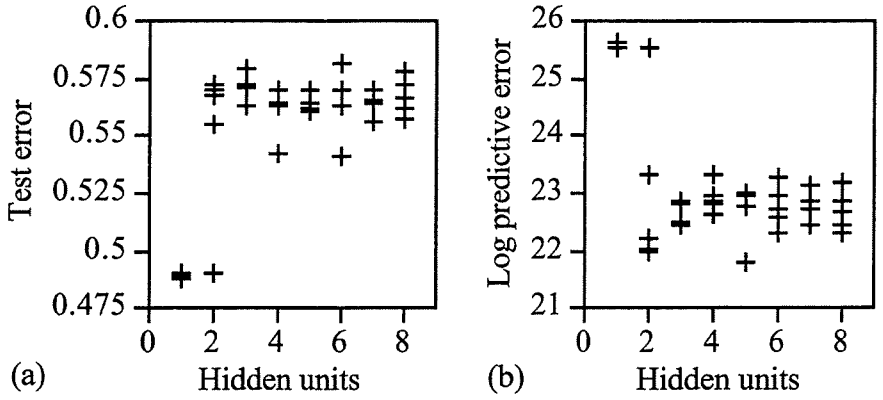


Fig. 9.14: Test error and log predictive error for the models of % retained austenite versus the number of hidden units. The greater the number of hidden units the more complex the model. Note that unlike the test error, the log predictive error will be a maximum for the best model.

From these models the best 10 were chosen using the highest log predictive error. The test errors of committee models formed with increasing number of these models were calculated and are shown in fig. 9.15a.

The optimum committee is that with the lowest test error. In this case a committee of eight models was chosen containing models of 1, 2 and 4 hidden units. These eight models were then retrained on all of the experimental data starting from the best fits found in the first training. Predictions from the committee of new models are shown in fig. 9.15b compared to the data on which they were trained.

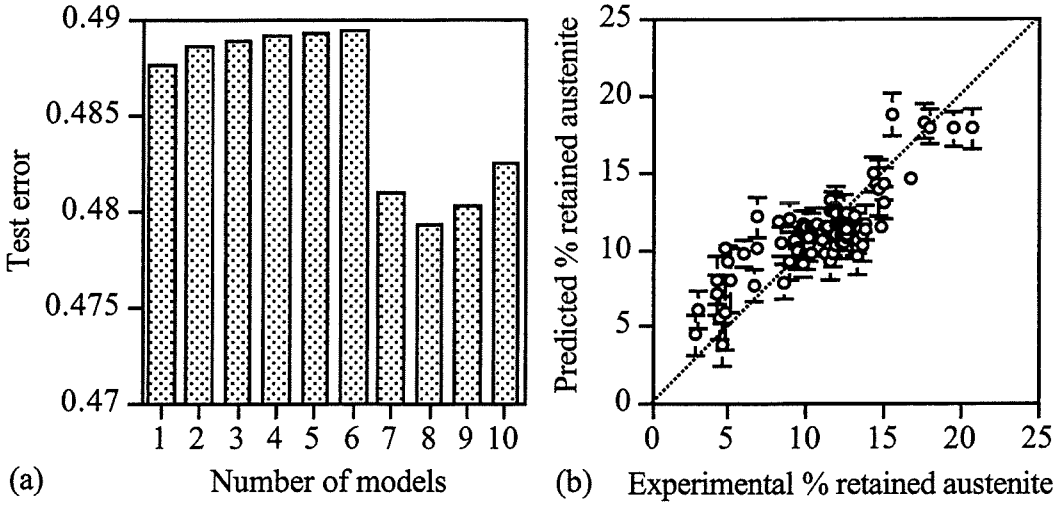


Fig. 9.15(a): Test errors for committee models of % retained austenite. Fig. 9.15(b): Committee predictions of % retained austenite versus experimental values on which the models were trained.

The error bars are only for 67% confidence and should be doubled to obtain 95% confidence. Any lack of confidence a model has in its predictions can be from two sources. The first is a

lack of data in that area, for example, making predictions out of the range of data used to train the model. The second is scatter in the data used to train the model. The calculated error in these predictions is due to the need to set error limits on the training because of the 10% error in the experimental measurements.

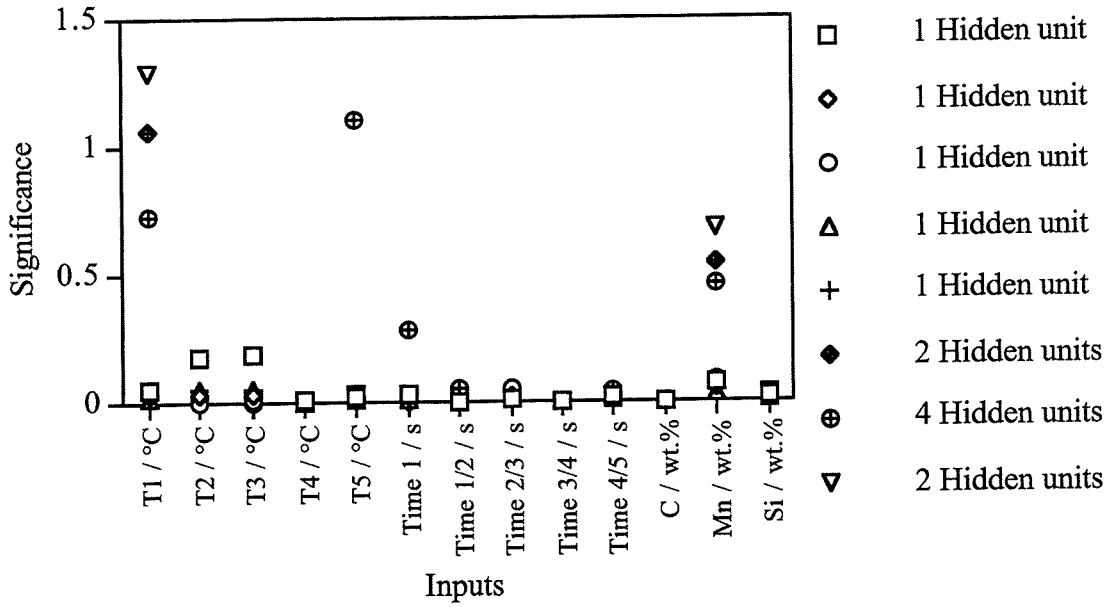


Fig. 9.16: Model perceived significance of the inputs for the models within the % retained austenite committee.

The model perceived significance of each input is shown in fig. 9.16 for each model in the % retained austenite committee. The significance, $\sigma_w$, is rather like a partial correlation coefficient in that it represents the amount of variation in the output that can be attributed to any particular input and does not necessarily represent the sensitivity of the output to each of the inputs. As expected the retained austenite content correlates strongly with intercritical annealing and bainite transformation temperatures (T1 and T5).

To determine the sensitivity of the model to the individual input parameters predictions were made when only varying one parameter at a time. The input values to be kept constant were chosen as those for a training set of data (set 2 in table 9.1) and inputs were each then varied within the limits shown in table 9.1. The resulting predictions are shown in fig. 9.17†.

*9.5.1.2 Discussion*

The confidence limits are large for the predictions shown in fig. 9.17, which is to be expected as the noise level ($\sigma_v$) was set to 0.14 before training to allow for noise in the experimental data.

[† Many of the predictions discussed are illustrated again in the discussion sections for clarity.]

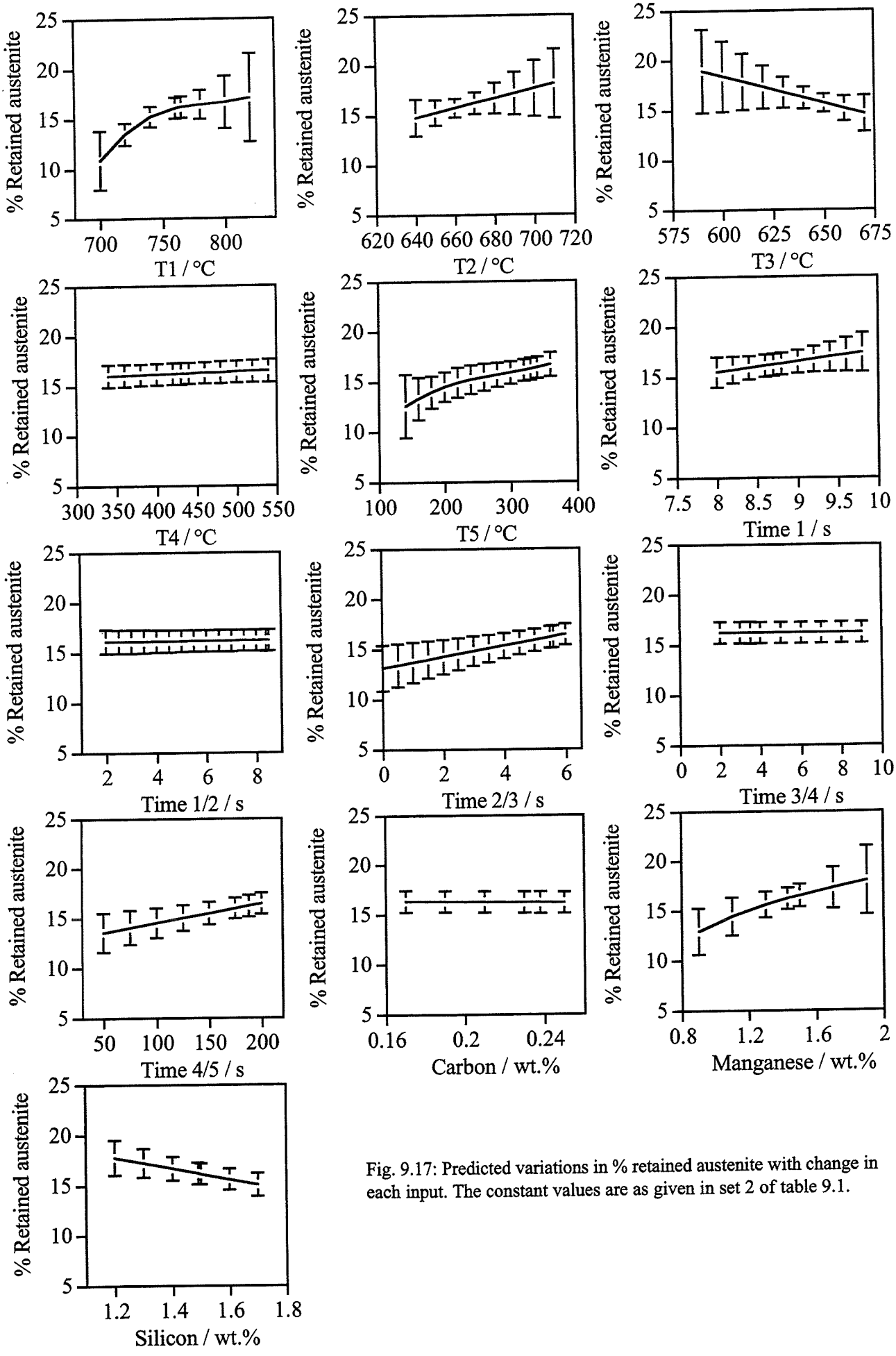


Fig. 9.17: Predicted variations in % retained austenite with change in each input. The constant values are as given in set 2 of table 9.1.

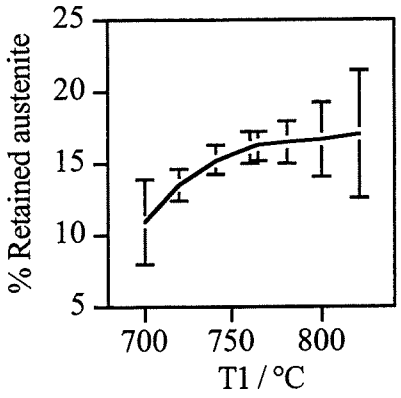


Fig. 9.18: Predicted variation in % retained austenite with change in temperature T1. The other input values being given in set 2 of table 9.1.

An increase in T1, which is within the intercritical range leads to a significant increase in the amount of austenite that is retained at ambient temperature. This is because a larger fraction of austenite forms as T1 is raised. This in turn leads to a greater fraction of bainite during subsequent transformation and hence more austenite is retained. Naturally, the effect must saturate as T1 approaches the $Ae_3'$ temperature (calculated to be 749.2 °C) and there is an indication in fig. 9.18 that this does indeed happen.

Note that in these calculations a change in T1 is studied whilst keeping all other variables fixed. This may not be possible to achieve in practice.

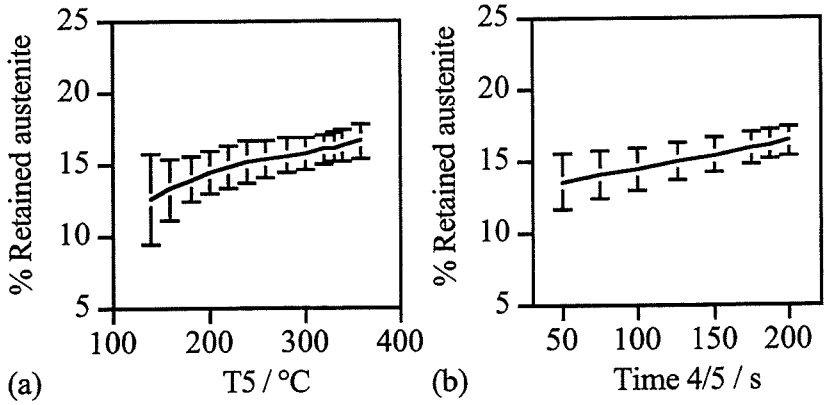


Fig. 9.19: Predicted variation in % retained austenite with change in temperature T5 and time 4/5. The other values being as given in set 2 of table 9.1.

At higher T5 temperatures (up to about 400 °C) more bainite and less martensite will form. Thus more films of stabilised austenite are retained as predicted in fig. 9.19a. Lower transformation temperatures can also lead to the formation of lower bainite which, due to cementite precipitation, can consume more austenite before the reaction is completed.

Longer times between the lower temperatures time 4/5 (T4 is 430 °C and T5 is 330 °C) allow more bainite to form and so more austenite is retained (fig. 9.19b). Further transformation to bainite, beyond about 15 minutes [Sakuma *et al.*, 1992], can lead to a decrease in the austenite content as the optimum bainite content is exceeded and the austenite is consumed without a gain in stability. This was not modelled as the experimental times were too short.

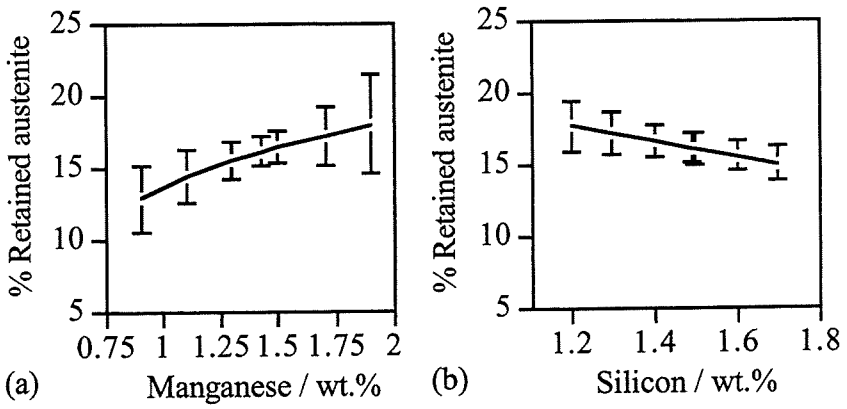


Fig. 9.20: Predicted variation in % retained austenite with change in (a) manganese and (b) silicon concentrations. The other values are as given in set 2 of table 9.1.

Manganese is an austenite stabiliser [Andrews, 1956] and this is shown by the predicted rise in retained austenite content with increasing concentration (fig. 9.20a).

Silicon is known to prevent the formation of cementite and thus forces carbon to remain in the austenite. This should increase the retained austenite content as shown experimentally in fig. 9.8 but is not in agreement with the sensitivity of the model in fig. 9.20b. It should be noted that the silicon concentrations used here are all more than is necessary to prevent cementite precipitation. Once this is achieved silicon stabilises the ferrite over austenite [Andrews, 1956].

The mechanical properties models require an input of retained austenite. Due to the large confidence limits of this committee model, the bainite and martensite theoretical models described in Chapters 4 and 7 should be used to calculate this input value rather than using this neural network committee model.

### 9.5.2 Yield strength and ultimate tensile strength

*9.5.2.1 Results*

Models with and without retained austenite as an input, as well as the temperatures, times and compositions, were produced to predict ultimate tensile strength (UTS) and yield strength

(YS). The analysis showed that retained austenite is an essential input and so was included in the following models.

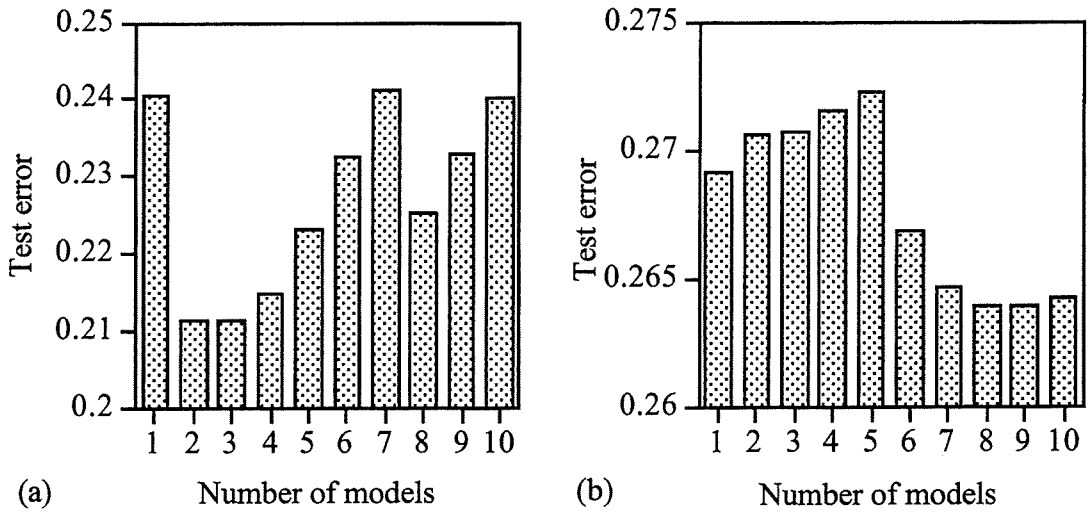


Fig. 9.21: Test errors for committee models of (a) yield strength and (b) ultimate tensile strength.

The best models were chosen as those with the highest log predictive error values and committees of increasing size were formed from them (fig. 9.21). A committee of two models (2 and 6 hidden units) was chosen for yield strength and one of nine models (1, 2, 4 and 5 hidden units) for UTS.

The models in each committee were retrained on the whole of the experimental data and the committee predictions are shown in figs. 9.22a and b compared to the training data. The correlation is good and many of the error bars are too small to be drawn.

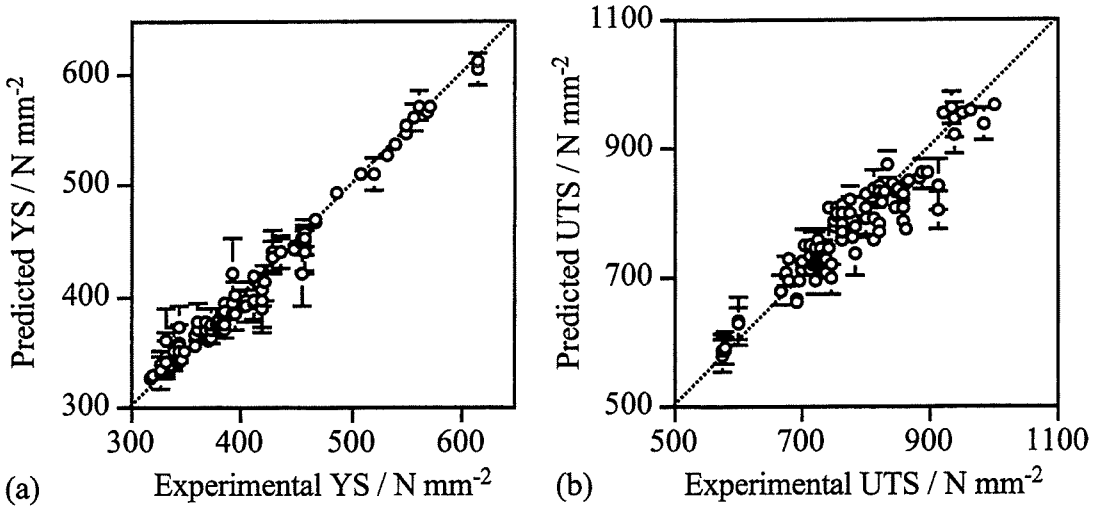


Fig. 9.22: Committee predictions of (a) yield strength and (b) ultimate tensile strength versus experimental values on which the models were trained.

The model perceived significance ($\sigma_w$) for each model in the committees is shown in fig. 9.23 for ultimate tensile strength and fig. 9.24 for yield strength. It can be seen that the significance of the manganese content is low for both of the models and that the retained austenite content is more significant in the prediction of yield strength than the ultimate tensile strength.

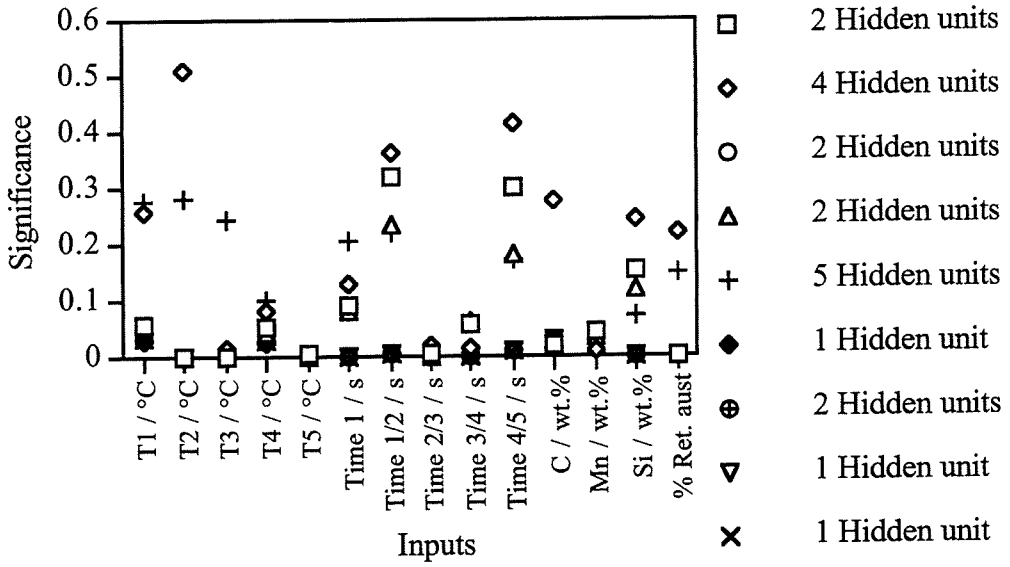


Fig. 9.23: Model perceived significance of the inputs for the models within the ultimate tensile strength committee.

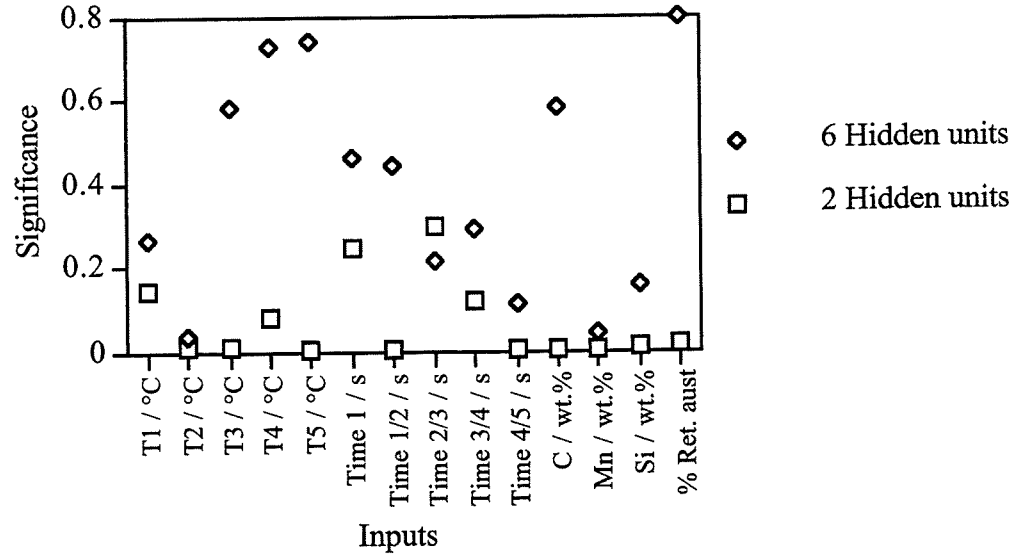


Fig. 9.24: Model perceived significance of the inputs for the models within the yield strength committee.

The sensitivity of these committees to the input values was tested using the values given in set 2 of table 9.1. The resulting predictions are shown in figs. 9.25 and 9.26.

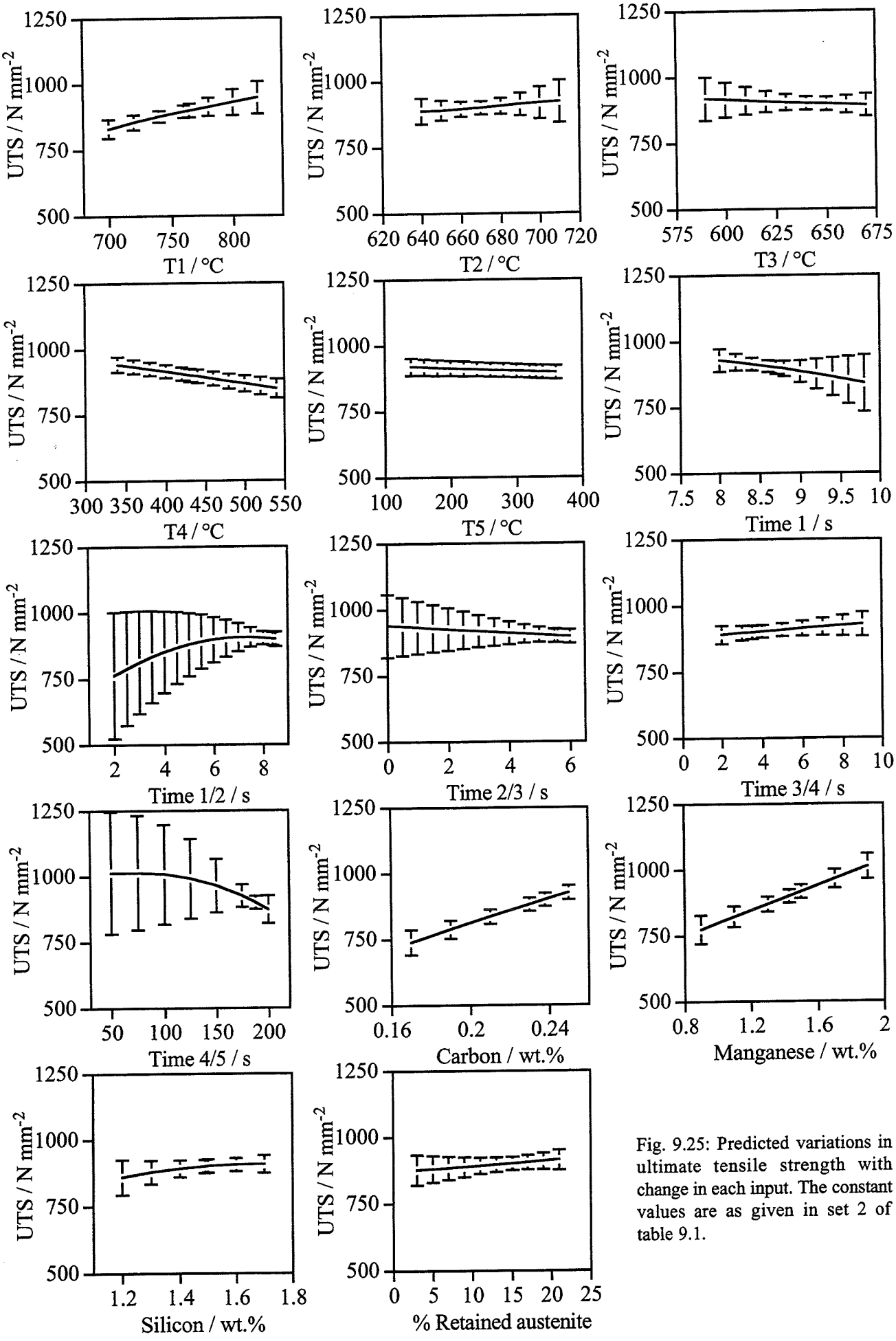


Fig. 9.25: Predicted variations in ultimate tensile strength with change in each input. The constant values are as given in set 2 of table 9.1.

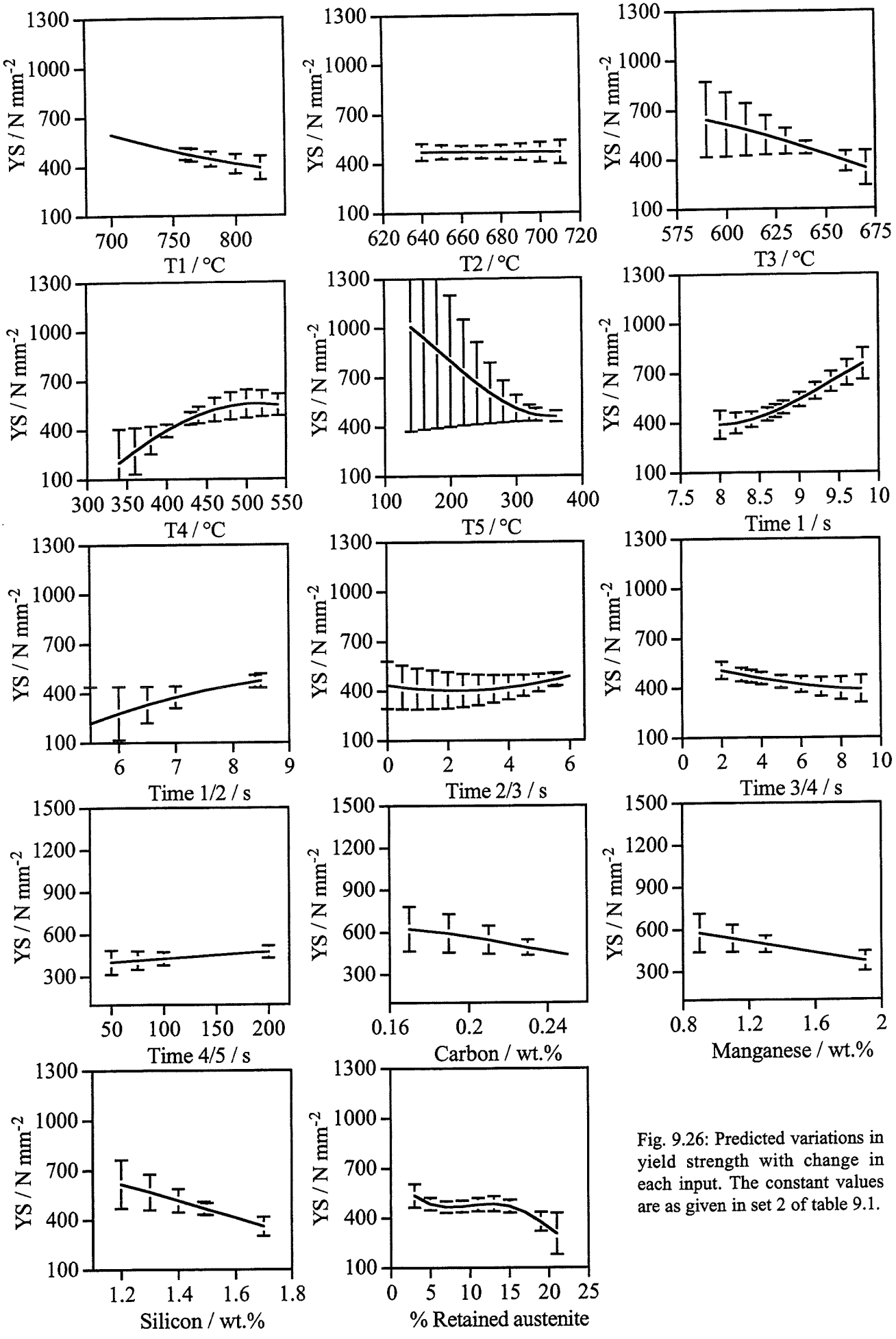


Fig. 9.26: Predicted variations in yield strength with change in each input. The constant values are as given in set 2 of table 9.1.

*9.5.2.2 Discussion*

Dislocations in ferrite, caused by the martensitic transformation of austenite, lead to continuous yielding [Marder, 1981]. The yield strengths of continuous yielding specimens are low as a result of the residual stresses and dislocations caused by martensite transformation on quenching to room temperature and the martensite contributes to higher ultimate tensile strengths.

Discontinuous yielding specimens can contain dispersed regions consisting of bainite and retained austenite [Sakuma *et al.*, 1992]. As the fraction of bainite is increased by isothermal transformation, martensite formation, ferrite dislocation density, and residual stresses are reduced. Therefore Lüders band formation is required to initiate yielding and this leads to higher yield strengths. However the presence of bainite lowers the ultimate tensile strength than if martensite were present. Hence changes in the relative quantities of martensite and bainitic ferrite will lead to a variation in the mechanical properties.

The quantity of allotriomorphic ferrite present prior to bainite transformation is critical. Large volume fractions can lead to high austenite carbon contents and prevent enough bainite forming. On the other hand, too little ferrite can result in not enough carbon stabilising the austenite to martensite decomposition. Raising the temperature T1 increases the proportion of austenite in relation to allotriomorphic ferrite content. This lowers the stability of the austenite and allows martensite to form. Hence the ultimate tensile strength increases with higher T1 temperatures and the yield strength decreases (fig. 9.27).

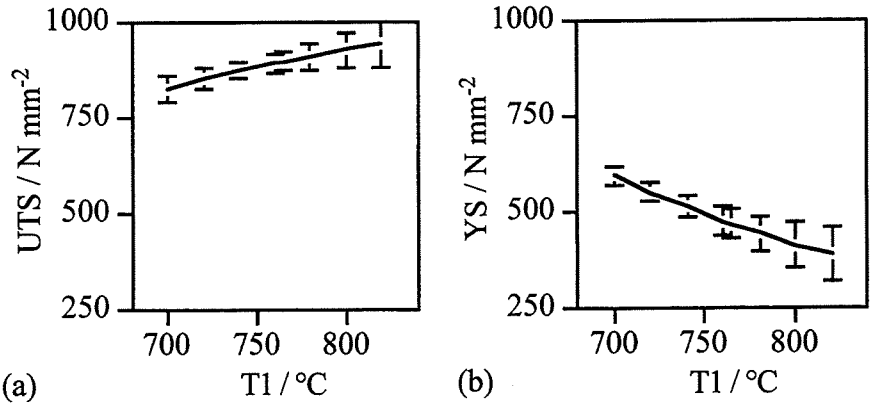


Fig. 9.27: Predicted variation in (a) ultimate tensile strength and (b) yield strength with change in temperature T1. The other values are as given in set 2 of table 9.1.

As all the values of T3, used in these predictions, are below the calculated $Ae_3'$ temperature (749 °C) allotriomorphic ferrite (or pearlite) may form. A lower transformation temperature results in a finer microstructure and thus a higher strength. The model predictions for yield

strength agree with this but the ultimate tensile strength committee shows little dependence on T3 (figs. 9.28a and b).

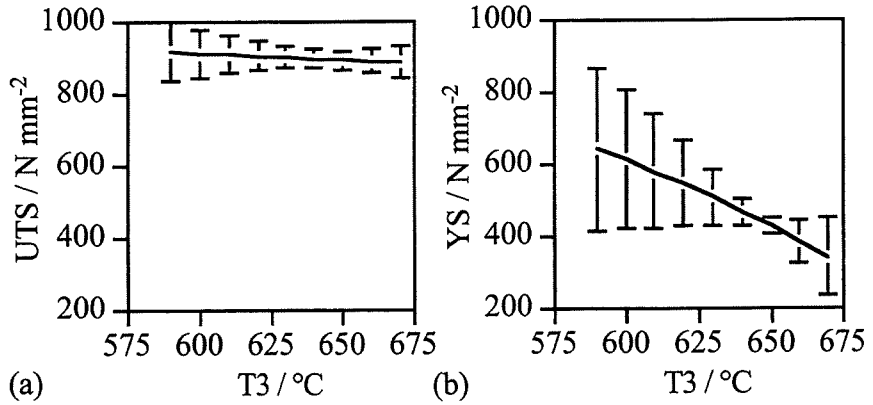


Fig. 9.28: Predicted variation in (a) ultimate tensile strength and (b) yield strength with change in temperature T3. The other values are as given in set 2 of table 9.1.

Lower T4 temperatures result in finer bainite microstructures which increase both the yield and ultimate tensile strengths. This is consistent with fact that the calculated ultimate tensile strength increases with decreasing T4 but the trend for the yield strength cannot be assessed due to large error bars (figs. 9.29a and b).

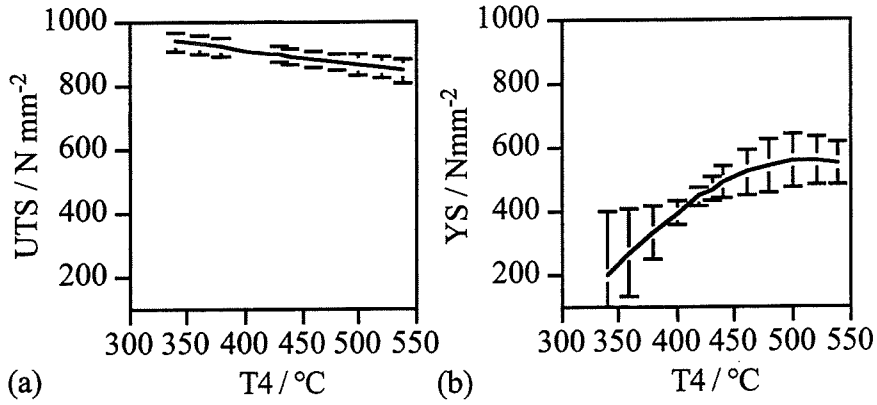


Fig. 9.29: Predicted variation in (a) ultimate tensile strength and (b) yield strength with change temperature T4. The other values are as given in set 2 of table 9.1.

As with the austenite model there is little statistical significance in many of the predicted variations as a function of the time parameters. This might be a consequence of the limited variation in the training data times and perhaps because other factors such as retained austenite, and heat treatment temperatures are more important. This can be seen for yield strength in fig. 9.24 where the model perceived significances of each input are compared.

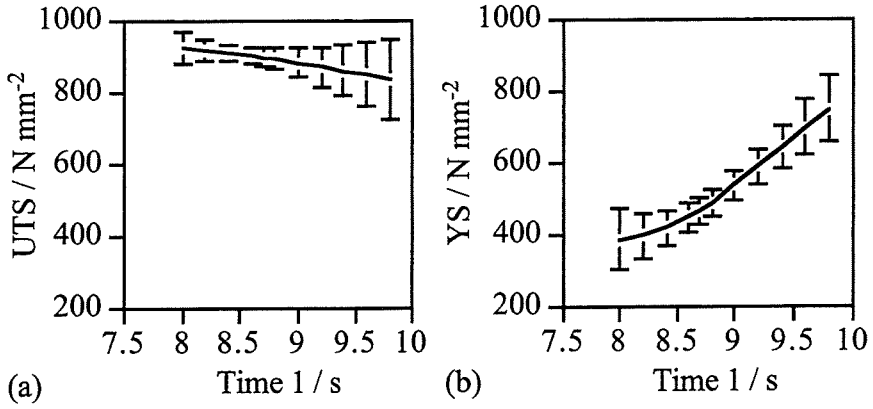


Fig. 9.30: Predicted variation in (a) ultimate tensile strength and (b) yield strength with change in time at T1. The other values are as given in set 2 of table 9.1.

The exception to this is the yield strength dependence on time at T1 (765 °C). Increasing this time results in more time to form austenite and dissolve carbides. Thus more bainite is able to form on subsequent cooling. This increases the yield strength and the UTS is not significantly affected [Sakuma *et al.*, 1992] (fig. 9.30).

We would expect an increase in time 4/5 to affect yield strength by extending the time to form bainite (fig. 9.3) [Sakuma *et al.*, 1992], but there is not much significance in the perceived variation. This may be due to more martensite forming rather than bainite, and thus no time dependency. Also there may be little variation because both reactions are faster than the minimum of 50 seconds tested here. Once a reaction has reached completion, longer times cannot affect it.

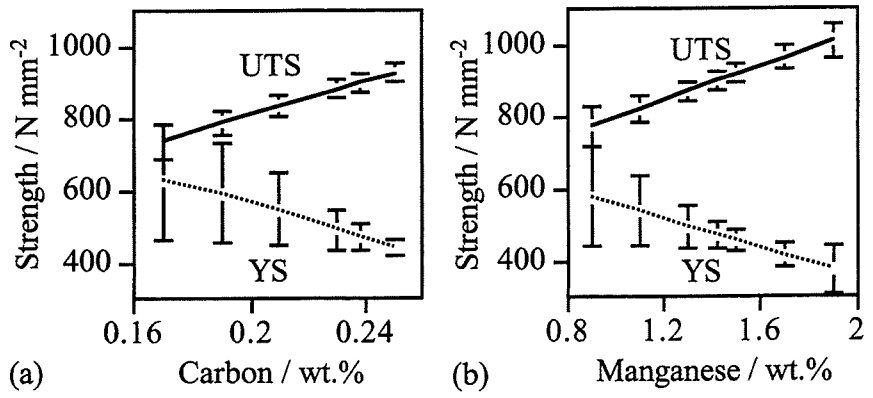


Fig. 9.31: Predicted variation in ultimate tensile strength (UTS) and yield strength (YS) with change in (a) carbon and (b) manganese concentrations. The other values are as given in set 2 of table 9.1.

Carbon and manganese are both austenite stabilisers [Andrews, 1956]. If we increase the amount of carbon or manganese, less bainite and more martensite forms, thus lowering the

yield strength and increasing the ultimate tensile strength. The models predict this (figs. 9.31a and b).

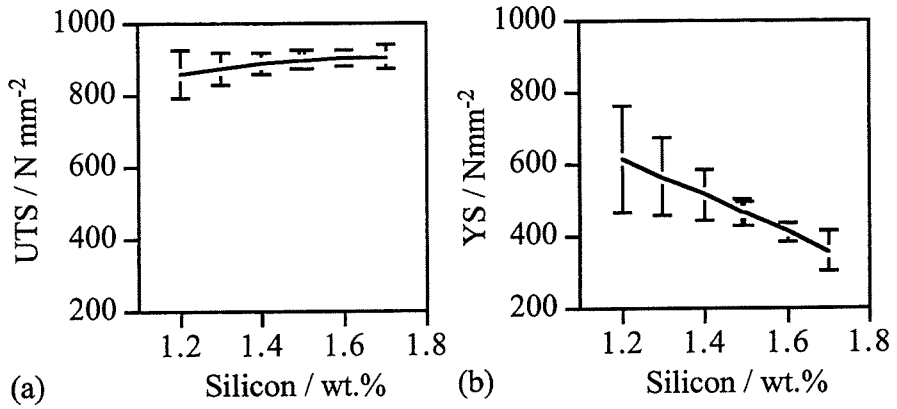


Fig. 9.32: Predicted variation in (a) ultimate tensile strength and (b) yield strength with change in silicon concentration. The other values are as given in set 2 of table 9.1.

Silicon prevents the formation of cementite in the austenite, thus increasing the carbon content of the austenite and so less bainite and more martensite will form from it, reducing the yield strength and increasing the ultimate tensile strength (fig. 9.32).

There is little dependence of the strengths on the measured volume fractions of retained austenite. This may be because it is the stability of the austenite (related to the amount of bainite) rather than its volume fraction which is the more important variable. Another explanation is that the volume fraction of retained austenite is not an independent variable and its effect is included in the other inputs.

### 9.5.3 Uniform elongation model

*9.5.3.1 Results*

Models of uniform elongation (U-El) were trained using the same inputs as for the ultimate tensile strength model plus an input of yield strength. This was found necessary in order to increase reliability. A committee of four models (containing models with 1 and 2 hidden units) was found to be optimum (fig. 9.33a) and the predictions by a committee of these retrained models gave a correlation with the experimental data as shown in fig. 9.33b.

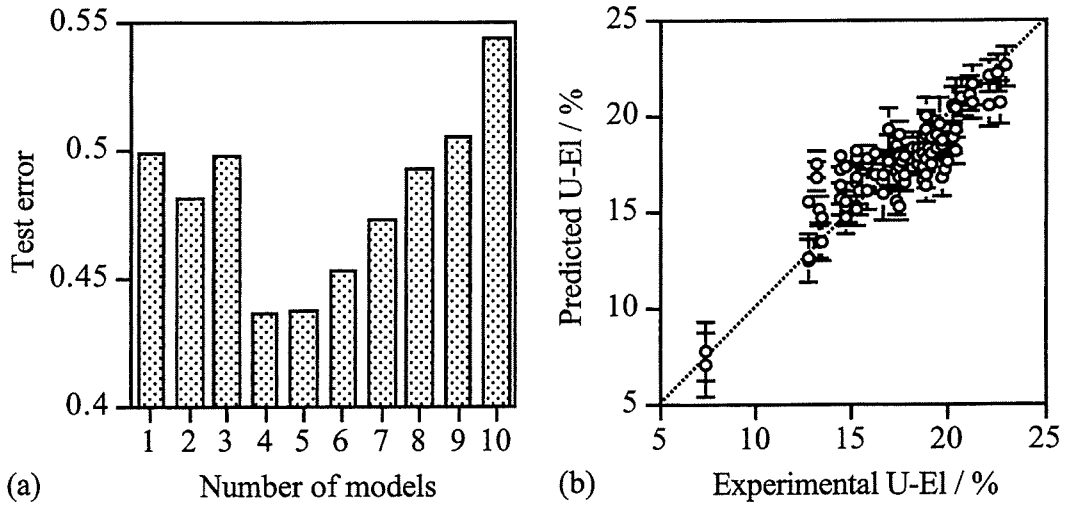


Fig. 9.33: (a) Test error of U-El committees with increasing number of models. (b) Comparison of predicted U-El values with the experimental data on which the models were trained.

The model perceived significances of the inputs for this committee model are shown in fig. 9.34. As expected, the uniform elongation correlates strongly with carbon content of the alloy.

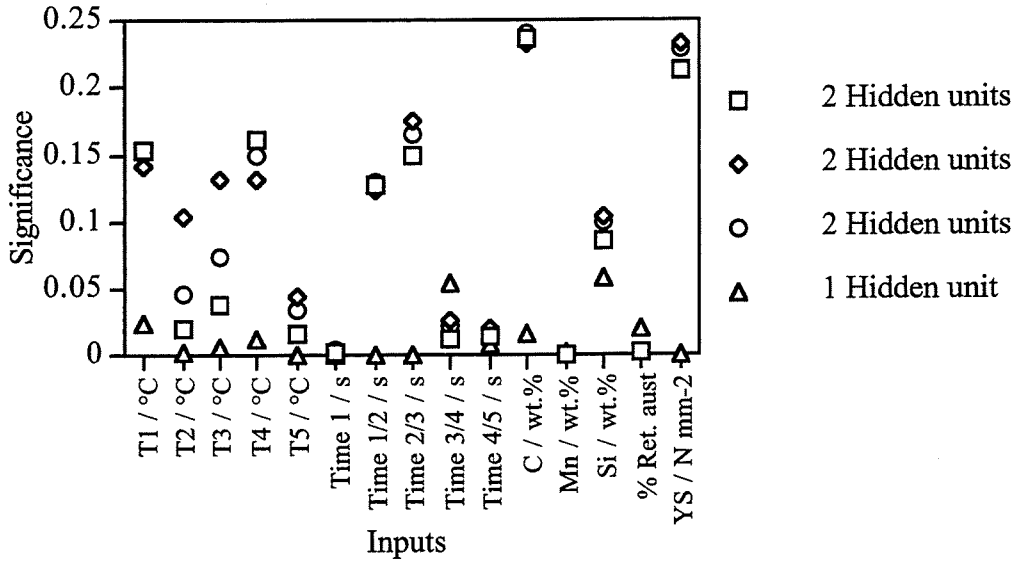


Fig. 9.34: Model perceived significance of the inputs for the models within the uniform elongation committee.

Each input to this committee of models was varied, whilst the others were kept to the values in set 2 (table 9.1). The results are shown in fig. 9.35.

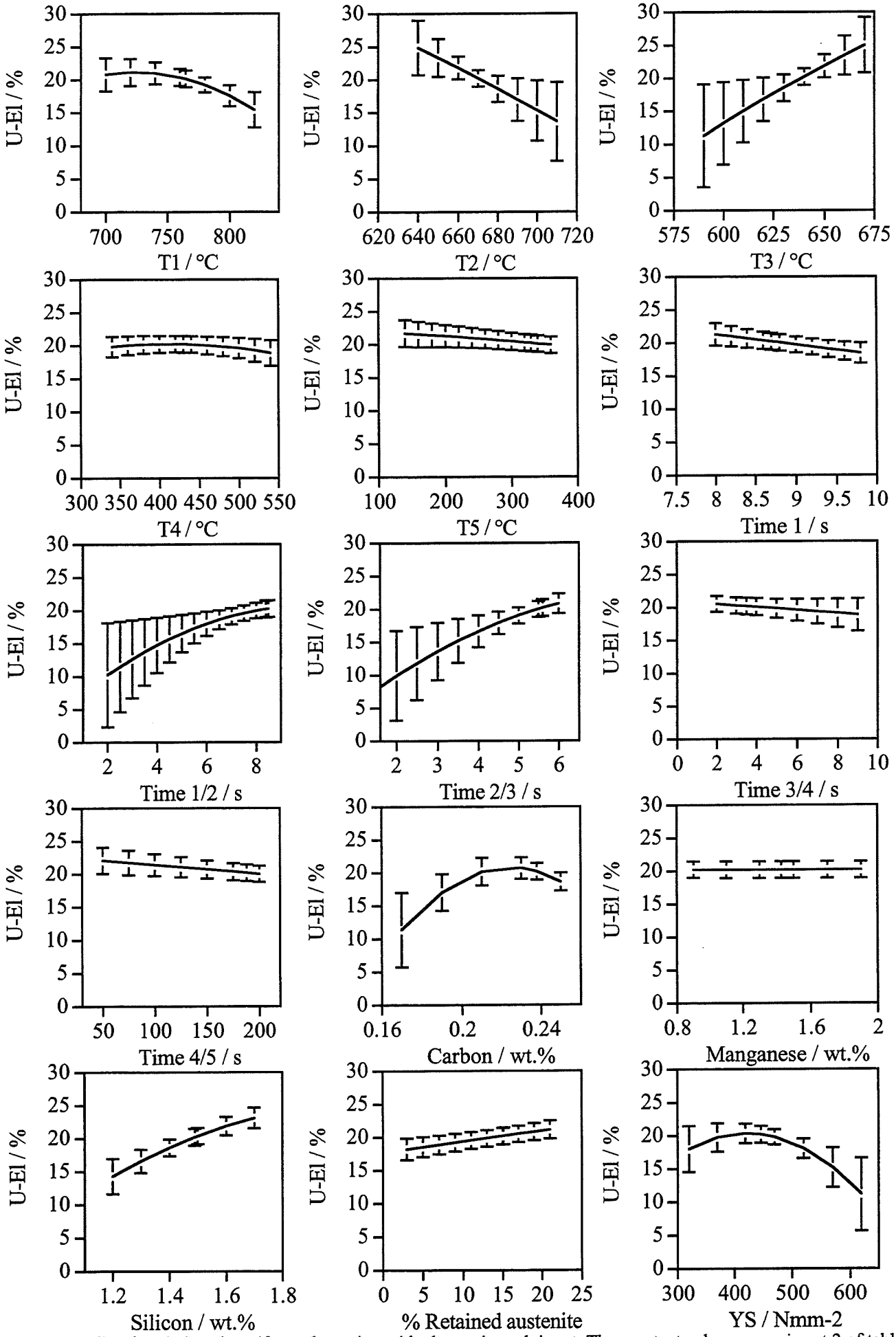


Fig. 9.35: Predicted variations in uniform elongation with change in each input. The constant values are as in set 2 of table 9.1.

*9.5.3.2 Discussion*

Transformation induced plasticity (TRIP) is the enhancement of work hardening by the transformation of austenite to martensite on deformation. If micronecking takes place during deformation in such a material the necked region is hardened more by strain-induced martensite than the rest of the specimen, so the neck no longer grows and deformation occurs in an adjacent region [Bressanelli and Moskowitz, 1966; Tamura *et al.*, 1970]. Thus elongation is dependent on the TRIP effect and on the stability and quantity of the austenite.

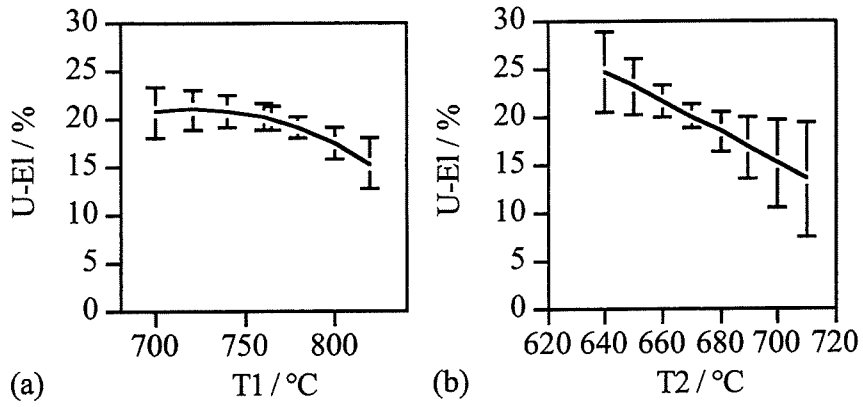


Fig. 9.36: Predicted variation in uniform elongation with change in (a) T1 and (b) T2 temperatures. The other values are as given in set 2 of table 9.1.

Increasing either T1 or T2 decreases the predicted elongation (figs. 9.36a and b). This is in agreement with the results found by Matsumura *et al.* [1987] (fig. 9.1) in which the higher temperatures increased the bainite volume fraction, but reduced the allotriomorphic ferrite and austenite volumes, thus lowering the ductility of the sample.

A decrease in the T3 temperature may lead to the formation of pearlite, thus reducing the ductility, as predicted by the neural network committee (fig. 9.37a).

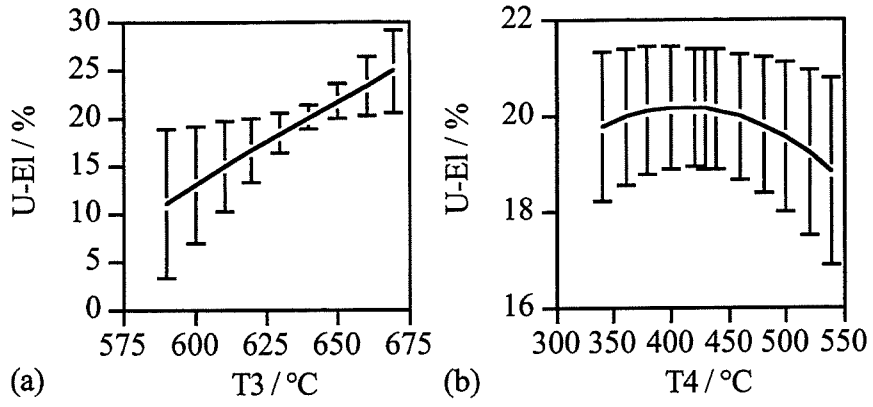


Fig. 9.37: Predicted variation in uniform elongation with change in (a) T3 and (b) T4 temperatures. The other values are as given in set 2 of table 9.1.

There is not much significance in the predictions when varying the lower temperatures, T4 and T5, but the trend in T4 (fig. 9.37b) does agree with the literature [Hanzaki *et al.*, 1995] in that the elongation goes through a maximum at about 400 °C due to the volume of bainite being large enough to stabilise the retained austenite without consuming too much of it.

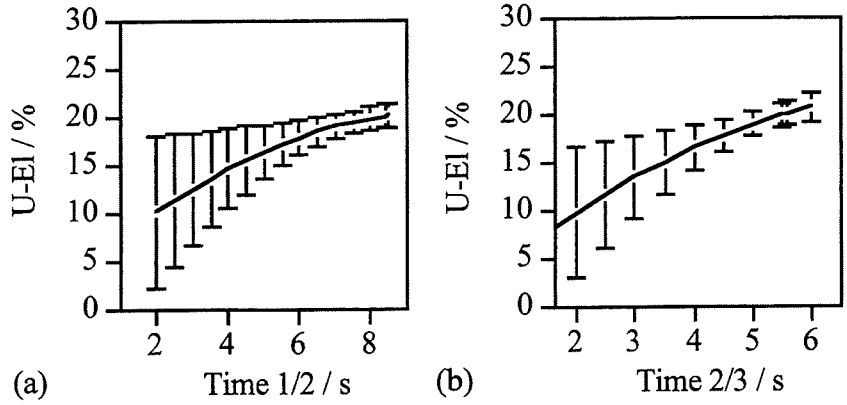


Fig. 9.38: Predicted variation in uniform elongation with change in times between (a) T1 and T2 and (b) T2 and T3 temperatures. The other values are as given in set 2 of table 9.1.

Longer times 1/2 and 2/3 will allow more allotriomorphic ferrite to form. This is more ductile than the bainitic ferrite and hence leads to an increase in the elongation (fig. 9.38).

At low carbon contents there is not enough austenite stabilised and thus the elongation is reduced, but at high carbon concentrations less bainite can form before the carbon content reaches the $T_0$ line, hence not enough austenite is retained in thin film form. This explains the maximum predicted in fig. 9.39a.

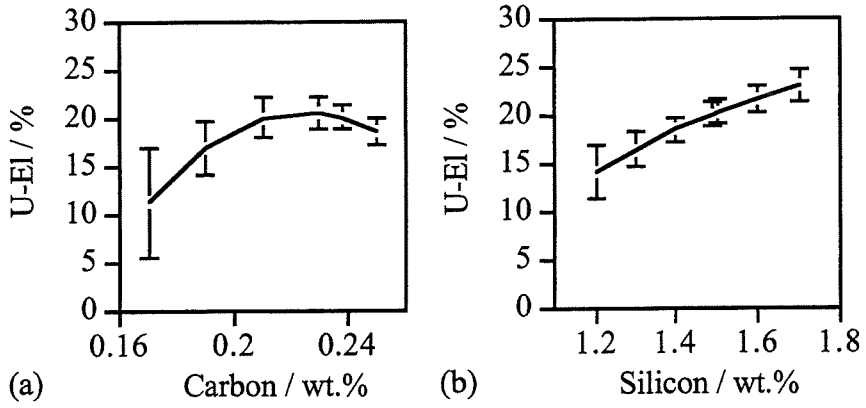


Fig. 9.39: Predicted variation in uniform elongation with change in (a) carbon and (b) silicon concentrations. The other values being as given in set 2 of table 9.1.

Silicon prevents the formation of cementite, thus raising the carbon content of the austenite and stabilising it, which in turn increases the elongation (fig. 9.39b) [Tsukatani *et al.*, 1991].

This is in agreement with the prediction for the variation of elongation with % retained austenite (fig. 9.40a), though the stability of the austenite might be more important than the volume fraction for improving elongation [Matsumura *et al.*, 1987].

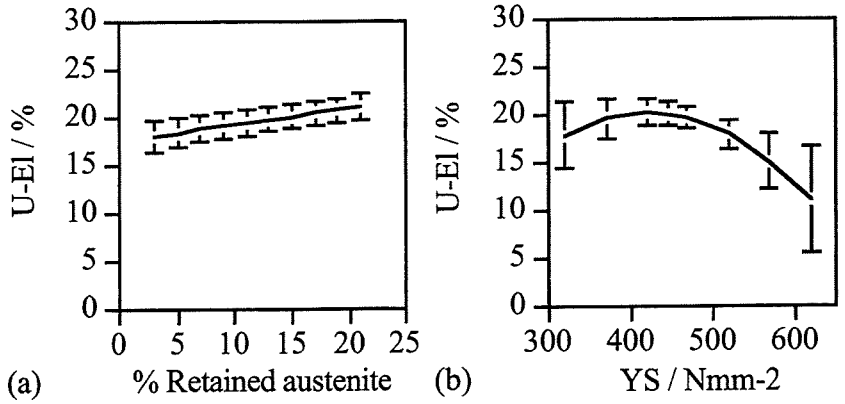


Fig. 9.40: Predicted variation in uniform elongation with change in (a) % retained austenite and (b) yield strength. The other values are as given in set 2 of table 9.1.

The yield strength of a sample increases with volume fraction of bainite [Sakuma *et al.*, 1992]. Thus a higher yield strength correlates to a higher bainite fraction and we see the predicted maximum in fig. 9.40b as expected for bainite fraction variation [Hanzaki *et al.*, 1995].

It should be noted that, as this model requires an input of yield strength, the errors will be additive as the output from one model is an input in another.

### 9.5.4 Formability

A combination of high strength and large elongation is desired in the properties of these steels. To represent this we use a formability index which is the UTS multiplied by U-El. Combining the neural network predictions requires the confidence limits to be taken into account. These are calculated thus:

For an equation in which $A \times B = C$, the errors in $C$ are calculated as:

$$c = C \times \sqrt{\left(\frac{a}{A}\right)^2 + \left(\frac{b}{B}\right)^2} \qquad (9.10)$$

where $A$, $B$ and $C$ are the values and $a$, $b$ and $c$ are their respective confidence limits.

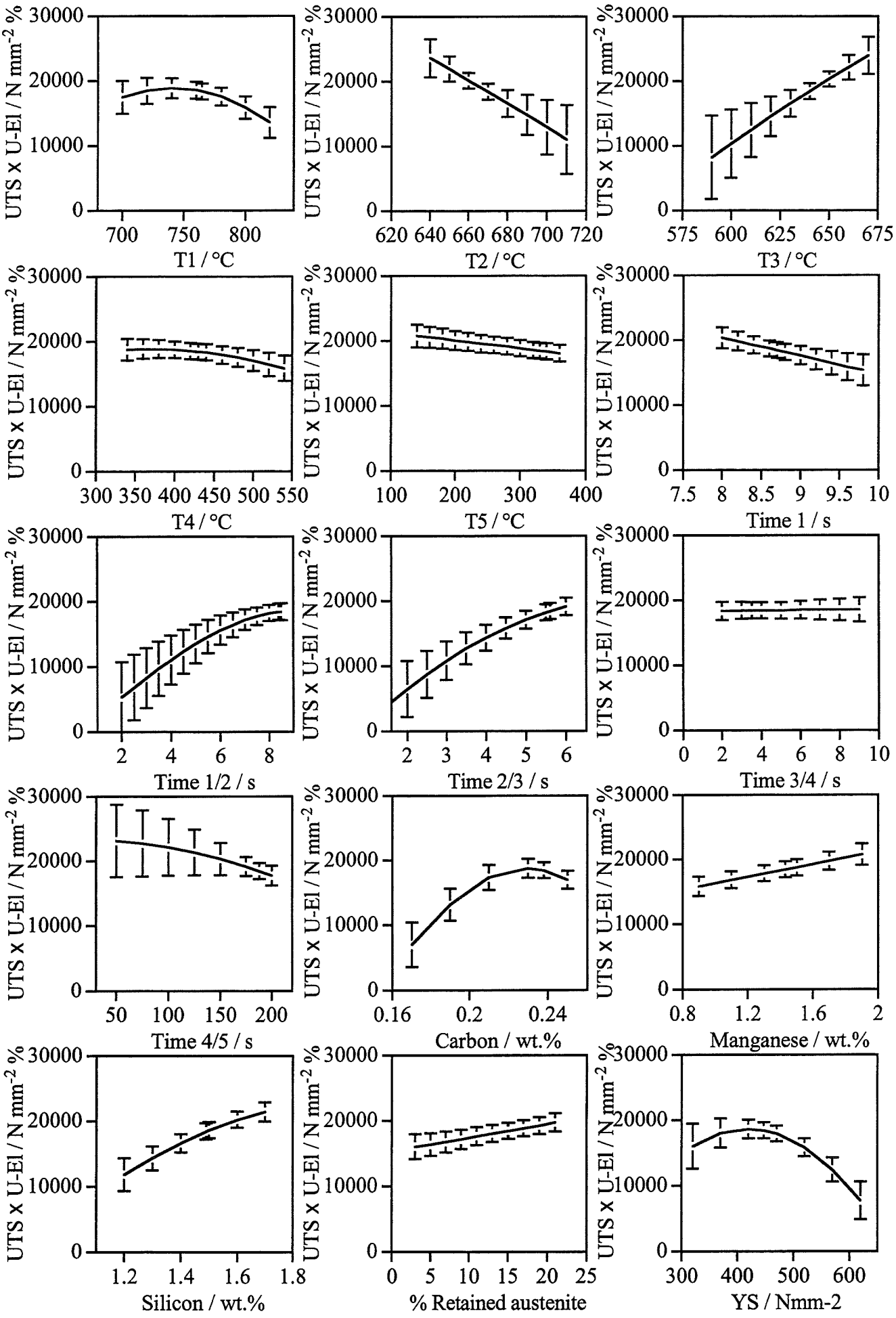


Fig. 9.41: Predicted variations in formability (UTS x U-El) with change in each input. The constant values are set 2 of table 9.1.

Fig. 9.41 shows the sensitivity of this formability to the inputs. Again, mainly due to the uncertainty of the U-El predictions, the confidence limits are large and little meaning can be derived from the significance of each input.

However we do note that the trends are very similar to those for U-El except that there is no variation with time 3/4 and there is a large variation with manganese content. The latter being due to the strength improving with martensite content, which increases with higher manganese concentrations. This increase in strength outweighs any decrease in elongation due to the presence of martensite.

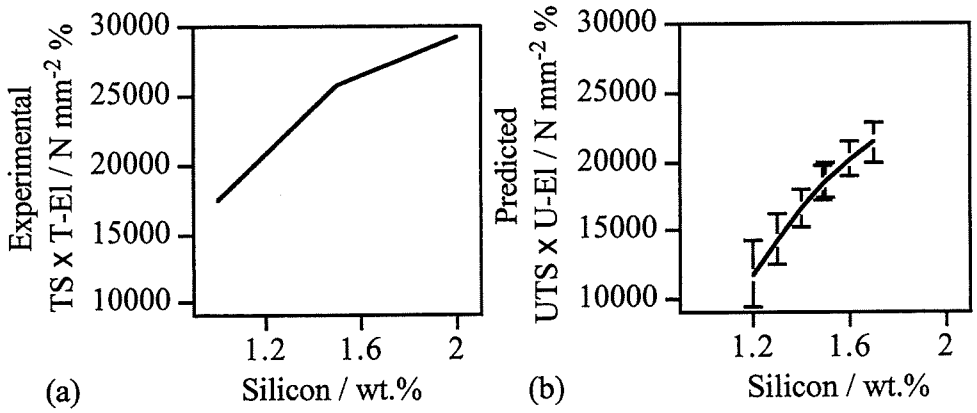


Fig. 9.42: (a) experimental and (b) predicted variation in formability index with change in silicon concentration. The experimental values are from [Tsukatani *et al.*, 1991]. The constant values used in the prediction are as given in set 2 of table 9.1.

Agreement can be found when comparing the predicted change in formability with variation in temperature T1 and experimental results in fig. 9.1. Also the rise in formability with silicon content is as shown by Tsukantani *et al.* [1991] (figs. 9.42a and b).

## 9.6 Conclusions

Four neural network committee models have been trained on data provided by British Steel Wales to predict the % retained austenite, ultimate tensile strength (UTS), yield strength (YS) and uniform elongation (U-El) of steel samples continuously annealed within the ranges shown in table 9.1. The models have been assessed on sensitivity to each input and the confidence of the models in the predictions have been calculated.

A product of the UTS and U-El predictions was calculated as an aid to predict formability and it was observed that most of the trends in sensitivity to input values were the same as in the U-El predictions, hence confirming that the stability of austenite dominates formability.

Due to measurement inaccuracies, or the small range of values used in the training data, only some of the predicted trends can be considered to be statistically meaningful. This work emphasises the need for a more meaningful design of experimental research programmes.

# 10. Future Work

One of the most exciting developments from the present work has been the much improved theory for the bainite transformation. The theory is based on the key assumption, that the rate of nucleation at the highest temperature where displacive transformations occur ($T_h$), is independent of the chemical composition of the steel. This assumption is justified by the original derivation of the universal nucleation function. However, the derivation revealed a scatter in the experimental data by about ± 20 °C. This scatter is a hindrance in some instances of alloy design and requires further investigation. The model currently does not account for the effect of solutes on the strength of austenite. This may be important in the context of displacive transformations. In addition, it would be useful to obtain direct measurements of the nucleation rate of bainite as a function of $T_h$ in order to give greater confidence in the model.

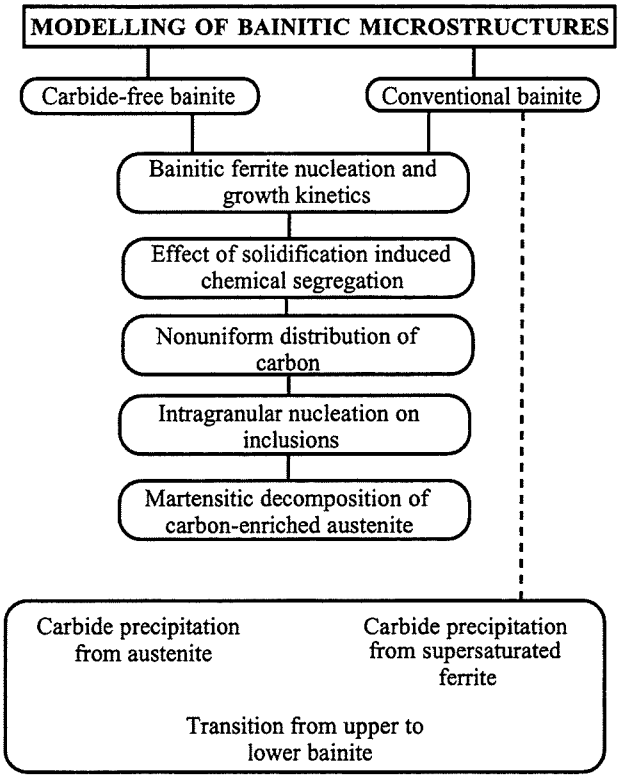


Fig. 10.1: Flow chart summarising the aspects of transformation which need to be addressed in order to be able to generally predict the microstructure of bainitic steels [Takahashi and Bhadeshia, 1991].

Another major area of proposed research could include the precipitation of carbides during the bainite transformation (fig. 10.1). The current model is restricted in its application to carbide-free microstructures whereas the more usual bainite also has cementite as a phase. There would naturally be an increase in the complexity of the theory, but one would start with

a simple modification whereby the enrichment of austenite is made a function of carbide precipitation, with the fraction of carbides related directly to that of the bainitic ferrite.

Silicon-rich steels are now common in the context of bainitic microstructures. There is, however, no theory capable of predicting the minimum or optimum quantity of silicon that is needed to suppress the precipitation of cementite. Most alloys are therefore based on empirical experiments.

The correlation between the surface relief caused by the displacive bainite transformation and the crystallographic theory for this transformation has never been confirmed by experiment. The use of an atomic force microscope to measure the surface relief of an individual bainite sub-unit and then electron microscopy to examine the crystallography of the same sub-unit would be a suitable experimental method to achieve this. This might lead to the ability to calculate the energy absorbed by plastic deformation and thus the strain energy in bainitic ferrite.

There is great need for a fundamental approach to the modelling of mechanical properties, including deformation and constraint effects. This could increase the understanding of such properties and allow predictions outside the realm of available experimental data to be made. It would also reduce the need to collate vast quantities of experimental data, which are required for training neural network models, and avoid models inheriting experimental inaccuracies.

# A1. Analysis of the Takahashi and Bhadeshia Bainite Kinetics Model

## A1.1 Introduction

Takahashi and Bhadeshia [1991] used phase transformation theory to model the development of microstructure in high-silicon steels of the type being investigated here. Their model was not fully tested against experimental data, but forms a reasonable alternative framework for the discussion and estimation of the microstructure of these steels. The model has as inputs the C, Mn, Si, Ni, Mo, Cr and V concentrations of steel and permits both continuous cooling transformation and isothermal transformation to bainite to be studied.

The purpose of the work presented here was to assess the model (known as *mixmicro.for*) with the help of some published experimental data on continuously annealed steels. This was necessary in order to understand the limitations of the model and to justify and lay the foundations for the more fundamental approach presented earlier in the thesis.

## A1.2 Theory

Takahashi and Bhadeshia's model for the overall transformation kinetics of bainite is based on an earlier method by Bhadeshia [1982a] for the calculation of the 1% transformation *TTT* (time-temperature-transformation) diagram of steels.

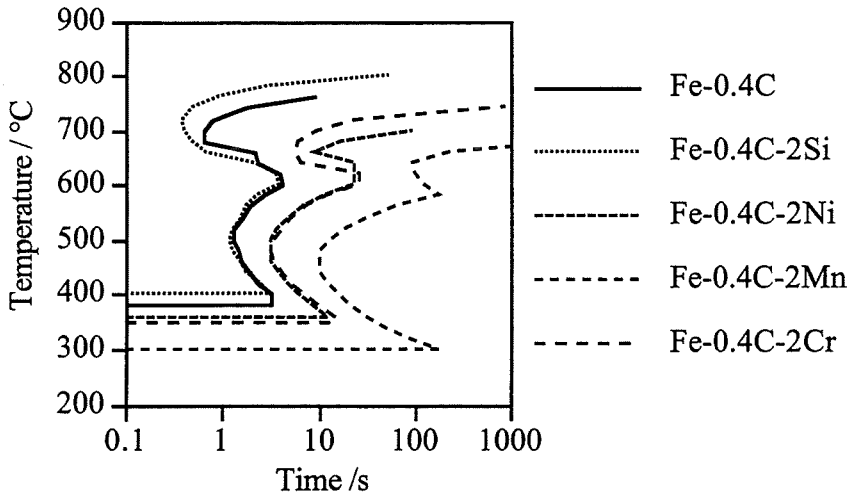


Fig. A1.1: Calculated *TTT* diagrams showing the reaction initiation C-curves for a series of steels with compositions in wt.%.

The *TTT* diagram consists essentially of two C-curves, one at higher temperatures for reconstructive transformations and one at lower temperatures for displacive transformations such as Widmanstätten and bainitic ferrite. These curves are affected differently by alloying elements as shown in fig. A1.1.

The *TTT* diagrams were calculated using Russell's [1969] theory which deals with the incubation time for a reaction, and hence the curves for the start of transformation only [Bhadeshia, 1982a]. The general form of the equation was modified to allow a temperature dependence in the activation enthalpy and entropy for diffusion, to give:

$$\ln\left|\frac{\tau_b(\Delta G_m)^p}{T^z}\right| = \frac{Q'}{RT} + C_7 \qquad \text{(A1.1)}$$

where $\tau_b$ is the time period before the onset of a detectable amount of isothermal transformation, $\Delta G_m$ is the chemical free energy change accompanying the formation of one mole of nucleating phase, $T$ is the absolute temperature, $R$ is the gas constant, $p$ is an exponent whose magnitude is a function of the nature of the nucleus, and $z$, $Q'$ and $C_7$ are constants obtained by maximising the correlation coefficient when using experimental values (table A1.1). Different values of the constants were found for the two C-curves, shear and diffusional, thus the two different curves were predicted [Bhadeshia, 1982a]. The use of this equation is empirical because of the fitting constants and the broad interpretation of $\tau_b$, which has a specific meaning in Russell's theory but is taken to be the onset of transformation in Bhadeshia's model.

| Constant $Q'$ x $10^{-6}$ J mol$^{-1}$ | Constant - $C_7$ x $10^{-2}$ | Correlation coefficient | Exponent $p$ | Constant $z$ | C-curve |
|---|---|---|---|---|---|
| 0.2432 | 1.350 | 0.97428 | 5 | 20 | Shear |
| 0.6031 | 1.905 | 0.91165 | 4 | 20 | Diffusional |

Table A1.1: Fitting constants for equation A1.1 [Bhadeshia, 1982a].

The shear curve was further adapted by the inclusion of Widmanstätten and bainitic ferrite nucleation theory (section 2.3.3) so that, if nucleation was impossible, the incubation time would be set to infinity and the experimentally-observed flat top to the curve predicted.

The model is obviously restricted to the initiation of transformation and has since been used in a whole range of calculations for steels. Nevertheless it cannot by itself predict the evolution of microstructure. On the other hand, the C-curve for 10% transformation, for example, can be estimated by assuming that it is equivalent to that for a steel whose composition is enriched with

carbon by the 10% transformation. The reaction initiation curve for this enriched steel then is equivalent to the 10% transformation curve for the unenriched steel.

A "family" of curves can thus be estimated for compositions with ever-increasing carbon concentrations, and hence increasing degrees of transformation due to the fact that the carbon concentration of residual austenite increases with the degree of transformation. Scheil's rule [Christian, 1975; Kuban *et al.*, 1986] was then used to convert the *TTT* diagrams for continuous cooling (fig. A1.2). Assuming that the additivity principle applies to each of the C-curves in the *TTT* diagram the degree of transformation can be calculated from the point where:

$$\int_0^t \Delta t / \tau_f\{T\} = 1 \qquad \text{(A1.2)}$$

where $\tau_f\{T\}$ is the incubation time at temperature $T$ for the C-curve representing a fraction $f$ of reaction, $\Delta t$ is the time interval spent at the temperature $T$, and $t$ is the time which is defined to be zero at the bainite-start temperature.

With the addition of the Khan and Bhadeshia [1990a] martensite transformation model (Chapter 7) the final retained austenite volume fractions can be predicted.

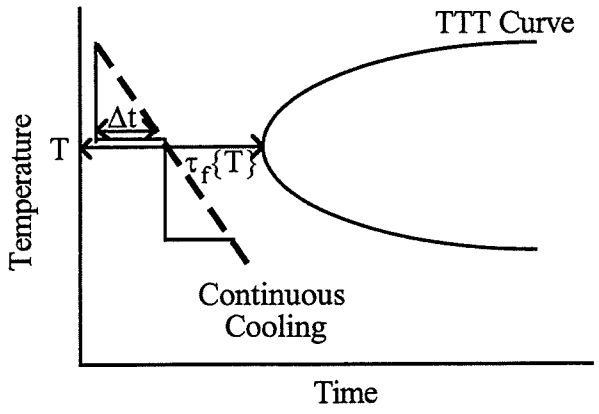


Fig. A1.2: Scheil's rule splits the continuous cooling curve into isothermal steps of time $\Delta t$ in which a fraction of the incubation time is achieved.

## A1.3 Experimental

| Steel | C | Si | Mn | Nb | S | P | Al | Prior ferrite | Cooling rate (°C/s) |
|---|---|---|---|---|---|---|---|---|---|
| A | 0.22 | 1.55 | 1.55 | 0.035 | - | - | 0.028 | 0.46±0.08 | 5 |
| B | 0.19 | 1.50 | 1.54 | - | - | - | 0.024 | 0.46±0.08 | 5 |
| C | 0.396 | 1.52 | 0.816 | - | 0.006 | 0.0092 | 0.033 | 0.56±0.04 | 5 |
| D | 0.38 | 1.29 | 1.73 | | 0.006 | 0.013 | 0.041 | 0 | - |

Table A1.2: Compositions of steels (wt.%), prior ferrite in volume fraction. Steels A and B [Hanzaki *et al.*, 1995], steel C [Bandoh *et al.*, 1988], steel D present work.

For steels A and B, after austenitisation at 1200 °C to dissolve the Nb(CN) and AlN precipitates, the samples were thermomechanically processed at 1050 °C to obtain a uniform statically recrystallised austenite grain structure. The specimens were then cooled and held isothermally at 700 °C for a fixed period of time in order to obtain a given amount of allotriomorphic ferrite. This was followed by a quench in a salt bath, the temperature of which was held in the austenite-to-bainite transformation range. The isothermal holding temperature and duration in the salt bath were varied to produce different bainitic microstructures. The specimens were then air cooled to room temperature [Hanzaki *et al.*, 1995].

Steel C was prepared from cold-rolled sheets of 0.8 mm thickness. These were heated and held isothermally at a temperature between $Ac_1$ (759 °C) and $Ac_3$ (843 °C) for a time $t_1$ and then quenched to a temperature in the austenite-to-bainite transformation range and held isothermally for a time $t_2$ before air cooling [Bandoh *et al.*, 1988]. ($Ac_1$ and $Ac_3$ temperatures were calculated using Andrews' formulae [1965], see section 2.7).

Cylindrical samples (8 mm diameter and 12 mm length) of steel D were homogenised as in section 3.7 and then heat-treated in a thermomechanical simulator (section 3.1). The heat treatment was 1000 °C for 300 s followed by a gas quench to a range of bainite transformation temperatures and held for 1200 s before quenching to room temperature.

## A1.4 The Program Inputs

The effect of alloying elements on the bainite transformation was modelled for C, Mn, Si, Ni, Mo, Cr and V.

The intercritical annealing (between $Ac_1$ and $Ac_3$) was assumed to produce only austenite and allotriomorphic ferrite. The volume fraction of this ferrite was required as an input for the program to predict the rest of the microstructure because of it increasing the carbon content of the austenite and decreasing the overall volume fractions of the other phases.

Modelling the austenite-to-bainite isothermal hold required an input of the hold temperature and duration. The final cooling to room temperature was modelled using the input cooling rate; air cooling was taken to be 5 °C $s^{-1}$.

## A1.5 Microstructure

The retained austenite measurements for steels A and B were performed using X-ray diffraction [Hanzaki *et al.*, 1995].

The volume fraction of allotriomorphic ferrite was measured directly from micrographs for steels A and B [Hanzaki *et al.*, 1995: figs. 6(a) and 6(b)]. This was done by point counting, as described in section 3.5, using a square grid of points at 5 mm spacing. The value obtained was 0.46 ± 0.08, where the error represents 95% confidence limits. Micrographs were only available for steel A and so the approximation was made that steel B had the same volume fraction of prior ferrite as steel A.

The phase measurements for steel C were carried out using image analysis after etching and the amount of retained austenite was determined using X-ray diffraction as the etch could not distinguish between austenite and martensite [Bandoh *et al.*, 1988]. The volume fraction of prior ferrite used in the program (0.56 ± 0.04) was an average of the measured results [Bandoh *et al.*, 1988: fig. 8].

The dilatation readings for steel D were converted into volume fraction of bainite formed as discussed in Chapter 4.

## A1.6 Results and Discussion

### A1.6.1 Retained austenite volume fractions

Fig. A1.3 shows that the model gives reasonable predictions of the volume fraction of retained austenite and that this value depends on the composition of the steel. However the variation within any given steel is not satisfactorily reproduced.

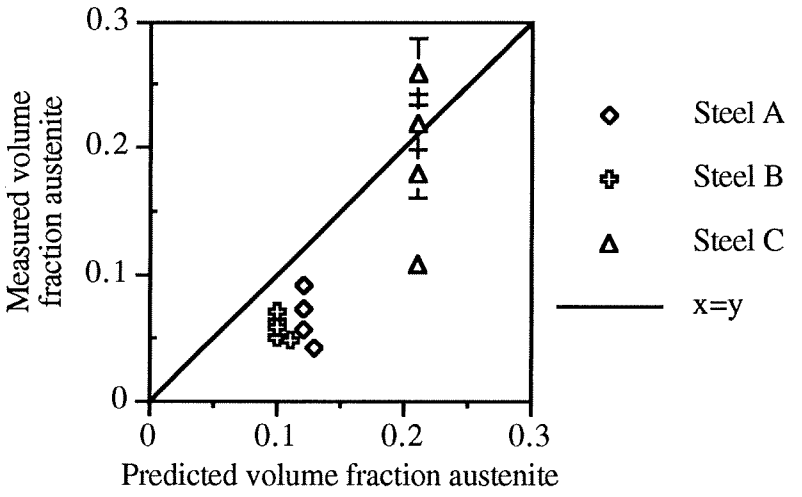


Fig. A1.3: Comparison of measured volume fractions of austenite with those predicted.

The measurement accuracy was estimated to be ± 10% of the value which is typical for X-ray diffraction measurements of austenite. The error bars are only visible in fig. A1.3 for the larger volume fractions.

### A1.6.2 Retained austenite fractions as a function of time.

The experimental data (figs. A1.4a and b) indicate a maximum in the retained austenite content as a function of time during isothermal transformation to bainite. The rise is due to an increase in the carbon content of the retained austenite as the quantity of bainite increases. This higher carbon content stabilises the retained austenite so that less transforms to martensite on cooling. As further bainite forms, beyond the maximum, there is less austenite to be retained and so the volume fraction decreases again.

The model predictions show no variation of volume fraction austenite with hold time, but the values are roughly the same as the experimental and do change with composition. It is likely that the experimental results have substantial errors (greater then the estimated measurement accuracy), which could not be estimated because the original publications are not adequately detailed.

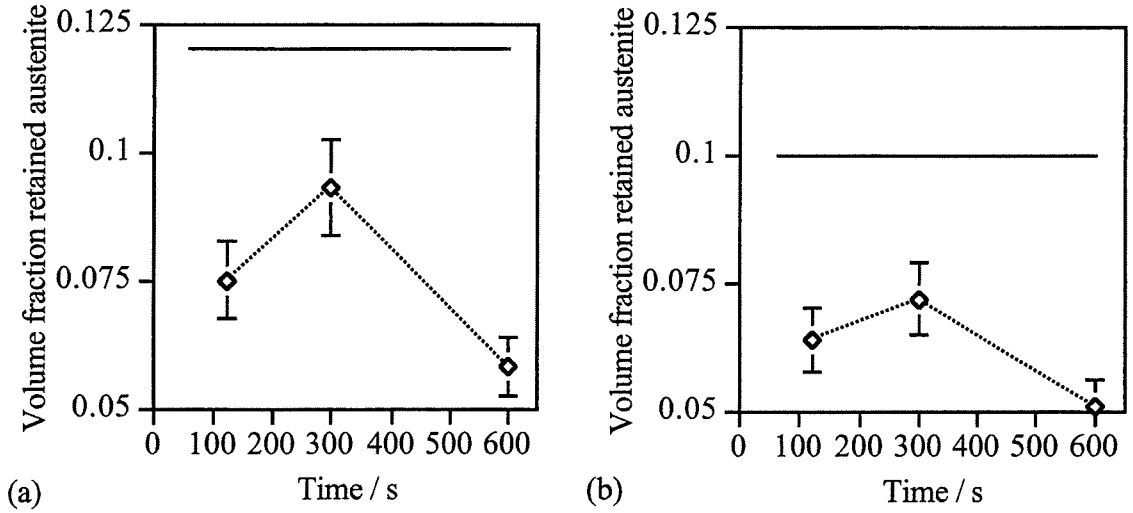


Fig. A1.4: Predicted (solid line) and experimental (dotted line) results of volume fraction retained austenite vs. isothermal hold time at 400 °C for (a) steel A and (b) steel B.

### A1.6.3 Retained austenite fractions as a function of temperature.

The experimental curves (figs. A1.5a and b) rose to a maximum and then decreased slightly with further increase in temperature.

At low temperatures the bainite that forms is lower bainite, thus some of the carbon is in the form of carbides, rather than in the retained austenite. This means more bainite can form before the carbon content of the austenite reaches the $T_0'$ curve, leading to a decrease in the retained austenite content.

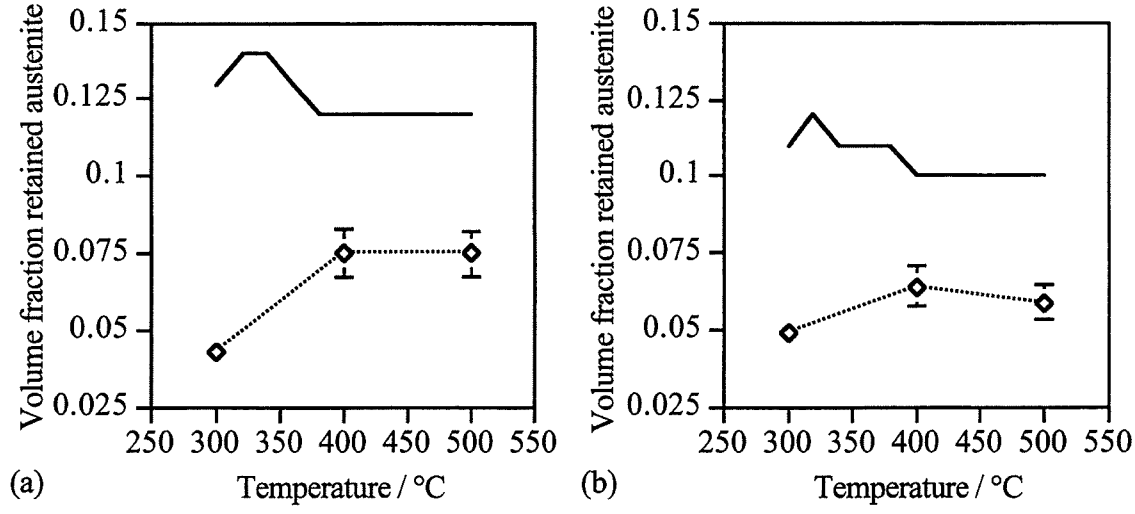


Fig. A1.5: Predicted (solid line) and experimental (dotted line) results of volume fraction retained austenite vs. isothermal hold temperature for 120 s for (a) steel A and (b) steel B.

At high temperatures there is less driving force for the nucleation of bainite, so there are fewer sheaves of bainite formed [Hanzaki *et al.*, 1995]. This means the morphology of the austenite is more blocky, rather than thin films, and so is more susceptible to transformation to martensite.

The predicted values of volume fraction retained austenite were higher than those measured, but not vastly different. The theory does not include the formation of lower bainite, thus should only predict the decrease in values at higher temperatures, which agrees with the results (figs. A1.5a and b). There was also a maximum predicted at a lower temperature which is inconsistent with the reported data. Note that the predicted variations are probably less than the accuracy of the experimental method.

Steel A contains niobium which increases the hardenability and slightly decreases $M_s$ temperature by solid solution strengthening of the parent austenite [Hanzaki *et al.*, 1995]. Thus the overall effect of the niobium is to increase the amount of retained austenite. This can be seen in the experimental results in figs. A1.4 and A1.5, but the predictions should not show this effect because Nb is not one of the elements included in the calculations. Note the higher austenite predictions for steel A are due to the higher carbon content of the steel.

### A1.6.4 Variations in the microstructure of steel C with time.

The predicted values shown in fig. A1.7a were for a different hold temperature (300 °C) than the experimental (400 °C, fig. A1.7b) as the program failed to predict a correct bainite start temperature for such high alloy steels.

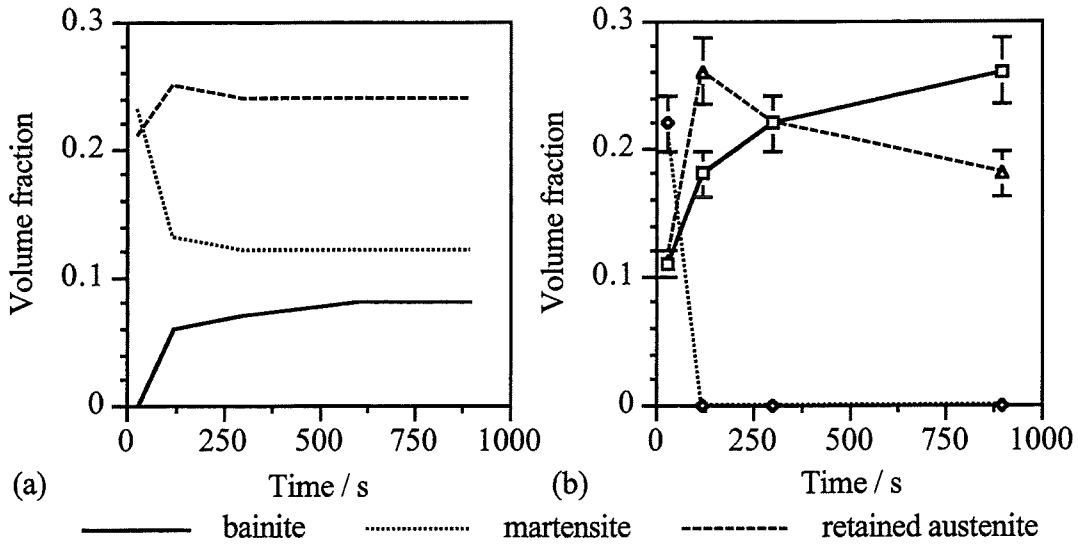


Fig. A1.7: Volume fraction of phases vs. isothermal hold time (a) predicted at 300 °C and (b) experimental at 400 °C [Bandoh *et al.*, 1988].

Martensite - the variations predicted were of a form similar to those observed, but the volume fraction became constant more rapidly in the calculated data. The decrease in volume fraction of martensite is due to the larger fraction of bainite.

Austenite - the shape of the curve and the values were predicted well. The volume fraction is low at first because of the relatively low carbon content of the austenite. With further transformation to bainite the austenite becomes more stable leading to an increase in retained austenite. With longer hold times more austenite transforms to bainite thus reducing the volume fraction retained.

Bainite - the shape of the curve is predicted well, though the fractions are underestimated. As time increased the reaction got further towards completion, thus the volume fraction increased and became constant.

### A1.6.5 Bainite transformation kinetics

The calculated bainite kinetics for steel D at various temperatures are compared with the experimental results in fig. A1.8. It was only possible to predict for two of the temperatures as the others were outside the predicted bainite transformation range ($M_S$ 323 C - $B_S$ 472 °C). It was also noted that pearlite formed during the 480 °C hold and lower bainite in the 330 °C hold, thus these results can be ignored in the present context.

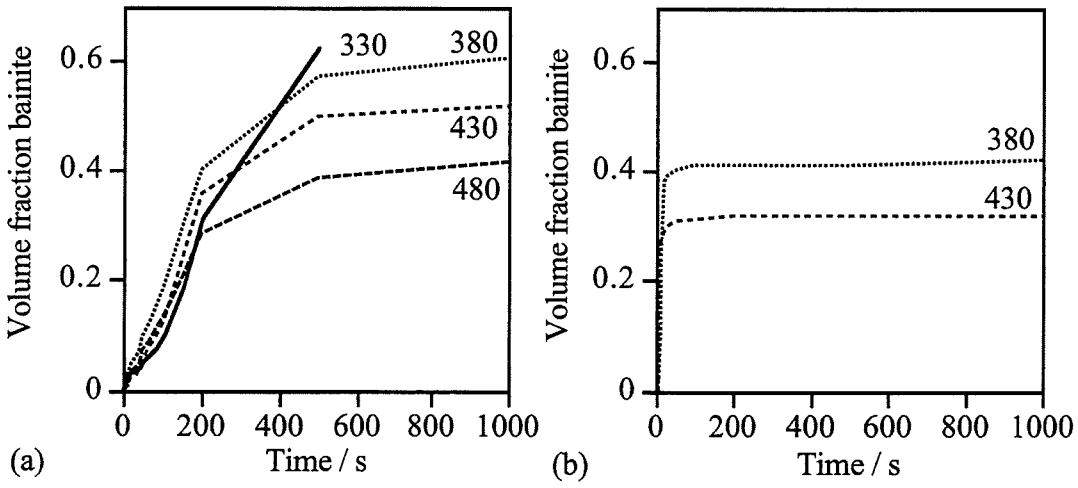


Fig. A1.8: Measured (a) and predicted (b) bainite kinetics for homogenised steel D.

As shown in fig. A1.8b the predicted kinetics were much faster than those measured and a constant bainite volume fraction was reached rapidly. Also the predicted total was considerably lower than that found experimentally. This last point might be explained in Chapter 4 with the use of $T_0$ and not $T_0'$ lines to calculate the maximum.

## A1.7 Conclusions

An assessment of published data has demonstrated that, whereas reasonable predictions can be made using phase transformation theory, there are significant discrepancies in detail. This may partly be due to inadequate experimental data, but may also be a consequence of poor predictions of the transformation kinetics.

For these reasons this model was later abandoned in preference of the more fundamental approach described in Chapter 4.

# A2. The Bainite Kinetics Program

## A2.1 Contents

A2.2 : MAP† format description of the computer program, the inputs and outputs.

A2.3 : Flow chart.

A2.4 : Tree diagram of functions and subroutines.

A2.5 : The FORTRAN source code.

[† MAP is The Materials Algorithms Project which consists of a perpetual FORTRAN library of complete programs and elementary subroutines and functions that enable the user to develop new concepts in materials science and metallurgy using existing methods as a foundation.

Web page: http://www.msm.cam.ac.uk/map/mapmain.html
Email: map@msm.cam.ac.uk]

## A2.2 MAP Format of Bainite Kinetics Program

Program speed.v11.for

### A2.2.1 Provenance

Naomi Chester June 1997. Based on model by G.I. Rees and H.K.D.H. Bhadeshia.

New subroutines: aread, cool2, fact, fine, funct, intan, iso, mucg, mucgread, mv, newf2, rough.

### A2.2.2 Purpose

To model bainite transformation kinetics during isothermal and continuous cooling heat treatments, including compensation for allotriomorphic ferrite formed during intercritical annealing. Also to predict the formation of martensite from the remaining austenite.

### A2.2.3 Description

A key part of this model is the function NEWF2 which contains an equation for the time to form a certain volume fraction of bainite. This equation used is a solution of equation (28) in [1] which has been integrated correctly. The integration uses a standard solution found in [2]. It also includes a linear change in the bainite platelet size with transformation temperature [3].

The program starts within subroutine MUCGREAD that reads the steel composition, isothermal temperature and austenite grain size. Intercritical annealing is taken into account, the composition converted into mole fractions and various other values calculated.

The constants are read in and the maximum volume fraction of bainite calculated using the Lever Rule [4] applied to the $T_0$ or $T_0'$ line.

Within the subroutine ISO the calculation option is chosen from: (1) isothermal, all volume fractions, (2) isothermal, one volume fraction, (3) one step continuous cooling and (4) many step continuous cooling.

For mode (1) the time for transformation is calculated for a series of volume fractions of bainite increasing by 0.01 until reaching the maximum possible.

For mode (2) the time for transformation is calculated for the required volume fraction of bainite.

For mode (3) the subroutine COOL2 is used. In this the cooling curve is cut into 50 equal sized isothermal steps. The Scheil method [5] is used which involves calculating the time required at a temperature to form the already formed volume fraction, adding the time for the temperature step and then calculating the new volume fraction at this temperature for the total time.

For mode (4) the time temperature steps are read in from a file called "cooling" and each step is cut into 20 isothermal steps. The calculations are then the same as for mode (3).

For each step the martensite start temperature ($M_S$) of the remaining austenite is calculated [6] and the bainite transformation will stop if this $M_S$ is above the present transformation temperature. After the bainite reaction has stopped the volume fraction of martensite which will form is calculated.

### A2.2.4 References

[1] Rees, G.I. and Bhadeshia, H.K.D.H.: Materials Science and Technology, 8, November 1992, 985-993.
[2] Rectorys, K.: "Survey of Applicable Mathematics", ILIFFE Books Ltd, London, 543, equation no. 410.
[3] L.C. Chang, "Bainite Transformation and Novel Bainitic Rail Steels" (PhD Thesis, Cambridge, 1995) pp. 46.
[4] Reed-Hill, R.E.: "Physical Metallurgy Principles", second edition, University Series in Basic Engineering, D. Van Nostrand Company, New York, 524 - 527.
[5] Christian, J.W.: "The Theory of Transformations in Metals and Alloys", Second edition, Pergamon Press, Oxford, (1975), 545.
[6] H.K.D.H. Bhadeshia, Metal Science, 15, (1981), 175-180.
[7] Bhadeshia, H.K.D.H.: J. Phys. (Orsay), vol 43, (C4), (1982), pp 443-448.

### A2.2.5 Parameters

*A2.2.5.1 Input*

K(8) - real array, the input composition of the steel in wt.% (corresponding to the alloying elements C, Si, Mn, Ni, Mo, Cr, V, Fe (Fe not entered, is assumed to be the remainder)).

TEMP - real, the input isothermal temperature in °C (converted in MUCGREAD into K)

ND - real, the grain size of the parental austenite in micrometers.

CNT - real, an array of 4 constants optimised for this equation with experimental data from [7]. The value for CNT(1) has been adjusted so that when the bainite platelet size is allowed to vary the CNT(1) value is its original value (0.34458D+02) at the temperature 405 °C. The values are:
CNT(1) = 0.57919D-06
CNT(2) = 0.14750D+03
CNT(3) = 0.20980D+05
CNT(4) = 0.30327D+02

ANS - real, the input answer for whether there is intercritical annealing or not. Yes: ANS = 1, No: ANS = 0 (only applies within subroutine INTAN).

VPRIOR - real, the input volume fraction of prior ferrite formed during the intercritical annealing, only required if ANS = 1.

TEMPI - real, the input intercritical annealing temperature in °C, only required if ANS = 1.

IN - integer, the input choice of calculation mode:
Isothermal, all volume fractions: IN = 1
Isothermal, one volume fraction: IN = 2
Continuous cooling one step: IN = 3
Continuous cooling many steps: IN = 4

ITO - integer, the input choice of whether $T_0$ or $T_0'$ lines are used for calculating the maximum volume fraction of bainite:
$T_0$: ITO = 0
$T_0'$: ITO = 1

VOL - real, the volume fraction input if IN = 2.

ST - real, the input start temperature for the cooling in °C, only required if IN = 3.

FT - real, the input finish temperature for the cooling in °C, only required if IN = 3.

TIME - real, the input time taken to cool from ST to FT in s, only required if IN = 3.

cooling - file, a file containing time and temperature pairs, only needed if IN = 4.
Time in s and temperature in °C. Typical "cooling" file:

| | |
|---|---|
| 0 | 600 |
| 125 | 350 |
| 175 | 300 |
| 300 | 20 |

*A2.2.5.2 Output*

out - file, into which the results of the calculations and the input parameters are printed. This information is also printed to the computer screen.

### A2.2.6 Example

*A2.2.6.1 Example input*

Isothermal, with intercritical annealing, all volume fractions, $T_0$ line used.

K(1) =0.38
K(2) =1.29
K(3) =1.73
K(4) = 0
K(5) = 0
K(6) = 0
K(7) = 0
TEMP = 430
ND = 16
ANS = 1
VPRIOR = 0.2
TEMPI = 800
IN = 1
ITO = 0

*A2.2.6.1 Example output*

out file:

**********

** Bainite Transformation Kinetics **

Cambridge University

Naomi Chester and Harry Bhadeshia

Program Version 11.0

CHEMICAL COMPOSITION

| | | | |
|---|---|---|---|
| Carbon | 0.380 wt.% | Silicon | 1.290 wt.% |
| Manganese | 1.730 wt.% | Nickel | 0.000 wt.% |
| Molybdenum | 0.000 wt.% | Chromium | 0.000 wt.% |
| Vanadium | 0.000 wt.% | | |

Austenite grain size (microns) = 16.
Allotriomorphic ferrite fraction = 0.20
Enriched carbon concentration (wt.%) = 0.473
Isothermal transformation temperature (°C) = 430.
Maximum volume fraction of bainite = 0.30

Values of model constants

K1/u (mm-1 s) = 0.58D-06
Lambda 1 = 0.15D+03
K2 (J/mol) = 0.21D+05
Lambda 2 = 0.30D+02

XBARN (mole fraction) = 0.0213
XTO (mole fraction) = 0.0339
XTO400 (mole fraction) = 0.0232

Calculated using $T_0$ line

| Fraction | Time (s) | u ($mm^3$) | Ms (°C) |
|---|---|---|---|
| 0.01 | 25.4 | 0.20D-07 | 273. |
| 0.02 | 43.9 | 0.20D-07 | 271. |
| 0.02 | 58.7 | 0.20D-07 | 268. |
| 0.03 | 71.2 | 0.20D-07 | 266. |
| 0.04 | 82.1 | 0.20D-07 | 264. |
| 0.05 | 92.0 | 0.20D-07 | 261. |
| 0.06 | 101.1 | 0.20D-07 | 259. |
| 0.06 | 109.5 | 0.20D-07 | 257. |
| 0.07 | 117.5 | 0.20D-07 | 254. |
| 0.08 | 125.0 | 0.20D-07 | 252. |
| 0.09 | 132.3 | 0.20D-07 | 249. |
| 0.10 | 139.4 | 0.20D-07 | 247. |
| 0.10 | 146.3 | 0.20D-07 | 244. |
| 0.11 | 153.1 | 0.20D-07 | 242. |

| | | | |
|---|---|---|---|
| 0.12 | 159.8 | 0.20D-07 | 239. |
| 0.13 | 166.4 | 0.20D-07 | 236. |
| 0.14 | 173.1 | 0.20D-07 | 233. |
| 0.14 | 179.7 | 0.20D-07 | 230. |
| 0.15 | 186.5 | 0.20D-07 | 227. |
| 0.16 | 193.3 | 0.20D-07 | 224. |
| 0.17 | 200.3 | 0.20D-07 | 221. |
| 0.18 | 207.5 | 0.20D-07 | 218. |
| 0.18 | 214.8 | 0.20D-07 | 214. |
| 0.19 | 222.5 | 0.20D-07 | 211. |
| 0.20 | 230.5 | 0.20D-07 | 208. |
| 0.21 | 238.9 | 0.20D-07 | 204. |
| 0.22 | 247.8 | 0.20D-07 | 200. |
| 0.22 | 257.3 | 0.20D-07 | 197. |
| 0.23 | 267.6 | 0.20D-07 | 193. |
| 0.24 | 278.9 | 0.20D-07 | 189. |
| 0.25 | 291.5 | 0.20D-07 | 185. |
| 0.26 | 305.9 | 0.20D-07 | 181. |
| 0.26 | 322.6 | 0.20D-07 | 176. |
| 0.27 | 342.9 | 0.20D-07 | 172. |
| 0.28 | 369.2 | 0.20D-07 | 167. |
| 0.29 | 407.0 | 0.20D-07 | 163. |
| 0.30 | 478.0 | 0.20D-07 | 158. |

Ms of Residual Austenite (°C) = 158.
Fraction of martensite = 0.26 to 0.39
Fraction of retained austenite = 0.25 to 0.11

### A2.2.7 Second example

*A2.2.7.1 Input*

Continuous cooling, no intercritical annealing, $T_0'$ line used
K(1) = 0.38
K(2) = 1.29
K(3) = 1.73
K(4) = 0
K(5) = 0
K(6) = 0
K(7) = 0
ND = 16

ANS = 0
IN = 3
ITO = 1
ST = 500
TIME = 3000

*A2.2.7.2 Output*

out file:

**********

** Bainite Transformation Kinetics **

Cambridge University

Naomi Chester and Harry Bhadeshia

Program Version 11.0

CHEMICAL COMPOSITION

| | | | | | |
|---|---|---|---|---|---|
| Carbon | 0.380 | wt.% | Silicon | 1.290 | wt.% |
| Manganese | 1.730 | wt.% | Nickel | 0.000 | wt.% |
| Molybdenum | 0.000 | wt.% | Chromium | 0.000 | wt.% |
| Vanadium | 0.000 | wt.% | | | |

Austenite grain size (microns) = 16.
Allotriomorphic ferrite fraction = 0.00
Enriched carbon concentration (wt.%) = 0.380

Values of model constants

| | | |
|---|---|---|
| K1/u ($mm^{-1}$ s) | = | 0.58D-06 |
| Lambda 1 | = | 0.15D+03 |
| K2 (J/mol) | = | 0.21D+05 |
| Lambda 2 | = | 0.30D+02 |

Continuous cooling transformation
Start temperature (C) = 500.
Finish temperature (C) = 20.
Cooling time (s) = 3000.

Calculated using $T_0'$ line

| Fraction | CTEMP | Time | u ($mm^3$) | XTO | XTO400 | Ms (°C) |
|---|---|---|---|---|---|---|

| | | | | | | |
|---|---|---|---|---|---|---|
| 0.00 | 500.0 | 0.0 | 0.00D-00 | 0.026 | 0.015 | 319. |
| 0.00 | 476.0 | 150.0 | 0.00D-00 | 0.028 | 0.018 | 303. |
| 0.17 | 452.0 | 300.0 | 0.22D-07 | 0.031 | 0.021 | 261. |
| 0.36 | 428.0 | 450.0 | 0.19D-07 | 0.034 | 0.023 | 221. |
| 0.44 | 404.0 | 600.0 | 0.17D-07 | 0.037 | 0.025 | 188. |
| 0.51 | 380.0 | 750.0 | 0.14D-07 | 0.040 | 0.028 | 148. |
| 0.57 | 356.0 | 900.0 | 0.12D-07 | 0.043 | 0.031 | 108. |
| 0.62 | 332.0 | 1050.0 | 0.89D-08 | 0.046 | 0.034 | 65. |
| 0.66 | 308.0 | 1200.0 | 0.64D-08 | 0.050 | 0.038 | 24. |
| 0.69 | 284.0 | 1350.0 | 0.50D-08 | 0.054 | 0.041 | -18. |
| 0.72 | 260.0 | 1500.0 | 0.50D-08 | 0.058 | 0.045 | -70. |
| 0.74 | 236.0 | 1650.0 | 0.50D-08 | 0.062 | 0.048 | -143. |
| 0.77 | 212.0 | 1800.0 | 0.50D-08 | 0.065 | 0.052 | -273. |
| 0.78 | 188.0 | 1950.0 | 0.50D-08 | 0.067 | 0.055 | -273. |
| 0.78 | 164.0 | 2100.0 | 0.50D-08 | 0.068 | 0.058 | -273. |
| 0.81 | 140.0 | 2250.0 | 0.50D-08 | 0.069 | 0.060 | -273. |
| 0.81 | 116.0 | 2400.0 | 0.50D-08 | 0.069 | 0.061 | -273. |
| 0.81 | 92.0 | 2550.0 | 0.50D-08 | 0.069 | 0.062 | -273. |
| 0.81 | 68.0 | 2700.0 | 0.50D-08 | 0.069 | 0.063 | -273. |
| 0.82 | 44.0 | 2850.0 | 0.50D-08 | 0.069 | 0.063 | -273. |
| 0.82 | 20.0 | 3000.0 | 0.50D-08 | 0.068 | 0.063 | -273. |

Retained austenite fraction at 20 °C = 0.18

Martensite fraction = 0.00

### A2.2.8 Auxiliary routines (all routines used in this program)

afeg
analy
aread
axto
bound
cg
cool2
energy
fact
fine
fto1
funct
gmaax
g91

intan
iso
mart
marta
martb
mart2
mstart
mucg
mucgread
mv
newf2
omega
rcool
reed
reedi
rough
xalph

### A2.2.9 Key words

Bainite kinetics
Isothermal transformation
Continuous cooling
Intercritical annealing

## A2.3 Flow Chart for Bainite Kinetics Program

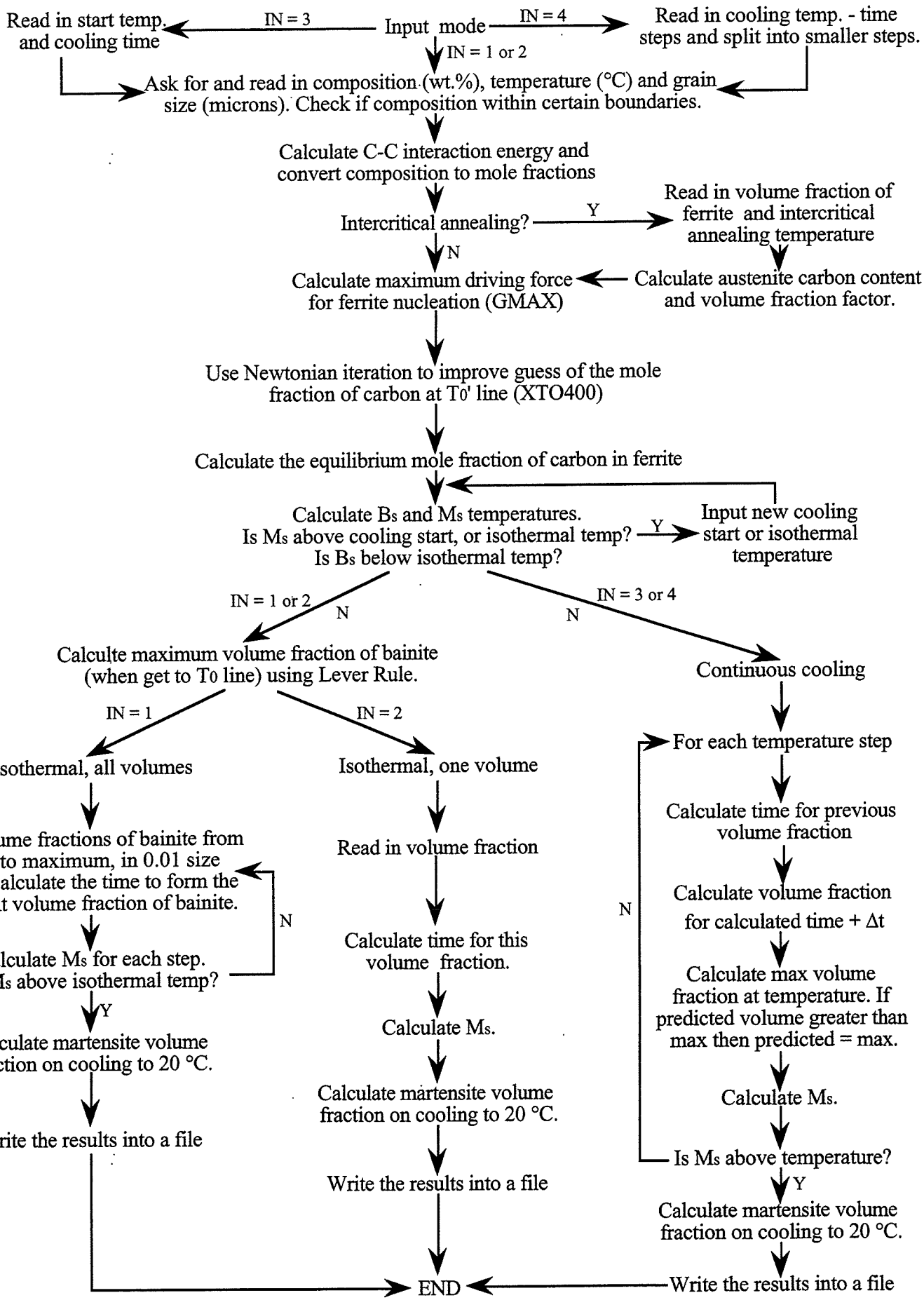

## A2.4 Tree of Bainite Kinetics Program

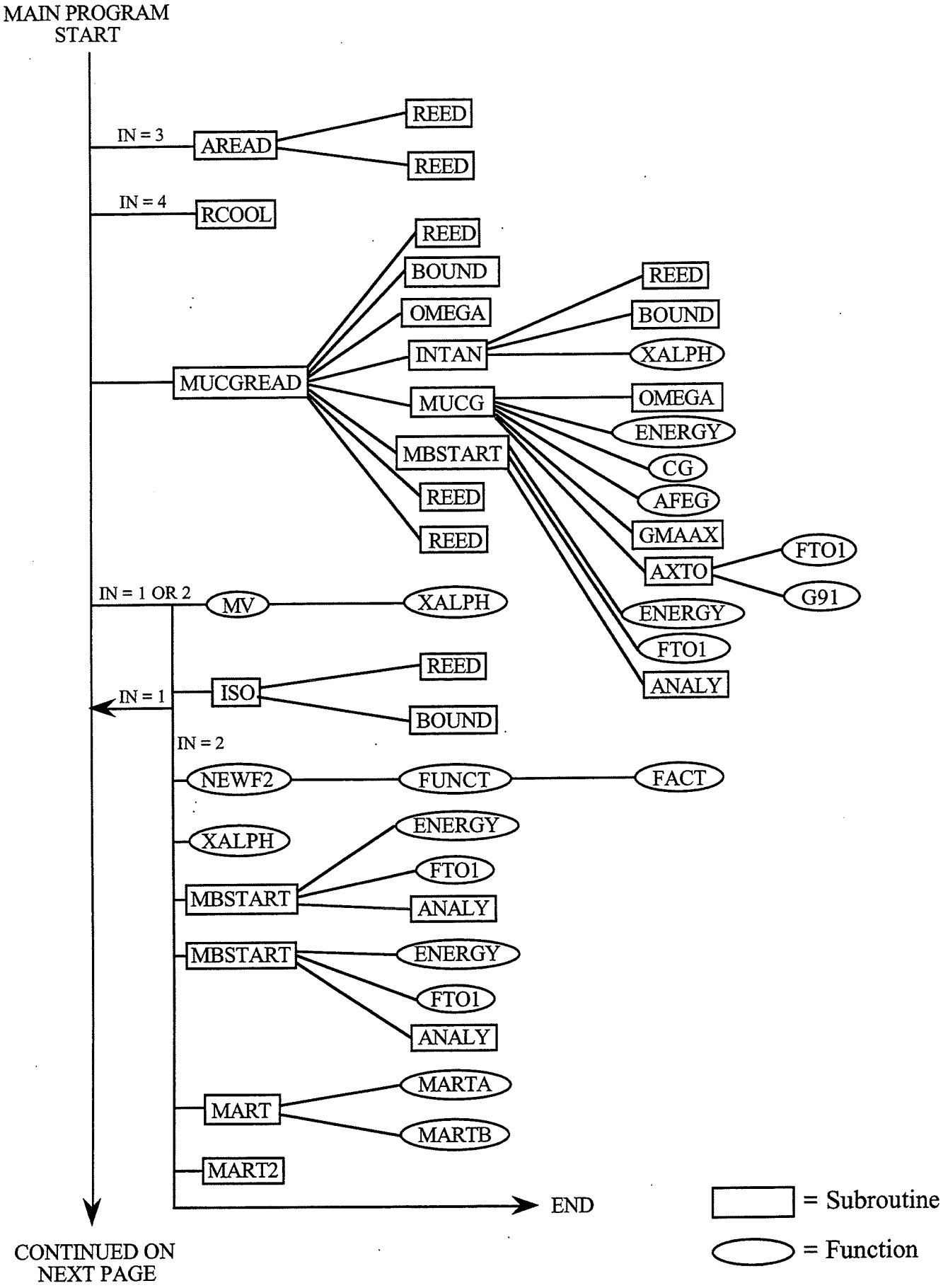

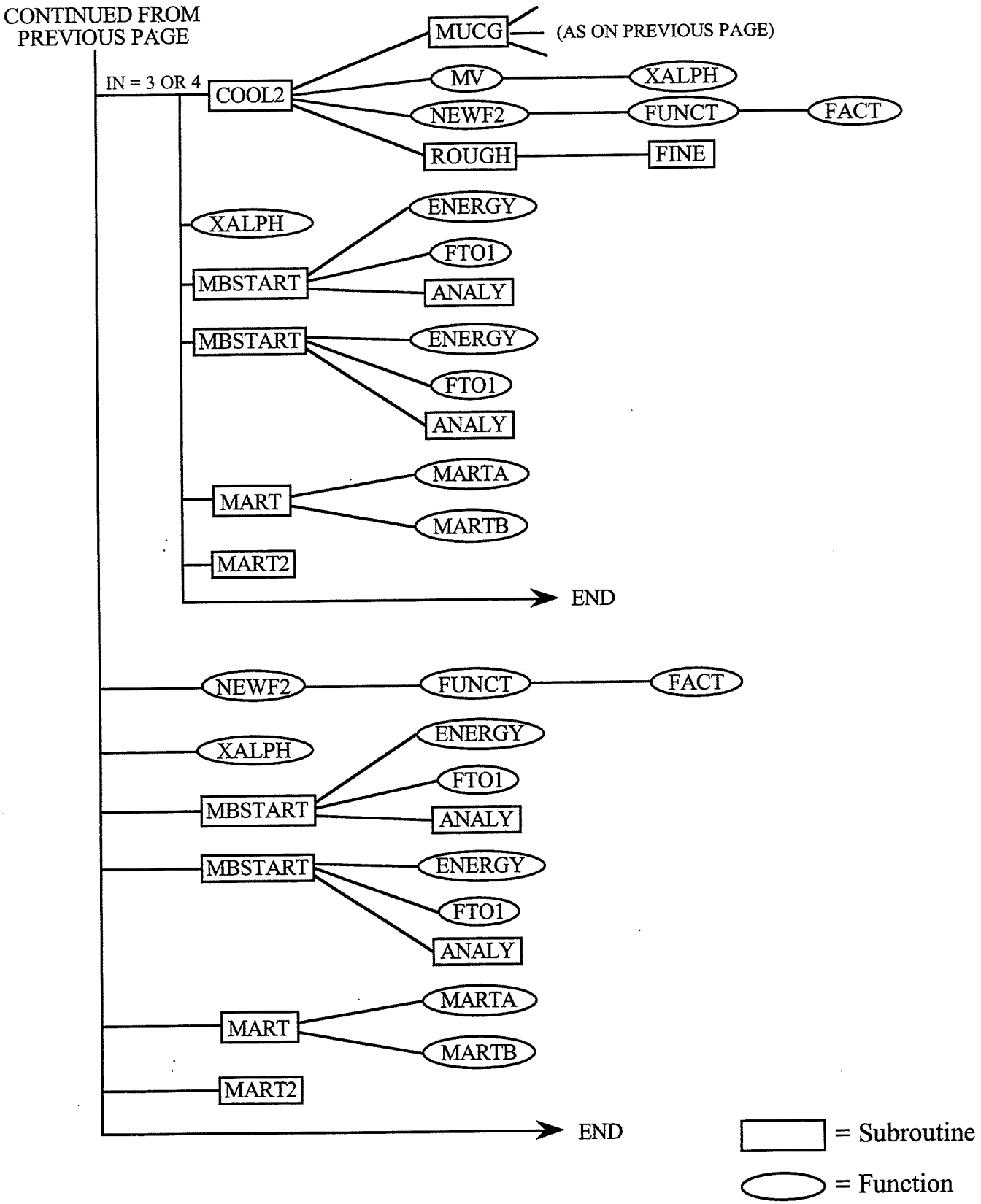
CONTINUED FROM PREVIOUS PAGE
IN = 3 OR 4
COOL2
MUCG
(AS ON PREVIOUS PAGE)
MV
XALPH
NEWF2
FUNCT
FACT
ROUGH
FINE
XALPH
ENERGY
FTO1
MBSTART
ANALY
MBSTART
ENERGY
FTO1
ANALY
MARTA
MART
MARTB
MART2
END
NEWF2
FUNCT
FACT
XALPH
ENERGY
FTO1
MBSTART
ANALY
MBSTART
ENERGY
FTO1
ANALY
MARTA
MART
MARTB
MART2
END
= Subroutine
= Function

```
C ****************** BAINITE TRANSFORMATION KINETICS **********
C
          PROGRAM MAIN
C
          IMPLICIT DOUBLE PRECISION (A-H,K-Z),INTEGER (I,J)
          DIMENSION CNT(4),C(8),K(8),AV(1000),ACTEMP(1000),AU(1000),
      &                 AXTO(1000),AXTO400(1000),COTEMP(1000),
      &                 COTIME(1000),ATIME(1000)
C
         WRITE(*,22)
         READ (*,*) IN
22       FORMAT (20X,' ** Heat treatment details for Bainite **'//
      & 22X,' Isothermal transformation                    = 1'/
      & 22X,' Time to isothermally achieve given fraction = 2'/
      & 22X,' Continuous cooling one step                  = 3'/
      & 22X,' Continuous cooling many steps                = 4'/)
C
         IF(IN .EQ. 3) CALL AREAD(ST,FT,TIME2)
         IF(IN .EQ. 3) KTEMP=ST
C
         WRITE(*,223)
         READ (*,*) ITO
223      FORMAT (20X,'Stop at To = 0'/
      &  20X,'or stop at To-dashed = 1')
C
C number each temperature step is divided into for continuous cooling
         AB4=100.0
C
         IF(IN .EQ. 4) THEN
          CALL RCOOL(AB4,J2,JS,COTEMP,COTIME)
          KTEMP=COTEMP(1)
C
C so that printout is correct:
          ST=COTEMP(1)
          FT=COTEMP(J2)
          TIME2=COTIME(J2)
         ENDIF
C
          CALL MUCGREAD(C,K,KBAR,DGM,KTEMP,XTO400,XTO,
      &                 XBARN,ND,FF,T10,T20,W,W1,IN,MS0,XBAR,BS)
C
               OPEN (UNIT=3,FILE='out')
C
C set version number
               AVER=11.0
C
C Set kinetic constants
               CNT(1)=0.57919D-06
               CNT(2)=0.14750D+03
               CNT(3)=0.20980D+05
               CNT(4)=0.30327D+02
C -------------------------------------------------
               IF(IN .EQ. 1 .OR. IN .EQ. 2)THEN
C
C              Calculate the maximum fraction of bainite during
C              isothermal transformation at KTEMP,allowing for
C              the carbon enrichment caused by prior ferrite
C
               IF(ITO .EQ. 0) THEN
               MAXVOL=MV (KTEMP,XTO,XBARN)
               ELSE
               MAXVOL=MV (KTEMP,XTO400,XBARN)
               ENDIF
               MAV=MAXVOL*FF
C
               IF (BS .LT. KTEMP-273) GOTO 40
               IF (XBARN .GT. XTO400) GOTO 50
C
               WRITE(3,3) AVER, KBAR,K(2),K(3),K(4),K(5)
      &             ,K(6),K(7),ND,(1.0-FF),K(1),KTEMP-273,MAV
               WRITE(*,3) AVER, KBAR,K(2),K(3),K(4),K(5)
      &             ,K(6),K(7),ND,(1.0-FF),K(1),KTEMP-273,MAV
               ELSE
               WRITE(3,12) AVER, KBAR,K(2),K(3),K(4),K(5)
      &             ,K(6),K(7),ND,(1.0-FF),K(1)
               WRITE(*,12) AVER, KBAR,K(2),K(3),K(4),K(5) &
                    ,K(6),K(7),ND,(1.0-FF),K(1)
               ENDIF
C-------------------------------------------------------
      WRITE (3,2) CNT(1),CNT(2), CNT(3),CNT(4)
      WRITE (*,2) CNT(1),CNT(2), CNT(3),CNT(4)
C
      PSI=0.0D0
      CALL ISO (IN,VA,MAV,FF)
C
C     ------------------------------------------
C     Calculate time to achieve specified fraction
C     ------------------------------------------
      IF (IN .EQ. 2) THEN
20          PSI=VA/MAXVOL
```

```
            IF (VA .GE. MAXVOL) GOTO 9
            TIME=NEWF2(KTEMP,DGM,PSI,MAXVOL,ND,CNT,XBARN,U)
            VA=VA*FF
C
            WRITE(*,8) XBARN,XTO,XTO400
            WRITE(3,8) XBARN,XTO,XTO400
                IF(ITO .EQ. 0) THEN
                 WRITE(*,23)
                 WRITE(3,23)
                ELSE
                 WRITE(*,24)
                 WRITE(3,24)
                ENDIF
                WRITE(*,5)
                WRITE(3,5)
                WRITE(3,15) VA,TIME,U
                WRITE(*,15) VA,TIME,U
                XRICH=(XBAR-XALPH(KTEMP)*(1.0D+00-FF+VA))/(FF-VA)
C*****************************************************************
                JTLOW=200+273
                JTHIGH=500+273
                 CALL MBSTART(T10,T20,W,W1,JTLOW,
     &                        JTHIGH,MS,XRICH,1,BS)
                IF(MS .GE. 280.0D0)THEN
                 JTLOW=(MS-80)+273
                 JTHIGH=(MS+80)+273
                ELSE
                 JTLOW=200+273
                 JTHIGH=400+273
                ENDIF
C*****************************************************************
                CALL MBSTART(T10,T20,W,W1,JTLOW,JTHIGH,MS,XRICH,1,BS)
                CALL MART(MS,20.0D+00,FF-VA,VMART,VAUSTR)
                CALL MART2(MS,20.0D+00,FF-VA,VMART2,VAUSTR2)
                WRITE(*,11)MS,VMART,VMART2,VAUSTR,VAUSTR2
                WRITE(3,11)MS,VMART,VMART2,VAUSTR,VAUSTR2
                GOTO 9
            ENDIF
C           -------------------------------------------
C           Calculate fraction during continuous cooling
C           -------------------------------------------
            IF (IN .GE. 3) THEN
                CALL COOL2 (K,ND,CNT,FF,AV,ACTEMP,AU,AXTO,AXTO400,ATIME
     &                    ,ICALC,ST,FT,TIME2,J2,COTIME,COTEMP,IN,ITO,BS)
                WRITE(3,6)ST-273,FT-273,TIME2
                WRITE(*,6)ST-273,FT-273,TIME2
C
C To write out the number of steps in the cooling curve
                IF (IN.EQ. 4) THEN
                    WRITE(3,19)JS
                    WRITE(*,19)JS
                ENDIF
C
                IF(ITO .EQ. 0) THEN
                    WRITE (*,23)
                    WRITE (3,23)
                ELSE
                    WRITE (*,24)
                    WRITE (3,24)
                ENDIF
C
                WRITE (*,7)
                WRITE (3,7)
                DO 21 I=1,ICALC
                    KTEMP2=ACTEMP(I)+273
                    VA=AV(I)
                    XRICH=(XBAR-XALPH(KTEMP2)*(1.0D+00-FF+VA))/(FF-VA)
C*****************************************************************
C New temperature ranges for MS calculations (avoid jump at 500 C).
                IF(I  .EQ. 1)THEN
                    JTLOW=200+273
                    JTHIGH=500+273
                    CALL MBSTART(T10,T20,W,W1,JTLOW,
     &                           JTHIGH,MS,XRICH,1,BS)
                ENDIF
                    IF(MS .GE. 280.0D0)THEN
                     JTLOW=(MS-80)+273
                     JTHIGH=(MS+80)+273
                    ELSE
                     JTLOW=200+273
                     THIGH=400+273
                    ENDIF
C*****************************************************************
                IF(MS .GT. -273.0) THEN
                    CALL MBSTART(T10,T20,W,W1,JTLOW,
     &                           JTHIGH,MS,XRICH,1,BS)
                ENDIF
                WRITE(3,4) AV(I),ACTEMP(I),ATIME(I),AU(I),
     &                     AXTO(I),AXTO400(I),MS
                WRITE(*,4) AV(I),ACTEMP(I),ATIME(I),AU(I),
```

```
     &                    AXTO(I),AXTO400(I),MS
                IF(MS .LT. FT-273 .AND. I .EQ. ICALC) THEN
                    WRITE(*,14) FT-273,(FF-VA)
                    WRITE(3,14) FT-273,(FF-VA)
                    GOTO 21
                ENDIF
                IF(MS .GT. ACTEMP(I)) THEN
                    CALL MART(MS,FT-273,FF-VA,VMART,VAUSTR)
                    CALL MART2(MS,FT-273,FF-VA,VMART2,VAUSTR2)
                    WRITE(*,11)MS,VMART,VMART2,VAUSTR,VAUSTR2
                    WRITE(3,11)MS,VMART,VMART2,VAUSTR,VAUSTR2
                    GOTO 9
                ENDIF
21      CONTINUE
                GOTO 9
        ENDIF
C           ------------------------------------------------
C           Calculate fraction during isothermal transformation
C           ------------------------------------------------
                WRITE(*,8) XBARN,XTO,XTO400
                WRITE(3,8) XBARN,XTO,XTO400
                IF(ITO .EQ. 0) THEN
                    WRITE (*,23)
                    WRITE (3,23)
                ELSE
                    WRITE (*,24)
                    WRITE (3,24)
                ENDIF
                WRITE (*,16)
                WRITE (3,16)
                DO 10 I=1,100
                    VA=I*0.010D0
                    PSI=VA/MAXVOL
                    IF (VA .GE. MAXVOL)THEN
                      VA=VA-0.01
                      VA=VA*FF
                      GOTO 18
                     ENDIF
                TIME=NEWF2(KTEMP,DGM,PSI,MAXVOL,ND,CNT,XBARN,U)
                VA=VA*FF
                XRICH=(XBAR-XALPH(KTEMP)*(1.0D+00-FF+VA))/(FF-VA)
C*****************************************************************
                    JTLOW=200+273
                    JTHIGH=500+273
                    CALL MBSTART(T10,T20,W,W1,JTLOW,
     &                          JTHIGH,MS,XRICH,1,BS)
                  IF(MS .GE. 280.0D0)THEN
                    JTLOW=(MS-80)+273
                    JTHIGH=(MS+80)+273
                  ELSE
                    JTLOW=200+273
                    JTHIGH=400+273
                  ENDIF
C*****************************************************************
                CALL MBSTART(T10,T20,W,W1,JTLOW,JTHIGH,MS,XRICH,1,BS)
                    WRITE (3,17) VA,TIME,U,MS
                    WRITE (*,17) VA,TIME,U,MS
10              CONTINUE
18                  IF(MS .GT. 20.0D+00) THEN
                      CALL MART(MS,20.0D+00,FF-VA,VMART,VAUSTR)
                      CALL MART2(MS,20.0D+00,FF-VA,VMART2,VAUSTR2)
                      WRITE(*,11)MS,VMART,VMART2,VAUSTR,VAUSTR2
                      WRITE(3,11)MS,VMART,VMART2,VAUSTR,VAUSTR2
                    ENDIF
C*****************************************************************
C
          GOTO 9
40        WRITE (*,*) '       ** Temperature above Bs ***'
          GOTO 9
50        WRITE (*,*) 'Enriched carbon content higher than XTO400'
          GOTO 9
C
C       -------------------------------------------------
C                 Format statements only
C       -------------------------------------------------
1         FORMAT(10X,' Maximum volume fraction of bainite =',
     &             F8.2//)
2         FORMAT(10X, ' Values of model constants '//
     &    15X, 'K1/u (mm-1 s)    = ',D10.2/
     &    15X, 'Lambda 1         = ',D10.2/
     &    15X, 'K2 (J/mol)       = ',D10.2/
     &    15X, 'Lambda 2         = ',D10.2/)
3         FORMAT(///
     &10X,'*******************************************',
     &'**************'//
     &20X,'**   Bainite Transformation Kinetics  **'//
     &20X,'          Cambridge University '/
     &20X,'    Naomi Chester and Harry Bhadeshia'///
     &10X,' Program Version ',F3.1 /
     &10X,' CHEMICAL COMPOSITION'///
```

```
     &10X,' Carbon      ',F6.3,'  wt.%',9X,' Silicon  ',F6.3,'  wt.%'/
     &10X,' Manganese   ',F6.3,'  wt.%',9X,' Nickel   ',F6.3,'  wt.%'/
     &10X,' Molybdenum  ',F6.3,'  wt.%',9X,' Chromium ',F6.3,'  wt.%'/
     &10X,' Vanadium    ',F6.3,'  wt.%'//
     &10X,' Austenite grain size (microns)              = ', F8.0/
     &10X,' Allotriomorphic ferrite fraction            = ', F8.2/
     &10X,' Enriched carbon concentration (wt.%)        = ', F8.3/
     &10X,' Isothermal transformation temperature (C)   = ', F8.0/
     &10X,' Maximum volume fraction of bainite          = ', F8.2/
     &//)
4     FORMAT (5X,F10.2,F10.1,F12.1,D14.2,2F8.3,F8.0)
5     FORMAT( 20X,'Fraction   Time (s)     u (mm3)      ')
6     FORMAT(10X,' Continuous cooling transformation '/
     &       15X,' Start temperature  (C)     = ',F8.0/
     &       15X,' Finish temperature (C)     = ',F8.0/
     &       15X,' Cooling time (s)           = ',F8.0/)
7     FORMAT( 10X,'Fraction  CTEMP        Time      u (mm3)    '
     &                ,' XTO      XTO400   Ms (C)')
8     FORMAT(15X,' XBARN    (mole fraction)  = ',F8.4/
     &       15X,' XTO     (mole fraction)    = ',F8.4/
     &       15X,' XTO400  (mole fraction)    = ',F8.4//)
11    FORMAT(//10X,' Ms of Residual Austenite (C)    = ',F8.0/
     &         10X,' Fraction of martensite          = ',F8.2
     &           , '   to',F7.2/
     &         10X,' Fraction of retained austenite = ', F8.2
     &           , '   to' ,F7.2/)
12    FORMAT(///
     &10X,'*********************************************',
     &'**************'//
     &20X,'**   Bainite Transformation Kinetics  **'//
     &20X,'          Cambridge University '/
     &20X,'    Naomi Chester and Harry Bhadeshia'///
     &10X,' Program Version ',F3.1 /
     &10X,' CHEMICAL COMPOSITION'///
     &10X,' Carbon      ',F6.3,'  wt.%',9X,' Silicon    ',F6.3,'  wt.%'/
     &10X,' Manganese   ',F6.3,'  wt.%',9X,' Nickel     ',F6.3,'  wt.%'/
     &10X,' Molybdenum  ',F6.3,'  wt.%',9X,' Chromium   ',F6.3,'  wt.%'/
     &10X,' Vanadium    ',F6.3,'  wt.%'//
     &10X,' Austenite grain size (microns)       = ', F8.0/
     &10X,' Allotriomorphic ferrite fraction     = ', F8.2/
     &10X,' Enriched carbon concentration (wt.%) = ', F8.3/
     &//)
14    FORMAT(//10X,' Retained austenite fraction at ',F6.0,' C = '
     &          ,F8.2/
     &       10X,  ' Martensite fraction = 0.00')
15    FORMAT (15X,F10.2,F12.1,D14.2,2F8.3,F8.0)
16    FORMAT( 20X,'Fraction   Time (s)     u (mm3)     Ms (C) ')
17    FORMAT (15X,F10.2,F12.1,D14.2,F8.0)
19    FORMAT (15X,' Number of cooling steps = ',I6//)
23    FORMAT (15X,'Calculated using To line'//)
24    FORMAT (15X,'Calculated using To-dashed line'//)
C      ------------------------------------------------------------
C
9     STOP
      END
C
C*********************************************************************
C*********************************************************************
C*********************************************************************
C AFEG AFEG LN ACTIVITY OF IRON IN GAMMA
      DOUBLE PRECISION FUNCTION AFEG(XEQ,AJ)
      DOUBLE PRECISION XEQ,AJ,DEQ,TEQ
      DEQ=DSQRT(1-2*(1+2*AJ)*XEQ+(1+8*AJ)*XEQ*XEQ)
      TEQ=5*DLOG((1-XEQ)/(1-2*XEQ))
      TEQ=TEQ+DLOG(((1-2*AJ+(4*AJ-1)*XEQ-DEQ)/(2*AJ*(2*XEQ-1)))**6)
      AFEG=TEQ
      RETURN
      END
C
C*********************************************************************
C Linear regression
C H. K. D. H. Bhadeshia, 1989
C
C CONST is the best fit slope of the regression line
C CORR is the correlation coefficient
C J is set to the number of x,y pairs input into the subroutine
C J9 is the number of x,y pairs which are not to be
C included in the analysis. Only the first J-J9 pairs are analysed
C JB is set to 1 if the regression results need to be printed(NOT USED)
C SLOPE is the best fit slope of the regression line
C X is an array of x values
C Y is an array of y values
C
      SUBROUTINE ANALY(J,J9,CONST,SLOPE,CORR,X,Y,JB)
      IMPLICIT REAL*8(A-H,K-Z),INTEGER(I,J)
      DOUBLE PRECISION X(100),Y(100)
C
      J8=J-J9
      AX=0.0D+00
      AY=0.0D+00
```

```
        AX2=0.0D+00
        AY2=0.0D+00
        AXY=0.0D+00
C
        DO 1 I=1,J8
          AX=AX+X(I)
          AY=AY+Y(I)
          AXY=AXY+X(I)*Y(I)
          AX2=AX2+X(I)*X(I)
          AY2=AY2+Y(I)*Y(I)
1       CONTINUE
C
        CONST=(AY*AX2-AX*AXY)/(J8*AX2-AX*AX)
        SLOPE=((J8*AXY-AX*AY)/(J8*AX2-AX*AX))
        CORR=(J8*AXY-AX*AY)/(DSQRT((J8*AX2-AX*AX)*
       &(J8*AY2-AY*AY)))
C
C       IF(JP .EQ. 1)WRITE(*,2)CONST,SLOPE,CORR,JP
2       FORMAT('   INTERCEPT=',D12.4,'    SLOPE=',D10.3,
       &'       CORRELATION=',F8.4, I10)
C
           RETURN
           END
C*********************************************************************
C Subroutine for heat treatment parameters during continuous cooling
C
        SUBROUTINE AREAD(ST,FT,TIME)
        IMPLICIT REAL*8(A-H,K-Z),INTEGER(I,J)
C
C read start and finish temperatures, cooling time
9       WRITE (*,2)
        CALL REED (ST)
        FT=20.00D+00
        IF (ST .LT. FT) THEN
         WRITE (*,4)
         CALL REED (ST)
        ENDIF
        WRITE (*,5)
        CALL REED(TIME)
C
C convert to absolute temperatures
        ST=ST+273.0D0
        FT=FT+273.0D0
C
2       FORMAT(30X,' Start temperature (C) ?')
4       FORMAT(30X,' Start temperature must exceed finish temperature'/
       &        35X,' Enter start temperature again ')
5       FORMAT(30X,' Cooling time (s) ?')
C
        RETURN
        END
C*********************************************************************
        SUBROUTINE AXTO(H,S,H1,S1,XTO,T,W,W1,F,AJ,AJ1,STORE,J)
        IMPLICIT REAL*8(A-H,K-Z),INTEGER(I,J)
        J=0
1       DFTO=FTO1(H,S,XTO,T,W,W1,H1,S1,F,AJ,AJ1)+STORE
        J=J+1
        IF (DABS(DFTO) .LE. 10.0D+00) GOTO 2
        G9=G91(XTO,T,W,W1,H1,S1,F,H,S,AJ,AJ1)
        IF (J  .GE. 9) GOTO 2
        XTO=XTO-DFTO/G9
        IF (XTO  .LE. 1.0D-12) GOTO 3
        GOTO 1
3       XTO=0.0000D+00
2       RETURN
        END
C
C*********************************************************************
        SUBROUTINE BOUND(A,B,C)
        DOUBLE PRECISION A,B,C
2        WRITE(*,1)B,C
1       FORMAT(12X,' Input value out of bounds'/
       &14X,' The limits are ',D12.4,' to ', D12.4/)
        CALL REED(A)
        IF(A .LT. B .OR. A .GT. C)GOTO 2
        RETURN
        END
C
C*********************************************************************
C CG DOUBLE PRECISION FUNCTION GIVING LFG LN(ACTIVITY)
C OF CARBON IN AUSTENITE
        DOUBLE PRECISION FUNCTION CG(X,T,W,R)
        DOUBLE PRECISION J,DG,DUMMY,T,R,W,X
        J=1.0-DEXP(-W/(R*T))
             IF(X    .LE. 1.0D-10) THEN
                CG=DLOG(1.0D-10)
             ELSE
                DG=DSQRT(1-2*(1+2*J)*X+(1+8*J)*X*X)
                DUMMY=5*DLOG((1-2*X)/X)+6*W/(R*T)+((38575.0)-(
       &        13.48)*T)/(R*T)
```

```
            CG=DUMMY+DLOG(((DG-1+3*X)/(DG+1-3*X))**6)
          ENDIF
        RETURN
        END
C*************************************************************
C Continuous cooling calculations.
C
        SUBROUTINE COOL2(K,ND,CNT,FF,AV,ACTEMP,AU,
       &           AXTO,AXTO400,ATIME,ICALC,ST,FT,TIME,J2,
       &           COTIME,COTEMP,IN,ITO,BS)
        IMPLICIT REAL*8 (A-H,K-Z), INTEGER (I,J)
        DOUBLE PRECISION CNT(4),C(8),K(8),AV(1000),ACTEMP(1000),
       &AU(1000),AXTO(1000),AXTO400(1000),COTEMP(1000),
       &COTIME(1000),ATIME(1000)
C
C ICALC divides the temperature interval into discrete steps (if IN=3)
C ICALC cannot be increased beyond 1000 without modifying the
C matrix dimensions in both subroutine and main program
          ICALC=21
C
C Reset matrices
C
          DO 1 I=1,1000
            AV(I)=0.0D+00
            ACTEMP(I)=0.0D+00
            AU(I)=0.0D+00
            AXTO(I)=0.0D+00
            AXTO400(I)=0.0D+00
1         CONTINUE
C
        VA=0.0D0
        PSI=0.0D0
C
        IF (IN .EQ. 4) THEN
           ICALC=J2
           GOTO 333
        ENDIF
C
        DTIME=0.0
        DTEMP=ST-FT
        DTEMP=DTEMP/(ICALC-1)
C-------------------------------------------------------
333     DO 10 J=1,ICALC
           X=J-1
        IF (IN .EQ. 4) THEN
           TEMP=COTEMP(J)
           IF(J .GT. 1) DTIME=COTIME(J)-COTIME(J-1)
        ELSE
           TEMP=ST-(X*DTEMP)
           IF(J .GT. 1) DTIME=TIME/(ICALC-1)
        ENDIF
        CALL MUCG(C,K,TEMP,ND,DGM,XTO400,XTO,XBARN,T10,T20,W,W1)
           IF (BS .LT. TEMP-273) THEN
            V=0.0000D+00
            CTEMP=TEMP-273.0D0
            GOTO 20
           ENDIF
           IF(ITO .EQ. 0) THEN
            MAXVOL=MV (KTEMP,XTO,XBARN)
            ELSE
            MAXVOL=MV (KTEMP,XTO400,XBARN)
            ENDIF
        PSI=VA/MAXVOL
        PTIME=NEWF2(TEMP,DGM,PSI,MAXVOL,ND,CNT,XBARN,U)
        TTIME=PTIME+DTIME
        CALL ROUGH(TEMP,DGM,MAXVOL,ND,CNT,XBARN,TTIME,VOL)
        CTEMP=TEMP-273.0D0
        V=VOL*FF
        VA=VOL
C
20        AV(J)=V
          ACTEMP(J)=CTEMP
          AU(J)=U
          AXTO(J)=XTO
          AXTO400(J)=XTO400
C
          IF (IN .EQ. 3) THEN
             ATIME(J)=DTIME*(J-1)
          ELSE
             ATIME(J)=COTIME(J)
          ENDIF
C
10      CONTINUE
C
        RETURN
        END
C*************************************************************
C       ENERGY
        DOUBLE PRECISION FUNCTION ENERGY(T,T10,T20)
        DOUBLE PRECISION T,T10,T20,F,T7
```

```
      T7=T-100*T20
      IF (T7 .LT. 300) GOTO 1
      IF (T7 .LT. 700) GOTO 2
      IF (T7 .LT. 940) GOTO 3
      F=-8.88909+0.26557*(T7-1140)-1.04923D-3*((T7-1140)**2)
      F=F+2.70013D-6*((T7-1140)**3)-3.58434D-9*((T7-1140)**4)
      GOTO 4
1     F=1.38*T7-1499
      GOTO 4
2     F=1.65786*T7-1581
      GOTO 4
3     F=1.30089*T7-1331
4     ENERGY=(141.0*T10 + F)*4.187
      RETURN
      END
C*****************************************************************
C Calculates the factorial of number passed to it
C
      DOUBLE PRECISION FUNCTION FACT(IY)
      IMPLICIT DOUBLE PRECISION (A-H,L-Z)
      IMPLICIT INTEGER (I-K)
      A=1.0D0
      DO 20 J=1,IY
      A=J*A
20    CONTINUE
      FACT=A
      END
C*****************************************************************
C Finer search for volume fraction for a given temperature.
C
      SUBROUTINE FINE(TEMP,DGM,MAXVOL,ND,CNT,XBARN,TTIME,VHIGH,VOL)
      IMPLICIT REAL*8 (A-H,K-Z), INTEGER (I,J)
      DOUBLE PRECISION CNT(4)
C
       VLOW=VHIGH-0.01D0
       DO 30 I=1,100
          VA=VLOW+(I*0.00010D0)
20        PSI=VA/MAXVOL
          TIME=NEWF2(TEMP,DGM,PSI,MAXVOL,ND,CNT,XBARN,U)
          IF (TIME .GT. TTIME) GOTO 31
30     CONTINUE
C
31     VOL=VA
C
       RETURN
       END
C*****************************************************************
C
      DOUBLE PRECISION FUNCTION FTO1
     &(H,S,X,T,W,W1,H1,S1,F,AJ,AJ1)
     DOUBLE PRECISION R,X,T,T60,ZEN1,ZEN2,ZENER,W,W1,H1,S1,F,
     &AJ,AJ1,D,D11,H,S
      D=DSQRT(1-2*(1+2*AJ)*X+(1+8*AJ)*X*X)
      D11=DSQRT(9-6*X*(2*AJ1+3)+(9+16*AJ1)*X*X)
      T60=T*(1-X)/(28080*X)
      IF (T60 .GT. 1.0) GOTO 18
      IF (T60 .GT. 0.25) GOTO 17
      ZEN1=0.2307+42.7974*T60-233.8631*T60*T60+645.4485*T60*T60*T60
     &-954.3995*(T60**4)+711.8095*(T60**5)-211.5136*(T60**6)
      ZEN2=-2.6702+45.6337*T60-225.3965*T60*T60+567.7112*(T60**3)
     &-771.6466*(T60**4)+538.1778*(T60**5)-151.3818*(T60**6)
      GOTO 16
17    ZEN2=1
      ZEN1=3.295
16    ZENER=(((ZEN2*X)**2)*(-50898.56)/(1-X))+ZEN1*T*X*0.6623741
      ZENER=ZENER*4.187
      GOTO 15
18    ZENER=0.0
15    R=8.31432
      FTO1=X*R*T*DLOG(X*X)+X*(H1-(H)-(S1-(S)
     &)*T+4*W1-6*W)-R*T*(1-X)*DLOG((1-X)**4)+5*R*T*(1-2*X)*DLOG(1-2*X)
     &-R*T*X*DLOG(((D-1+3*X)/(D+1-3*X))**6)-R*T*(1-X)*DLOG(((1-2*AJ+(4
     &*AJ-1)*X-D)/(2*AJ*(2*X-1)))**6)+3*R*T*X*DLOG(3-4*X)+R*T*
     &X*DLOG(((D11-3+5*X)/(D11+3-5*X))**4)+(1-X)*F+ZENER
      RETURN
      END
C
C*****************************************************************
C Function which is an infinite series (20 steps done here)
C
      DOUBLE PRECISION FUNCTION FUNCT(X)
      IMPLICIT DOUBLE PRECISION (A-H,L-Z)
      IMPLICIT INTEGER (I-K)
C
      B=0.0D0
       DO 10 I=1,20
         A=FACT(I)
         C=X**I
         B=(C/(A*I))+B
10     CONTINUE
```

```
        FUNCT=B
C
        END
C
C*****************************************************************
        SUBROUTINE GMAAX(A1,A,W1,F,R,T,X,AFE,H1,S1)
        IMPLICIT REAL*8(A-H,K-Z)
C CALCULATION OF THE OPTIMUM NUCLEUS C CONTENT AND ACTIVITY OF C IN
C FERRITE NUCLEUS
C
C Estimate a value for X
C February 1991
         X=6.3998D-07*T-3.027D-04
         IF(X .LT. 0.1D-07)X=1.0D-08
         IF(X .GT. 0.32D-03)X=0.32D-03
C Estimation complete
C
        AJ1=1.0D+00-DEXP(-W1/(R*T))
1       D1=DSQRT(9.0D+00-6.0D+00*X*(2.0D+00*AJ1+3.0D+00)
       &+(9.0D+00+16.0D+00*AJ1)*X*X)
        B1=((D1-3.0D+00+5.0D+00*X)/(D1+3.0D+00-5.0D+00*X))
        B2=((3.0D+00-4.0D+00*X)/X)
        B3=(H1 - S1*T + 4.0D+00*W1)/(R*T)
        A1=DLOG(B1*B1*B1*B1*B2*B2*B2)+B3
C
        IF(X .GT. 1.0D-08)THEN
           A1FE=DLOG(1.0D+00-X)
        ELSE
           A1FE=X
        ENDIF
C
        TEST=F+R*T*(A1FE-AFE) - R*T*(A1-A)
C
C Newton iteration
C
        IF (DABS(TEST) .GT. 10.0) THEN
           DA1=(3.0D+00*X/(3.0D+00-4.0D+00*X))*(
       &    (4.0D+00*X-3.0D+00)/(X*X)-4.0D+00/X)
           DA2=(0.5D+00/D1)*(-12.0D+00*AJ1-18.0D+00+
       &    18.0D+00*X+32.0D+00*AJ1*X)
           DA2=4.0D+00*(((DA2+5.0D+00)/(D1-3.0D+00+5.0D+00*X))
       &    -((DA2-5.0D+00)/(D1+3.0D+00-5.0D+00*X)))
           DA1=DA1+DA2
           DA1FE=1.0D+00/(X-1.0D+00)
           ERROR=TEST/(R*T*(DA1FE-DA1))
           IF (ERROR .GT. X) ERROR = 0.3D+00*X
           X=DABS(X-ERROR)
           GOTO 1
        ENDIF
C End of iteration
        RETURN
        END
C*****************************************************************
C
        DOUBLE PRECISION FUNCTION G91(XTO,T,W,W1,H1,S1,F,
       &H,S,AJ,AJ1)
        DOUBLE PRECISION R,XTO,T,W,W1,H1,S1,F,AJ,AJ1,FD,FD1,DT5,
       &DT6,DZEN1,DZEN2,DZEN3,V1,V2,V3,V4,V5,V6,V7,V8,V9,G1,
       &DZEN6,DZEN7,DZEN8,H,S
        R=8.31432
        FD=DSQRT(1-2*(1+2*AJ)*XTO+(1+8*AJ)*XTO*XTO)
        FD1=DSQRT(9-6*XTO*(2*AJ1+3)+(9+16*AJ1)*XTO*XTO)
        DT5=28080*XTO/(1-XTO)
        DT6=T/DT5
        IF (DT6 .GT. 1.0) GOTO 48
        IF (DT6 .LT. 0.25) GOTO 47
        DZEN1=0.2307+42.7974*DT6-233.8631*(DT6**2)+645.4485*(DT6**3)
       &-954.3995*(DT6**4)+711.8095*(DT6**5)-211.5136*(DT6**6)
        DZEN2=-2.6702+45.6337*DT6-225.3965*(DT6**2)+567.7112*(DT6**3)
       &-771.6466*(DT6**4)+538.1778*(DT6**5)-151.3818*(DT6**6)
        GOTO 46
47      DZEN2=1
        DZEN1=3.295
46      DZEN3=(((DZEN2*XTO)**2)*(-50898.56)/(1-XTO))+DZEN1*T*XTO*
       &(0.6623741)
        DZEN3=DZEN3*4.187
        GOTO 45
48      DZEN3=0.0
45      V1=FD-1+3*XTO
        V2=FD+1-3*XTO
        V3=1-2*AJ+(4*AJ-1)*XTO-FD
        V4=2*AJ*(2*XTO-1)
        V5=FD1-3+5*XTO
        V6=FD1+3-5*XTO
        V7=(XTO-1-2*AJ+8*XTO*AJ)/FD
        V8=(9*XTO-9-6*AJ1+16*AJ1*XTO)/FD1
        V9=H1-(H)-(S1-(S))*T-6*W+4*W1
        G1=2+DLOG(XTO**2)+4+DLOG((1-XTO)**4)-10-DLOG((1-2*XTO)**10)
       &-DLOG((V1/V2)**6)-6*((XTO/V1)*(V7+3+V1*(3-V7)/V2))
       &+DLOG((V3/V4)**6)-6*((1-XTO)/V3)*(4*AJ*(1-(V3/V4))-V7)
```

```
      &+3*(DLOG(3-4*XTO)-4*XTO/(3-4*XTO))+DLOG((V5/V6)**4)+4*(XTO
      &/V5)*(V8+5+(V5/V6)*(5-V8))
       IF (DT6  .GT. 1.0) GOTO 90
       DZEN6=(-3.3948+13.6112*DT6-13.4376*(DT6**2))*T/(28080*
      &((1-XTO)**2))
       DZEN7=(-3.3118+15.7462*DT6-23.2449*(DT6**2))*T/(28080*
      &((1-XTO)**2))
       DZEN8=50898*((DZEN2*XTO)**2)/((1-XTO)**2)+(-50898*(2*
      &DZEN2*DZEN6*(XTO**2)+2*XTO*(DZEN2**2))/(1-XTO))+DZEN1
      &*T*0.6623741+DZEN7*T*XTO*0.6623741
       GOTO 91
90     DZEN8=0.0
91     G91=V9+R*T*G1+DZEN8-F
       RETURN
       END
C ***************************************************************
C Intercritical annealing calculations.
C
        SUBROUTINE INTAN (FGAMMA,C,CGAMMA)
        IMPLICIT DOUBLE PRECISION (A-H,K-Z),INTEGER (I,J)
        DIMENSION C(8)
C
C FGAMMA is the fraction of austenite in intercritically annealed sample
C VPRIOR is the ferrite at intercritical annealing temperature
C CGAMMA is the carbon concentration of residual austenite (wt %)
C CALPHA is the solubility of carbon in ferrite at intercritical
C temperature (wt %)
C
         CBAR=C(1)
         CGAMMA=CBAR
C
            WRITE (*,1)
            READ (*,*) ANS
            IF(ANS .EQ. 0) THEN
               FGAMMA=1.0D+00
               GOTO 4
            ENDIF
C
            WRITE (*,2)
             CALL REED(VPRIOR)
            IF(VPRIOR .LT. 0.0D-00 .OR. VPRIOR .GT. 1.0D+00)
     &         CALL BOUND(VPRIOR, 0.0D-00, 1.0D+00)
            WRITE (*,3)
            READ (*,*) CTEMP
            KTEMP=CTEMP+273.15
C
C Calculate C concentration in ferrite, crudely convert to wt%
C
            CALPHA=(1201.15/55.84)*XALPH(KTEMP)
C
C Estimate carbon-enrichment of austenite due to prior ferrite
C
            FGAMMA = 1.0D+00 - VPRIOR
            CGAMMA = (CBAR-CALPHA*VPRIOR)/(FGAMMA)
C
1        FORMAT(30X,' Intercritically annealed ? (Yes = 1, No = 0)')
2        FORMAT(30X,' Fraction of allotriomorphic ferrite ?')
3        FORMAT(30X,' Intercritical anneal temperature (°C) ?')
4       RETURN
        END
C***************************************************************
C Reads in which mode is required.
C
        SUBROUTINE ISO(IN,VOL,MAV,FF)
        IMPLICIT REAL*8 (A-H,K-Z), INTEGER (I,J)
C
        IF (IN .EQ. 1) GOTO 10
        IF (IN .EQ. 2) GOTO 20
C
10      VOL=0.0D0
        RETURN
C
20       WRITE (*,1)
         CALL REED (VF)
         IF (VF .LT. 0.0D0 .OR. VF .GT. MAV)
     &    CALL BOUND(VF,0.0D0,MAV)
         VOL=VF*1.0D0
         VOL=VOL/FF
        RETURN
C
1       FORMAT (30X,' Volume fraction of bainite ?')
C
        RETURN
        END
C
C ***************************************************************
C H. K. D. H. Bhadeshia
C
C To calculate the fraction of martensite as a function of the
C undercooling below the Ms temperature using the method of
```

```
C S. A. Khan and H. K. D. H. Bhadeshia
C Materials Science and Engineering A A129 (1990) 257-272
C
      SUBROUTINE MART(MS,TQ,VAUST,VMART,VAUSTR)
C
      IMPLICIT DOUBLE PRECISION (A-H,K-Z)
C
C guess a value for the volume fraction of martensite, VMART
      IF(MS-TQ .GT. 70.0D+00)THEN
       VMART=0.5D+00
      ELSE
         MART=0.05D+00
      ENDIF
C
1     A=MARTA(VMART,MS,TQ)
      B=MARTB(VMART)
       IF(DABS(A) .GT. 0.01D+00)THEN
        VMART=DABS(VMART - A/B)
        IF(VMART .GE. 1.0D+00) VMART=0.99D+00
        GOTO 1
       ENDIF
C
      VMART=VMART*VAUST
      VAUSTR=VAUST-VMART
C
      RETURN
      END
C ***************************************************************
C H. K. D. H. Bhadeshia
C
C Function subroutine for estimating MARTA
C
C To help calculate the fraction of martensite as a function of the
C undercooling below the Ms temperature using the method of
C S. A. Khan and H. K. D. H. Bhadeshia
C Materials Science and Engineering A A129 (1990) 257-272
C
      DOUBLE PRECISION FUNCTION MARTA(VMART,MS,TQ)
      IMPLICIT REAL*8(A-H,K-Z), INTEGER(I,J)
C
      M=0.0029D+00
      MARTA=(-(DLOG(1.0D+0-VMART))/VMART)-M*(MS-TQ)-1.0D+0
C
      RETURN
      END
C ***************************************************************
C H. K. D. H. Bhadeshia
C
C To help calculate the fraction of martensite as a function of the
C undercooling below the Ms temperature using the method of
C S. A. Khan and H. K. D. H. Bhadeshia
C Materials Science and Engineering A A129 (1990) 257-272
C
C  Function subroutine for estimating GDASH (derivative of MARTA)
C
      DOUBLE PRECISION FUNCTION MARTB(VMART)
      IMPLICIT DOUBLE PRECISION (A-H,L-Z)
C
      MARTB=(1.0D+0/((1.0D+0-VMART)*VMART))
     &+((DLOG(1.0D+0-VMART))/(VMART*VMART))
C
      RETURN
      END
C ***************************************************************
C H. K. D. H. Bhadeshia
C
C To calculate the fraction of martensite as a function of the
C undercooling below the Ms temperature using the method of
C D. P. Koistinen and R. E. Marburger
C Acta Metallurgica 7 (1959) 59
C
      SUBROUTINE MART2(MS,TQ,VAUST,VMART,VAUSTR)
C
      IMPLICIT DOUBLE PRECISION (A-H,K-Z)
C
C guess a value for the volume fraction of martensite, VMART
         VMART=1.0D+00-DEXP(-0.011*(MS-TQ))
         VMART=VMART*VAUST
         VAUSTR=VAUST-VMART
C
      RETURN
      END
C***************************************************************
C To calculate the martensite-start temperature
C H. K. D. H. Bhadeshia, University of Cambridge
C
C MS is the martensite-start temperatures in degrees centigrade
C BS is the bainite-start temperatures in degrees centigrade
C
C JTLOW, JTHIGH  are set
```

```
C They define the range over which calculations are done
C IT defines the temperature interval at which calculations done C
C Particular caution needed in passing JHIGH & JLOW to MBSTART,
C bearing in mind that these are integers.
C
C T10 and T20 are defined by subroutine OMEGA. They are functions
C of the substitutional solute content of the alloy.
C W and W1 represent the carbon-carbon interaction energies in
C austenite and ferrite respectively, in Joules per mole.
C X1 is the carbon concentration in mole fraction
C
      SUBROUTINE MBSTART(T10,T20,W,W1,JTLOW,JTHIGH,MS,X1,JB,BS)
C
      IMPLICIT REAL*8 (A-H,K-Z), INTEGER (I,J)
      DOUBLE PRECISION DCTEMP(100), FTO(100)
C
C Initialize J1 and J2
      J1=0
      J2=0
C
C  Initialise FT0 and DCTEMP
       DO 22 IL=1,100
        FTO(IL)=0.0D+00
        DCTEMP(IL)=0.0D+00
22     CONTINUE
C
C Guess a value of XTO, the carbon concentration (mole fraction)
C given by the T-zero curve of the Temperature versus Carbon plot
C (phase diagram)
C
      XTO=0.07D+00
C
C R is the universal gas constant
C
      R=8.3143D+00
C
C H is the excess partial molar enthalpy of solution of carbon in
C austenite
C S is the excess partial molar entropy of solution of carbon in
C austenite
C H is in Joules per mole, S is in Joules per mole per K
C G. J. Shiflet, J. R. Bradley and H. I. Aaronson, Metallurgical
C Transactions
C A, 9A (1978) 999.
C
      H=38575.0D+00
      S=13.48D+00
C
C This is to ensure that JTLOW, JTHIGH, JT are not changed on exit
C
      ITLOW=JTLOW
      ITHIGH=JTHIGH
2     IT=(ITHIGH-ITLOW)/20
      IF(IT .LT. 5)THEN
       ITHIGH=5*IT+ITLOW
       GOTO 2
      ENDIF

      IF(ITLOW .LT. 413)THEN
       ITLOW=413
       ITHIGH=513
      ENDIF
C
C H1 is the excess partial molar enthalpy of solution of carbon in
C ferrite
C S1 is the excess partial molar entropy of solution of carbon in
C ferrite
C H1 is in Joules per mole, S1 is in Joules per mole per K
C J. A. Lobo and G. H. Geiger, Metallurgical Transactions A 7A (1976),
C pages 1347 and 1359.
C
      DO 1 J= ITLOW,ITHIGH,IT
C
       J1=J1+1
       KTEMP=J
C
       IF (KTEMP .GE. 1000.0) THEN
        H1=105525.0D+00
        S1=45.34521D+00
       ELSE
        H1=111918.0D+00
        S1=51.44D+00
       ENDIF
C
C Calculate the free energy change for the transformation of austenite
C to ferrite of the same chemical composition
C
      F=ENERGY(KTEMP,T10,T20)
      AJ=1.0D+00-DEXP(-W/(R*KTEMP))
```

```
        AJ1=1.0D+00-DEXP(-W1/(R*KTEMP))
        FTO(J1)=FTO1(H,S,X1,KTEMP,W,W1,H1,S1,F,AJ,AJ1)
C
C Calculate the temperature in degrees centigrade
C
        DCTEMP(J1)=KTEMP-273.0D+00
C
1       CONTINUE
C
C Linear regression to obtain the free energy change for the
C transformation of austenite to ferrite of the same chemical
C composition, as a function of the temperature
C
        CALL ANALY(J1,0,CONST,SLOPE,CORR,DCTEMP,FTO,JB)
C
        IF(JB .EQ. 0) THEN
           BS=(-400.0-CONST)/SLOPE
        ENDIF
C
C Calculate the martensite-start temperatures
C Modification made February 1991 to allow for large carbon
C concentrations
C Based on Metal Science paper on thermodynamics of martensitic
C transformations in plain carbon steels
C
C H. K. D. H. Bhadeshia, Metal Science 15 (1981) 175-177
C H. K. D. H. Bhadeshia, Metal Science 15 (1981) 178-180
C
        XMS=X1
        IF(XMS .GT. 0.0594D+00)XMS=0.0594D+00
        MS=(-1086.9D+00 + 2941.8D+00*XMS - 9.6016D+05*XMS*XMS
       &+ 2.5382D+07*XMS*XMS*XMS - 1.8488D+08*XMS*XMS*XMS*XMS
       & - CONST)/SLOPE
        IF(MS .le. -273.00)MS=-273.15
C
           RETURN
           END
C*************************************************************
C This subroutine calculates GMAX and XTO400 (volume fraction of
C bainite at T0' line). Adaption of MUCG46, N Chester 19/10/95
C
        SUBROUTINE MUCG(C,K,T,ND,GMAX,XTO400,XTO,XBARN,T10,T20,W,W1)
        IMPLICIT REAL*8 (A-H,K-Z), INTEGER (I,J)
        DOUBLE PRECISION C(8),K(8)
C
        CALL OMEGA(C,K,W,XBARN,T10,T20,0)
        FTO=-1.0
        X1=C(1)
        XA=0.001D+00
        R=8.31432D+00
        W1=48570.0D+00
        H=38575.0D+00
        S=13.48D+00
        XEQ=0.2D+00
        XTO=0.07D+00
        XTO400=0.06D+00
C
        CTEMP=T-273.00D+00
        IF (T .LE. 1000.0) GOTO 22
        H1=105525.0D+00
        S1=45.34521D+00
        GOTO 19
22      H1=111918.0D+00
        S1=51.44D+00
19      F=ENERGY(T,T10,T20)
        AJ=1.0D+00-DEXP(-W/(R*T))
        AJ1=1.0D+00-DEXP(-W1/(R*T))
        A=CG(X1,T,W,R)
        AFE=AFEG(X1,AJ)
C
        CALL GMAAX(A1,A,W1,F,R,T,X,AFE,H1,S1)
        GMAX=R*T*(A1-A)
        CALL AXTO(H,S,H1,S1,XTO400,T,W,W1,F,AJ,AJ1,400.0D+00,J99)
        CALL AXTO(H,S,H1,S1,XTO,T,W,W1,F,AJ,AJ1,0.0D+00,J98)
C
        RETURN
        END
C*************************************************************
C This subroutine reads in composition, temperature and grain size.
C
        SUBROUTINE MUCGREAD(C,K,KBAR,GMAX,T,XTO400,XTO,
       &                    XBARN,ND,FF,T10,T20,W,W1,IN,MS0,XBAR,BS)
        IMPLICIT REAL*8 (A-H,K-Z), INTEGER (I,J)
        DOUBLE PRECISION C(8),K(8)
C
        WRITE(*,707)
707     FORMAT(19X,' Carbon wt.% ?')
        CALL REED(K(1))
        IF(K(1) .LT. 0.1D-03 .OR. K(1) .GT. 2.0D+00)
       &CALL BOUND(K(1),0.1D-03,2.0D+00)
```

```
        KBAR=K(1)
       WRITE(*,708)
       CALL REED(K(2))
       IF(K(2) .LT. 0.0D+00 .OR. K(2) .GT. 2.5D+00)
      &CALL BOUND(K(2),0.0D+00,2.5D+00)
708    FORMAT(19X,' Silicon wt.% ?')
       WRITE(*,709)
       CALL REED(K(3))
       IF(K(3) .LT. 0.0D+00 .OR. K(3) .GT. 3.5D+00)
      &CALL BOUND(K(3),0.0D+00,3.5D+00)
709    FORMAT(19X,' Manganese wt.% ?')
       WRITE(*,710)
       CALL REED(K(4))
       IF(K(4) .LT. 0.0D+00 .OR. K(4) .GT. 4.5D+00)
      &CALL BOUND(K(4),0.0D+00,4.5D+00)
710    FORMAT(19X,' Nickel wt.% ?')
711    FORMAT(19X,' Molybdenum wt.% ?')
       WRITE(*,711)
       CALL REED(K(5))
       IF(K(5) .LT. 0.0D+00 .OR. K(5) .GT. 1.5D+00)
      &CALL BOUND(K(5),0.0D+00,1.5D+00)
712    FORMAT(19X,' Chromium wt.% ?')
       WRITE(*,712)
       CALL REED(K(6))
       IF(K(6) .LT. 0.0D+00 .OR. K(6) .GT. 3.5D+00)
      &CALL BOUND(K(6),0.0D+00,3.5D+00)
713    FORMAT(19X,' Vanadium wt.% ?')
       WRITE(*,713)
       CALL REED(K(7))
       IF(K(7) .LT. 0.0D+00 .OR. K(7) .GT. 1.5D+00)
      &CALL BOUND(K(7),0.0D+00,1.5D+00)
715    FORMAT(19X,' Grain Size microns ?')
       WRITE(*,715)
       CALL REED(ND)
C
       CALL OMEGA (C,K,W,XBAR,T10,T20,0)
C
       IF(IN .GE. 3) THEN
        CALL INTAN (FF,K,CRICH)
        K(1)=CRICH
        CALL MUCG (C,K,T,ND,GMAX,XTO400,XTO,XBARN,T10,T20,W,W1)
        XRICH=C(1)
        JTLOW=200+273
        JTHIGH=500+273
        CALL MBSTART(T10,T20,W,W1,JTLOW,JTHIGH,MS0,XRICH,0,BS)
        IF(MS0+273 .GT. T) THEN
         WRITE(*,2)MS0
         CALL REED(CTEMP1)
         T=CTEMP1+273
        ENDIF
        RETURN
       ENDIF
C
714    FORMAT(23X,' Isothermal transformation temperature deg.C ?'/)
       WRITE(*,714)
       CALL REED(TEMP)
C
       TEMP=TEMP+273
       T=TEMP*1.0D+00
       CALL INTAN (FF,K,CRICH)
       K(1)=CRICH
       CALL MUCG (C,K,T,ND,GMAX,XTO400,XTO,XBARN,T10,T20,W,W1)
       XRICH=C(1)
       JTLOW=200+273
       JTHIGH=500+273
       CALL MBSTART(T10,T20,W,W1,JTLOW,JTHIGH,MS0,XRICH,0,BS)
       IF(MS0+273 .GT. T) THEN
        WRITE(*,3)MS0
        CALL REED(CTEMP1)
        T=CTEMP1+273
       ENDIF
C
       IF(BS+273 .LT. T) THEN
        WRITE(*,4)BS
        CALL REED(CTEMP1)
        T=CTEMP1+273
       ENDIF
C
2      FORMAT(10X,' The start temperature is below Ms  (',F8.0,')'/
      &       10X,' Please input new value of start Temperature (C)'/)
3      FORMAT(10X,' Isothermal trans. temperature below Ms (',F8.0,')'/
      &       10X,' Input new value of transformation temperature (C)'/)
4      FORMAT(10X,' Isothermal trans. temperature above Bs (',F8.0,')'/
      &       10X,' Input new value of transformation temperature (C)'/)
C
       RETURN
       END
C*********************************************************************
C Calculates maximum volume fraction of ferrite at To'line.
C
```

```
      DOUBLE PRECISION FUNCTION MV (T,XTO,XBARN)
      IMPLICIT DOUBLE PRECISION (A-H,L-Z),INTEGER (I-K)
         XA=XALPH(T)
         MV=(XTO-XBARN)/(XTO-XA)
      END
C*****************************************************************
C NEWF2 the t=function corrected from Gethin's paper
C
      DOUBLE PRECISION FUNCTION NEWF2 (TK,GM0,PSI,THETA,ND,CD,XB,U)
      IMPLICIT DOUBLE PRECISION (A-H,L-Z),INTEGER (I-K)
      PARAMETER (R=8.314D0,RR=2540D0)
      DIMENSION CD(4)
      C1=CD(1)
C
C*****************************************************************
C SET NEW U HERE
C
C Linear change in UW sub-unit width from Chang's data (in μm)
C
      TC=TK-273
      UW=TC*0.001077D0-0.2681D0
C
C to ensure a lower limit to plate size
C
      IF(UW .LT. 0.05)UW=0.05
C
C Converting from μm into mm.
C UT is sub-unit thickness assumed to be 10 microns.
C
      UT=1.0D-2
      UT2=UT**2
      U=UW*1.0D-3
      U=U*UT2
C
C*********************************************************
      C1=C1/U
      BETA=CD(2)*(1.0D0- CD(4)*XB)
C To prevent -ve beta values:
      IF (BETA .LT. 0.0) BETA=0.0001D0
      C2=CD(3)
      GSM=ND
      GNT= 3.636*(TK-273.15) -2540D0
C
      A=1.0D0/(THETA*GSM*C1)
      B=THETA*BETA
      GAMMA=C2*(GM0-GNT)/(RR*R*TK)
      C=C2/(R*TK)+C2*GM0/(RR*R*TK)
      E=GAMMA/B
      F=A*(B+1.0D0)
      FST=DEXP(C)/F
      GA=1.0D0+(B*PSI)
C
      IF (GA .LT. 0.0D0) THEN
        GA=-GA
      ENDIF
C
      LGA=DLOG(GA)
      GB=(GAMMA*PSI)+E
      GB=-GB
      FGB=FUNCT(GB)
      GC=-E
      FGC=FUNCT(GC)
      G=LGA+FGB-FGC
      HA=1.0D0-PSI
      LHA=DLOG(HA)
      HB=HA*GAMMA
      FHB=FUNCT(HB)
      FHC=FUNCT(GAMMA)
      H=LHA+FHB-FHC
      SND=G*DEXP(E)-H*DEXP(-GAMMA)
C
      NEWF2=FST*SND
      END
C*****************************************************************
C
      SUBROUTINE OMEGA(C,K,W,XBARN,T10,T20,J)
C SUBROUTINE TO CALCULATE THE CARBON CARBON INTERACTION ENERGY IN
C AUSTENITE, AS A FUNCTION OF ALLOY COMPOSITION. BASED ON .MUCG18
C THE ANSWER IS IN JOULES PER MOL.   **7 OCTOBER 1981**
      DOUBLE PRECISION C(8),K(8),W,P(8),B1,B2,Y(8),T10,T20,B3,XBARN
      INTEGER U,J
      B3=0.0D+00
      IF(J .EQ. 1) GOTO 2
      C(8)=K(1)+K(2)+K(3)+K(4)+K(5)+K(6)+K(7)
      C(8)=100.0D+00-C(8)
      C(8)=C(8)/55.84D+00
      C(1)=K(1)/12.0115D+00
      C(2)=K(2)/28.09D+00
      C(3)=K(3)/54.94D+00
      C(4)=K(4)/58.71D+00
```

```
      C(5)=K(5)/95.94D+00
      C(6)=K(6)/52.0D+00
      C(7)=K(7)/50.94D+00
2     B1=C(1)+C(2)+C(3)+C(4)+C(5)+C(6)+C(7)+C(8)
      DO 107 U=2,7
      Y(U)=C(U)/C(8)
107   CONTINUE
      DO 106 U=1,8
      C(U)=C(U)/B1
106   CONTINUE
      XBARN=C(1)
      B2=0.0D+00
      T10=Y(2)*(-3)+Y(3)*2+Y(4)*12+Y(5)*(-9)+Y(6)*(-1)+Y(7)*(-12)
      T20=-3*Y(2)-37.5*Y(3)-6*Y(4)-26*Y(5)-19*Y(6)-44*Y(7)
      P(2)=2013.0341+763.8167*C(2)+45802.87*C(2)**2-280061.63*C(2)**3
     &+3.864D+06*C(2)**4-2.4233D+07*C(2)**5+6.9547D+07*C(2)**6
      P(3)=2012.067-1764.095*C(3)+6287.52*C(3)**2-21647.96*C(3)**3-
     &2.0119D+06*C(3)**4+3.1716D+07*C(3)**5-1.3885D+08*C(3)**6
      P(4)=2006.8017+2330.2424*C(4)-
     54915.32*C(4)**2+1.6216D+06*C(4)**3
     &-2.4968D+07*C(4)**4+1.8838D+08*C(4)**5-5.5531D+08*C(4)**6
      P(5)=2006.834-2997.314*C(5)-37906.61*C(5)**2+1.0328D+06*C(5)**3
     &-1.3306D+07*C(5)**4+8.411D+07*C(5)**5-2.0826D+08*C(5)**6
      P(6)=2012.367-9224.2655*C(6)+33657.8*C(6)**2-566827.83*C(6)**3
     &+8.5676D+06*C(6)**4-6.7482D+07*C(6)**5 +2.0837D+08*C(6)**6
      P(7)=2011.9996-6247.9118*C(7)+5411.7566*C(7)**2
     &+250118.1085*C(7)**3-4.1676D+06*C(7)**4
      DO 108 U=2,7
      B3=B3+P(U)*Y(U)
      B2=B2+Y(U)
108   CONTINUE
      IF (B2 .EQ. 0.0D+00) GOTO 455
      W=(B3/B2)*4.187
      GOTO 456
455   W=8054.0
456   CONTINUE
      RETURN
      END
C C*****************************************************************
C To read in continuous cooling many steps option. The time temperature
C pairs are read from file "cooling".The time in seconds and the
C temperature in Deg.C with a limit of 100 lines.
C Typical "cooling" file:
C       0     600
C       125   350
C       175   300
C       300   20
C
      SUBROUTINE RCOOL(AB4,J2,J3,COTEMP,COTIME)
      IMPLICIT REAL*8 (A-H,K-Z), INTEGER (I,J)
      DOUBLE PRECISION COTEMP(1000),COTIME(1000),RTEMP(100),RTIME(100)
C
      OPEN (UNIT=4, FILE='cooling')
C
      DO 47 J=1,100
        READ(4,*,END=51) RTIME(J), RTEMP(J)
47    CONTINUE
51    J3=J-1
C
C To divide each time and temperature interval into AB4 steps (this is
C set in the main program). STEMP and STIME are arrays of the step
sizes.
C COTIME and COTEMP are arrays of the time temp pairs for the calculation.
C
      DO 48 JA=1,J3-1
        STEMP=(RTEMP(JA)-RTEMP(JA+1))/AB4
        STIME=(RTIME(JA+1)-RTIME(JA))/AB4
C
          DO 49 IA=1,AB4
            I=AB4*(JA-1)+IA
            COTEMP(I)=RTEMP(JA)-STEMP*(IA-1)
            COTIME(I)=RTIME(JA)+STIME*(IA-1)
49          CONTINUE
48    CONTINUE
C
      J2=AB4*(J3-1)+1
        COTEMP(J2)=RTEMP(J3)
        COTIME(J2)=RTIME(J3)
C
C To convert the temperature into K.
C
        DO 52 J5=1,J2
          COTEMP(J5)=COTEMP(J5)+273.0D0
52      CONTINUE
C
        RETURN
        END
C
C*****************************************************************
      SUBROUTINE REED(A)
```

```
      DOUBLE PRECISION A
996   READ(*,*,ERR=999)A
        GOTO 998
999     WRITE(*,997)
997     FORMAT(19X,' Incorrect Input. Try again'/)
        GOTO 996
998   RETURN
      END
C*****************************************************************
      SUBROUTINE REEDI(I)
      INTEGER I
996   READ(*,*,ERR=999)I
        GOTO 998
999     WRITE(*,997)
997     FORMAT(19X,' Incorrect Input. Try again'/)
        GOTO 996
998   RETURN
      END
C*****************************************************************
C Roughly searches for volume fraction for a given temperature.
C
      SUBROUTINE ROUGH(TEMP,DGM,MAXVOL,ND,CNT,XBARN,TTIME,VOL)
      IMPLICIT REAL*8 (A-H,K-Z), INTEGER (I,J)
      DOUBLE PRECISION CNT(4)
C
      DO 10 I=1,100
      VA=I*0.010D0
20    PSI=VA/MAXVOL
      IF (VA .GE. MAXVOL) GOTO 9
      TIME=NEWF2(TEMP,DGM,PSI,MAXVOL,ND,CNT,XBARN,U)
      IF (TIME .GT. TTIME) GOTO 11
10    CONTINUE
9     WRITE (*,200) 'MAXIMUM VOLUME FRACTION REACHED'
      GOTO 12
11    VHIGH=VA
      CALL FINE(TEMP,DGM,MAXVOL,ND,CNT,XBARN,TTIME,VHIGH,VOL)
200   FORMAT (A33)

12    RETURN
      END
C
C*****************************************************************
C Function giving the equilibrium mole fraction of carbon in ferrite
C based on Harry's paper on first order quasichemical theory,
C Metal Science
C
      DOUBLE PRECISION FUNCTION XALPH(T)
      IMPLICIT DOUBLE PRECISION (A-H,L-Z),INTEGER (I-K)
C
        CTEMP=(T-273.0D+00)/900.0D+00
C
      XALPH=0.1528D-02-0.8816D-02*CTEMP+0.2450D-01*CTEMP*CTEMP
     &-0.2417D-01*CTEMP*CTEMP*CTEMP+
     &0.6966D-02*CTEMP*CTEMP*CTEMP*CTEMP
C
      RETURN
      END
```

# A3. Neural Network Model Weights and Training Data

Tables A3.1 - A3.23 contain the weights for normalised variables in the neural network models obtained in Chapter 9. These correspond to equations 9.3 and 9.4 and are listed in the order:

$$\theta_1^{(1)}, w_{1,1}^{(1)} \ldots w_{1,x}^{(1)}$$
$$\theta_2^{(1)}, w_{2,1}^{(1)} \ldots w_{2,x}^{(1)}$$
$$\theta_y^{(1)}, w_{y,1}^{(1)} \ldots w_{y,x}^{(1)}$$
$$\theta^{(2)}, w_1^{(2)} \ldots w_x^{(2)}$$

where $x$ is an input and $y$ identifies a hidden unit. $\theta$ is the bias and is analogous to the constant that appears in linear regression. The superscript notation (1) or (2) refers to which equation the weights are to be used (9.3 or 9.4).

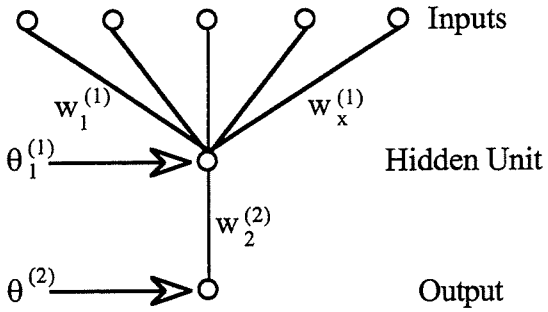


Fig. A3.1: Diagram of the weights and biases in a neural network model containing one hidden unit.

For a single hidden unit there is one weight per input, a further weight for the output and two biases (fig. A3.1).

## A3.1 Retained Austenite

A committee of 8 models with 1, 2 and 4 hidden units. There were 13 input parameters. The weight tables are presented in descending order of fit.

| | | | | | |
|---|---|---|---|---|---|
| 0.000537619 | 0.0492481 | 0.155856 | -0.163249 | 0.00968566 | 0.0238558 |
| 0.0254547 | 0.000629609 | 0.0101369 | -6.57514e-05 | 0.0171435 | -4.59796e-05 |
| 0.0690534 | -0.0187623 | -0.143381 | 6.84789 | | |

Table A3.1: Weights for retained austenite model with 1 hidden unit and a seed of 20.

| | | | | | |
|---|---|---|---|---|---|
| -0.000618133 | -0.033312 | -0.024149 | 0.0287098 | -0.00588781 | -0.0145777 |
| -0.0177492 | -7.80163e-05 | -0.0228914 | 4.46956e-05 | -0.0100962 | 0.00048466 |
| -0.0447813 | 0.0101894 | -0.0631179 | -10.4112 | | |

Table A3.2: Weights for retained austenite model with 1 hidden unit and a seed of 30.

| | | | | | |
|---|---|---|---|---|---|
| 0.00118188 | 0.055009 | -5.85153e-05 | -0.00591788 | 0.00925847 | 0.0236962 |
| 0.0306216 | 6.68017e-05 | 0.0464261 | -7.68356e-05 | 0.0161583 | -0.00157895 |
| 0.0743485 | -0.0155732 | -0.0393078 | 6.36646 | | |

Table A3.3: Weights for retained austenite model with 1 hidden unit and a seed of 40.

| | | | | | |
|---|---|---|---|---|---|
| 0.000222593 | 0.0260571 | 0.0413907 | -0.0450957 | 0.00488746 | 0.0119953 |
| 0.0138537 | 0.000267404 | 0.0135376 | -7.90853e-06 | 0.00846756 | -0.000485586 |
| 0.0354019 | -0.00890418 | -0.0915615 | 13.2335 | | |

Table A3.4: Weights for retained austenite model with 1 hidden unit and a seed of 10.

| | | | | | |
|---|---|---|---|---|---|
| -0.000387199 | -0.027035 | -0.0383296 | 0.0421992 | -0.00499496 | -0.0122402 |
| -0.0142754 | -0.000244748 | -0.0148768 | 1.21177e-05 | -0.00856206 | 0.000533694 |
| -0.0365664 | 0.0090201 | -0.0869032 | -12.7426 | | |

Table A3.5: Weights for retained austenite model with 1 hidden unit and a seed of 1.

| | | | | | |
|---|---|---|---|---|---|
| -0.0749704 | -0.664493 | -0.00963669 | 0.0130402 | -0.0011544 | -0.0149944 |
| 0.000917641 | -3.79915e-05 | -0.00911471 | 0.000335518 | -0.0150464 | 0.00120722 |
| -0.330556 | 0.0167117 | 0.0817853 | -1.2396 | 0.00320618 | -0.00845175 |
| 0.000679623 | 0.00882113 | -0.000472343 | 1.61222e-05 | 0.00375394 | -0.000188349 |
| 0.00175201 | -0.00081917 | -0.62037 | -0.0081591 | -1.5004 | -12.5718 |
| 6.71653 | | | | | |

Table A3.6: Weights for retained austenite model with 2 hidden units and a seed of 1.

| | | | | | |
|---|---|---|---|---|---|
| -0.00145754 | 0.278379 | 6.77434e-05 | -7.89667e-05 | 2.37204e-05 | -0.179214 |
| 0.16877 | -0.00948014 | 0.00448947 | -0.000102669 | 0.00026958 | -0.0010804 |
| -0.160724 | -0.008845 | 0.00744063 | 0.282936 | -0.00124526 | -0.000513944 |
| -3.98739e-05 | 1.53165 | 0.297386 | -0.0198947 | -0.0216873 | 0.000142431 |
| -0.0308321 | 0.000841004 | -0.0686768 | 0.0138116 | -0.251961 | -0.759121 |
| -0.000243622 | 0.000248623 | -4.7183e-05 | -0.769213 | -0.20761 | -0.0297512 |
| -0.0249185 | 0.000190348 | -0.0294688 | 0.00086719 | -0.431274 | 0.0169083 |
| 0.188124 | -0.828297 | 0.00082466 | 0.000465074 | 4.49118e-05 | 0.796212 |
| -0.0938257 | -0.0339469 | -0.00529882 | -0.000153133 | 0.0174383 | -0.00228826 |
| -0.435649 | -0.013044 | -2.0343 | 2.7789 | -4.22994 | -5.26855 |
| 4.17197 | | | | | |

Table A3.7: Weights for retained austenite model with 4 hidden units and a seed of 10.

| | | | | | |
|---|---|---|---|---|---|
| -0.0846068 | 1.49029 | 6.2825e-05 | 0.00371517 | -0.0014524 | -0.014257 |
| 9.41757e-05 | -2.02024e-05 | -0.00690554 | 1.53449e-05 | -0.0048838 | 0.0005947 |
| 0.775639 | 0.0129791 | 0.0928957 | 0.844711 | 2.95236e-05 | -0.00587588 |
| 0.00225618 | 0.02292 | -0.000169505 | 5.0612e-05 | 0.0188285 | -2.60275e-05 |
| 0.0214708 | -0.000802884 | 0.434894 | -0.0251764 | -1.07212 | -4.35859 |
| 7.73141 | | | | | |

Table A3.8: Weights for retained austenite model with 2 hidden units and a seed of 30.

## A3.2 Yield Strength

A committee of 2 models with 2 and 6 hidden units. There were 14 input parameters. The weight tables are presented in descending order of fit.

| | | | | | |
|---|---|---|---|---|---|
| 0.833466 | 0.0651181 | 0.0220706 | 0.883525 | -1.08081 | 0.602749 |
| -0.280207 | -0.746416 | 0.0462761 | 0.38541 | -0.159941 | 0.889689 |
| -0.0250618 | -0.0134693 | 0.0551993 | -0.0367135 | -0.478415 | -0.00462896 |
| -0.218665 | 1.18196 | -0.815816 | 0.0775957 | 0.463187 | 0.0135306 |
| 0.168339 | 0.00917768 | 0.300835 | -0.00547206 | -0.0384006 | -0.094265 |
| 0.584553 | 0.117311 | 0.00290337 | 0.155522 | -0.39347 | -1.00308 |
| 0.229028 | -0.169371 | 0.17294 | 0.397591 | -0.103792 | 0.815778 |
| 0.0260648 | 0.0964815 | 0.916508 | 0.221457 | -0.344788 | 0.00916489 |
| 0.790902 | -0.21815 | 0.845765 | -0.772696 | -0.0915246 | -0.314301 |
| 0.0346805 | -0.0257427 | 0.208533 | 0.0211061 | 0.123069 | -0.133024 |
| 0.448737 | 0.0844361 | -0.0073643 | -0.615781 | -0.0279251 | 0.359423 |
| -0.399805 | 0.319393 | -0.0704633 | -0.276299 | 0.0633161 | -0.505363 |
| 0.00388376 | -0.0743583 | 0.364314 | 0.301421 | 0.100056 | -0.0046915 |
| -0.0598978 | -0.523518 | -0.521318 | -0.540964 | 0.379694 | -0.223113 |
| -0.0697011 | 0.0312937 | 0.027753 | -0.0134397 | 0.226129 | 1.6348 |
| 2.93864 | 15.4753 | 9.7645 | -20.2238 | -15.1793 | -8.85401 |
| 12.0786 | | | | | |

Table A3.9: Weights for yield strength model with 6 hidden units and a seed of 20.

| | | | | | |
|---|---|---|---|---|---|
| 0.382497 | -0.129877 | -0.00310377 | -0.00586001 | 0.0644091 | -0.00329309 |
| 0.229575 | 0.000809014 | 0.272588 | -0.106672 | 2.71199e-06 | 0.00385221 |
| 0.00221424 | 0.00858095 | 0.0146814 | 0.282983 | 0.133082 | 0.00539285 |
| 0.00461024 | -0.0737129 | -0.00348868 | -0.228649 | -0.00384313 | -0.263196 |
| 0.101136 | 3.01162e-06 | 0.00323877 | 0.00307325 | 0.00490695 | -0.00195759 |
| 15.5053 | -24.6265 | -25.2863 | | | |

Table A3.10: Weights for yield strength model with 2 hidden units and a seed of 10.

## A3.3 Ultimate Tensile Strength

A committee of 9 models with 1, 2, 4 and 5 hidden units. There were 14 input parameters. The weight tables are presented in descending order of fit.

| | | | | | |
|---|---|---|---|---|---|
| 0.330451 | 0.0650035 | 0.000172329 | 0.000743799 | 0.0426999 | -0.00208254 |
| 0.0955632 | 0.333062 | 0.00243667 | -0.053599 | 0.278717 | 0.00713798 |
| 0.040887 | -0.153529 | -2.21092e-06 | 0.416127 | -0.0321399 | 0.000185403 |
| 0.00075107 | -0.0458265 | -0.00218427 | -0.0751246 | -0.255225 | 0.00371906 |
| 0.046485 | -0.269145 | 0.018529 | 0.00800755 | 0.110012 | -5.85703e-06 |
| -14.313 | 19.712 | 21.7687 | | | |

Table A3.11: Weights for ultimate tensile strength model with 2 hidden units and a seed of 30.

| | | | | | |
|---|---|---|---|---|---|
| -0.00790874 | -0.27899 | -0.380815 | -0.00837879 | 0.0110555 | 0.000277403 |
| -0.0591783 | 0.298384 | -0.0064766 | 0.00753196 | -0.175968 | 0.232829 |
| 0.00476203 | 0.0758025 | 0.160669 | 0.0713157 | 0.123349 | -0.00158511 |
| -0.0023968 | 0.0729471 | 0.000195555 | 0.11472 | 0.371065 | -0.00854107 |
| -0.00973366 | 0.665898 | -0.277319 | 0.00373672 | -0.347435 | -0.103452 |
| -0.104014 | 0.075222 | 0.288441 | 0.00806166 | 0.0887756 | -0.000478388 |
| 0.111369 | 0.138965 | 0.010195 | 0.00507052 | 0.18011 | 0.190726 |
| -0.00380484 | -0.0547197 | 0.249489 | -0.0625821 | -0.350471 | -0.822786 |
| -0.00426123 | -0.0309256 | -0.000270452 | -0.119319 | 0.407853 | 0.0116776 |
| -0.00320048 | 0.14164 | -0.178668 | -0.00480162 | -0.0935038 | -0.202255 |
| -3.57903 | 17.9258 | 13.12 | -18.055 | -14.774 | |

Table A3.12: Weights for ultimate tensile strength model with 4 hidden units and a seed of 10.

| | | | | | |
|---|---|---|---|---|---|
| -0.422858 | 0.0319458 | -0.00021087 | -0.00073329 | 0.0459186 | 0.00219195 |
| 0.0750037 | 0.25432 | -0.00372226 | -0.0466271 | 0.268292 | -0.0188017 |
| -0.0080941 | -0.109178 | 2.2904e-06 | 0.337369 | 0.0652678 | 0.000195318 |
| 0.000725795 | 0.0427465 | -0.00206709 | 0.0956578 | 0.333037 | 0.0024276 |
| -0.0538223 | 0.277865 | 0.00711284 | 0.0414283 | -0.153048 | 6.67591e-07 |
| -14.4164 | -21.567 | 19.5144 | | | |

Table A3.13: Weights for ultimate tensile strength model with 2 hidden units and a seed of 20.

| | | | | | |
|---|---|---|---|---|---|
| 0.414077 | 0.0645498 | 0.000132397 | 0.000124379 | 0.0361944 | 0.000416954 |
| 0.088581 | 0.262632 | 0.000676634 | -0.0629744 | 0.182401 | 0.00481065 |
| 0.0309148 | -0.127429 | 5.28622e-06 | 0.339601 | -0.0300074 | 0.000194717 |
| 0.000179513 | -0.0319128 | -0.00217507 | -0.0589505 | -0.168181 | 0.00111903 |
| 0.0449846 | -0.135882 | 0.0112183 | 0.00296659 | 0.0777705 | -3.80794e-06 |
| -21.3909 | 27.0904 | 34.0823 | | | |

Table A3.14: Weights for ultimate tensile strength model with 2 hidden units and a seed of 10.

| | | | | | |
|---|---|---|---|---|---|
| -0.0595495 | -0.445077 | -0.0705869 | -0.0474318 | -0.0416904 | -7.91144e-05 |
| -0.264812 | 0.139315 | -0.00381867 | 0.0038929 | -0.047365 | 0.00233703 |
| 0.00203773 | 0.00477637 | 0.134716 | -0.131451 | 0.0405845 | -0.295353 |
| -0.235701 | 0.0891375 | 0.000188541 | 0.134468 | -0.112064 | -0.00167728 |
| 0.000718421 | -0.126167 | 0.00286124 | 0.00178863 | 0.0714577 | -0.0336535 |
| 0.101997 | 0.200008 | 0.0705999 | 0.184312 | 0.0784613 | -1.14708e-05 |
| 0.226274 | 0.235181 | -0.00949705 | -0.000948203 | 0.241071 | 0.00260374 |
| 0.00193701 | -0.0659436 | 0.00563479 | 0.00832074 | 0.248538 | 0.350768 |
| 0.193162 | -0.0291734 | 5.66293e-05 | -0.0303021 | -0.280153 | -0.00109851 |
| 0.00199024 | -0.0537915 | 0.00258196 | 0.00198379 | -0.00744766 | 0.114116 |
| 0.0327456 | 0.00437027 | 0.00112483 | -0.0746368 | -0.089382 | 2.16008e-05 |
| -0.0470753 | 0.0256466 | -0.00243291 | -0.00354489 | 0.00136843 | 0.00258422 |
| 0.00209756 | -0.00890297 | -0.191452 | 1.83842 | 34.5784 | 34.9858 |
| 32.293 | 31.5135 | 36.2214 | | | |

Table A3.15: Weights for ultimate tensile strength model with 5 hidden units and a seed of 30.

| | | | | | |
|---|---|---|---|---|---|
| 7.18574e-06 | 0.0280388 | 7.59428e-05 | 0.000512567 | -0.024596 | -0.00469626 |
| 5.31359e-06 | 0.00291819 | 1.82775e-05 | 0.000201319 | 0.00756748 | 0.0254333 |
| 0.0370985 | 0.00163303 | 0.000521083 | 0.145461 | 15.7738 | |

Table A3.16: Weights for ultimate tensile strength model with 1 hidden unit and a seed of 40.

| | | | | | |
|---|---|---|---|---|---|
| -1.03156e-05 | -0.0299337 | -9.59362e-05 | -0.00051832 | 0.0262458 | 0.00499575 |
| -6.55011e-06 | -0.0031024 | -5.5072e-06 | -0.000209644 | -0.00810931 | -0.0271363 |
| -0.0395977 | -0.00173411 | -0.000537129 | 1.79358e-08 | -0.00478871 | -1.51709e-05 |
| -8.18318e-05 | 0.00413994 | 0.00078927 | -2.01436e-06 | -0.000489717 | -8.71733e-07 |
| -3.30848e-05 | -0.00128215 | -0.00432819 | -0.00619712 | -0.000273773 | -8.50061e-05 |
| 0.145213 | -14.4224 | -2.27307 | | | |

Table A3.17: Weights for ultimate tensile strength model with 2 hidden units and a seed of 1.

| | | | | | |
|---|---|---|---|---|---|
| 1.65084e-05 | 0.0308895 | 9.16619e-05 | 0.00051376 | -0.0270636 | -0.00514023 |
| -4.83468e-06 | 0.00319935 | 1.65749e-05 | 0.000207847 | 0.00837274 | 0.0279874 |
| 0.0408203 | 0.00177353 | 0.000545944 | 0.14503 | 14.3322 | |

Table A3.18: Weights for ultimate tensile strength model with 1 hidden unit and a seed of 10.

| | | | | | |
|---|---|---|---|---|---|
| -1.64456e-05 | -0.0306521 | -0.000110695 | -0.000539852 | 0.0268581 | 0.00510879 |
| 1.2462e-07 | -0.00318281 | 2.75937e-07 | -0.000228107 | -0.00830785 | -0.0277747 |
| -0.0405104 | -0.00176914 | -0.000557189 | 0.145054 | -14.4427 | |

Table A3.19: Weights for ultimate tensile strength model with 1 hidden unit and a seed of 20.

## A3.4 Uniform Elongation

A committee of 4 models with 1, and 2 hidden units. There were 15 input parameters. The weight tables are presented in descending order of fit.

| | | | | | |
|---|---|---|---|---|---|
| 0.324847 | 0.0973322 | -0.0155961 | -0.00377167 | -0.109419 | -0.0107546 |
| -0.00278642 | -0.0800611 | -0.0907129 | 0.00540165 | 0.00578078 | 0.151846 |
| 7.42742e-07 | 0.061911 | 0.00160607 | 0.140966 | 0.455974 | -0.179658 |
| -0.0102144 | 0.0457155 | 0.185331 | 0.0134962 | -0.000809051 | 0.14539 |
| 0.176815 | -0.0104836 | -0.0139256 | -0.277414 | 4.04587e-07 | -0.0905203 |
| 0.00252468 | -0.249592 | -44.8759 | 71.915 | 52.6989 | |

Table A3.20: Weights for uniform elongation model with 2 hidden units and a seed of 10.

| | | | | | |
|---|---|---|---|---|---|
| -0.315328 | -0.0949368 | -0.0446524 | 0.0666553 | 0.0925177 | 0.0298967 |
| 0.00289897 | 0.0811414 | 0.112951 | -0.0157874 | -0.00977704 | -0.156625 |
| -3.5625e-07 | -0.0766632 | -0.00197732 | -0.160224 | -0.443606 | 0.165402 |
| 0.113 | -0.150423 | -0.148241 | -0.0452427 | 0.00129753 | -0.138891 |
| -0.205261 | 0.0266137 | 0.0195545 | 0.271559 | -7.03894e-07 | 0.111001 |
| -0.00185935 | 0.268884 | -47.2655 | -77.0965 | -57.6806 | |

Table A3.21: Weights for uniform elongation model with 2 hidden units and a seed of 30.

| | | | | | |
|---|---|---|---|---|---|
| 0.443427 | -0.175431 | -0.0500678 | 0.0874011 | 0.16705 | 0.0317634 |
| -0.00115285 | 0.145285 | 0.191251 | -0.0201657 | -0.0160811 | -0.279178 |
| -6.33213e-07 | -0.104119 | 0.00205703 | -0.262669 | -0.335752 | -0.102225 |
| -0.00622443 | 0.0283703 | 0.106208 | 0.0226152 | 0.00309402 | 0.0861644 |
| 0.105905 | -0.0119387 | -0.00766359 | -0.163897 | 1.44118e-06 | -0.0748531 |
| -0.002016 | -0.159382 | -43.9973 | 52.7813 | -68.735 | |

Table A3.22: Weights for uniform elongation model with 2 hidden units and a seed of 20.

| | | | | | |
|---|---|---|---|---|---|
| -8.90282e-06 | 0.0201785 | 0.000353638 | 0.00250617 | -0.00868515 | 4.45312e-05 |
| 8.04338e-06 | -1.04504e-06 | -3.621e-06 | 0.047013 | 0.00599365 | -0.0138024 |
| 0.000635666 | -0.052187 | -0.0158835 | 0.000140863 | 0.137076 | -6.60567 |

Table A3.23: Weights for uniform elongation model with 1 hidden unit and a seed of 40.

## A3.5 Training Data

Table A3.24 contains data, measured at British Steel, which were used in developing the neural networks. T1 - T5 are the temperatures, in °C, as shown in fig. A3.2.

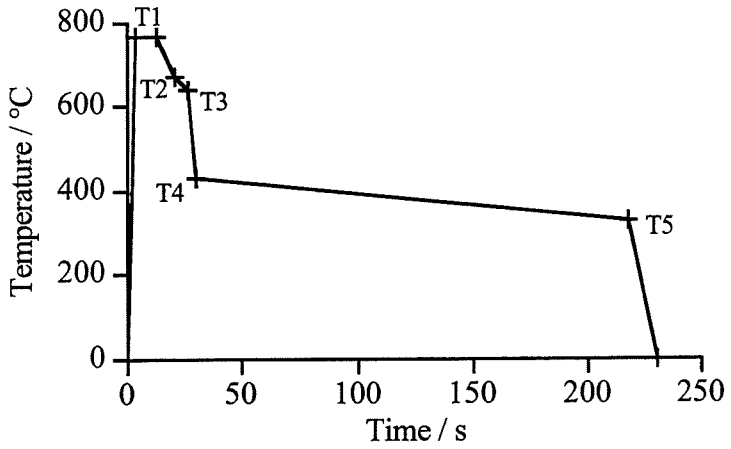


Fig. A3.2: Simplified annealing cycle indicating temperatures used as inputs to the neural network models.

The time (in seconds) at temperature T1 is t1 and t1/2 etc. are the times between the temperatures T1 and T2 etc. C, Mn and Si are the alloying elements in wt.% and RA is the % retained austenite. YS and UTS are the yield strength and ultimate tensile strength in N $mm^{-2}$ and U-El is the uniform elongation in %.

| T1 | T2 | T3 | T4 | T5 | t1 | t1/2 | t2/3 | t3/4 | t4/5 | C | Mn | Si | RA | YS | TS | U-El |
|---|---|---|---|---|---|---|---|---|---|---|---|---|---|---|---|---|
| 766.4 | 676.0 | 676.0 | 424.0 | 355.0 | 9.30 | 2.80 | 0.00 | 2.80 | 105.90 | 0.171 | 1.440 | 1.410 | 13.7 | 368.2 | 734.7 | 13.1 |
| 762.7 | 664.0 | 664.0 | 448.0 | 352.0 | 9.30 | 2.80 | 0.00 | 2.80 | 105.90 | 0.171 | 1.440 | 1.410 | 12.4 | 368.2 | 734.7 | 13.1 |
| 790.4 | 702.0 | 702.0 | 519.0 | 271.0 | 9.35 | 2.85 | 0.00 | 1.80 | 192.15 | 0.171 | 1.440 | 1.410 | 12.5 | 383.7 | 713.4 | 14.8 |
| 779.9 | 708.0 | 708.0 | 507.0 | 315.0 | 9.35 | 2.85 | 0.00 | 1.80 | 192.15 | 0.171 | 1.440 | 1.410 | 11.8 | 383.7 | 713.4 | 14.8 |
| 759.4 | 696.0 | 696.0 | 487.0 | 248.0 | 9.10 | 2.80 | 0.00 | 5.05 | 186.90 | 0.171 | 1.440 | 1.410 | 13.2 | 360.4 | 730.4 | 17.4 |
| 778.4 | 694.0 | 694.0 | 503.0 | 301.0 | 9.10 | 2.80 | 0.00 | 5.05 | 186.90 | 0.171 | 1.440 | 1.410 | 13.0 | 360.4 | 730.4 | 17.4 |
| 730.3 | 670.0 | 670.0 | 501.0 | 324.0 | 9.80 | 2.15 | 0.00 | 4.60 | 186.60 | 0.171 | 1.440 | 1.410 | 12.0 | 427.9 | 690.2 | 15.3 |
| 721.4 | 690.0 | 690.0 | 482.0 | 252.0 | 9.80 | 2.15 | 0.00 | 4.60 | 186.60 | 0.171 | 1.440 | 1.410 | 11.7 | 427.9 | 690.2 | 15.3 |
| 694.9 | 662.0 | 662.0 | 395.0 | 299.0 | 9.05 | 2.85 | 0.00 | 5.05 | 186.10 | 0.171 | 1.440 | 1.410 | 4.7 | 457.2 | 603.7 | 19.7 |
| 705.5 | 661.0 | 661.0 | 459.0 | 333.0 | 9.05 | 2.85 | 0.00 | 5.05 | 186.10 | 0.171 | 1.440 | 1.410 | 4.3 | 457.2 | 603.7 | 19.7 |
| 803.4 | 705.0 | 705.0 | 439.0 | 183.0 | 9.10 | 2.85 | 0.00 | 3.90 | 188.25 | 0.171 | 1.440 | 1.410 | 11.2 | 332.3 | 778.7 | 18.9 |
| 793.2 | 686.0 | 686.0 | 440.0 | 203.0 | 9.10 | 2.85 | 0.00 | 3.90 | 188.25 | 0.171 | 1.440 | 1.410 | 14.8 | 332.3 | 778.7 | 18.9 |
| 802.8 | 706.0 | 706.0 | 448.0 | 218.0 | 9.55 | 3.10 | 0.00 | 3.20 | 187.70 | 0.171 | 1.440 | 1.410 | 6.9 | 390.7 | 913.2 | 13.5 |
| 790.0 | 693.0 | 693.0 | 474.0 | 231.0 | 9.55 | 3.10 | 0.00 | 3.20 | 187.70 | 0.171 | 1.440 | 1.410 | 8.8 | 390.7 | 913.2 | 13.5 |
| 734.9 | 680.0 | 680.0 | 517.0 | 185.0 | 9.70 | 3.20 | 0.00 | 5.70 | 190.80 | 0.171 | 1.440 | 1.410 | 10.1 | 412.3 | 697.4 | 14.4 |
| 750.0 | 682.0 | 682.0 | 401.0 | 201.0 | 9.80 | 2.10 | 0.00 | 7.10 | 186.20 | 0.171 | 1.440 | 1.410 | 10.2 | 390.9 | 704.4 | 15.9 |
| 759.9 | 700.0 | 700.0 | 489.0 | 210.0 | 9.40 | 2.50 | 0.00 | 9.25 | 185.05 | 0.171 | 1.440 | 1.410 | 11.0 | 421.6 | 719.8 | 15.5 |
| 716.7 | 658.0 | 658.0 | 510.0 | 253.0 | 9.05 | 3.50 | 0.00 | 2.17 | 52.58 | 0.171 | 1.440 | 1.410 | 3.0 | 452.5 | 581.0 | 18.8 |
| 712.3 | 664.0 | 664.0 | 502.0 | 256.0 | 9.05 | 3.50 | 0.00 | 2.17 | 52.58 | 0.171 | 1.440 | 1.410 | 4.5 | 452.5 | 581.0 | 18.8 |
| 711.2 | 664.0 | 664.0 | 502.0 | 256.0 | 8.00 | 4.55 | 0.00 | 2.50 | 51.90 | 0.171 | 1.440 | 1.410 | 2.8 | 455.6 | 576.9 | 18.9 |
| 705.8 | 655.0 | 655.0 | 509.0 | 257.0 | 8.00 | 4.55 | 0.00 | 2.50 | 51.90 | 0.171 | 1.440 | 1.410 | 4.6 | 455.6 | 576.9 | 18.9 |
| 773.7 | 696.0 | 696.0 | 522.0 | 195.0 | 9.40 | 3.20 | 0.00 | 2.50 | 189.95 | 0.171 | 1.440 | 1.410 | 11.1 | 402.5 | 711.3 | 19.0 |
| 753.5 | 671.0 | 671.0 | 535.0 | 216.0 | 9.40 | 3.20 | 0.00 | 2.50 | 189.85 | 0.171 | 1.440 | 1.410 | 13.2 | 402.5 | 711.3 | 19.0 |
| 725.5 | 607.0 | 607.0 | 369.0 | 353.0 | 9.80 | 3.50 | 0.00 | 4.70 | 67.45 | 0.171 | 1.440 | 1.410 | 9.9 | 447.5 | 664.9 | 18.5 |
| 725.7 | 612.0 | 612.0 | 381.0 | 323.0 | 9.80 | 3.50 | 0.00 | 4.70 | 67.45 | 0.171 | 1.440 | 1.410 | 8.9 | 447.5 | 664.9 | 18.5 |
| 750.0 | 636.0 | 636.0 | 360.0 | 363.0 | 9.65 | 3.35 | 0.00 | 4.20 | 67.75 | 0.171 | 1.440 | 1.410 | 12.6 | 386.4 | 740.2 | 20.4 |
| 740.3 | 632.0 | 632.0 | 364.0 | 348.0 | 9.65 | 3.35 | 0.00 | 4.20 | 67.75 | 0.171 | 1.440 | 1.410 | 12.2 | 386.4 | 740.2 | 20.4 |
| 737.8 | 640.0 | 640.0 | 441.0 | 182.0 | 9.75 | 5.75 | 0.00 | 2.85 | 188.75 | 0.171 | 1.440 | 1.410 | 11.9 | 456.7 | 700.3 | 19.4 |
| 736.5 | 648.0 | 648.0 | 446.0 | 204.0 | 9.75 | 5.75 | 0.00 | 2.85 | 188.75 | 0.171 | 1.440 | 1.410 | 9.9 | 456.7 | 700.3 | 19.4 |
| 736.5 | 648.0 | 648.0 | 446.0 | 204.0 | 9.75 | 5.75 | 0.00 | 2.50 | 189.10 | 0.171 | 1.440 | 1.410 | 8.4 | 454.4 | 674.0 | 16.3 |
| 807.3 | 669.0 | 669.0 | 486.0 | 191.0 | 9.75 | 5.80 | 0.00 | 3.70 | 188.40 | 0.171 | 1.440 | 1.410 | 12.0 | 335.7 | 804.0 | 14.8 |
| 740.7 | 666.0 | 666.0 | 464.0 | 177.0 | 9.45 | 5.45 | 0.00 | 3.05 | 188.75 | 0.171 | 1.440 | 1.410 | 11.2 | 392.3 | 677.7 | 14.8 |
| 709.5 | 648.0 | 648.0 | 447.0 | 168.0 | 9.45 | 5.45 | 0.00 | 3.05 | 188.75 | 0.171 | 1.440 | 1.410 | 4.3 | 392.3 | 677.7 | 14.8 |
| 739.8 | 659.0 | 659.0 | 468.0 | 196.0 | 9.45 | 5.80 | 0.00 | 2.80 | 188.80 | 0.171 | 1.440 | 1.410 | 13.5 | 454.9 | 745.9 | 17.5 |

Table A3.24: Database on which the mechanical properties and retained austenite neural network models (Chapter 9) were trained.

| T1 | T2 | T3 | T4 | T5 | t1 | t1/2 | t2/3 | t3/4 | t4/5 | C | Mn | Si | RA | YS | TS | U-El |
|---|---|---|---|---|---|---|---|---|---|---|---|---|---|---|---|---|
| 712.6 | 642.0 | 642.0 | 466.0 | 172.0 | 9.45 | 5.80 | 0.00 | 2.90 | 188.80 | 0.171 | 1.440 | 1.410 | 6.8 | 454.9 | 745.9 | 17.5 |
| 791.0 | 665.0 | 665.0 | 444.0 | 170.0 | 9.40 | 5.50 | 0.00 | 3.05 | 188.60 | 0.171 | 1.440 | 1.410 | 12.7 | 342.1 | 802.9 | 17.5 |
| 807.9 | 665.0 | 665.0 | 450.0 | 182.0 | 9.40 | 5.50 | 0.00 | 3.05 | 188.60 | 0.171 | 1.440 | 1.410 | 12.7 | 342.1 | 802.9 | 17.5 |
| 746.5 | 661.0 | 661.0 | 414.0 | 200.0 | 9.45 | 5.50 | 0.00 | 3.00 | 188.60 | 0.171 | 1.440 | 1.410 | 13.0 | 393.2 | 724.9 | 20.5 |
| 721.3 | 646.0 | 646.0 | 430.0 | 158.0 | 9.45 | 5.50 | 0.00 | 3.00 | 188.60 | 0.171 | 1.440 | 1.410 | 8.6 | 393.2 | 724.9 | 20.5 |
| 813.4 | 696.0 | 696.0 | 278.0 | 135.0 | 9.10 | 5.50 | 0.00 | 4.30 | 185.80 | 0.171 | 1.440 | 1.410 | 9.3 | 419.5 | 984.8 | 12.9 |
| 789.1 | 672.0 | 672.0 | 205.0 | 151.0 | 9.15 | 5.50 | 0.00 | 8.85 | 182.50 | 0.171 | 1.440 | 1.410 | 9.5 | 435.6 | 937.1 | 7.4 |
| 793.3 | 593.0 | 593.0 | 275.0 | 186.0 | 9.15 | 5.50 | 0.00 | 8.85 | 182.50 | 0.171 | 1.440 | 1.410 | 10.0 | 435.6 | 937.1 | 7.4 |
| 807.6 | 680.0 | 680.0 | 456.0 | 155.0 | 9.15 | 5.20 | 0.00 | 3.30 | 188.20 | 0.171 | 1.440 | 1.410 | 10.6 | 377.7 | 822.8 | 18.5 |
| 790.8 | 696.0 | 696.0 | 278.0 | 135.0 | 9.10 | 5.50 | 0.00 | 4.30 | 185.80 | 0.171 | 1.440 | 1.410 | 9.3 | 419.5 | 984.8 | 12.9 |
| 789.1 | 672.0 | 672.0 | 205.0 | 151.0 | 9.15 | 5.50 | 0.00 | 8.85 | 182.50 | 0.171 | 1.440 | 1.410 | 9.5 | 435.6 | 937.1 | 7.4 |
| 793.3 | 593.0 | 593.0 | 275.0 | 186.0 | 9.15 | 5.50 | 0.00 | 8.85 | 182.50 | 0.171 | 1.440 | 1.410 | 10.0 | 435.6 | 937.1 | 7.4 |
| 807.6 | 680.0 | 680.0 | 456.0 | 155.0 | 9.15 | 5.20 | 0.00 | 3.30 | 188.20 | 0.171 | 1.440 | 1.410 | 10.6 | 377.7 | 822.8 | 18.5 |
| 790.8 | 670.0 | 670.0 | 410.0 | 198.0 | 9.15 | 5.20 | 0.00 | 3.30 | 188.20 | 0.171 | 1.440 | 1.410 | 11.4 | 377.7 | 822.8 | 18.5 |
| 790.8 | 670.0 | 670.0 | 410.0 | 198.0 | 9.10 | 5.20 | 0.00 | 3.35 | 188.20 | 0.171 | 1.440 | 1.410 | 11.4 | 384.9 | 845.3 | 15.3 |
| 794.5 | 682.0 | 682.0 | 476.0 | 198.0 | 9.10 | 5.20 | 0.00 | 3.35 | 188.20 | 0.171 | 1.440 | 1.410 | 12.3 | 384.9 | 845.3 | 15.3 |
| 787.8 | 669.0 | 669.0 | 431.0 | 148.0 | 9.15 | 5.50 | 0.00 | 2.75 | 188.45 | 0.171 | 1.440 | 1.410 | 12.4 | 325.5 | 828.1 | 19.8 |
| 795.4 | 659.0 | 659.0 | 423.0 | 183.0 | 9.15 | 5.50 | 0.00 | 2.75 | 188.45 | 0.171 | 1.440 | 1.410 | 12.6 | 325.5 | 828.1 | 19.8 |
| 788.9 | 665.0 | 665.0 | 496.0 | 161.0 | 9.10 | 5.50 | 0.00 | 3.10 | 188.30 | 0.171 | 1.440 | 1.410 | 11.0 | 417.9 | 752.6 | 17.8 |
| 790.4 | 666.0 | 666.0 | 511.0 | 206.0 | 9.10 | 5.50 | 0.00 | 3.10 | 188.30 | 0.171 | 1.440 | 1.410 | 8.1 | 417.9 | 752.6 | 17.8 |
| 790.4 | 666.0 | 666.0 | 511.0 | 206.0 | 9.15 | 3.50 | 0.00 | 5.05 | 188.30 | 0.171 | 1.440 | 1.410 | 12.1 | 413.3 | 816.6 | 14.4 |
| 769.4 | 669.0 | 669.0 | 510.0 | 193.0 | 9.15 | 3.50 | 0.00 | 5.05 | 188.30 | 0.171 | 1.440 | 1.410 | 11.9 | 413.3 | 816.6 | 14.4 |
| 773.9 | 688.0 | 688.0 | 495.0 | 197.0 | 9.15 | 5.50 | 0.00 | 3.40 | 188.15 | 0.171 | 1.440 | 1.410 | 12.2 | 375.2 | 763.9 | 17.6 |
| 770.9 | 699.0 | 699.0 | 520.0 | 200.0 | 9.15 | 5.50 | 0.00 | 3.40 | 188.15 | 0.171 | 1.440 | 1.410 | 12.5 | 375.2 | 763.9 | 17.6 |
| 772.8 | 684.0 | 684.0 | 507.0 | 160.0 | 9.10 | 5.50 | 0.00 | 3.00 | 186.75 | 0.171 | 1.440 | 1.410 | 6.9 | 330.5 | 823.1 | 13.3 |
| 785.1 | 702.0 | 702.0 | 502.0 | 183.0 | 9.10 | 5.50 | 0.00 | 3.00 | 186.75 | 0.171 | 1.440 | 1.410 | 13.6 | 330.5 | 823.1 | 13.3 |
| 785.1 | 702.0 | 702.0 | 502.0 | 183.0 | 9.10 | 5.50 | 0.00 | 2.50 | 188.20 | 0.171 | 1.440 | 1.410 | 12.7 | 341.5 | 787.1 | 12.8 |
| 740.1 | 686.0 | 686.0 | 489.0 | 192.0 | 9.10 | 5.50 | 0.00 | 2.50 | 188.20 | 0.171 | 1.440 | 1.410 | 13.2 | 341.5 | 787.1 | 12.8 |
| 756.4 | 694.0 | 694.0 | 431.0 | 158.0 | 9.10 | 5.50 | 0.00 | 3.40 | 187.70 | 0.171 | 1.440 | 1.410 | 4.9 | 381.9 | 859.4 | 17.4 |
| 790.9 | 708.0 | 708.0 | 462.0 | 204.0 | 9.10 | 5.50 | 0.00 | 3.40 | 187.70 | 0.171 | 1.440 | 1.410 | 12.5 | 381.9 | 859.4 | 17.4 |
| 771.5 | 697.0 | 697.0 | 449.0 | 154.0 | 9.15 | 5.55 | 0.00 | 3.35 | 187.35 | 0.171 | 1.440 | 1.410 | 6.0 | 378.4 | 756.8 | 19.2 |
| 802.9 | 710.0 | 710.0 | 479.0 | 192.0 | 9.15 | 5.55 | 0.00 | 3.35 | 187.35 | 0.171 | 1.440 | 1.410 | 12.2 | 378.4 | 756.8 | 19.2 |
| 802.9 | 710.0 | 710.0 | 479.0 | 192.0 | 9.10 | 5.50 | 0.00 | 3.35 | 187.95 | 0.171 | 1.440 | 1.410 | 12.2 | 381.4 | 762.9 | 20.0 |
| 775.7 | 698.0 | 698.0 | 484.0 | 191.0 | 9.10 | 5.50 | 0.00 | 3.35 | 187.95 | 0.171 | 1.440 | 1.410 | 12.6 | 381.4 | 762.9 | 20.0 |

Table A3.24 (continued): Database on which the mechanical properties and retained austenite neural network models (Chapter 9) were trained.

| T1 | T2 | T3 | T4 | T5 | t1 | t1/2 | t2/3 | t3/4 | t4/5 | C | Mn | Si | RA | YS | TS | U-El |
|---|---|---|---|---|---|---|---|---|---|---|---|---|---|---|---|---|
| 777.5 | 673.0 | 673.0 | 425.0 | 160.0 | 9.10 | 5.50 | 0.00 | 3.60 | 188.80 | 0.171 | 1.440 | 1.410 | 4.7 | 341.6 | 755.5 | 15.9 |
| 783.5 | 678.0 | 678.0 | 456.0 | 206.0 | 9.10 | 5.50 | 0.00 | 3.60 | 188.80 | 0.171 | 1.440 | 1.410 | 13.4 | 341.6 | 755.5 | 15.9 |
| 783.5 | 678.0 | 678.0 | 456.0 | 206.0 | 9.10 | 5.45 | 0.00 | 3.65 | 187.90 | 0.171 | 1.440 | 1.410 | 13.8 | 336.5 | 763.1 | 18.8 |
| 759.0 | 672.0 | 672.0 | 457.0 | 182.0 | 9.10 | 5.45 | 0.00 | 3.65 | 187.90 | 0.171 | 1.440 | 1.410 | 13.1 | 336.5 | 763.1 | 18.8 |
| 759.5 | 640.0 | 640.0 | 461.0 | 210.0 | 9.10 | 5.70 | 0.00 | 4.00 | 188.00 | 0.196 | 1.470 | 1.580 | 10.2 | 326.0 | 859.0 | 20.4 |
| 762.2 | 647.0 | 647.0 | 465.0 | 182.0 | 9.10 | 5.70 | 0.00 | 4.00 | 188.00 | 0.196 | 1.470 | 1.580 | 10.3 | 316.0 | 831.0 | 20.7 |
| 785.5 | 662.0 | 662.0 | 479.0 | 197.0 | 9.10 | 5.60 | 0.00 | 4.00 | 188.00 | 0.196 | 1.470 | 1.580 | 9.3 | 342.0 | 884.0 | 19.1 |
| 767.6 | 644.0 | 644.0 | 356.0 | 181.0 | 8.80 | 5.40 | 0.00 | 4.40 | 188.00 | 0.196 | 1.470 | 1.580 | 9.8 | 345.0 | 835.0 | 16.9 |
| 768.3 | 689.0 | 689.0 | 490.0 | 298.0 | 9.50 | 5.40 | 0.00 | 4.00 | 188.00 | 0.196 | 1.470 | 1.580 | 9.8 | 384.0 | 745.0 | 17.9 |
| 784.2 | 690.0 | 690.0 | 457.0 | 299.0 | 9.20 | 5.70 | 0.00 | 4.00 | 188.00 | 0.196 | 1.470 | 1.580 | 10.5 | 350.0 | 865.0 | 17.7 |
| 757.5 | 665.0 | 665.0 | 410.0 | 263.0 | 9.10 | 5.50 | 0.00 | 4.20 | 188.00 | 0.196 | 1.470 | 1.580 | 11.1 | 320.0 | 850.0 | 21.3 |
| 780.1 | 668.0 | 668.0 | 422.0 | 302.0 | 9.10 | 5.80 | 0.00 | 4.00 | 188.00 | 0.196 | 1.470 | 1.580 | 10.3 | 371.0 | 895.0 | 15.3 |
| 728.5 | 676.0 | 659.0 | 494.0 | 341.0 | 8.40 | 8.40 | 5.70 | 3.50 | 188.00 | 0.171 | 1.420 | 1.730 | 12.0 | 521.0 | 721.0 | 19.6 |
| 735.7 | 680.0 | 658.0 | 466.0 | 321.0 | 8.60 | 8.30 | 5.70 | 3.50 | 188.00 | 0.171 | 1.420 | 1.730 | 15.0 | 486.0 | 717.0 | 18.9 |
| 750.9 | 680.0 | 653.0 | 448.0 | 326.0 | 8.70 | 8.30 | 5.60 | 3.50 | 188.00 | 0.171 | 1.420 | 1.730 | 14.9 | 466.0 | 722.0 | 22.0 |
| 765.9 | 685.0 | 660.0 | 457.0 | 336.0 | 8.80 | 8.30 | 5.60 | 3.50 | 188.00 | 0.171 | 1.420 | 1.730 | 14.3 | 465.0 | 741.0 | 21.3 |
| 800.9 | 692.0 | 661.0 | 452.0 | 324.0 | 8.70 | 8.30 | 5.80 | 3.50 | 188.00 | 0.249 | 0.940 | 1.650 | 14.6 | 372.0 | 817.0 | 20.5 |
| 748.3 | 683.0 | 667.0 | 474.0 | 332.0 | 8.70 | 8.30 | 5.70 | 3.50 | 188.00 | 0.249 | 0.940 | 1.650 | 9.4 | 508.0 | 766.0 | 23.0 |
| 729.4 | 675.0 | 653.0 | 450.0 | 325.0 | 8.70 | 8.20 | 5.90 | 3.50 | 188.00 | 0.249 | 0.940 | 1.650 | 5.2 | 556.0 | 721.0 | 16.9 |
| 740.3 | 675.0 | 657.0 | 458.0 | 322.0 | 8.80 | 8.30 | 5.70 | 3.50 | 188.00 | 0.249 | 0.940 | 1.650 | 11.5 | 542.0 | 780.0 | 22.7 |
| 707.5 | 652.0 | 633.0 | 463.0 | 329.0 | 8.70 | 8.30 | 5.70 | 3.50 | 188.00 | 0.255 | 1.940 | 1.210 | 18.1 | 616.0 | 921.0 | 16.7 |
| 713.1 | 659.0 | 638.0 | 460.0 | 331.0 | 8.60 | 8.40 | 5.70 | 3.60 | 188.00 | 0.255 | 1.940 | 1.210 | 17.7 | 568.0 | 1003.0 | 16.3 |
| 710.7 | 653.0 | 635.0 | 479.0 | 313.0 | 8.50 | 8.40 | 5.70 | 3.60 | 188.00 | 0.255 | 1.940 | 1.210 | 20.7 | 550.0 | 964.0 | 19.3 |
| 706.1 | 649.0 | 632.0 | 463.0 | 344.0 | 8.60 | 8.40 | 5.70 | 3.50 | 188.00 | 0.255 | 1.940 | 1.210 | 19.4 | 562.0 | 950.0 | 18.1 |
| 730.5 | 658.0 | 645.0 | 492.0 | 351.0 | 8.60 | 8.40 | 5.80 | 3.50 | 188.00 | 0.255 | 1.940 | 1.210 | 15.5 | 550.0 | 935.0 | 16.7 |
| 720.1 | 667.0 | 648.0 | 485.0 | 339.0 | 8.70 | 8.30 | 5.70 | 3.50 | 188.00 | 0.238 | 1.430 | 1.490 | 11.6 | 615.0 | 857.0 | 21.1 |
| 728.4 | 668.0 | 649.0 | 457.0 | 350.0 | 8.80 | 8.20 | 5.70 | 3.50 | 188.00 | 0.238 | 1.430 | 1.490 | 14.4 | 572.0 | 839.0 | 22.0 |
| 734.0 | 672.0 | 647.0 | 455.0 | 332.0 | 8.70 | 8.30 | 5.70 | 3.50 | 188.00 | 0.238 | 1.430 | 1.490 | 16.8 | 533.0 | 890.0 | 22.6 |
| 764.6 | 670.0 | 640.0 | 430.0 | 330.0 | 8.70 | 8.40 | 5.60 | 3.50 | 188.00 | 0.238 | 1.430 | 1.490 | 15.1 | 447.0 | 904.0 | 22.1 |

Table A3.24 (continued): Database on which the mechanical properties and retained austenite neural network models (Chapter 9) were trained.

# A4. The Austenite Formation Program

## A4.1 Contents

A4.2 : MAP† format description of the computer program, the inputs and outputs.

A4.3 : The FORTRAN source code.

[† MAP is The Materials Algorithms Project which consists of a perpetual FORTRAN library of complete programs and elementary subroutines and functions that enable the user to develop new concepts in materials science and metallurgy using existing methods as a foundation.

Web page: http://www.msm.cam.ac.uk/map/mapmain.html
Email: map@msm.cam.ac.uk]

## A4.2 MAP Format of Austenite Formation Program

Program aust.for

### A4.2.1 Provenance

Naomi Chester, April 1996. Incorporating an $Ac_1$ and $Ac_3$ neural network model by L. Gavard and H.K.D.H. Bhadeshia, November 1994.

New subroutine: vaust.

### A4.2.2 Purpose

To calculate the volume fraction of austenite formed during intercritical annealing. This uses Gavard et al.'s [1] neural network model for predicting the $Ac_1$ and $Ac_3$ temperatures as a function of alloy content and heating rate.

### A4.2.3 Description

The key part of this model is subroutine VAUST which contains equation 6.1 (Chapter 6) for the calculation the volume fraction of austenite with knowledge of the $Ac_1$, $Ac_3$ and intercritical annealing temperatures.

The constants used in this equation were optimised using data from dilatation curves taken during heating of three different alloys at a variety of heating rates.

In the main program the composition, heating rate and annealing temperatures are input. The subroutines WEIGH and WEIGHB read in the weight files for the neural network models and subroutines AC1TEMP and AC3TEMP calculate the $Ac_1$ and $Ac_3$ temperatures respectively.

The constants for the austenite equation are set and, for each annealing temperature, the austenite volume fraction is calculated.

### A4.2.4 References

[1] Gavard, L., Bhadeshia, H.K.D.H., MacKay, D.J.C. and Suzuki, S. (1996): *Materials Science and Technology*, **12**, 453-463.

### A4.2.5 Parameters

*A4.2.5.1 Inputs*

ACINPUT - file containing the compositions (wt.%), heating rate (°C $s^{-1}$), number of annealing temperatures and list of temperatures (°C).

AW - real, an array containing the input data from the ACINPUT file:
AW(1) - AW(21) Compositions (wt.%): C, Si, Mn, S, P, Cu, Ni, Cr, Mo, Nb, V, Ti, Al, B, W, As, Sn, Zr, Co, N, O.
AW(22) Heating rate (°C $s^{-1}$)
AW(23) Number of annealing temperatures.
AW(24) - onwards Annealing temperatures (°C).

AC1 - file containing data required for the $Ac_1$ neural network [Gavard et al., 1996; MAP].

AC3 - file containing data required for the $Ac_3$ neural network [Gavard et al., 1996; MAP].

*A4.2.5.2 Outputs*
AC1 - real, the $Ac_1$ temperature (°C).

AC3 - real, the $Ac_3$ temperature (°C).

PRE - real, the predicted volume fraction of austenite (for each annealing temperature).

### A4.2.6 Example

*A4.2.6.1 Example input file*

| | |
|---|---|
| 0.19 | C (wt.%) |
| 1.61 | Si |
| 1.45 | Mn |
| 0.00 | S |
| 0.00 | P |
| 0.00 | Cu |
| 0.0 | Ni |
| 0.0 | Cr |
| 0.0 | Mo |
| 0.0 | Nb |
| 0.0 | V |
| 0.00 | Ti |
| 0.00 | Al |
| 0.000 | B |
| 0.0 | W |
| 0.000 | As |
| 0.000 | Sn |
| 0.000 | Zr |
| 0.0 | Co |
| 0.000 | N |
| 0.000 | O |
| 30.0 | Heating rate (°C/s) |
| 2 | No. of temperatures |
| 800 | List of temperatures (°C) |
| 900 | |

*A4.2.6.2 Example output*

| | | | |
|---|---|---|---|
| Carbon | 0.190 wt.% | Silicon | 1.610 wt.% |
| Manganese | 1.450 wt.% | Sulphur | 0.000 wt.% |
| Phosphorus | 0.000 wt.% | Copper | 0.000 wt.% |
| Nickel | 0.000 wt.% | Chromium | 0.000 wt.% |
| Molybdenum | 0.000 wt.% | Niobium | 0.0000 wt.% |
| Vanadium | 0.000 wt.% | | |
| Titanium | 0.000 wt.% | Aluminium | 0.000 wt.% |
| Boron | 0.0000 wt.% | Tungsten | 0.000 wt.% |
| Arsenic | 0.000 wt.% | Tin | 0.000 wt.% |
| Zirconium | 0.000 wt.% | Cobalt | 0.000 wt.% |
| Nitrogen | 0.0000 wt.% | Oxygen | 0.0000 wt.% |

| Temp(°C) | Ac1(°C) | Ac3(°C) | Heat rate(°C/s) | Predicted v.f. Austenite |
|---|---|---|---|---|
| 800.0 | 702.1 | 935.7 | 30.0000 | 0.48045 |
| 900.0 | 702.1 | 935.7 | 30.0000 | 0.86995 |

### A4.2.7 Auxiliary routines

ac1temp

ac3temp

vaust

weigh

weighb

writo

### A4.2.8 Key words

$Ac_1$ temperature

$Ac_3$ temperature

Austenite

Intercritical annealing

```
C Program to calculate the amount of austenite formed during
C intercritical annealing. This uses L. Gavard's neural network
C model for predicting Ac1 and Ac3 temperatures.
C Naomi Chester April 1996.
C
      PROGRAM MAIN
      IMPLICIT DOUBLE PRECISION (A-H,L-Z),INTEGER (I-K)
      DIMENSION W1(4,22), W2(4),THETA1(4),
     &  AMIN(23),AMAX(23),AW(100), W1B(2,22), W2B(2),THETB1(2),
     &  CNT(3),TEMP(2000),AC1(2000),AC3(2000)

      OPEN(UNIT=1, FILE='ACINPUT')
      DO 1 I=1,100
         READ(1,*,END=2)AW(I)
1     CONTINUE
2     IDAT=AW(23)
C
      CALL WEIGH(AMIN,AMAX,THETA1,THETA2,W1,W2)
      CALL AC1TEMP(AW,W1,W2,THETA1,THETA2,AMIN,AMAX,Y1)

      CALL WEIGHB(AMIN,AMAX,THETB1,THETB2,W1B,W2B)
      CALL AC3TEMP(AW,W1B,W2B,THETB1,THETB2,AMIN,AMAX,Y3) C
      DO 13 J1=1,IDAT
         AC1(J1)=Y1
         AC3(J1)=Y3
         II=23+J1
         TEMP(J1)=AW(II)
13    CONTINUE
C
C Set constants
      CNT(1)=0.20631D-01
      CNT(2)=0.84904D+00
      CNT(3)=0.11905D-06
C
      WRITE(*,996)
      DO 20 JA=1, IDAT
         IF (TEMP(JA) .GT. AC3(JA)) THEN
           PRE=1.0D0
           GOTO 22
         ENDIF
         IF (TEMP(JA) .LT. AC1(JA)) THEN
           PRE=0.0D0
           GOTO 22
         ENDIF
         CALL VAUST(PRE,CNT,JA,TEMP,AC1,AC3)
22       WRITE (*,997) TEMP(JA),AC1(JA),AC3(JA),AW(22),PRE
20    CONTINUE
C
996   FORMAT (10X,'  Temp(C)       Ac1(C)      Ac3(C)',
     & '  Heat rate(C/s)  Predicted v.f. Austenite')
997   FORMAT (6X,3F12.1,F10.4,6X,D14.5)
C
      END
C*************************************************************
C Copyright H K D H Bhadeshia, University of Cambridge
C November 1994
C
C Based on paper by Gavard, Bhadeshia, MacKay and Suzuki
C Materials Science and Technology, Vol. 12, 1996, 453-463.
C
C To use the output from neural network analysis
C to predict austenite formation in steels
C
C The coefficients, in the form of weights are stored in a
C file called AC1 in unit 4
C
C X contains normalized values of the input variables
C W1 and W2 contain the weights
C THETA1 and THETA2 are the biases
C Y is the output (normalized)
C AMIN and AMAX contain the minimum and maximum unnormalized
C values of the input variables and of the output
C
      SUBROUTINE AC1TEMP(AW,W1,W2,THETA1,THETA2,AMIN,AMAX,Y)
      IMPLICIT REAL*8(A-H,K-Z), INTEGER(I,J)
      DOUBLE PRECISION  W1(4,22), W2(4),THETA1(4), H(4),
     &  AMIN(23),AMAX(23),AW(100),X(22)
C
C Remember to set matrix dimensions according to number of
C inputs and number of hidden units. Currently set at 100
C and 10 respectively.
C
      AVER=1.2
C
C Set error at +- 20% for 95 % error limits
C units are in joules
      ERROR=40.0d+00
C
C Set number of inputs
```

```
        IN=22
C
C Set number of hidden units
        IHID=4
C
C Set number of heating rates calculated IIMAX=5
        II=0
C
C Read a set of unnormalized inputs
C
        DO 222 I=1,IN
            X(I)=AW(I)
222     CONTINUE
        CALL WRITO(AW)
C
C One of the variables, in this case the heating rate HT, is to be
C varied, so at first normalize IN-1 variables
C
        DO 1 I=1,IN-1
            X(I) = ((X(I) -AMIN(I))/(AMAX(I)-AMIN(I)))-0.5D+00
1       CONTINUE
C
        HT = AW(22)*1.0D0
        X(IN) = ((HT -AMIN(IN))/(AMAX(IN)-AMIN(IN)))-0.5D+00
C
C IERROR = 0 implies that all inputs are within the range of the
C training dataset for the neural network. Thus, the 95% confidence
C error bars amount to about +- 11%
C
C IERROR = 1 implies that some inputs are out of the range of the
C training dataset for the neural network. THhe 95% confidence
C error bars MAY then be greater than +-11%.
C See Gavard, Bhadeshia, MacKay and Suzuki for details
C
        DO 11 J=1,IN
            IF(X(J) .LT. -0.5D+00 .OR. X(J) .GT. 0.5D+00) THEN
              IERROR=1
              GOTO 12
            ELSE
              IERROR=0
            ENDIF
11      CONTINUE
12      CONTINUE
C
C Read all weights, and theta parameters
C
C Do calculation of the normalized output value for the given set
C of normalized input
C
C First equation
          DO 6 I=1,IHID
             A=0.0D+00
C
             DO 5 J=1,IN
               A=A+W1(I,J)*X(J)
5            CONTINUE
C
             H(I)=DTANH(A+THETA1(I))
6         CONTINUE
C
C Second equation
          A=0.0D+00
          DO 7 I=1,IHID
             A=A+W2(I)*H(I)
7         CONTINUE
C
          Y = A+THETA2
          Y=(Y+0.5D+00)*(AMAX(IN+1)-AMIN(IN+1))+AMIN(IN+1)
C
C Prevent temperature from acquiring a negative value
          IF(Y .LT. 0.0D+00)Y=0.0D+00
C
90        FORMAT(F10.2)
C
300       WRITE(*,*)
C
          RETURN
          END
C*****************************************************************
C*****************************************************************
C To read the weights obtained from the neural network
C representation of weld metal Charpy toughness
C H K D H Bhadeshia, University of Cambridge
C
          SUBROUTINE WEIGH(AMIN,AMAX,THETA1,THETA2,W1,W2)
          IMPLICIT REAL*8(A-H,K-Z), INTEGER(I,J)
          DOUBLE PRECISION W1(4,22), W2(4),THETA1(4),
         &  AMIN(23),AMAX(23)
C
          AVER=1.2
```

```
C
C Set number of inputs
      IN=22
C
C Set number of hidden units
      IHID=4
C
      OPEN(UNIT=2, FILE='AC1')
      DO 20 I=1,IN+1
         READ(2,*) IDUM, AMIN(I),AMAX(I)
20    CONTINUE
C
      DO 2 I=1,IHID
         READ(2,*) THETA1(I)
         DO 3 J=1,IN
           READ(2,*) W1(I,J)
3        CONTINUE
2     CONTINUE
C
       READ(2,*) THETA2
       DO 21 I=1,IHID
          READ(2,*) W2(I)
21     CONTINUE
C
      RETURN
      END
C*********************************************************************
C*********************************************************************
C Printing for the neural network representation of Ac1 and Ac3
C temperatures.
C H K D H Bhadeshia, University of Cambridge
C
      SUBROUTINE WRITO(A)
C
      DOUBLE PRECISION A(100)

      WRITE(*,4) A(1),A(2),A(3),A(4), A(5),A(6),A(7),A(8),A(9),
     &      A(10),A(11)
C
      WRITE(*,923) A(12),A(13),A(14),A(15),
     &      A(16),A(17),A(18),A(19),A(20),
     &      A(21)
C
4      FORMAT(
     &10X,' Carbon              ',F6.3,'  wt.%',
     &9X,' Silicon             ',F6.3,'  wt.%'/
     &10X,' Manganese          ',F6.3,'  wt.%',9X,
     &' Sulphur                ',F6.3,'  wt.%'/
     &10X,' Phosphorus         ',F6.3,'  wt.%',
     &9X,' Copper              ',F6.3,'  wt.%'/
     &10X,' Nickel             ',F6.3,'  wt.%',9X,
     &' Chromium               ',F6.3,'  wt.%'/
     &10X,' Molybdenum         ',F6.3,'  wt.%   ',6X,
     &' Niobium                ',F6.4,' wt.%   '/
     &10X,' Vanadium           ',F6.3,'  wt.%   ',9X)

923      FORMAT(
     &10X,' Titanium           ',F6.3,'  wt.%',
     &9X,' Aluminium           ',F6.3,'  wt.%'/
     &10X,' Boron              ',F6.4,' wt.%',9X,
     &' Tungsten               ',F6.3,'  wt.%'/
     &10X,' Arsenic            ',F6.3,'  wt.%',
     &9X,' Tin                 ',F6.3,'  wt.%'/
     &10X,' Zirconium          ',F6.3,'  wt.%',9X,
     &' Cobalt                 ',F6.3,'  wt.%'/
     &10X,' Nitrogen           ',F6.4,' wt.%   ',6X,
     &' Oxygen                 ',F6.4,' wt.%   '/)

      RETURN
      END

C*********************************************************************
C Copyright H K D H Bhadeshia, University of Cambridge
C November 1994
C
C Based on paper by Gavard, Bhadeshia, MacKay and Suzuki
C Materials Science and Technology, Vol. 12, 1996, 453-463.
C
C Program predicts the Ac3 temperature of steel as a function of
C the chemical composition and the heating rate
C It does not give detailed error bars,
C which are discussed in the original paper.
C
C To use the output from neural network analysis
C to predict austenite formation in steels
C
C The coefficients, in the form of weights are stored in a file
C called AC3 in unit 4
C
```

```
C X contains normalized values of the input variables
C W1 and W2 contain the weights
C THETB1 and THETB2 are the biases
C Y is the output (normalized)
C AMIN and AMAX contain the minimum and maximum unnormalized values
C of the input variables and of the output
C
        SUBROUTINE AC3TEMP(AW,W1B,W2B,THETB1,THETB2,AMIN,AMAX,Y)
        IMPLICIT REAL*8(A-H,K-Z), INTEGER(I,J)
        DOUBLE PRECISION W1B(2,22), W2B(2),THETB1(2), H(4),
       &  AMIN(23),AMAX(23),AW(100),X(22)
C
C Remember to set matrix dimensions according to number of inputs
C and number of hidden units. Currently set at 100 and 10
C respectively.
C
        AVER=1.2
C
C Set error at +- 20% for 95 % error limits
C units are in joules
        ERROR=40.0d+00
C
C Set number of inputs
        IN=22
C
C Set number of hidden units
        IHID=2
C
C Set number of heating rates calculated IIMAX=5
        II=0
C
C Read a set of unnormalized inputs
        DO 222 I=1,IN
            X(I)=AW(I)
222     CONTINUE
C
C One of the variables, in this case the heating rate HT, is to be
C varied, so at first normalize IN-1 variables
        DO 1 I=1,IN-1
            X(I) = ((X(I) -AMIN(I))/(AMAX(I)-AMIN(I)))-0.5D+00
1       CONTINUE
C
        HT =AW(22)*1.0D0
        X(IN) = ((HT -AMIN(IN))/(AMAX(IN)-AMIN(IN)))-0.5D+00
C
C IERROR = 0 implies that all inputs are within the range of the
C training dataset for the neural network. Thus, the 95%
C confidence error bars amount to about +- 11%
C
C IERROR = 1 implies that some inputs are out of the range of the
C training dataset for the neural network. THhe 95% confidence
C error bars MAY then be greater than +-11%. See Gavard, Bhadeshia,
C MacKay and Suzuki for details
C
        DO 11 J=1,IN
            IF(X(J) .LT. -0.5D+00 .OR. X(J) .GT. 0.5D+00) THEN
               IERROR=1
               GOTO 12
            ELSE
               IERROR=0
            ENDIF
11      CONTINUE
12      CONTINUE
C
C Read all weights, and theta parameters
C
C Do calculation of the normalized output value for the given set
C of normalized input
C
C First equation
C
         DO 6 I=1,IHID
            A=0.0D+00
C
            DO 5 J=1,IN
              A=A+W1B(I,J)*X(J)
5           CONTINUE
C
            H(I)=DTANH(A+THETB1(I))
6        CONTINUE
C
C Second equation
C
         A=0.0D+00
         DO 7 I=1,IHID
            A=A+W2B(I)*H(I)
7        CONTINUE
C
         Y = A+THETB2
         Y=(Y+0.5D+00)*(AMAX(IN+1)-AMIN(IN+1))+AMIN(IN+1)
```

```
C
C Prevent temperature from acquiring a negative value
C
          IF(Y .LT. 0.0D+00)Y=0.0D+00
C
90        FORMAT(F10.2)
C
300       WRITE(*,*)
C
          RETURN
          END
C*****************************************************************
C*****************************************************************
C To read the weights obtained from the neural network
C representation of weld metal Charpy toughness
C H K D H Bhadeshia, University of Cambridge
C
          SUBROUTINE WEIGHB(AMIN,AMAX,THETB1,THETB2,W1B,W2B)
          IMPLICIT REAL*8(A-H,K-Z), INTEGER(I,J)
          DOUBLE PRECISION W1B(2,22), W2B(2),THETB1(2),
      &   AMIN(23),AMAX(23)
C
          AVER=1.2
C
C Set number of inputs
          IN=22
C
C Set number of hidden units
          IHID=2
C
          OPEN(UNIT=2, FILE='AC3')
          DO 20 I=1,IN+1
             READ(2,*) IDUM, AMIN(I),AMAX(I)
20        CONTINUE
C
          DO 2 I=1,IHID
             READ(2,*) THETB1(I)
             DO 3 J=1,IN
               READ(2,*) W1B(I,J)
c              WRITE(*,91) W1B(I,J)
3            CONTINUE
2         CONTINUE
C
          READ(2,*) THETB2
          DO 21 I=1,IHID
             READ(2,*) W2B(I)
21        CONTINUE
C
          RETURN
          END
C*****************************************************************
          SUBROUTINE VAUST(VA,CNT,JA,TEMP,AC1,AC3)
          IMPLICIT DOUBLE PRECISION (A-H,L-Z),INTEGER (I-K)
          DIMENSION CNT(3),TEMP(2000),AC1(2000),AC3(2000)
C
          TT=(TEMP(JA)-AC1(JA))/(AC3(JA)-AC1(JA))
          TTS=TT**CNT(2)
          TB=CNT(3)/(TEMP(JA)+273.0D0)
          C1=CNT(1)*DEXP(-TB)
          TOP=DEXP(-C1*TTS)
          TC=CNT(3)/(AC3(JA)+273.0D0)
          Q=EXP(-TC)
          C3=1-DEXP(-C1*Q)
          VA=(1.0D0-TOP)/C3
          RETURN
          END
C
C CNT(1) IS K0, CNT(2) IS N, CNT(3) IS Q/k, C1 IS K AND C3 IS A
C often C1=CNT(1) for optimum constants. This is because TB is
C very small and so exp(TB) is approx. 1.
```

# References


Ali, A., Ahmed, M., Hashmi, F.H. and Khan, A.Q. (1993): *Metallurgical Transactions A*, **24A**, 2145-2150.

Ali, A. and Bhadeshia, H.K.D.H. (1989): *Materials Science and Technology*, **5**, 398-402.

Ali, A. and Bhadeshia, H.K.D.H. (1990): *Materials Science and Technology*, **6**, 781-784.

Andrews, K.W. (1956): *Journal of The Iron and Steel Institute*, **184**, 414-425.

Andrews, K.W. (1965): *Journal of The Iron and Steel Institute*, **203**, 721-727.

Ashley, C. (1995): *Automotive Engineer*, **20**, No. 6, 28-32.

Ashley, S. (1997): *Mechanical Engineering*, **119**, No. 2, 56-61.

Atkinson, C., Akbay, T. and Reed, R.C. (1995): *Acta Metall. Mater.*, **43**, 2013-2031.

Automotive Engineer (1994): *Automotive Engineer*, **19**, No. 1, 20.

Bandoh, S., Matsumura, O. and Sakuma, Y. (1988): *Transactions ISIJ*, **28**, 569-574.

Bell, T. and Owen, W.S. (1967): *Trans. Met. Soc. AIME*, **239**, 1940.

Bhadeshia, H.K.D.H. (1980): *Acta Metallurgica*, **28**, 1103-1114.

Bhadeshia, H.K.D.H. (1981a): *Acta Metallurgica*, **29**, 1117-1130.

Bhadeshia, H.K.D.H. (1981b): *Metal Science*, **15**, 175-177.

Bhadeshia, H.K.D.H. (1981c): *Metal Science*, **15**, 178-180.

Bhadeshia, H.K.D.H. (1982a): *Metal Science*, **16**, 159-165.

Bhadeshia, H.K.D.H. (1982b): *Metal Science*, **16**, 167-169.

Bhadeshia, H.K.D.H. (1982c): *Journal De Physique*, **43**, No. 12, 443-447.

Bhadeshia, H.K.D.H. (1984): *Int. Conf. on Phase Transformations in Ferrous Alloys*, (Edited by Marder, A.R. and Goldstein, J.I.), ASM, Cleveland, OH, 335-340.

Bhadeshia, H.K.D.H. (1988): *Proc. Int. Conf.: Phase Transformations '87* (Edited by Lorimer, G.W.), Institute of Metals, London, 309-314.

Bhadeshia, H.K.D.H. (1992): *"Bainite in Steels"*, Institute of Materials, London.

Bhadeshia, H.K.D.H. (1995): *Materials World*, (March 1995), 128-130.

Bhadeshia, H.K.D.H. and Christian, J.W. (1990): *Metallurgical Transactions A*, **21A**, 767-797.

Bhadeshia, H.K.D.H., David, S.A., Vitek, J.M. and Reed, R.W. (1991): *Materials Science and Technology*, **7**, 686-698.

Bhadeshia, H.K.D.H. and Edmonds, D.V. (1979): *Metallurgical Transactions A*, **10A**, 895-907.

Bhadeshia, H.K.D.H. and Edmonds, D.V. (1980): *Acta Metallurgica*, **28**, 1265-1273.

Bhadeshia, H.K.D.H. and Edmonds, D.V. (1983a): *Metal Science*, **17**, 411-419.

Bhadeshia, H.K.D.H. and Edmonds, D.V. (1983b): *Metal Science*, **17**, 420-425.

Bhadeshia, H.K.D.H., MacKay, D.J.C. and Svensson, L.-E., (1995): *Materials Science and Technology*, **11**, 1046-1051.

Bhadeshia, H.K.D.H., Svensson, L.-E. and Gretoft, B (1987): *Proceedings of an International Conference on Welding Metallurgy of Structural Steels*, (Edited by J.Y. Koo), The Metallurgical Society of AIME, 517-529.

Bhadeshia, H.K.D.H. and Waugh, A.R. (1981): *Proceedings of International Conference on Solid Phase Transformations*, (Edited by Aaronson, H.I.), TMS AIME, Pennsylvania, 993-997.

Bhadeshia, H.K.D.H. and Waugh, A.R. (1982): *Acta Metallurgica*, **30**, 775-784.

Bilby, B.A. and Christian, J.W. (1956): "*The Mechanism of Phase Transformations in Metals*", The Institute of Metals, London, 121-172.

Binnig, G., Quate, C.F. and Gerber, C. (1986): *Physical Review Letters*, **56**, No. 9, 930-933.

Bowles, J.S. and Mackenzie, J.K. (1954): *Acta Metallurgica*, **2**, 129-137.

Bradley, J.R., Rigsbee, J.M. and Aaronson, H.I. (1977): *Metallurgical Transactions A*, **8A**, 323-333.

Brandt, M.L. and Olson, G.B. (1992): *Gilbert R. Speich Symposium*, (Edited by Krauss, G. and Rappas, P.E.), AIME, Warrendale, PA, USA, 257-265.

Bressanelli, J.P. and Moskowitz, A. (1966): *Trans ASM*, **59**, 223-239.

Cahn, J.W. (1956): *Acta Metallurgica*, **4**, 449-459.

Chang, L.C. and Bhadeshia, H.K.D.H. (1994): *Materials Science and Engineering*, **A184**, L17-L19.

Chang, L.C. (1995): *"Bainite Transformations and Novel Bainitic Rail Steels"*, (Ph.D. Thesis, Cambridge, 1995), 46.

Christian, J.W. (1975): *"The Theory of Transformations in Metals and Alloys"*, second edition, Pergamon Press, Oxford.

Christian, J.W. (1979): "*ICOMAT '79*", International Conference on Martensitic Transformations, Cambridge, Massachusetts, 220-234.

Cullity, B.D. (1978): *"Elements of X-ray diffraction"*, second edition, Addison-Wesley Publishing, 410-415.

Edmonds, D.V. and Cochrane, R.C. (1990): *Metallurgical Transactions A*, **21A**, 1527-1540.

Fisher, J.C. (1949): *Metals Transactions*, **185**, 688-690.

Fowler, R.H. and Guggenhiem, E.A. (1939): *"Statistical Thermodynamics"*, New York,

Cambridge University Press.

Gavard, L., Bhadeshia, H.K.D.H., MacKay, D.J.C. and Suzuki, S. (1996): *Materials Science and Technology*, **12**, 453-463.

Girault, E. (1997): Ph.D. Thesis, Department of Metallurgy and Materials Engineering, K.U. Leven, Belgium, to be submitted in 1998.

Hanzaki, A.Z., Hodgsson, P.D. and Yue, S. (1995): *ISIJ International*, **35**, No.1, 79-85.

Hillert, M. (1953): *Acta Metallurgica*, **1**, 764-766.

Hillert, M., Nilsson, K. and Torndahl, L.-E. (1971): *Journal of the Iron and Steel Institute*, **209**, 49-66.

Hultgren, A. (1947): *Transactions of the ASM*, **39**, 915-985.

Imai, Y., Izumiyama, M. and Tsuchiys, M (1965): *Sci. Rep. Res. Inst. Tohoku University*, **A17**, 173.

Jacques, P., Girault, E, Van Humbeeck, J., Aernoudt, E and Delannay, F. (1997): *IV European Symposium on Martensitic Transformations (Esomat '97)*, Enschede, The Netherlands, July 1997, in press.

Khan, S.A. and Bhadeshia, H.K.D.H. (1990a): *Materials Science and Engineering*, **A129**, 257-272.

Khan, S.A. and Bhadeshia, H.K.D.H. (1990b): *Metallurgical Transactions A*, **21A**, 859-875.

Kinsman, K.R. and Aaronson, H.I. (1967): *"Transformation and Hardenability in Steels"*, Climax Molybdenum Co., Ann Arbor, Michigan, 33-38.

Ko, T. and Cottrell, S.A. (1952): *Journal of the Iron and Steel Institute*, **172**, 307-313.

Koistinen, D.P. and Marburger, R.E. (1959): *Acta Metallurgica*, **7**, 59-60.

Kruska, J.U. and Freier, K. (1994): *Proceedings of the Symposium on "High-Strength Sheet Steels for the Automobile industry"*, (Edited by Pradhan, R.) Iron and Steel Society, Warrendale, 1994, 159.

Kuban, M.B., Hawbolt, E.B. and Brimacombe, J.K. (1986): *Metallurgical Transactions A*, **17A**, 1493-1503.

Lacher, J.R. (1937): *Proc. Cambridge Philos. Soc.*, **33**, 518.

Lin, F., Meier, D., Hoyt, D., Van Slambrouck, T. and Leckenby, J. (1993): *Materials World*, (July 1993), 393-395.

Lowe, K. (1997): *Materials World*, **5**, No. 5, 272-273.

MacKay, D.J.C. (1992a): *Neural Computation*, **4**, 415.

MacKay, D.J.C. (1992b): *Neural Computation*, **4**, 448.

MacKay, D.J.C. (1992c): *Neural Computation*, **4**, 698.

MacKay, D.J.C. (1993): *Darwin College Journal*, Cambridge, 81.

MacKay, D.J.C. (1997): *"Mathematical Modelling of Weld Phenomena"*, (Editors: Cerjak, H. and Bhadeshia, H.K.D.H.), The Institute of Materials, 359-389.

Magee, C.L. (1969): *"Phase Transformations"*, American Society of Metals, Metals Park, OH, 115-156.

MAP: Materials Algorithms Project, http://www.msm.cam.ac.uk/map/mapmain.html

Marder, A.R. (1981): *Metallurgical Transactions A*, **12A**, 1569-1579.

Matsumura, O., Sakuma, Y. and Takechi, H. (1987): *Trans. ISIJ*, **27**, 570-579.

McDougall, P.G. and Wayman, C.M. (1992): *"Martensite"*, ASM International, (Edited by Olson and Owen), 81.

Miihkinen, V.T.T. and Edmonds, D.V. (1987a): *Materials Science and Technology*, **3**, 422-431.

Miihkinen, V.T.T. and Edmonds, D.V. (1987b): *Materials Science and Technology*, **3**, 432-440.

Mujahid, S.A. and Bhadeshia, H.K.D.H. (1992): *Acta Metall. Matter.*, **40**, No. 2, 389-396.

Nelson, J.B. and Riley, D.P. (1945): *Proc. Phys. Soc.*, (London), **57**, 160.

Nishiyama, Z. (1978): *"Martensitic Transformation"*, (Edited by Fine, M., Meshii, M. and Wayman, C.), Academic Press Inc., London, 273-275.

Ohmori, Y. (1971): *Transactions ISIJ*, **11**, 95-101.

Oldaker, A.R. (1997): Private communication, Rolls-Royce Motor Cars Limited.

Owen, W.S. (1954): *Trans. ASM*, **46**, 812.

Papadimitriou, G. and Foularis, G (1997): *IV European Symposium on Martensitic Transformations (Esomat '97)*, Enschede, The Netherlands, July 1997, in press.

Reed-Hill, R.E. (1973): *"Physical Metallurgy Principles"*, second edition, University Series on Basic Engineering, D. Van Nostrand Company, New York, 524-527.

Rees, G.I. and Bhadeshia, H.K.D.H. (1992a): *Materials Science and Technology*, **8**, 985-993.

Rees, G.I. and Bhadeshia, H.K.D.H. (1992b): *Materials Science and Technology*, **8**, 994-996.

Rectorys, K. (1969): *"Survey of Applicable Mathematics"*, ILIFFE Books Ltd, London, 543.

Russell, K.C. (1969): *Acta Metallurgica*, **17**, 1123-1131.

Sakuma, Y., Matsumura, O. and Takechi, H. (1991): *Metallurgical Transactions A*, **22A**, 489-498.

Sakuma, Y., Matlock, D.K. and Krauss, G. (1992): *Metallurgical Transactions A*, **23A**, 1221-1232.

Sakuma, Y., Matlock, D.K. and Krauss, G. (1993): *Materials Science and Technology*, **9**, 718-724.

Sandvik, B.P.J. (1982): *Metallurgical Transactions A*, **13A**, 777-787.

Scheil, E. (1935): *Arch. Eisenhuttenwesen*, **12**, 565.

Self, P., Bhadeshia, H.K.D.H. and Stobbs, W.M.(1981): *Ultramicroscopy*, **6**, 29-40.

Seiko Instruments (1993): *"SPA300 Scanning Probe Microscope Operation Manual"*, Seiko Instruments, Inc.

Srinivasan, G.R. and Wayman, C.M. (1968): *Acta Metallurgica*, **16**, 621-636.

Swallow, E. and Bhadeshia, H.K.D.H. (1996): *Materials Science and Technology*, **12**, 121-125.

Takahashi, M. and Bhadeshia, H.K.D.H. (1991): *Materials Transactions, JIM*, **32**, No. 8, 689-696.

Tamura, I., Maki, T. and Hato, H. (1970): *Transactions ISIJ*, **10**, 163-172.

Tomita, Y. and Okawa, T. (1993): *Materials Science and Engineering*, **A172**, 145-151.

Tsukatani, I., Hashimoto, S. and Inoue, T. (1991): *ISIJ International*, **31**, No. 9, 992-1000.

Wakasa, K. and Nakamura, T. (1977): *Journal of Materials Science*, **12**, 1438-1442.

Yang, J.R. and Bhadeshia, H.K.D.H. (1989): *Materials Science and Engineering*, **A118**, 115-170.

Young, C.H. and Bhadeshia, H.K.D.H. (1994): *Materials Science and Technology*, **10**, 209-214.

Zackay, V.F., Parker, E.R., Fahr, D. and Busch, R. (1967): *Transactions of The ASM*, **60**, 252-259.

Zener, C. (1946): *Trans. Met. Soc. AIME*, **167**, 550-583.